



SCIENTIFIC PROGRAM



Feb 24 - Mar 01

2019

22ND INTERNATIONAL WORKSHOP ON QUANTITATIVE MSK IMAGING (QMSKI)

MESSAGE FROM THE ORGANIZING COMMITTEE CO-CHAIRS



Dear Delegates,

We warmly welcome you to the 22nd International Workshop on Quantitative Musculoskeletal Imaging (QMSKI) hosted in the heart of the Canadian Rocky Mountains. This meeting brings together researchers from around the world to present scientific advancements in musculoskeletal imaging.

This year, a major decision was made to change the name from the International Bone Densitometry Workshop. This change reflects a healthy growth in the competency of our community from bone density towards all musculoskeletal imaging. This growth comes from our strength as a community to bring together fundamental science, pragmatic clinical knowledge, and novel imaging technologies for the betterment of musculoskeletal health.

We hope your time at the workshop inspires ideas, challenges your paradigms, and builds productive connections. Welcome to QMSKI 2019.

Your conference chairs,



Dr. Steven Boyd
McCaig Institute for Bone and Joint Health
University of Calgary



Dr. Angela M. Cheung
Centre of Excellence in Skeletal Health Assessment
University of Toronto

OUR SPONSORS

This workshop would not have been possible without financial support from our industry and academic partners. Please, visit their booths and thank them for their continued support of our workshop.

GOLD SPONSORS



BRONZE SPONSORS



EXHIBITORS



AWARD SPONSORS & SUPPORTERS



CONFERENCE HISTORY

The first International Bone Densitometry Workshop (IBDW) was held in San Francisco, USA in 1979, organized by Dr. Harry K. Genant, MD. This was just 8 years after the EMI head scanner prototype was developed and 8 years before the introduction of the first commercially available DXA scanner. The meeting brought together international researchers and clinicians to ask the question how these technologies could improve the lives of patients with skeletal diseases.

Over the years, the conference changed in scope to include all musculoskeletal imaging research and was renamed to the International Workshop on Quantitative Musculoskeletal Imaging (QMSKI) in 2019. The 22nd workshop will carry the torch by asking how new technologies and scientific findings can be used to better understand musculoskeletal health. Specifically, the application of technologies such as SPA/SXA, DPA/DXA/VXA, QCT/vQCT/HRCT, pQCT/HRpQCT, μ CT, QUS, MRI/QMR, FEA/ μ FEA to measuring BMD, BMC, macrostructure, microstructure, and bone strength are of continued scientific interest. This year, new technologies and applications are appearing. Entire scientific session on artificial intelligence and microgravity are possible. Application and insight grow abundant in our search for understanding and treating musculoskeletal disease.

Although times change, one constant is that to understand musculoskeletal diseases, one must peer inside the body. Our future is bright as new imaging technologies develop, quantitative analysis becomes more sophisticated, and the next generation of scholars dare to push the frontier.

ORGANIZING COMMITTEE

CO-CHAIRS

Dr. Steven Boyd

Dr. Angela Cheung, MD

LOCAL ORGANIZING COMMITTEE

Danielle Whittier

Bryce Besler

Sarah Manske

Andres Kroker

Lauren Burt

Tannis Kemp

Mariya Shtil

Ryan Michael Plett

Alyssa Mudryk

Ying Zhu

Chantal de Bakker

Jacob George

Andrew Michalski

James Tomasson

SCIENTIFIC SESSION CHAIRS

Sharmila Majumdar

Pascal Laugier

Bert van Rietbergen

Lindsie Blencowe

Gianluca Lori

Mariya Shtil

John Shepherd

Ling Qin

Claus Glüer

Bryce Besler

Rachel Whyte

Felicitas Flohr

Harry Genant

Angela Cheung

Harry van Lenthe

Steven Boyd

Ali Ghasem-Zadeh

Maximilian Rummeler

Mary Bouxsein

Ralph Müller

Andy Kin On Wong

Nicholas Mikolajewicz

Chantal de Bakker

Lindsay Loundagin

Itabashi Akira

James Griffith,

Klaus Engelke

Fjola Johannsdottir

Leon de Jong

Ariane Scheuren

SCIENTIFIC ADVISORY BOARD



Bert van Rietbergen
Eindhoven University of Technology



Claus Glüer
Kiel University



Harry Genant
University of California, San Francisco



James Griffith
Chinese University of Hong Kong



John Shepherd
University of Hawaii



Klaus Engelke
University of Erlangen



Mary Bouxsein
Harvard University



Pascal Laugier
Pierre and Marie Curie University



Ralph Müller
ETH Zurich



Sharmila Majumdar
University of California, San Francisco



Xiaoguang Cheng
Beijing Jishuitan Hospital

SCIENTIFIC REVIEW COMMITTEE



Akira Itabashi
Kubojima Clinic



Andreas Mandelis
University of Toronto



Andy Kin On Wong
University of Toronto



David Cooper
University of Saskatoon



Didier Hans
University of Lausanne



Elise Morgan
Boston University



Françoise Peyrin
University Lyon



Harry van Lenthe
KU Leuven



Heather Macdonald
University of British Columbia



Julio Carballido-Gamio
University of Colorado Denver



Kay Raum
Charité Universitätsmedizin Berlin



Leigh Gabel
University of Calgary



Ling Qin
Chinese University of Hong Kong



Marta Erlandson
University of Saskatoon



Philipp Schneider
University of Southampton



Philippe Zysset
Universität Bern



Sarah Manske
University of Calgary



Thomas Link
University of California, San Francisco



Tobias Bäuerle
Universitätsklinikum Erlangen



Tony Keaveny
University of California, Berkeley



X. Edward Guo
Columbia University



X. Sherry Liu
University of Pennsylvania



After a fragility fracture, your osteoporosis patient is 5 times more likely to suffer another fragility fracture within a year.¹

Reference: 1. van Geel TACM, *et al.* Clinical subsequent fractures cluster in time after first fractures. *Ann Rheum Dis* 2009;68:99-102.

© 2019 Amgen Canada Inc. All rights reserved.

AMGEN[®]

GENERAL INFORMATION

During your time at the conference, you may have questions. Please first refer to this document and the website, qmski.org. Organizers will be wearing a red and black flannel shirt for the first two days of the conference. Please ask them any questions. Should you need additional help, please consult with the information below.

Remember, at -30°C with moderate wind, you can have frostbite in 10 minutes. Beyond the weather, you should have little to no risk of personal harm during the conference as the bears are (mostly) asleep.

EMERGENCY

Emergency Services	911	Ambulance, Fire Department, Police
--------------------	-----	------------------------------------

QMSKI

QMSKI	info@qmski.org	This email will be monitored throughout the conference.
-------	--	---

HOTEL

Fairmont Chateau Lake Louise	1 (403) 522-3511	Hotel contact if needed.
------------------------------	------------------	--------------------------

TRAVEL

Roam Transit	http://roamtransit.com	Consult bus times at the above website, or ask the hotel concierge for other options.
--------------	---	---

KEYNOTE: ANDREW J. FEUSTEL

(PH.D.) NASA ASTRONAUT

Andrew J. Feustel was selected by NASA in 2000. The Lake Orion, Michigan native has a Ph.D. in the Geological Sciences, specializing in Seismology, and is a veteran of two spaceflights. In 2009, Dr. Feustel served on STS-125. That mission launched on Atlantis and was the fifth and final mission to service the Hubble Space Telescope that improved the observatory's capabilities through 2014. Dr. Feustel also served on STS-134, launching on Endeavour to deliver the Alpha Magnetic Spectrometer and an ExPress Logistics Carrier to the International Space Station. Feustel most recently served as Commander on the International Space Station for Expedition 55 and 56.

Dr. Feustel enjoys auto restoration, guitar, water and snow skiing and is a fan of automotive and motorcycle racing. He holds degrees from Oakland Community College, Purdue University and Queen's University. At Queens he completed a Ph.D. in Geological Sciences, specializing in Seismology.



SUNDAY, FEBRUARY 24TH, 2019

REGISTRATION

16:00 - 19:00

Mount Temple Ballroom

WELCOME RECEPTION

19:00 - 21:00

Victoria Ballroom

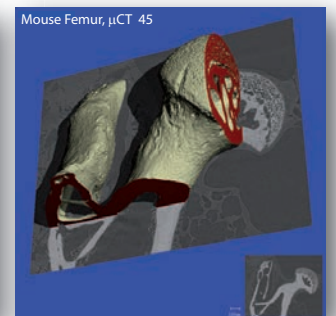
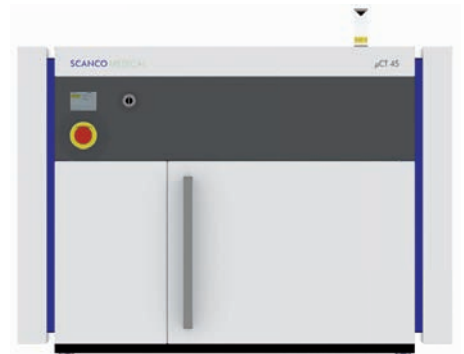
While socializing, appetizers and drinks will be available. A full dinner will not be served.

SCANCO MEDICAL

Discover our latest MicroCT systems

μ CT 45 - μ CT 90

- small footprint (desktop)
- automatic sample changer
- large field of view
- excellent image quality
- streamlined, advanced 3D analysis



www.scanco.ch
www.microct.com
info@scanco.ch

30-90 kVp, 8W, filter changer, automatic sample changer
FOV μ CT 45: ϕ 10-50 x H 120 mm, μ CT 90: ϕ 10-90 x H 120 mm
8k x 8k image matrix, reconstruction cluster, 64-bit analysis SW

MONDAY, FEBRUARY 25TH, 2019

BREAKFAST

07:00 - 08:30

Lago Italian Kitchen

INTRODUCTORY REMARKS

08:30 - 08:45

Mount Temple Ballroom

Co-Chairs Steven Boyd, Angela Cheung

CLINICAL APPLICATIONS - OSTEOARTHRITIS

08:45 - 10:00

Mount Temple Ballroom

Session Chairs: Sharmila Majumdar, Lindsie Blencowe

Andres Kroker, Sarah L Manske, Nicholas Mohtadi, Peter Salat, Richard E Walker, Steven K Boyd

The Longitudinal Effects of Acute Anterior Cruciate Ligament Tears on Bone Microarchitecture During the First 8 Months Post-Injury

Rachel DA Whyte, Abinaa Chandrakumar, Joseph Zmuda, Ryan Cvejkus, Andy Kin On Wong

Bone and Muscle Differences in Afro-Caribbean Men With Both Knee Osteoarthritis and Osteoporosis: The Tobago Bone Health Study

Qianqian Pang, Yuping Xu, Weibo Xia, Ling Qin

Alterations of Bone Geometry, Density, and Microarchitecture in Chinese Male Patients With Primary Hypertrophic Osteoarthropathy: A Case-Control Study

Serena Bonaretti, Garry Gold, Gary Beaupre

pyKNEER: Reproducible Workflow for Automatic Segmentation and Analysis of Femoral Knee Cartilage

Christine Chappard, Juan FPJ Abascal, Suzanne Bussod, Stéphanie Uk, Salim S Si-Mohamed, Philippe Douek, Françoise Peyrin
Feasibility of Photon Counting Spectral CT to Assess Knee Cartilage

COFFEE BREAK

10:00 - 10:30

Heritage Hall

MACHINE LEARNING & ARTIFICIAL INTELLIGENCE

10:30 - 12:00

Mount Temple Ballroom

Session Chairs: John Shepherd, Bryce Besler

Radhika Tibrewala, Valentina Pedoia, Carla Kinnunen, Tijana Popovic, Richard Souza, Sharmila Majumdar
Deep Learning-Based Automatic Estimation of Volume and Fat Fraction in Abductor Muscles and Their Associations With T1p and T2 in Hip Osteoarthritis Patients

Michael Wong, Bennett Ng, Ian Pagano, Andrea Garber, Steven Heymsfield, John Shepherd
Using Body Shape to Predict Bone Mineral Content and Density

Paul A Bromiley, Joes Staal, Eleni P Kariki, Raymond Hyatt, M Kassim Javaid, Emily Russell, Terence O'Neill, Kenneth Poole, Daniel Chappell, Rizwan Rajak, Timothy F Cootes
Computer-Aided Opportunistic Identification of Vertebral Fragility Fractures in Computed vvTomography Images: A Multi-Site Study

Valentina Pedoia, Jinhee Lee, Felix Liu, Sharmila Majumdar
Discovering Knee Pain Progression Image Biomarkers Using Deep Learning

Danielle E Whittier, Sarah L Manske, Richard E Walker, Emma O Billington, David A Hanley, Prism Schneider, Steven Boyd
Bone Microarchitecture Combined With Supervised Machine Learning Outperforms Current Clinical Risk Factors When Predicting Hip Fracture Risk

Claudia Iriondo, Valentina Pedoia, Sharmila Majumdar
Evaluating Shape Biomarker Preservation in Neural Network Segmentations

LUNCH BREAK

12:00 - 13:30

Lago Italian Kitchen

Lunch is followed by optional MSK activities. Details will be announced during lunch.

MICROGRAVITY AND THE MSK SYSTEM

13:30 - 15:00

Mount Temple Ballroom

Session Chairs: Harry Genant, Steven Boyd

Keynote: Andrew Feustel
Effects of Extended Microgravity on the Human Body: Bone and Joints in Space

Jean D Sibonga
The Programmatic Utility of Hip QCT in Long-duration Astronauts

Anna-Maria Liphardt, Gert-Peter Bruegemann, Frank Zaucke, Felix Eckstein, Wilhelm Bloch, Annegret Mündermann, Seungbum Koo, Joachim Mester, Anja Niehoff
Cartilage Health During Long-Duration Space Flight – The ESA CARTILAGE Study

Leigh Gabel, Paul A Hulme, Anna-Maria Liphardt, Martina Heer, Jean D Sibonga, Scott M Smith, Steven K Boyd
The Effect of Long-Duration Spaceflight on Bone Microarchitecture and Density

Katelyn Burkhart, Brett Allaire, Dennis Anderson, David Lee, Tony Keaveny, Mary L Bouxsein
Effect of Long Duration Spaceflight on Vertebral Strength and Trunk Muscle Morphology

POSTER SESSION I & COFFEE BREAK

15:00 - 16:00

Heritage Hall

P01 Guillaume Renaud, Pieter Kruizinga, Didier Cassereau, Pascal Laugier
Imaging the Bone Cortex With Ultrasound Using a Conventional Array Transducer

P03 Johannes Schneider, Gianluca Iori, Donatien Ramiandrisoa, Maroua Hammami, Melanie Gräsel, Christine Chappard, Reinhard Barkmann, Pascal Laugier, Quentin Grimal, Jean-Gabriel Minonzio, Kay Raum
Estimation of Cortical Porosity and Thickness using Ultrasonic Bi-directional Axial Transmission at 500 kHz – an Ex-vivo Study on Human Tibiae

P05 Mariya Shtil, Andres Kroker, Richard E Walker, Sarah Manske, Nicholas Mohtadi, Steven K Boyd
Bone Marrow Lesion Mechanical Strength Characteristics Post-Acute Knee Injury With HR-pQCT

P07 Elhadi Sariali, Quentin Grimal
Pre-Operative Bone Mineral Density Positively Correlates With the Clinical Result of Cementless Total Hip Arthroplasty After 2 Years

P09 Chantal MJ de Bakker, Lauren A Burt, Leigh Gabel, David A Hanley, Steven K Boyd
Association of Parity and Lactation History With Early Postmenopausal Changes in Bone Density and Strength

P11 Luis Carrenoco, Luis Perez Poro, Juan Francisco Vivanco, Heidi-Lynn Ploeg
Trabecular Tissue Stress-Strain Field With Micro-CT Finite Element Analysis

P13 Phil Salmon
X-ray Dosimetry for in Vivo MicroCT Scans: Mosfet Personal Skin Detectors Compared With Modeled Output From Tungsten Anode Sources

P15 Paul A Bromiley, Eleni P Kariki, Timothy F Cootes
Prevalence of Osteoporotic Vertebral Fractures in the UK Biobank Study - A Preliminary Analysis

P17 Phillip JC Spanswick, Danielle E Whittier, Cory Kwong, Robert Korley, Steven K Boyd, Prism S Schneider
Alterations in Bone Density Due to Fracture Healing at the Distal Radius Is Correlated With Age

P19 Karen Mys, Peter Varga, Filip Stockmans, Boyko Gueorguiev, Caroline E Wyers, Joop PW van den Bergh, G Harry van Lenthe
Influence of the Analysis Software to Calculate Direct Bone Structural Parameters

P21 Ying Zhu, Dragana Ponjevic, John R Matyas, Steven K Boyd
Contrast-Enhanced X-Ray Microscopy of Articular Cartilage for Quantitative Analysis

P23 Rachel DA Whyte, Jonathan D Adachi, Andy Kin On Wong
Development of a Subchondral Knee Bone-Muscle Imaging Protocol on pQCT

FRACTURES AND IMPLANTS

16:00 - 17:30

Mount Temple Ballroom

Session Chairs: Mary Bouxsein, Nicholas Mikolajewicz

Lindsay L Loundagin, David M L Cooper, W Brent Edwards

Relationship Between Osteocyte Lacunar Morphology and the Fatigue Life of Human Cortical Bone

Vincent A Stadelmann, Keith Thompson, Ursula Eberli, Fintan Moriarty

A Rat Model of Implant Fixation With Dynamic Histomorphometry of the Peri-Implant Space After Contamination With Low Virulence Micro-Organisms

Timo Damm, Olga Will, Jana Humbert, Claus-C Glüer

In-Vivo Monitoring of Degradable Processes of Bioresorbable Implants in Bone

Ifaz T Haider, Paul Kostenuik, W Brent Edwards

Regional Discrepancies in Proximal Femur and Femoral Shaft Strain Following Two Years of Simulated Zoledronic Acid Treatment

Ling Wang, Yongbin Su, Yandong Liu, Ruopei Yang, Zhe Guo, Minghui Yang, Xinbao Wu, Manyi Wang, Xiaoguang Cheng, Klaus Engelke

Differences in Hip Geometry Between Female Subjects with and without Acute Hip Fracture

Chantal E Kawalilak, Saija A Kontulainen, Morteza A Amini, Josje AG van Rens, Cathy M Arnold, James D Johnston

Comparison of Finite-Element-Derived Strength, Cortical and Trabecular Bone Micro-architecture in Postmenopausal Women With and Without Recent Distal Radius Fracture

DINNER

18:00 - 19:30

Victoria Ballroom

WORKSHOPS

19:30 - 21:00

Two Locations Detailed Below

Sign-up is required for workshop attendance and will be available at the registration desk.

Serena Bonaretti

Hands-on transparent QMSKI: Open-access data, reproducible workflows, and interactive publications

Beehive/Lakeshore

Bert van Rietbergen

High Resolution Image Processing – From Acquisition to Outputs

Mount Temple Ballroom

TUESDAY, FEBRUARY 26TH, 2019

BREAKFAST

07:00 - 08:30

Lago Italian Kitchen

ADVANCED MORPHOMETRICS

08:30 - 10:00

Mount Temple Ballroom

Session Chairs: Itabashi Akira, Fjola Johannesdottir

Natalie Reznikov, Ammar Alshegri, Mathieu Gendron, Nicolas Piché, Iskandar Tamimi, Jun Song, Faleh Tamimi
Topological Properties of Trabecular Bone and Their Biomechanical Significance

A Teodora Dinescu, Yizhong Hu, Sanchita Agarwal, Elizabeth Shane, X Edward Guo
Individual Trabecula Segmentation (ITS) Based Analysis of XCTII Compared to Gold-Standard μ CT Scans of the Human Distal Radius and Tibia

Vincent A Stadelmann, Birgitta Gatenholm, Carl Anders Lindahl, Mats Brittberg
An Automatic MicroCT Workflow for Relating Subchondral Bone Morphology to the Overlying Cartilage Damage in Osteoarthritic Human Knees

Diego Rossinelli, Tor Hildebrand
High-Performance 3D Image Processing for Large-Scale Structure Analysis Workflows

Bryce A Besler, Leigh Gabel, Lauren A Burt, Nils D Forkert, Steven K Boyd
Level Set Motion as a Framework for Computational Modeling of Bone Adaptation

Nicholas Ohs, Duncan Betts, Stephanie Sebastian, Bert van Rietbergen, Ralph Müller, Patrik Christen
Super-Resolution Images Reduce Voxel Size Effects of a Load-Adaptive Bone Remodelling Algorithm

COFFEE BREAK

10:00 - 10:30

Heritage Hall

QUANTITATIVE ULTRASOUND

10:30 - 12:00

Mount Temple Ballroom

Session Chairs: Pascal Laugier, Gianluca Iori

Adalbert Raimann, Johannes Schneider, Andrea Boni-Mikats, Radka Tuskova, Patricia Feil, Sarah Mehany, Peter Pietschmann, Martin Krssak, Gabriele Haeusler, Janina Patsch, Kay Raum
Low Sound Wave Propagation in Cortical Bone as a Novel, Non-Invasive Imaging Biomarker in Children and Adolescents With Hypophosphatemic Rickets

Donatien Ramiandrisoa, Sylvie Fernandez, Christine Chappard, Martine Cohen-Solal, Jean-Gabriel Minonzio
Comparison of in Vivo Cortical Parameters Obtained at the Radius by HR-pQCT and Bi-Directional Axial Transmission

Quentin Grimal, Pascal Laugier
Quantitative Ultrasound Assessment of Cortical Bone: Is Ultrasonic Velocity a Surrogate of Porosity?

Leon de Jong, Anton Nikolaev, Anna Greco, Jurgen J Fütterer, Chris L de Korte
Automated 3D Ultrasound for Quantitative Assessment of Mechanical Properties of Skeletal Muscle

Lawrence H Le, Tho NHT Tran, Mauricio D Sacchi, Dean Ta, Jacob L Jaremko
Correlation between the Gold-Standard DXA with Axial- Transmission Ultrasonic Velocity and Attenuation for Osteoporosis Diagnosis: A Pilot Study

Juan Du, Huong Nhuyen Minh, Gianluca Iori, Kay Raum
Estimation of Cortical Micromorphology from High-Frequency Ultrasound Backscatter

LUNCH BREAK

12:00 - 13:30

Lago Italian Kitchen

Lunch is followed by optional MSK activities. Details will be announced during lunch.

DXA 2.0

13:30 - 15:00

Mount Temple Ballroom

Session Chairs: Ling Qin, Rachel Whyte

Madeline Dwyer, Scott Fung, David Wong, Jordan Feld, Florence Wong, Queenie Wong, Diana Yau, Anita Colquhoun, Angela M Cheung
Ascites Distorts Trabecular Bone Score and Hip/Spine Bone Mineral Density

Sheldon Derkatch, Steven Reda, Davis McClarty, Mark Bryanton, Mike Davidson, Bill Leslie
Automated Detection of Vertebral Fractures on Dual Xray Absorptiometry Vertebral Fracture Assessment Images Using Supervised Machine Learning via a Trained Convolutional Neural Network

Lindsie A Blencowe, Nahid Raja, Lora M Giangregorio, Angela M Cheung, B Catharine Craven
Standardization of a Knee DXA Protocol - Is It Time?

John A Shepherd, Bennett K Ng, Benjamin J Hinton, Thomas K Wolfgruber
Approaches to Analyzing DXA Data Using Convolution Neural Networks

Franck Michelet, François De Guio, Christophe Lelong, Didier Hans
Impact of Thickness-Based Correction for Soft Tissue Effects on TBS

Thomas K Wolfgruber, Bennett K Ng, Benjamin J Hinton, John A Shepherd
Direct Hip Fracture Risk Assessment Using a Deep Learning Approach

POSTER SESSION II & COFFEE BREAK

15:00 - 16:00

Mount Temple Ballroom

P02 Ryleigh White, Diane Krueger, Francois De Guio, Franck Michelet, Didier Hans, Neil Binkley
A Feasibility Study Using The Texture Research Investigational Platform (TRIP) to Assess Bone Texture on VFA Lateral Spine Images To Discriminate Vertebral Fracture – Application of a Modified TBS Algorithm

P04 Ryleigh White, Diane Krueger, Francois De Guio, Franck Michelet, Didier Hans, Paul Anderson, Neil Binkley
An Exploratory Study of the Texture Research Investigational Platform (Trip) to Evaluate Bone Texture Score of Distal Femur DXA Scans – A TBS-Based Approach

P06 Vincent A Stadelmann, Lucie Bourgoin, Nicolas Bonnet
Automatic Quantification of Intermuscular Fat in Standard Mouse Proximal Tibia microCT Scan

P08 Lauren A Burt, Erik M Groves, Kelly Quipp, Steven K Boyd
Side-To-Side Differences in Bone Density and Strength at the Distal Tibia in Canadian Figure Skaters

P10 Ling Wang, Xiaoguang Cheng, J Keenan Brown, Li Xu, Zhe Guo, Glen M Blake
The Correction of Quantitative Computed Tomography Measurements of Vertebral Bone Mineral Density for Marrow Fat Using Magnetic Resonance Imaging

P12 Ryan M Plett, Lauren A Burt, Emma O Billington, David A Hanley, Steven K Boyd
The Calgary Vitamin D Study - Bone Density, Strength and Microarchitecture Differences Associated With Lower Limb Arterial Calcification: Baseline Comparisons of a Randomized Controlled Trial

P14 Lun M Wong, Lin Shi, Fan Xiao, James F Griffith
Fully Automated Segmentation of Wrist Bones in Early Rheumatoid Arthritis

P16 Alejandro Morales Martinez, Io Flament, Felix Liu, Jinhee Lee, Peng Cao, Sharmila Majumdar, Valentina Pedoia
Large-scale Knee Osteoarthritis Prediction from Spherical Coordinate Encoding of Bone Shape with Deep Learning Classifier

P18 Ling Wang, Rui Zhang, Xin Gao, Xiaoguang Cheng
Discrimination of Hip Fracture Type for Men With Spatial Differences in the Distribution of Bone

P20 Leigh Gabel, Heather M Macdonald, Heather A McKay
Assessing the Muscle-Bone Interaction in Pediatric Studies Using HR-pQCT

P22 Nicholas J Yee, Andrew S Michalski, Ryan M Plett, Steven K Boyd
Comparing Predicted Failure Regions of Femurs With Dynamic Hip Screws With Varying Tip Apex Distances Using CT-Based Finite Element Analysis

P24 Enisa Shevroja, Olivier Lamy, Berengere Aubry-Rozier, Gabriel Hans, Elena Gonzalez Rodriguez, Delphine Stoll, Didier Hans
The Impact of the New Trabecular Bone Score Algorithm Using a Different Correction Model Based on Soft Tissue Thickness on the Prediction of Incident Atraumatic Fracture Risk in Elderly Women: The OsteoLaus Study

CLINICAL APPLICATIONS – OSTEOPOROSIS I

16:00 - 17:30

Mount Temple Ballroom

Session Chairs: Angela Cheung, Ali Ghasem-Zadeh

Nicholas Mikolajewicz, Kim Wager, Michael Molloy-Bland, Nick Bishop, Andrew J Burghardt, Lars Folkestad, Anthony Hall, Ken Kozloff, Damien Lacroix, Pauline Lukey, Amaka C Offiah, Jay Shapiro, Bert van Rietbergen, Suzanne Morin, Bettina M Willie, Svetlana V Komarova, Francis H Glorieux
Relationship of Fracture Risk to HR-pQCT Measures of Bone Microarchitecture: A Systematic Review and Meta-Analysis

Emma O Billington, Lauren A Burt, Ryan M Plett, Marianne S Rose, Steven K Boyd, David A Hanley
Effects of Supplementation With Vitamin D3 400, 4000 or 10000 IU Daily for Three Years on Lower Limb Arterial Calcification: Secondary Analysis of a Randomized Controlled Trial

Ko Chiba, Narihiro Okazaki, Masako Ito, Makoto Osaki
Study on Normative Data of vBMD and Bone Microstructure Measured by Second-Generation HRpQCT in Japan: Comparison Between the Fixed and Relative Offset Methods

Svetlana V Komarova, Nicholas Mikolajewicz, Kim Wager, Michael Molloy-Bland, Anthony Hall, Bettina M Willie, Suzanne Morin, Francis H Glorieux
HR-pQCT Measures of Bone Microarchitecture for Fracture Risk Assessment: Patient Covariate Meta-Analysis

Marta C Erlandson, Lora Giangregorio, Andy Kin On Wong, Eva Szabo, Hunxian Hu, Angela M Cheung
Assessment of Muscle Quantity and Quality in Premenopausal, Postmenopausal and Women With Recurrent Falls

DINNER

18:00 - 19:30

Victoria Ballroom

WORKSHOP

19:30 - 21:00

Mount Temple Ballroom

Sign-up is required for workshop attendance and will be available at the registration desk.

Andrew J Burghardt, Philipp Schneider, Steven K Boyd
Working Group on Standardization of Quantitative Metrics for 3D Imaging

WEDNESDAY, FEBRUARY 27TH, 2019

BREAKFAST

07:00 - 08:30

Lago Italian Kitchen

PRE-CLINICAL IN VIVO IMAGING

08:30 - 10:00

Mount Temple Ballroom

Session Chairs: Ralph Müller, Chantal de Bakker

Samuel T Robinson, Yizhong Hu, X Edward Guo

Quantifying (Re)modeling Over 5 Weeks of Mechanical Loading Using Time-Lapse in vivo Micro- Computed Tomography

Ariane C Scheuren, Gisela A Kuhn, Ralph Müller

Coupling Longitudinal Micro-CT Imaging and Frailty Assessments: Advancing Applications in Aging Mouse Studies

Maximilian Rummeler, Fani Ziouti, Maureen E Lynch, Franziska Jundt, Bettina M Willie

Time-Lapse microCT-based in Vivo Imaging Reveals Load-Induced Targeted (Re)modeling at the Periosteal Surface in Mice With Multiple Myeloma Bone Disease

Zihui Li, Ren Yan N Kour, Kathryn S Stok

Reproducible Positioning of the Mouse Knee for Longitudinal MicroCT Studies

Phil Salmon, Behzad Javaheri, Andy Pitsillides

Profile of Trabecular Architecture Downstream of the Mouse Tibial Growth Plate and Where to Position The Volume-of-Interest for Trabecular Morphometry; Hint – Don't Scale with Bone Length

Felicitas R Flohr, Nina Derron, Jens Moeller, Ralph Müller

Printed Lacuno-Canalicular Network (pLCN): An Engineered 3D Environment for Multi-Modality Imaging of Osteocyte Networks

COFFEE BREAK

10:00 - 10:30

Heritage Hall

MRI IN MUSCULOSKELETAL SYSTEMS

10:30 - 12:00

Mount Temple Ballroom

Session Chairs: James Griffith, Leon de Jong

Vahid Abdollah, [Eric C Parent](#), Michele C Battié

Can Texture Analysis on MR Images Identify Intervertebral Disc Phenotypes Related to Back Pain?

[Destiny Francis](#), Alicia Gabilondo, Jeffrey F Dunn, John R Matyas, Sarah L Manske

Establishing an Imaging Protocol for Bone Marrow Lesions and Cysts in the Dunkin-Hartley Guinea Pig Knee Using Magnetic Resonance Imaging and Micro-Computed Tomography

[Vanessa Quinn-Laurin](#), Adrian Schankath, Laurence Stillwater, Ramin Mandegaran, Robert GW Lambert, Jacob L Jaremko

MRI Hip Joint Effusion Measurement by Two Different Techniques: Single Measurement vs Volumetric Quantitative Measurement

[Noor Shaikh](#), Honglin Zhang, John Street, David Wilson, Thomas Oxland

Upright MRI for Investigating Lumbar Muscle Morphometry, Posture, and Lordosis

[Oliver Chaudry](#), Frederike Sannmann, Wolfgang Kemmler, Klaus Engelke

Segmentation of Single Muscles of the Thigh in T1 Weighted MRI Images by Clustering Region Sizes

Po-hung Wu, Matthew Gibbons, Sarah Foreman, Julio Carballido-Gamio, Roland Krug, Jing Liu, Thomas Link, [Galateia Kazakia](#)

Multi-modality in vivo detection of cortical bone vasculature: Comparison of diabetes patients to healthy controls

LUNCH BREAK

12:00 - 13:30

Lago Italian Kitchen

Lunch is followed by optional MSK activities. Details will be announced during lunch.

NETWORKING EVENTS

13:30 - 19:00

Additional information on networking events will be announced at the conference.

THURSDAY, FEBRUARY 28TH, 2019

BREAKFAST

07:00 - 08:30

Lago Italian Kitchen

FINITE ELEMENT ANALYSIS & BONE STRENGTH

08:30 - 10:00

Mount Temple Ballroom

Session Chairs: Bert van Rietbergen, Mariya Shtil

Karamjot Sidhu, Steven Boyd, Aneal Khan

Modeling Bone Architecture and Fracture Risk in Hypophosphatasia by Image-Based Finite Element Analysis

Gianluca Iori, Johannes Schneider, Andreas Reisinger, Frans Heyer, Laura Peralta, Caroline Wyers, Melanie Gräsel, Reinhard Barkmann, Claus-C Glüer, JP van den Bergh, Dieter Pahr, Kay Raum

Large Pores Within the Cortical Bone of the Tibia Reflect Stiffness and Strength of the Proximal Femur

Denis E Schenk, Philippe K Zysset

Fast and Accurate Estimation of Colles' Fracture Load Based on Homogenized Finite Element Analysis of Double HR-pQCT Section

Yuanqiao Wu, Elise Morgan

The Effects of Boundary Conditions and Microarchitecture on the Accuracy of QCT-based Finite Element Model

Julio Carballido-Gamio, Sundeep Khosla, Andrew J Burghardt

The Relevance of Bone Shape in Colles' Fracture using HR-pQCT

Lindsay L Loundagin, W Brent Edwards

Effect of Peak Stress and Stressed Volume on the Fatigue Life of Bovine Cortical Bone

COFFEE BREAK

10:00 - 10:30

Heritage Hall

CLINICAL COMPUTED TOMOGRAPHY

10:30 - 12:00

Mount Temple Ballroom

Session Chairs: Claus Glüer, Felicitas Flohr

Carla Winsor, Leticia Campello, Muhammed Qasim, Ju Zhang, Xinshan Li, Corinne Henak, Perry Pickhardt, [Heidi-Lynn Ploeg](#), Marco Viceconti
A Phantom-Less Calibration Technique for Use in Femur Strength Prediction

[Johanna Baetz](#), Finn Brose, Philipp Messer-Hannemann, Frank Lampe, Michael M Morlock, Graeme M Campbell
QCT-Based Finite Element Estimation of Periprosthetic Fracture Sites

Eva Hufnagel, Peter Dankerl, [Klaus Engelke](#)
Internal BMD Calibration does not correct for table height dependent x-ray field inhomogeneity effects

[Jaime A Peña](#), Timo Damm, Stefan Reinhold, Reinhard Barkmann, Claus-C Glüer
Standardization of Bone Mineral Density and Microstructure for Spinal High Resolution Quantitative Computed Tomography in a Multicenter Setting

[Andrew S Michalski](#), Bryce A Besler, Steven K Boyd
Establishing a Population-Based Cohort From Opportunistic CT Assessment From Large Clinical Databases

[Karen Mys](#), Guozhi Zhang, Filip Stockmans, Caroline E Wyers, Joop PW van den Bergh, G Harry van Lenthe
Cone-Beam Computed Tomography as a Fast Alternative for High-Resolution Peripheral Computed Tomography

LUNCH BREAK

12:00 - 13:30

Lago Italian Kitchen

Lunch is followed by optional MSK activities. Details will be announced during lunch.

WORKSHOP

13:30 - 15:00

Mount Temple Ballroom

Sign-up is required for workshop attendance and will be available at the registration desk.

Stephanie Finzel, Klaus Engelke, Kathryn S Stok, Andrew J Burghardt, Sarah L Manske
Quantitative Imaging in Inflammatory Arthritis

POSTER SESSION & COFFEE BREAK

15:00 - 15:30

Heritage Hall

ADVANCED X-RAY IMAGING

15:30 - 17:00

Mount Temple Ballroom

Session Chairs: Harry van Lenthe, Maximilian Rummeler

Justin J Tse, Vasek Pitelka, Joy Dunmore-Buyze, Maria Drangova, David W Holdsworth
Quantifying Femoral- and Tibial-Subchondral Bone and Microvessel Changes in Rats with Surgically-Induced Osteoarthritis using Dual-Energy Micro-Computed Tomography

Colet EM ter Voert, RY Nigel Kour, Bente van Teeffelen, Kathryn S Stok
Optiray350 and Iomeron350 as Alternatives for Contrast-Enhanced Micro-Computed Tomography of Cartilage

Philipp Schneider, Orestis Katsamenis, Gareth Thomas, Anton Page, Simon Cox, Ian Sinclair, Peter Lackie
Why Every Hospital Should Have a Micro-CT: 3D X-Ray Histology, Let's Go Beyond Standard 2D Histology

Ali Ghasem-Zadeh, Rachel A Davey, Michele V Clarke, Cat Shore-Lorenti, Simon S Murray, Duncan Butler, Chris Hall, Peter Ebeling, Jeffrey D Zajac, Ego Seeman
Evaluation of bone microstructural of distal radius and distal tibia on human objects using phasecontrast synchrotron radiation computed tomography

Claire Acevedo
Investigating Bone Microstructure Using 3D Synchrotron Radiation Micro-Computed Tomography

Silke Christiansen, Lasse Kling, Leonid Mill, Anika Grüneboom, George Sarau, Martin Herrmann, Georg Schett, Andreas Maier
Improving the Study of Bone Diseases by Correlative Electron-, Ion- and X-ray Microscopy Including Their Analytical Techniques

BANQUET DINNER

18:00 - 21:30

Brewster Barn

A horse drawn sleigh will pick up guests from the hotel (starting at 17:30) and take them to the Brewster Barn.
Please dress for a 10 minute walk.

FRIDAY, MARCH 1ST, 2019

BREAKFAST

07:00 - 08:30

Lago Italian Kitchen

CLINICAL APPLICATIONS – OSTEOPOROSIS II

08:30 - 10:00

Mount Temple Ballroom

Session Chairs: Andy Kin On Wong, Lindsay Loundagin

Zully Ritter, Klaus Engelke, Dieter Felsenberg, Gabriele Ambrecht

Comparison of in Vivo Cortical Mikrostruktur and Porosity of Distal Tibia and Distal Radius HRpQCT Measurements From Male and Females of All Ages by Osteoporosis, Rheumatoid Arthritis, Gonarthrosis, and Healthy as an Early Indicator of Bone Fracture Risk

Ling Wang, Lu Yin, Xiaoguang Cheng, Kai Li, Wei Li, Wei Tian

The Association of Calcium Intake With Osteoporotic Vertebral Fractures and QCT Bone Mineral Density in a Large Chinese Cohort

Fiola Johannesdottir, Brett Allaire, Dennis E Anderson, Elizabeth J Samelson, Douglas P Kiel, Mary L Bouxsein

Computed Tomography - Based Texture Analysis Improves the Prediction of Incident Vertebral Fracture

Ali Ghasem-Zadeh, Roger Zebaze, Elizabeth J Atkinson, Yu Peng, Sundeep Khosla, Ego Seeman

Increased Cortical Porosity and Reduced Trabecular Density Are Not Necessarily Synonymous With Bone Loss and Microstructural Deterioration

Karen Mys, Peter Varga, Filip Stockmans, Boyko Gueorguiev, Caroline E Wyers, Joop PW van den Bergh, G Harry van Lenthe

X-Ray Scattering Is Limited in Cone-Beam Computed Tomography of Extremities

Johannes Willnecker

Imaging of Muscle and Bone with pQCT and the Relationship to Muscle Function

COFFEE BREAK

10:00 - 10:30

Heritage Hall

CLINICAL APPLICATIONS – INFLAMMATORY ARTHRITIS

10:30 - 12:00

Mount Temple Ballroom

Session Chairs: Klaus Engelke, Ariane Scheuren

Michael T Kuczynski, Scott Burnet, Stephanie Finzel, Kathryn S Stok, Steven K Boyd, Cheryl Barnabe, Sarah L Manske
Automated Detection of Joint Ankylosis in Joint Space Width Assessments in Hands Affected by Rheumatoid Arthritis Using HR-pQCT

Timo Meinderink, Fabian Stemmler, David Simon, Georg Schett, Klaus Engelke, Steven K Boyd, Arnd Kleyer, Anna-Maria Liphardt
Estimated Bone Strength of the Metacarpal Phalangeal Head Using Finite Elements Analysis – A Pilot Study

Dongze Wu, James F Griffith, Steven HM Lam, Priscilla Wong, Jiang Yue, Lin Shi, Edmund K Li, Isaac T Cheng, Tena K Li, Tracy Y Zhu, Vivian W Hung, Ling Qin, Lai-Shan Tam
Structural and Microstructural Intraarticular Bone Changes at the Metacarpal Heads in Patients With Psoriatic Arthritis Compared to Controls: A HR-pQCT Study

Cheng Tsz Ho, Qin Ling, Tam Lai Shan
Carotid Atherosclerosis Is Associated With Compromised Volumetric Bone Mineral Density and microarchitecture in Patients With Inflammatory Arthritis

Ursula Heilmeier, Andrew J Burghardt, Puneet Kapoor, Vivek Swarnakar, Reinhard Voll, Stephanie Finzel
Joint Space Analysis Of Metacarpal Joints Imaged Via High-Resolution Peripheral Quantitative Computed Tomography (HR-pQCT) Shows Structural Differences Between Patients With Hemochromatosis Hand Arthropathy And Healthy Controls

Scott C Brunet, Cheryl Barnabe, Glen Hazlewood, Peter Salat, Sarah L Manske
The Relationship Between Subclinical Inflammation and Bone Damage in Patients With Rheumatoid Arthritis

CLOSING REMARKS & LUNCH

12:00 - 12:15

Mount Temple Ballroom

The Longitudinal Effects of Acute Anterior Cruciate Ligament Tears on Bone Microarchitecture During the First 8 Months Post-Injury

Andres Kroker^{*1}, Sarah L Manske¹, Nicholas Mohtadi¹, Peter Salat¹, Richard E Walker¹, Steven K. Boyd¹

¹ McCaig Institute for Bone and Joint Health, University of Calgary

Introduction

Anterior cruciate ligament (ACL) tears are a sports-related knee injury that increase the risk of post-traumatic osteoarthritis (OA). The large impact forces between the tibia and femur often result in bone marrow lesions (BMLs), sites of high-signal intensities in certain magnetic resonance imaging (MRI) sequences, which are believed to be sites of trabecular micro-fractures. How human bone adapts to these injuries on a structural level is unknown, however, animal models indicate both loss of bone mineral density (BMD) and structural degradation throughout the injured knee. To our knowledge, no structural analysis of acute BMLs has been performed yet in humans. This is primarily due to the lack of non-invasive imaging modalities capable of imaging bone at sufficient resolution, a problem that has recently been overcome with the development of knee high-resolution peripheral quantitative computer tomography (HR-pQCT). The objective of this project is to assess bone structure in the weight-bearing regions in the knee and in BMLs for the first 8 months post-injury.

Methods

Fifteen participants, aged 22-45, with acute unilateral ACL tears were imaged using HR-pQCT and MRI at four time-points (baseline, 2, 4, and 8 months). Bone structure of the weight-bearing regions was assessed from HR-pQCT images directly, while bone structure of BMLs was assessed on HR-pQCT images

after applying BML volumes identified on T2 fat-saturated MRI sequences using rigid body registration.

Results

Substantial bone loss occurred in the injured knee, while the contralateral knee mostly was unaffected. In the injured knee, trabecular BMD was lost in both the femur and tibia (-4.6% to -15.8%). This loss was accompanied by changes to the trabecular network with decreased trabecular number (-3.1% to -7.8%) and increased trabecular separation (6.4% to 10.6%). Bone localized to BMLs was lost at an elevated rate as compared to the surrounding tissue outside the lesion, resulting in increased bone loss (-16.8% to -19.2%). This accelerated bone loss was accompanied by accelerated structural changes (trabecular thickness: -5.3% to -6.7%, trabecular number: -7.1% to -10.2%, trabecular separation: 6.6% to 12.9%).

Conclusion

These findings suggest that bone structure is markedly affected immediately following ACL tears in the entire weight-bearing regions and, even more so, localized to BMLs. The uninjured knee was mostly unaffected, suggesting an inflammatory response or changes to joint mechanics in the injured knee as opposed to systemic changes. These early structural bone changes may represent a key opportunity to intervene to prevent long-term OA development.

Bone and Muscle Differences in Afro-Caribbean Men with Both Knee Osteoarthritis and Osteoporosis: The Tobago Bone Health Study

Rachel D.A. Whyte^{*1,2}, Abinaa Chandrakumar¹, Joseph Zmuda³, Ryan Cvejkus³, Andy Kin On Wong^{1,2,4}

¹ CESH, JDMI, University Health Network

² Rehabilitation Sciences Institute, University of Toronto

³ Department of Epidemiology, Graduate School of Public Health, University of Pittsburgh

⁴ Department of Epidemiology, Dalla Lana School of Public Health, University of Toronto

Introduction

Previous analyses in postmenopausal women from the AMBERS study illustrated that bone and muscle properties for those with both knee osteoarthritis (KOA) and osteoporosis (OP) were no different from those with just OP but were of significantly poorer quality than those with KOA alone. We carried out similar analyses in men using data from the population-based Tobago Bone Health Study.

Objective

To determine differences in muscle and bone properties among men with KOA, OP, or both KOA+OP.

Methods

Afro-Caribbean men 33-92 years of age from the Tobago Bone Health Study completed peripheral quantitative CT (pQCT) at the 66% and 4% sites measuring muscle density (MD) and muscle cross sectional area (MCSA). 66% proximal tibia pQCT scans quantified total density, polar stress-strain index (SSIp), and cortical thickness. 4% distal tibia pQCT scans quantified total density, trabecular density, and SSIp. Total hip, lumbar spine and femoral neck DXA scans yielded areal bone density which were converted to T-scores to diagnose OP. Participants self-reported KOA diagnosis by their physician. General linear models compared bone and muscle properties between KOA+OP and those with neither disease, just KOA, or just OP. Binary logistic regression examined the odds of having

KOA+OP given previous history of any fractures, or knee fractures.

Results

In 2429 men (age: 59±10yrs, BMI: 27.5±4.9kg/m²), 6.75% had KOA. Of these, 15.8% also had OP and 16.5% also had low bone mass (LBM). 16.9% had only OP, and 18.4% LBM. Comparing men with KOA+OP to all other groups, 66% site cortical density was significantly lower. 4% site total density and SSIp were no different from the OP group but significantly lower compared to the KOA group or those with neither disease. These results were similar when comparing the KOA+OP group to men with either OP or LBM. There was no difference in MD and MCSA among all groups. Having a history of knee fractures regardless of trauma or fracture age was associated with KOA+OP (OR: 10.24 (1.13, 93.08)). However, only 5 of these occurred after age 40, and only 2 were non-traumatic.

Conclusion

These results suggest that men with KOA+OP represent a unique cohort of KOA patients with compromised bone. Treatment of their KOA may need to consider the potential for less intact bone to contribute towards OA development and progression. Prior knee fractures regardless of trauma may predispose individuals to KOA with abnormal bone phenotype. These results are consistent with our findings in postmenopausal women.

	KOA+OP vs. Neither				KOA+OP vs. OP				KOA+OP vs. KOA			
	B	Lower CI	Upper CI	N	B	Lower CI	Upper CI	N	B	Lower CI	Upper CI	N
T66 Total Density (mg/cm ³)	-101.24	-166.28	-36.21	1373	-29.37	111.20	1251.33	130	-48.16	-96.91	0.59	123
T66 SSIp (mm ⁴)	-275	-697	147	1373	129	-210	467	130	-396	-665	-128	123
T66 Cortical Density (mg/cm ³)	-47.35	-66.61	-28.08	1373	-16.00	42.45	10.45	130	-29.10	-48.99	-9.21	123
T66 Cortical Thickness (mm)	-0.863	-1.389	-0.337	1373	0.214	0.807	0.378	130	-0.510	-0.912	-0.108	123
T4 Total Density (mg/cm ³)	-81.03	-107.09	-54.97	1390	-12.76	40.95	15.42	133	-61.12	-81.31	-40.94	126
T4 Trabecular Density (mg/cm ³)	-56.49	-78.91	-34.06	1390	-5.19	27.65	17.28	133	-47.26	-63.42	-31.10	126
T4 SSIp (mm ⁴)	-1024	-1363	-685	1390	142	434	149	133	-809	-1040	-577	126
MCSA (mm ²)	-423.3	-1106.2	259.5	1376	-457.8	-1178.5	263.0	131	-20.3	-481.5	441.0	123
Muscle Density (mg/cm ³)	-0.77	-3.41	1.87	1239	0.17	4.31	4.64	90	-0.88	-3.46	1.71	103

All models adjusted for age, height, weight, current smoking, drinking ≥ 4 units per day, rheumatoid arthritis

Figure 1. Comparison of bone and muscle properties between those with KOA+OP versus single disease or neither disease

Alterations of Bone Geometry, Density, and Microarchitecture in Chinese Male Patients with Primary Hypertrophic Osteoarthropathy: A Case-Control Study

Qianqian Pang^{*1}, Yuping Xu^{*2}, Weibo Xia², Ling Qin¹

¹ Musculoskeletal Research Laboratory, Department of Orthopedics & Traumatology, The Chinese University of Hong Kong

²Department of Endocrinology, Key Laboratory of Endocrinology, Ministry of Health, Peking Union Medical College Hospital, Chinese Academy of Medical Sciences

Introduction

Primary hypertrophic osteoarthropathy (PHO) is a rare genetic disorder related to failures in prostaglandin metabolism. Disturbed prostaglandin E2 (PGE2) catabolism resulting in increased PGE2 level is suggested in the pathogenesis. Previous studies demonstrated that PGE2 can promote the activity of osteoclasts and osteoblasts. Plain radiographs of PHO patients in previous studies showed periosteal thickening along the diaphysis of the long bones and acroosteolysis at distal phalanges. Thus, it is supposed to have some bone structural changes in PHO patients. Previous studies had, however, not evaluated bone structure or bone strength in PHO patients. The aim of this study was to use high resolution peripheral quantitative computed tomography (HR-pQCT) for the first time evaluate peripheral bone microarchitecture and bone strength in PHO patients.

Methods

In this study, HR-pQCT was performed in 20 male PHO patients and 20 healthy controls. Areal bone mineral density (aBMD) and biochemical tests were performed in PHO pa-

tients only.

Results

The present study has first ever demonstrated bone structural changes in PHO patients by using HR-pQCT. In comparison with healthy controls, PHO patients had larger bone areas at both radius and tibia. In contrast, volumetricBMD (vBMD) were significantly lower by comparing to controls. Trabecular microstructure indices of bone fraction and thickness were found reduced in PHO patients. Besides, at the radius alone, PHO patients had decreased trabecular number and increased trabecular separation. Subgroups analysis revealed that PHOAR1 patients had inferior bone microstructure at the tibia alone, when compared with PHOAR2. Correlation analysis among HR-pQCT parameters, PGE2 level and bone resorption markers revealed PGE2 correlated negatively with bone vBMD, trabecular and cortical thickness in the tibia alone.

Conclusions

This study was first time to demonstrate bone structural changes in PHO patients using HR-pQCT.

pyKNEEr: Reproducible Workflow for Automatic Segmentation and Analysis of Femoral Knee Cartilage

Serena Bonaretti^{*1}, Garry Gold¹, Gary Beaupre²

¹ Department of Radiology, Stanford University

² Musculoskeletal Research Laboratory, VA Palo Alto Health Care System

Introduction

Knee osteoarthritis (OA) is a degenerative disease that leads to chronic disability, causing substantial economic and social impact. Magnetic resonance imaging is one of the main tools to quantify early stage and progression of OA by measuring cartilage morphology and relaxometry. Currently, there is a lack of standardized, open-access, and reproducible software to segment and analyze images of the knee femoral cartilage. Researchers mainly segment images manually or semi-automatically, using various commercial or in-house software. In addition, researchers usually perform post-segmentation analysis using commercial software (e.g. Excel, Matlab) and do not publish raw data, compromising results reproducibility. To promote open-science for quantitative musculoskeletal imaging, we have developed pyKNEEr, a fully-automatic workflow to preprocess, segment, and analyze femoral cartilage of the knee, using novel tools for open-source and reproducible science.

Methods

The workflow of pyKNEEr consists of three stages: image preprocessing, segmentation, and analysis. In preprocessing, images are geometrically aligned to a common cartesian system, and intensities are homogenized and enhanced. Segmentation is implemented using an atlas-based algorithm. It can be performed for a new subject image, or for the same subject in longitudinal or multimodal experiments. Currently, quantitative analysis of the images includes calculation of cartilage thickness using a near-neighbor algorithm and of cartilage volume. pyKNEEr is written in python, using SimpleITK to process images and Elastix [1] for the atlas-based segmentation. For each stage of pyKNEEr, there are one or more Jupyter Notebooks (<http://jupyter.org/>), an interactive web application that allows reproducible workflows and

can be used as a user interface. pyKNEEr is hosted on Github (<https://github.com/sbonaretti/pyKNEEr>). The documentation was created using Sphinx (<http://www.sphinx-doc.org/en/master/>). We validated our workflow on a dataset of 19 images from the Osteoarthritis Initiative (OAI). We assessed segmentation quality using the DICE coefficient, and we compared cartilage thickness and volume obtained with pyKNEEr vs. ground truth using Pearson's coefficient.

Results

Overlap between pyKNEEr's and ground truth segmentation resulted in an average DICE coefficient of 0.86. Person's coefficients were 0.96 for cartilage thickness and 0.98 for cartilage volume. All results are in the same range as the most recent findings in the literature [2]. Jupyter notebooks with results are on Github: https://github.com/sbonaretti/2019_QMSKI

Conclusion

We have introduced pyKNEEr, the first open-source, reproducible, and fully automatic workflow for segmentation and analysis of femoral knee cartilage.

References

- [1] S. Klein et al. IEEE Trans. Med. Imaging, 29, 1, 196–205, 2010. [2] B. Norman et al. Radiology, 288, 1, 177–185, 2018.

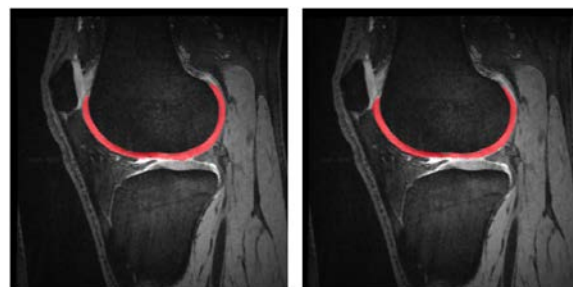


Figure 1. Segmentation of knee femoral cartilage. Left: Ground truth segmentation. Right: Segmentation with pyKNEEr

Feasibility of Photon Counting Spectral CT to Assess Knee Cartilage

Christine Chappard^{*1}, Juan F. P. J. Abascal², Suzanne Bussod², Stéphanie Uk², Salim S. Si-Mohamed², Philippe Douek², Françoise Peyrin²

¹ B2OA, UMR CNRS 7052, University Paris Diderot

²Univ.Lyon, INSA-Lyon, Université Claude Bernard Lyon 1, UJM-Saint Etienne, CNRS, Inserm, CREATIS UMR 5220, U1206, F-69100

Introduction

Osteoarthritis (OA) is a severe public health problem, which concerns a large percentage of patients and is estimated to increase on the next 10 years. It is associated with pains, problems in quality of life and disability. While the relevance of diagnostic imaging for assessing the integrity of the joint is well recognized, methods with sufficiently high resolution and image quality for detecting early OA are still lacking. Spectral Photon Counting CT (SPCCT), also called multicolor CT, is an emerging CT modality, which permits to acquire energy resolved data and brings additional information compared to standard CT. In this work, we evaluate the potential of SPPCT to image at the same time bone, meniscus and cartilage.

Methods

Knee specimens of both normal and subjects with different stages of OA were taken from l'Institut d'Anatomie Paris Descarte, France. The knees were imaged on a pre-clinical SPCCT system (Philips Healthcare) installed at Lyon, France. SPCCT data were acquired using 5 energy channels with a X-ray tube voltage of 120 kVp and a X-ray tube current of 100 mA. Fifty stacks of 8 slices were acquired to cover the entire knee (height 10 cm). After data acquisition, the projections on different energy bins were decomposed on a Compton/Photoelectric basis from which different mono-energetic (monoEs) images were reconstructed. For comparison to CT, the knees were also imaged on a High Resolution (HR) pQCT system (Scanco), at Hospital Lariboisière, Paris (voxel size, 82 μm), and registered to the SPCCT images.

Results

The processing of the SPCCT data provided monoEs images between 30 and 100 keV. We selected the 70 keV monoE images having the higher signal to noise ratio and showing the best contrast. Figure 1 compares registered HR-pQCT and SPCCT images of one normal and one with advanced osteoarthritis. Conversely to HR-pQCT, which clearly allows to image bone micro structure, SPCCT permits to see the cartilage and meniscus, as well as defects within cartilage. Micro calcifications were also visible at the periphery of the cartilage.

Conclusion

These preliminary results show that the development of the new generations of SPCCT devices is promising in the diagnosis of OA. In future works, a quantitative comparison of the SPCCT images with reference synchrotron monochromatic CT images will be performed.

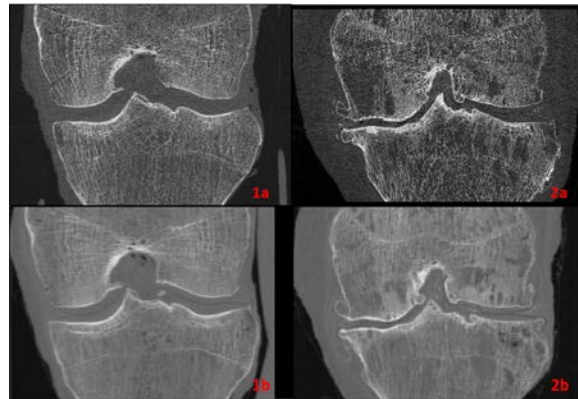


Figure 1. HR pQCT images (top) versus SPCCT monoE at 70keV images (bottom) of a normal specimen (1, left) and advanced osteoarthritic one (2, right).

Deep Learning-Based Automatic Estimation of Volume and Fat Fraction in Abductor Muscles and their Associations with T1 ρ and T2 in Hip Osteoarthritis Patients

Radhika Tibrewala^{*1}, Valentina Padoia¹, Carla Kinnunen¹, Tijana Popovic¹, Richard Souza¹, Sharmila Majumdar¹

¹ University of California San Francisco

Introduction

Muscle atrophy around the hip joint and muscle weakness has been identified in Osteoarthritis (OA). There is evidence that patients with hip OA have reduced volumes of the gluteus minimus (GMin) and gluteus medius (GMed) and increased fatty infiltration in GMin. While these reduced volumes computed by manual processing have been observed in patients with advanced OA (KL>2), there is a need to establish the relationship with biomarkers for OA like T1 ρ and T2 relaxation times in its early stages on larger samples. This study aimed: (i) to develop an automatic segmentation and quantification pipeline to estimate the volume and fat fraction in tensor fascia latae (TFL), GMed and GMin that allows for larger sample analysis and (ii) to study associations with T1 ρ and T2.

Methods

52 subjects with radiographic or symptomatic OA underwent (1) IDEAL SPGR (2)Oblique Axial T1w and (3) 3D sagittal combined T1 ρ /T2 MR imaging sequences. An ensemble 3D V-Net was developed to perform automatic volumetric segmentation, and trained with 37 manually segmented muscle masks performed by two skilled technicians (ICC>0.94). IDEAL volumes and a composite of IDEAL, fat and in-phase volumes were used as CNN inputs in the ensemble V-Net (dice loss, Adam optimizer, learning rate=1e-4, batch size=3, Tensorflow, 100 epochs, 3 hours, Nvidia Titan X GPU). Performance of the automatic segmentation was evaluated using Dice coefficient and ability to quantify fat fraction. Voxel Based Relaxometry (VBR) was used to quantify T1 ρ and

T2 relaxation times. Voxel based differences were evaluated with age, gender and BMI as adjusting factors in statistical analyses.

Results

An example of the manual vs automatic segmentation can be seen in Figure 1A-D for each muscle. Mean dice coefficients for the test sets were 0.85, 0.89 and 0.84 for the TFL, GMin and GMed respectively. Fat fractions, volume correlation and Bland Altman plots can be visualized in Figure 1E-F. 20.31% of the total voxels location in the deep acetabular cartilage showed significant T1 ρ and T2 prolongation in subjects with higher TFL fat fraction, 13.14% of the total voxels in the deep weight bearing femoral cartilage showed significant T1 ρ prolongation in subjects with higher GMin volume.

Conclusion

This study demonstrated a feasible, reliable and fast method of automatically segmenting the hip abductor muscles to find correlations with OA biomarkers.

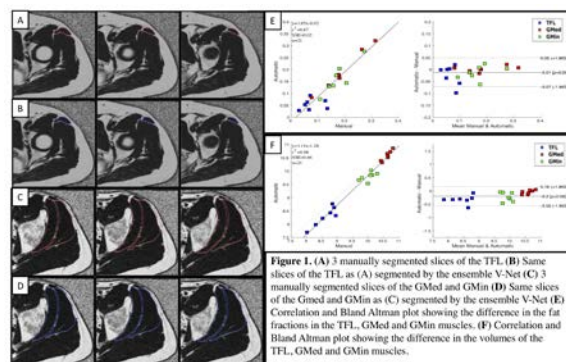


Figure 1. (A)-(D) Examples of automatically and manually segmented muscles (E)-(F) Correlations between manual, automatic fat fraction and volume estimates

Using Body Shape to Predict Bone Mineral Content and Density

Michael Wong^{*1}, Bennett Ng², Ian Pagano³, Andrea Garber⁴, Steven Heymsfield⁵, John Shepherd³

¹ University of Hawaii, Manoa

²University of California, Berkeley

³University of Hawaii Cancer Center

⁴University of California, San Francisco

⁵Pennington Biomedical Research Center

Introduction

Valuable health information such as lean, fat, and bone mass can be extracted from body shape. Different levels of fat and lean mass in children can impact their bone mass. Children may have a low bone density for many reasons including low physical activity or malnutrition. The criterion method for quantifying bone mineral content (BMC) and bone mineral density (BMD) in children is dual energy X-ray absorptiometry (DXA). However, because DXA uses ionizing radiation, it can only be used infrequently in children. Also, its cost (device and certified operator) limits its access in underdeveloped areas. In recent years, 3D optical (3DO) imaging has emerged as a versatile tool for health assessment. 3DO is inexpensive, doesn't require a trained operator, and doesn't use ionizing radiation. In this study, we asked if 3DO can generate estimates of bone density with high enough accuracy and precision to be clinically useful in evaluating children's bone health.

Methods

Participants (n=128) were recruited for the Shape Up! Kids study. Each participant (ages 5-17) received one DXA scan on a Hologic Discovery/A system for whole-body and regional measures. In addition, they received two 3DO scans on a Fit3D Proscanners. 476 automated circumference and length measurements were generated for each scan. Additional analysis was done using standardized meshes. Univariate linear regressions were used to test the agreement of 3DO and DXA using either variables of automated anthropometry. We compared the optically derived bone estimates to those derived using demo-

graphics alone.

Results

One hundred and nine children were used for this study after exclusions for poor scan quality or movement. Subtotal BMC and BMD was highly associated with 3DO anthropometry variables ($R^2=0.93$ and 0.88 , respectively) with $\%CV=3.25$ and 1.20 , respectively, and to a slightly higher extent than demographic variables alone ($R^2=0.89$ and 0.86 , respectively). However, lumbar spine BMC and BMD, derived from the whole body DXA, had a markedly stronger association with 3DO ($R^2=0.839$ and 0.866 , respectively) with a $\%CV=3.70$ and 2.77 , respectively, than with demographic variables alone ($R^2=0.76$ and 0.77 , respectively).

Conclusion

We conclude that 3DO surface scanning may be an accessible method to predict bone health status more precisely and accurately in children than demographic data alone.

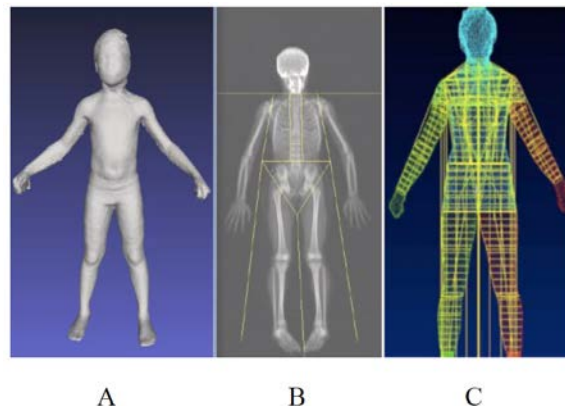


Figure 1. (A) Fit 3D scan, (B) DXA scan, (C) Example of Fit 3D automated anthropometry

Computer-aided Opportunistic Identification of Vertebral Fragility Fractures in Computed Tomography Images: A Multi-site Study

Paul A. Bromiley^{*1}, Joes Staal², Eleni P. Kariki³, Raymond Hyatt⁴, M. Kassim Javaid⁵, Emily Russell⁵, Terence O'Neill⁶, Kenneth Poole⁷, Daniel Chappell⁷, Rizwan Rajak⁸, Timothy F. Cootes¹

¹ Division of Informatics, Imaging and Data Sciences, University of Manchester

²Optasia Medical

³Radiology & Manchester Academic Health Science Centre, Manchester University Hospitals NHS Foundation Trust

⁴East Lancashire Hospitals NHS Trust

⁵Oxford Universities Hospital Trust

⁶Salford Royal NHS Foundation Trust

⁷Addenbrooke's Hospital

⁸Croydon Health Services NHS Trust

Introduction

Osteoporosis is a common skeletal disorder characterized by reduced bone mineral density and is associated with considerable increases in morbidity and mortality. Vertebral fragility fractures (VFFs) are an early manifestation and indicate a significantly increased risk of future fragility fractures. However, VFFs are under-diagnosed in clinical practice, particularly when identification is opportunistic [1]. For example, a recent audit at the Manchester Royal Infirmary [2] revealed an opportunistic reporting rate of 36% for VFFs on computed tomography (CT) volumes. The potential utility of computer-aided diagnostic (CAD) systems for VFF identification is therefore high.

Methods

A computer-aided VFF identification system, based on Random Forest Regression Voting Constrained Local Models (RFRV-CLMs), was developed to automatically localize vertebrae in CT volumes and segment their outlines [3] (see Fig. 1). An initial fracture classification was automatically generated by comparing vertebral body heights [4]. This machine learning system, in combination with radiologist over-read using the Genant et al. SQ method [5], was used by Optasia Medical as the basis of ASPIRE(TM), a commercial VFF case-finding service.

Evaluation

A retrospective audit was conducted using ASPIRE(TM) to identify VFFs in pseudonymised CT volumes of patients aged 50 years or over from five

UK NHS hospitals (Cambridge, Croydon, East Lancashire, Oxford and Salford), covering a 12-month period. To increase inter-reporter consistency, only moderate or severe fractures were considered. Findings were compared to the original radiology reports.

Results

A sample of 1638 (50.1% male) scans were used for analysis. VFFs were identified in 237 (53.4% male) patients ($14.5 \pm 1.7\%$, 95% CI). Prevalence did not vary significantly between sites. Four sites checked the original radiology reports and Fracture Liaison Service (FLS) referrals. The median reporting rate was 67.7% (IQR 55.7%, 74.5%) and the median FLS referral rate was 13.3% (IQR 10.8%, 22.0%).

Conclusions

An average of 1-in-7 patients had at least one VFF, with similar prevalence in men and women, in line with a recent worldwide review [6]. Whilst ASPIRE(TM) successfully identified unreported VFFs, the original reporting rate was higher than described in much of the literature. However, the FLS referral rate was low. We conclude that there is considerable scope for CAD systems in VFF identification and increasing FLS referrals is particularly important.

References

- [1] Am J Med 2016, 129(2):221.e1-221.e10.
- [2] Osteoporos Int 2016, 27(S2):621.
- [3] Proc. MICCAI CSI 2016, LNCS 10182:51-63.
- [4] Osteoporos Int 1993, 3:138-147.
- [5] J Bone Min Res 1993, 8(9):1137-48.
- [6] Osteoporos Int 2017, 28:1531-42.

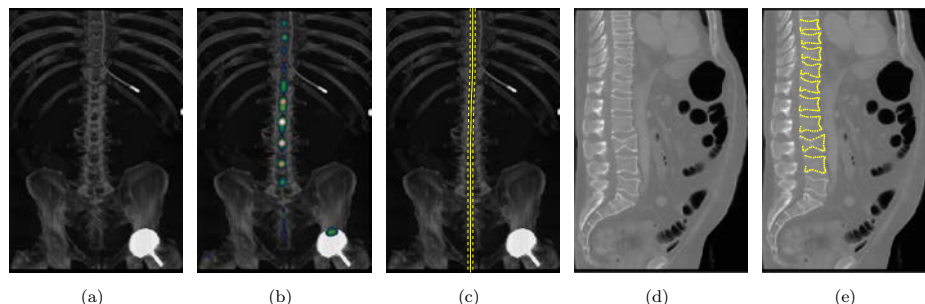


Figure 1. Automatic vertebral annotation: a) coronal MIP; b) vertebra detection; c) spinal midline extraction; d) sagittal image; e) vertebra segmentation.

Discovering Knee Pain Progression Image Biomarkers Using Deep Learning

Valentina Pedoia^{*1}, Jinhee Lee¹, Felix Liu¹, Sharmila Majumdar¹

¹ Radiology and Biomedical Imaging, University of California

Introduction

Deep learning computational models, specifically convolutional neural networks learn representations of images with multiple levels of abstraction analyzing data in their raw form. With its bases and strengths in this very concept, deep learning is revolutionizing the computer vision and medical imaging fields. Challenges that were unachievable for years as automatic segmentation, assisted image grading etc. are now tangible goals. Even more, the data-driven nature of deep learning allows us to uncover hidden information in image data, not just to automatize human tasks, but to create new knowledge. Despite the widely-perceived association between knee joint structural change and pain, a direct relationship has not been well established. Even less clear are the predictive abilities of imaging features regarding future pain trajectories. Accordingly, the goal of this study is to investigate the association between MRI image biomarkers learned using 3D convolutional neural network and pain trajectories.

Methods

A total of 4,796 subjects' repeated measures of KOOS pain score for both knees over 10-year study were obtained from the Osteoarthritis Initiative. 3D Double Echo Steady State MRI were used for the pain biomarker discovery. We temporally smoothed individual's pain curve by fitting a regression model using the orthogonal polynomials of degree 1 and two as the basis. The estimated parameters were standardized to be used as input into the Bayesian Gaussian mixture model (GMM) for clustering analysis. The parameters from regression were re-fitted against the selected Gaussian mixture model's means to obtain the posterior probabilities of each pain curve that describe the cluster membership. Deep learning model was used to regress the clusters probabilities. Our network is a 3D extension of the

DenseNet 121 architecture. The network was trained to learn the posterior probabilities of pain trajectory membership.

Results

The clustering analysis based on the GMM model identified three distinct pain trajectories: stable, worsening, progressively worsening (Figure 1A). Training Results: The mean squared error scores were 0.0148, 0.1556, 0.1549 for training(n=5,470), validation(n=1,368), and test(n=1,710) set, respectively. The accuracy, which measures whether the network correctly predicts the most probable clusters, were 0.9853, 0.8041, 0.7830 for training, validation, and test set, respectively. Figure 1B shows some examples of DL predicted pain curves.

Conclusions

We built a deep learning model that relates automatic learned MRI imaging biomarkers to temporal information of the knee pain. With our design we can provide, not only the point estimate but also the uncertainty incorporated into the problem.

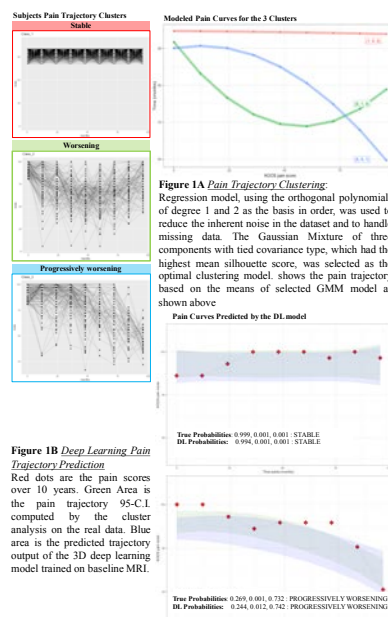


Figure 1A *Pain Trajectory Clustering*: Regression model, using the orthogonal polynomials of degree 1 and 2 as the basis in order, was used to reduce the inherent noise in the dataset and to handle missing data. The Gaussian Mixture of three components with tied covariance type, which had the highest mean silhouette score, was selected as the optimal clustering model. Shows the pain trajectory based on the means of selected GMM model as shown above

Figure 1B *Deep Learning Pain Trajectory Prediction*: Red dots are the pain scores over 10 years. Green Area is the pain trajectory 95-C.I. computed by the cluster analysis on the real data. Blue area is the predicted trajectory output of the 3D deep learning model trained on baseline MRI.

Figure 1. Pain Trajectory Clustering and Prediction

Bone Microarchitecture Combined with Supervised Machine Learning Outperforms Current Clinical Risk Factors when Predicting Hip Fracture Risk

Danielle E Whittier^{*1,2}, Sarah L Manske^{1,2}, Richard E Walker¹, Emma O Billington¹, David A Hanley^{1,2}, Prism Schneider^{1,2}, Steven Boyd^{1,2}

¹ McCaig Institute for Bone & Joint Health, University of Calgary, Calgary, AB

² Biomedical Engineering Graduate Program, University of Calgary, Calgary, AB

Introduction

Most individuals who have suffered a hip fracture are not classified as osteoporotic by DXA T-score. This is in large because areal bone mineral density (aBMD), albeit a strong predictor of bone strength, is limited in its ability to estimate fracture risk. Microarchitecture plays an important role, and high resolution peripheral quantitative computed tomography (HR-pQCT) provides in vivo diagnostic capabilities that can evaluate bone microarchitecture, which is independently correlated with fracture risk. However, the predictive power of HR-pQCT has been found to be only incrementally better than DXA in a recent meta-analysis indicating insufficient justification for its clinical application. This study aims to use machine learning to improve hip fracture prediction, and compare HR-pQCT with traditional clinical metrics.

Methods

Twenty-five women (aged 75.9 ± 9.1 years) with a prevalent hip fracture (<6 months) and twenty-five women (aged 71.9 ± 6.3 years) with no prior history of fragility fractures were scanned at their distal tibia with second-generation HR-pQCT (XtremeCT II, Scanco Medical, $61 \mu\text{m}$). Thirteen parameters describing bone area, mineral density, and microarchitecture were measured. The aBMD of the femoral neck (FN) was measured, and 10-year fracture risk was calculated using the FRAX[®] tool. Three supervised machine learning models were trained with: I) aBMD II) aBMD and 10-year fracture risk, and III) HR-pQCT parameters. All models included anthropometric metrics (height, weight, and BMI). Principle component analysis was used to reduce the HR-pQCT feature set while still accounting for over 95% of variance. Models were trained using support vector machines and tested using

ten-fold stratified random splits, with 26% of the dataset held out for testing in each fold. Performance was evaluated using area under the receiver operator characteristic (ROC) curve.

Results

Most women (60% hip fracture; 64% controls) in this study had FN T-Score in the osteopenic range, however hip fracture patients had a lower T-score on average (-2.3 vs -1.2 , $p < 0.001$). Figure 1 shows a comparison of the ROC curves from the classification models. Overall all machine learning models were shown to effectively classify fracture status. Model III, using only HR-pQCT and anthropometric parameters had the best performance, with an AUC of 0.90 ± 0.07 .

Discussion

Based on a modest cohort size, a machine learning approach was shown to improve hip fracture risk prediction. Of the three models tested, bone microarchitecture demonstrated the greatest potential to provide a novel clinical tool for improved estimation of hip fracture risk.

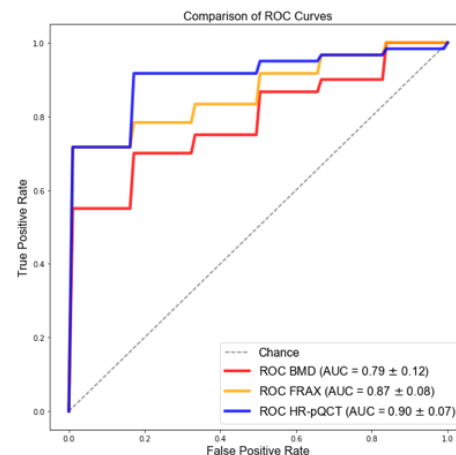


Figure 1. ROC curves of the three models built using clinical (Model I & II) and HR-pQCT (Model III) parameters to classify hip fracture patients.

Evaluating Shape Biomarker Preservation in Neural Network Segmentations

Claudia Iriondo^{*1,2}, Valentina Pedoia¹, Sharmila Majumdar¹

¹ Radiology and Biomedical Imaging, University of California, San Francisco
² Bioengineering, University of California, Berkeley

Introduction

Osteoarthritis (OA) is a common musculoskeletal condition, with symptomatic hip OA affecting up to 4.2% of the population. The pathophysiology of OA involves morphologic and biochemical changes, yet the precise etiology is unknown and treatment options are limited. MR imaging biomarkers (cartilage T1 ρ /T2, bone shape) can stage and predict the progression of OA. Deep-learning methods have shown high segmentation accuracy (mean distance, DSC), but there is limited research on biomarker preservation. This study presents a novel biomarker-aware approach for comparing segmentations from neural-networks.

Methods

Inference is run on hip MRI slices and masks stacked to create a binary volume of the proximal femur. Defects filled by interpolation, morphological closing, and 3D connected component analysis. A point cloud is created from slice boundaries, interpolated to isotropic dimensions, and landmark matched using spectral correspondence. The principal component (PC) and contrastive principal component (cPC) spaces are constructed from the registered GT segmentations. Inferred masks are registered and projected onto these spaces. Shape accuracy is assessed via (1) euclidean distance between each inferred shape and its GT and (2) feasibility of inferred segmentations (within 2SD in each PC).

Result

Both networks show similar mean distance performance across the ablation experiment (78,10,

and 5 training volumes), with Network₂ slightly outperforming Network₁ in Dataset₁₀. The greater trochanter had the highest mean distance errors, followed by the lateral shaft. The femoral neck had the lowest segmentation error, and the femoral head was accurately segmented by both networks in Dataset₁₀. Volumetric DSC performance was comparable between networks. Dataset₅ appeared to have ‘acceptable’ volumetric DSC (mean 0.85), but segmentations did not preserve the shape features of interest as seen by the significant deviation from the GT in the PC and cPC space (subtle shape variations within OA subgroups). Network₂ segmentations were marginally better at preserving shape biomarkers. With Dataset₇₈, 63% of segmentations by Network₂ fell within 2SD of all PCs, in comparison to 50% by Network₁. Feasibility DSC sharply decreased for both networks with Dataset₁₀ and Dataset₅. Additionally, Network₂ had higher feasibility scores in the PCs explaining the most shape variability. Despite comparable performance in classic segmentation metrics (mean distance, DSC), our results suggest Network₂ outperformed Network₁. Further interpretation of each PC/cPC in the context of OA is warranted.

Conclusion

We must adopt a biomarker-aware assessment of neural-network segmentations if bone shape is expected to reliably characterize OA progression (or for surgical planning, implant fitting, etc).

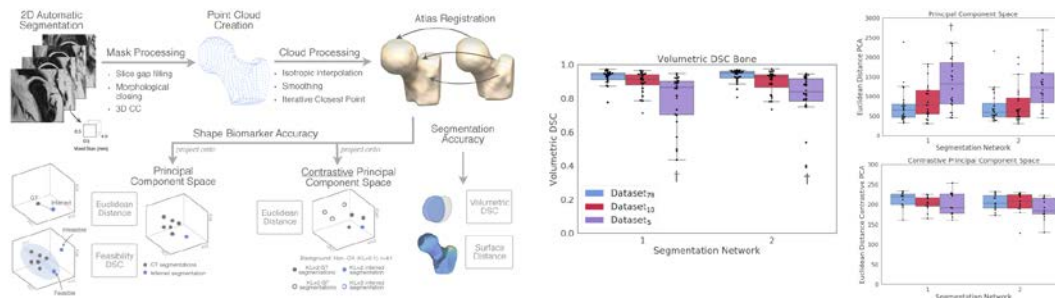


Figure 1. (L) Fully automatic pipeline for evaluating shape biomarker preservation (R) Comparison of segmentation accuracy and shape preservation metrics

The Programmatic Utility of Hip QCT in Long-duration Astronauts.

Jean D. Sibonga*¹

¹ Lead Bone Discipline, NASA Human Research Program

Introduction

DXA measurements of areal bone mineral density (aBMD) in astronauts after 4-6-month spaceflights suggest that the averaged monthly loss in aBMD is 1%; there is the concern that if loss occurs unabated over longer spaceflights, it may result in irreversible changes and premature osteoporosis in astronauts. DXA scans of astronauts serving on the International Space Station (ISS) are required testing to describe the effects of spaceflight, to evaluate the effects of in-flight countermeasures and to monitor restoration of skeletal health to baseline status. Flight investigations using QCT however have revealed that DXA does not capture all of the skeletal effects of spaceflight, including changes to cortical and trabecular hip sub-regions. Results from 2 spaceflight studies demonstrate added utility of QCT hip scans to evaluate countermeasure efficacy and full skeletal restoration.

Methods

Study 1: Ten untreated ISS astronauts agreed to Hip QCT scans to evaluate the enhancement of resistive exercise on the ARED (Advanced Resistive Exercise Device) with the addition of alendronate (Bis). Densitometry (DXA and QCT), biochemistry and finite element (FE) analyses in this ARED Control group were compared to data previously reported in alendronate-treated subjects (Bis+ARED, n=7), and ISS crewmembers flown before ARED was available (n=14-18). Study 2: Ten ISS astronauts (6 overlap with Study 1) agreed to Hip QCT scans at 2 years postflight to assess for incomplete recovery as an indicator for clinical follow-up.

Results

Study 1: Resistive exercise in the untreated ARED Controls did not prevent declines in trabecular vBMD for any region of the hip (Figure, where 1: $p < 0.05$ from Preflight and 2: $p < 0.05$ vs. ARED group) but prevented significant reductions in 1) cortical vBMD of the femur neck, 2) an FE estimate of hip strength and 3) aBMD of the femur neck. Combined Bis+ARED 1) prevented declines in trabecular and cortical vBMDs for all hip regions and in both estimates of FE hip strength; 2) prevented declines in aBMDs of all hip measurements; and 3) resulted in a significant increase in aBMD of lumbar spine.

Study 2: Areal BMD by DXA recovered in 9 of 10 astronauts at 1 year postflight while incomplete recovery of trabecular BMD by QCT was evident in 5 of 10 astronauts and persisted in 4 of the 5 astronauts 2 years postflight.

Conclusion

As an adjunct to DXA, QCT is necessary for a more complete assessment of recovery and of bone loss countermeasures.

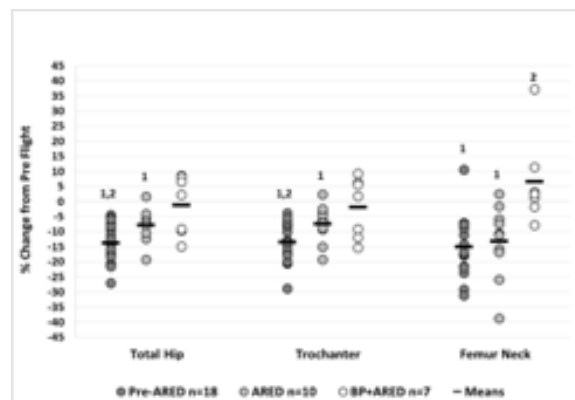


Figure 1.

Cartilage Health during Long-Duration Space Flight – The ESA CARTILAGE Study

Anna-Maria Liphardt*^{1,2}, Gert-Peter Bruegemann¹, Frank Zaucke³, Felix Eckstein^{4,5},
Wilhelm Bloch⁶, Annegret Mündermann⁷, Seungbum Koo⁸, Joachim Mester⁹, Anja Niehoff¹

¹ Institute of Biomechanics and Orthopaedics, German Sport University Cologne

² Friedrich-Alexander Universität Erlangen-Nürnberg (FAU), Department of Internal Medicine 3 – Rheumatology and Immunology, Universitätsklinikum Erlangen

³ Dr. Rolf M. Schwiete Research Unit for Osteoarthritis, Orthopaedic University Hospital Friedrichsheim

⁴ Institute of Anatomy, Paracelsus Medical University

⁵ Chondrometrics GmbH

⁶ Institute of Cardiovascular Research and Sport Medicine, Department of Molecular and Cellular Sport Medicine, German Sport University Cologne

⁷ Department of Orthopaedics, University Hospital Basel

⁸ School of Mechanical Engineering, Chung-Ang University

⁹ German Sport University Cologne, Training Science and Sport Informatics

Introduction

Changes to the mechanical environment of the human body greatly affect musculoskeletal homeostasis and prolonged exposure to microgravity causes muscle atrophy and bone loss. The goal of the ESA CARTILAGE study was to investigate the effect of microgravity exposure on articular cartilage health in astronauts. Articular cartilage health relies on appropriate mechanical stimulation of both chondrocytes and their surrounding extracellular matrix and immobilization can cause altered proteoglycan synthesis, and both thinning and softening of cartilage tissue. We hypothesized that a 5-6 months exposure to microgravity negatively affects cartilage morphology and metabolism.

Methods

12 USOS (United States orbital segment) astronauts with a mission length onboard the International Space Station (ISS) of 4 – 6 months participated in the study. Data collection of urine and blood samples in conjunction with magnet resonance imaging (MRI) of the knee joint was performed pre-flight (launch -60 days (L-60)) and post-flight (return +1 (R+1), +7 (R+7), +28 (R+28), +365 (R+365) days). Serum concentrations of biomarkers of cartilage health

(COMP, C2C, CPII, CS-846) were determined using commercially available enzyme-linked immunosorbent assays (ELISA). Cartilage thickness and volume were analyzed from MRI images.

Results

Preliminary results from 6 participants indicate that serum COMP concentration is not different from L-60 to R+1, however, values increase to R+7 (+ 20.7%, $p < 0.05$) and even further to R+30 (+ 24.0%, $p < 0.05$). Serum C2C, CPII and CS-846 levels show increased levels on R+1, R+7 and R+30 and serum C1,2C on R+1 and R+7, but at this stage of analysis with no statistical significance. MRI analysis is under investigation.

Discussion

This study is the first to provide data on the effect of microgravity on articular cartilage health. Changes in serum levels of cartilage biomarker turnover suggest that the cartilage extracellular matrix is sensitive to prolonged exposure to microgravity and that reduced mechanical loading during microgravity has the potential to initiate catabolic processes. Microgravity represents a unique model of unloading and will help to better understand the impact of immobility on cartilage health in the context of disease or lifestyle on earth.

The Effect of Long-Duration Spaceflight on Bone Microarchitecture and Density

Leigh Gabel*¹, Paul A. Hulme², Anna-Maria Liphardt^{3,4}, Martina Heer⁵, Jean D. Sibonga⁶,
Scott M. Smith⁶, Steven K. Boyd¹

¹ McCaig Institute for Bone and Joint Health, Department of Radiology, University of Calgary, Calgary, Canada

² McCaig Institute for Bone and Joint Health, University of Calgary, Calgary, Canada

³ Friedrich-Alexander Universität Erlangen-Nürnberg (FAU), Department of Internal Medicine, Rheumatology and Immunology, Universitätsklinikum Erlangen, Germany

⁴ Training Science and Sport Informatics, Biomechanics and Orthopaedics, German Sport University Cologne, Köln, Germany

⁵ Department of Nutrition and Food Science, Nutritional Physiology, University of Bonn, Bonn, Germany

⁶ Human Health and Performance Directorate, NASA Lyndon B. Johnson Space Center, Houston, USA

Introduction

Prolonged weightlessness from long-duration spaceflight increases rate of bone loss. It is unclear how microgravity differentially influences bone microarchitecture at weight-bearing and non-weight bearing skeletal sites. Thus, we aimed to examine the effect of spaceflight on bone microarchitecture and density at the distal tibia and radius.

Methods

We assessed 11 astronauts (10 men, 1 woman; 37.5 to 60.0 years at baseline) before and after missions to the international space station (mean duration 153 days). We scanned the distal tibia (22.5 mm site) and radius (9.5 mm site) of astronauts using 2nd generation high-resolution peripheral quantitative computed tomography (HR-pQCT, XtremeCTII, Scanco Medical). We performed 3D image registration and assessed standard morphological parameters including total bone mineral density (Tt.BMD) and trabecular BMD (Tb.BMD), number (Tb.N) and thickness (Tb.Th). An automated segmentation method was used to evaluate cortical BMD (Ct.BMD), thickness (Ct.Th) and porosity (Ct.Po). We compared bone variables at baseline and after spaceflight at the left tibia

and non-dominant radius using paired t-tests.

Results

At the weight-bearing distal tibia, astronauts experienced a significant reduction in Tt.BMD (5.8 mg/cm³, 1.7%, p=0.03), Tb.BMD (6.3 mg/cm³, 3.2%, p=0.01), Tb.Th (4.8 mm, 1.7%, p = 0.03) and Ct.BMD (13.0 mg/cm³, 1.4%, p<0.01) following spaceflight. At the non-weight bearing distal radius, astronauts demonstrated 0.7% lower Tb.Th (1.8 mm, p=0.03) and 0.9% greater Ct.BMD (8.7 mg/cm³, p=0.04) following spaceflight. Bone variables that did not significantly change following spaceflight included Tb.N, Ct.Th and Ct.Po at the tibia and radius, and Tt.BMD and Tb.BMD at the radius (p>0.05, for all).

Conclusion

Despite advanced resistant exercise training during spaceflight, prolonged exposure to microgravity is detrimental for bone microarchitecture and density at weight-bearing skeletal sites (tibia). Bone microarchitecture and density is preserved to a greater extent at non-weight bearing sites (radius). The small increase in cortical density at the radius may reflect increased reliance on the upper body for daily tasks during spaceflight.

Effect of Long Duration Spaceflight on Vertebral Strength and Trunk Muscle Morphology

Katelyn Burkhart^{1,2}, Brett Allaire³, Dennis Anderson¹, David Lee⁴, Tony Keaveny^{4,5}, Mary L. Bouxsein^{*1,2}

¹ Center for Advanced Orthopedic Studies, Beth Israel Deaconess Medical Center and Harvard Medical School

²Harvard-MIT Health Sciences and Technology Program

³Center for Advanced Orthopedic Studies, Beth Israel Deaconess Medical Center

⁴O.N. Diagnostics

⁵University of California at Berkeley

Introduction

The impact of long-duration (i.e., 6 months) spaceflight on vertebral bone strength, trunk muscle atrophy and risk of vertebral fracture has not previously been investigated.

Methods

We used previously collected computed tomography (CT) scans of the lumbar spine taken pre-flight, immediately post-flight and one to four years after return to Earth in 17 crewmembers with long-duration service on the International Space Station. We used CT based finite element analysis (CT-FEA) to estimate vertebral compressive strength and subject-specific musculoskeletal models to estimate the compressive forces applied to the vertebral bodies during routine activities as well as a few spaceflight-specific tasks.

Results

We found that 6 months of spaceflight led to a mean (\pm SD) $5.6 \pm 4.3\%$ decline in lumbar vertebral strength compared to baseline, with 65% of subjects experiencing deficits of greater than 5%. Notably, vertebral strength remained at this level after one to four years of recovery on Earth. The decline in vertebral strength was greater than the decline in DXA-aBMD ($-3.6 \pm 3.0\%$) and not associated with the decline in spine DXA-BMD. The cross-sectional area and density of paraspinal muscles were also reduced after spaceflight, with consistent recovery of muscle area, but not density, after one-year readaptation on Earth. Musculoskeletal models of the trunk showed a very slight increase in spinal loading post-flight, but in all individuals and simulated activities the

ratio of vertebral compressive load to vertebral compressive strength remained well below one, indicating a low risk of vertebral fracture. Altogether our findings confirm and extend previous studies showing significant declines in bone strength due to 6 months of spaceflight.

Discussion and Conclusion

This study was limited to examining crew members with mission durations of only 4-7 months, was conducted prior to availability of iRED and none of the subjects used bisphosphonates. Thus, future studies should investigate whether exercise and/or pharmacologic interventions can mitigate the bone and muscle losses we observed, and should determine nature of bone loss and trunk muscle atrophy in longer-duration missions. In particular, it is important to determine whether bone loss continues at the same rate, accelerates or plateaus with longer exposure to microgravity.

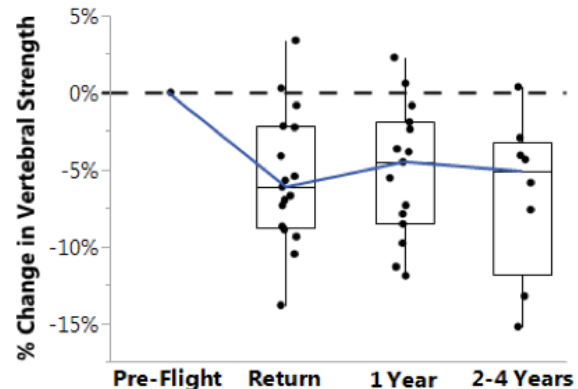


Figure 1. Spaceflight-induced changes in lumbar vertebral strength by CT-FEA

Imaging the Bone Cortex with Ultrasound Using a Conventional Array Transducer

Guillaume Renaud^{*1}, Pieter Kruizinga², Didier Cassereau³, Pascal Laugier¹

¹ Sorbonne Université, UPMC, CNRS UMR 7371, INSERM UMR S 1146, Laboratoire d'Imagerie Biomédicale

²Dept. Biomedical Engineering, ThoraxCenter, Erasmus Medical Center

³Sorbonne Université, ESPCI, UPMC, CNRS UMR 7371, INSERM UMR S 1146, Laboratoire d'Imagerie Biomédicale

Current clinical ultrasound scanners cannot be used to image the interior morphology of bones because these systems fail to address the complicated physics involved for accurate image reconstruction.

This work shows that ultrasound imaging of the cortical shell of a long bone is possible *in vivo* if refraction and elastic anisotropy of cortical bone are considered. Longitudinal and transverse ultrasound images of the radius and tibia of two healthy volunteers were obtained with a 2.5 MHz linear phased-array transducer and a programmable ultrasound scanner. Our method assumes a medium that is composed of different homogeneous layers. In the algorithm of image reconstruction we take wave refraction between the layers into account using a ray-tracing technique. The developed methodology leads to an estimation of the compressional wave-speed and anisotropy in cortical bone. Unlike the images reconstructed with the assumption of uniform wave-speed in the entire region of interest (conventional reconstruction), the endosteum is clearly visible in the images reconstructed with the method developed in

this work (see Figure). The wave-speed in cutaneous tissue, the wave-speed in cortical bone and the elastic anisotropy in cortical bone were evaluated by searching for optimal focus quality (maximum intensity and sharpness) in the ultrasound image. The estimated values of the ultrasonic wave-speed and anisotropy in cortical bone are in agreement with *ex vivo* studies reported in the literature. These optimal values lead to an estimation of the cortical thickness at the distal radius that agrees with the cortical thickness measured with high-resolution peripheral x-ray computed tomography. We also show that the elastic anisotropy of cortical bone must be considered in order to reconstruct accurate longitudinal ultrasound images.

Our approach is the first to achieve *in vivo*, with a conventional transducer array, a combined characterization of the thickness of the bone cortex, the ultrasonic compressional wave-speed in cortical bone and its anisotropy (magnitude and form). These parameters are of interest since they were proposed as biomarkers for cortical bone quality.

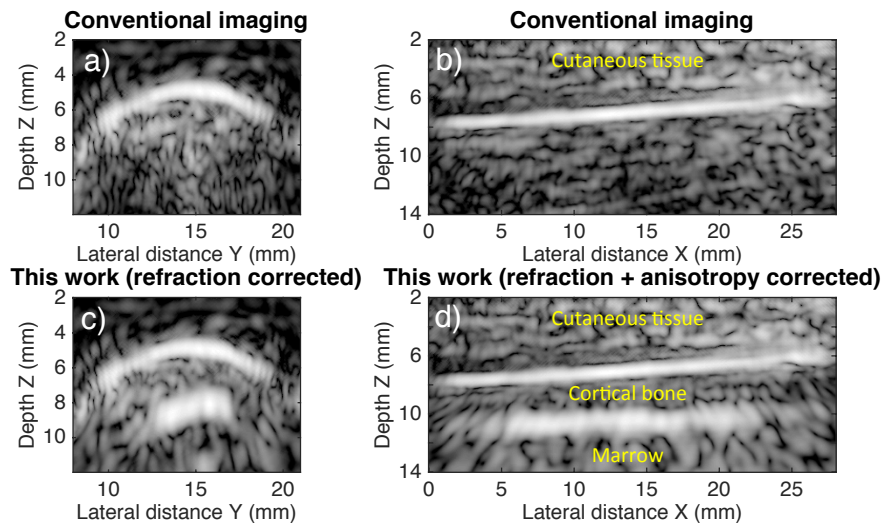


Figure 1. Transverse (panels a and c) and longitudinal (panels b and d) ultrasound images of the radius of a healthy volunteer.

Estimation of Cortical Porosity and Thickness using Ultrasonic Bi-directional Axial Transmission at 500 kHz – an Ex-vivo Study on Human Tibiae

Johannes Schneider¹, Gianluca Iori¹, Donatien Ramiandrisoa², Maroua Hammami³, Melanie Gräsel⁴, Christine Chappard⁵, Reinhard Barkmann⁴, Pascal Laugier³, Quentin Grimal³, Jean-Gabriel Minonzio⁶, Kay Raum^{*1}

¹ Berlin-Brandenburg School for Regenerative Therapies, Charité - Universitätsmedizin Berlin

² BleuSolid

³ Laboratoire d'Imagerie Biomédicale, Sorbonne University, CNRS, INSERM

⁴ Molecular Imaging North Competence Center, Universitätsklinikum Schleswig-Holstein

⁵ University Denis Diderot

⁶ Universidad de Valparaíso Escuela de Ingeniería Civil Informática

Introduction

In elderly people, the bone lost from the cortical bone compartment as a result of both reduced cortical thickness (Ct.Th) and increased cortical porosity (Ct.Po). The aim of this study was to validate the measurement of Ct.Po and Ct.Th at the tibia ex vivo using ultrasound bi-directional axial transmission (BDAT) at 500 kHz.

Methods

Nineteen left tibia specimens without soft tissue from human cadavers (6 male, 13 female, age: 69 – 94 years, mean: 83.7 ± 8.4 years) were provided by the Anatomy Institute of the University of Lübeck.

Guided waves were measured ex vivo at the antero-medial region using a 500-kHz BDAT probe (Azalée Paris, France). A 2D-transverse isotropic free plate model was fitted to the measured dispersion curves, whereas the model parameters assumed a constant matrix stiffness, but variable porosity Ct.Po and thickness Ct.Th. Additionally, the velocities of the first arriving signal (vFAS) and A0 mode (vA0) were measured. Reference Ct.Th values were obtained from site-matched microcomputed tomography (VivaCT 80, Scanco Medical, Brüttisellen, Switzerland; voxel size: 39 μm). 100-MHz scanning acoustic microscopy (pixel

size: 12 μm) provided the acoustic impedance of the tissue matrix. Rectangular parallelepiped samples of cortical bone tissue were harvested from the insonified region for Ct.Po characterization using a desktop μCT system (Skyscan 1172, Bruker MicroCT, Kontich, Belgium, voxel size: 7.4 μm) and CTan software (V1.16.1.0, Skyscan NV, Kontich, Belgium).

Results

The best predictions of Ct.Po ($R^2 = 0.83$, RMSE = 2.2 %) and Ct.Th ($R^2 = 0.92$, RMSE = 0.2 mm, one outlier excluded) were obtained from BDAT estimates. The second best predictors of Ct.Po and Ct.Th were vBMD ($R^2 = 0.77$, RMSE = 2.6 %) and vA0 ($R^2 = 0.28$, RMSE = 0.67 mm), respectively. One case with a discrepancy between BDAT and μCT based Ct.Th could be associated to a pronounced transitional region.

Conclusion

Ct.Th and Ct.Po were accurately predicted using BDAT. Our model-based predictions were not further improved, when we accounted for variations in matrix elasticity. Different thickness predictions are possible in bones with pronounced transitional regions. Clinical pilot studies are currently ongoing to quantify the in-vivo performance of this method.

Bone Marrow Lesion Mechanical Strength Characteristics Post-Acute Knee Injury with HR-pQCT

Mariya Shtil^{*1,2}, Andres Kroker^{1,2}, Richard E. Walker^{2,3}, Sarah Manske^{2,3}, Nicholas Mohtadi¹, Steven K. Boyd^{2,3}

¹ McCaig Institute for Bone and Joint Health, University of Calgary

² Biomedical Engineering Graduate Program, University of Calgary

³ McCaig Institute for Bone and Joint Health, Department of Radiology

Introduction

Bone marrow lesions (BMLs) occur in the peri-articular region following an impact or injury. When an anterior cruciate ligament (ACL) tear occurs, the distal femur and proximal tibia impact, creating a BML in 79% of patients. BMLs result as an accumulation of fluid due to microfractures and capillary leakage. Previous research indicates that increased bone remodeling occurs following microfractures, but the longitudinal process and its effect on mechanical strength post-injury is unknown in the presence/absence of BMLs. The aim of this study is to use finite element analysis (FEA) to determine the change in mechanical strength in the femur and the influence of the underlying the BML for 8 months post-acute injury.

Methods

15 patients between the ages of 18-40 with ACL tears were scanned at four time intervals (baseline, 2, 4, and 8 months) with high resolution peripheral quantitative computed tomography (HR-pQCT) and multiple MRI sequences. Since BMLs can be seen on MRI but not on CT, image registration of MRI to HR-pQCT was employed (SimpleITK). The segmented BML on the baseline visit was registered to the 2, 4 and 8-month visits to localize the BML throughout the healing process, and a neighbouring, volume-matched reference region was automatically defined. FEA software (FAIM, v8.0, Numerics88) and VTK were used to develop the FE model. To decrease computation time, only the BML-affected femoral condyle was used for FEA. The failure load was determined by employing a failure criterion that is defined as when a percentage of a critical volume (2.0%) exceeds a critical energy equiva-

lent strain (0.007) and the model is assumed to be linear elastic.

Results

The magnitude of yielded bone volume varied over the 8 months post-acute injury in the BML region while the reference region remained constant. The results show high variability and differences between patients. For one participant, at baseline, failure load was estimated at 5688 N and was reduced to 4001 N, 4071 N, and 3878 N at 2, 4, and 8-month time points, respectively. The volume of failed bone underlying the BML was 10.77 mm³, 2.23 mm³, 2.00 mm³, 1.85 mm³, respectively.

Conclusions

Changes to bone strength in the BML region occurred longitudinally in the 8 months post-acute injury, with the most significant change at 2 months post injury. The sustained loss of strength in the BML region suggests that bone remodelling continues throughout the 8-month period, despite the BML volume subsiding on MRI.

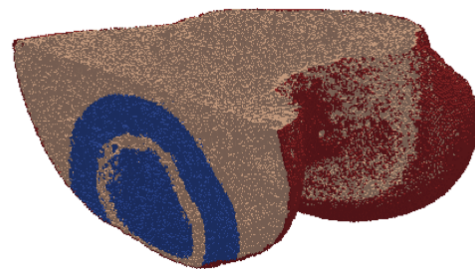


Figure 1. 3D Rendering of distal femur showing bone marrow lesion (inner blue circle) and surrounding reference region (outer blue circle).

Pre-Operative Bone Mineral Density Positively Correlates with the Clinical Result of Cementless Total Hip Arthroplasty After 2 Years

Elhadi Sariali¹, Quentin Grimal*¹

¹ Sorbonne Université, CNRS, INSERM, Laboratoire d'Imagerie Biomédicale

Introduction

Cementless implants are widely used for total hip arthroplasty (THA). The success of surgery largely depends on implant's primary stability. One of the biomechanical factors of primary stability is bone mechanical quality. The influence of volumetric bone mineral density (vBMD), a proxy of bone quality, on the clinical result of THA, is poorly documented. The objective of this study was to analyze the relationship between post-operative clinical result 2 years after cementless THA and pre-operative trabecular bone vBMD.

Methods

A former prospective study included patients operated for a cementless THA with an anatomical stem with short proximal fixation (Sariali et al 2016). Patients underwent a low dose computed tomography (CT) X-ray scanner, which was required for three-dimensional planning. The planning was used to determine the hip reconstruction objectives and the implant size. vBMD was calculated as the mean of Hounsfield (HU) values in a region of interest (ROI) in trabecular bone at the level of the calcar, behind the medial cortex, 10 mm above the apex of the lesser trochanter. The ROI was a parallelepiped box of 1 cm² cross-section and 1 mm thickness. The clinical result was evaluated two years after THA by means of questionnaires filled by the pa-

tients at home. The collected data was used to calculate a score of hip function and symptoms. We investigated the correlations between the scores and vBMD using multivariate statistics, accounting for age, BMI, and gender.

Results

50 patients were included (29 men and 21 women, mean age 62y. \pm 12; mean BMI 25.8, mean vBMD was 69.4 \pm 54 HU). The clinical score after two years was positively correlated to vBMD (R=0.42, p=0.002) and age (R=0.39, p=0.005). There was no correlation between vBMD and BMI.

Conclusion / Discussion

The results suggest that pre-operative trabecular bone vBMD positively influences the clinical result of cementless THA after 2 years. vBMD can be evaluated using the CT-scan data required for surgical planning. Our data suggest that it may be beneficial to include vBMD information in the 3D planning software. One important limitation of the work is the absence of calibration phantom imaged with the patient.

References

Sariali, E., Catonne, Y., & Pascal-Moussellard, H. (2016). Three-dimensional planning-guided total hip arthroplasty through a minimally invasive direct anterior approach. Clinical outcomes at five years' follow-up. *International Orthopaedics*, (L1d), 1–7.

Association of Parity and Lactation History with Early Postmenopausal Changes in Bone Density and Strength

Chantal MJ de Bakker^{*1}, Lauren A Burt¹, Leigh Gabel¹, David A Hanley¹, Steven K Boyd¹

¹ McCaig Institute for Bone and Joint Health, University of Calgary

Introduction

During pregnancy and lactation, the maternal skeleton undergoes transient bone loss. After weaning, bone mass is rapidly restored, and parity/lactation history does not appear to negatively impact postmenopausal areal bone mineral density (aBMD). However, recent studies using high-resolution peripheral quantitative computed tomography (HR-pQCT) found that breastfeeding-associated trabecular deteriorations persist at least 2.5 years post-weaning, while others suggested that lactation may be associated with long-term increases in cortical bone size. Thus, reproduction may induce differential long-term effects in the cortical vs. trabecular compartments, which would be masked in DXA-based aBMD measurements, but may nevertheless impact postmenopausal bone health. The aim of this study was to determine whether reproductive history was associated with altered patterns of trabecular or cortical bone loss post-menopause.

Methods

45 women from the Canadian Multicentre Osteoporosis Study (CaMos) Calgary cohort, who had begun the menopause transition and were less than 10-years post-menopause, were identified. Women were divided into three groups based on reproductive history: nulliparous (NP, n=10), parous with 6 months breastfeeding (P-BF, n=21). All women underwent HR-pQCT imaging of the distal radius and tibia at baseline and after five years to determine total, cortical, and trabecular volumetric BMD (Tt.BMD,

Ct.BMD, Tb.BMD) and failure load. Differences among groups and over time were evaluated using repeated-measures, two-way ANOVA. One-way ANOVA compared bone loss rates among groups. Spearman correlations evaluated relationships between total months of breastfeeding and bone loss rates in parous women.

Results

Average age at baseline was 56.6 years (no inter-group differences). Baseline BMD and failure load were not different between groups (Table 1). Over 5 years, Tt.BMD decreased significantly at both the tibia and radius in all groups. Tibial Ct.BMD also decreased in all groups, while radial Ct.BMD decreased in all groups except P-BF. At the tibia, Tb.BMD decreased in P-BF women only, and the rate of decline was greater for P-BF than for NP women (p=0.01). Total months of breastfeeding was negatively correlated with percent decrease in radial Ct.BMD (r=-0.37, p=0.03).

Conclusion

Reproductive history did not affect baseline bone density or strength in these early postmenopausal women. However, women who breastfed for more than 6 months showed altered rates of bone loss, the long-term implications of which remain to be determined. This effect varied by skeletal site and compartment, as breastfeeding was associated with elevated rates of tibial Tb.BMD loss, but reduced rates of radial Ct.BMD loss.

		Baseline			% Change over 5 Years			
		NP n=10	P-NBF n=14	P-BF n=21	NP n=10	P-NBF n=14	P-BF n=21	
Tibia	Tt.BMD (mgHA/cm ³)	322 ± 47	289 ± 52	277 ± 46	-3.14 ± 2.12	-2.60 ± 3.81	-4.76 ± 4.90	
	Ct.BMD (mgHA/cm ³)	932 ± 64	898 ± 61	895 ± 52	-4.79 ± 3.48	-3.12 ± 3.37	-4.00 ± 3.43	
	Tb.BMD (mgHA/cm ³)	182 ± 45	162 ± 30	165 ± 38	2.13 ± 5.01 [‡]	-1.10 ± 4.15	-3.82 ± 6.08 [#]	
	Failure Load (N)	5143 ± 674	4938 ± 669	5010 ± 858	-0.79 ± 2.96	0.57 ± 5.08	-1.11 ± 6.25	
Radius	Tt.BMD (mgHA/cm ³)	335 ± 42	322 ± 61	306 ± 56	-4.88 ± 2.11	-5.78 ± 5.78	-5.84 ± 6.69	
	Ct.BMD (mgHA/cm ³)	972 ± 46	956 ± 50	947 ± 37	-2.89 ± 2.54	-2.17 ± 1.93	-0.89 ± 1.96	
	Tb.BMD (mgHA/cm ³)	171 ± 38	150 ± 33	154 ± 32	1.46 ± 4.85	-2.16 ± 7.93	-1.62 ± 8.04	
	Failure Load (N)	1826 ± 232	1788 ± 228	1757 ± 347	-1.20 ± 7.08	-2.83 ± 9.75	-1.04 ± 8.33	

[#]: different from NP,
[‡]: different from P-NBF,
[‡]: different from P-BF,
p<0.05

italic % change:
significant difference
between baseline
and follow-up, p<0.05

Figure 1. HR-pQCT parameters (mean ± SD) for each group: nulliparous (NP), parous with <6 mo breastfeeding (P-NBF), and parous with >6 mo breastfeeding (P-BF)

Trabecular Tissue Stress-Strain Field with Micro-CT Finite Element Analysis

Luis Carrenoco¹, Luis Perez Poro¹, Juan Francisco Vivanco², Heidi-Lynn Ploeg^{*3}

¹ Dept de Ingenieria Mecanica Universidad Tecnica Federico Santa Maria

²Universidad Adolfo Ibanez

³Dept. Mechanical and Materials Engineering Human Mobility Research Centre Queen's University

Introduction

Systems biology models and tissue-level stress-strain fields are integrated in algorithms to predict trabecular bone adaptation. Tissue-level stress-strain fields can be calculated with finite element analyses (FEAs) of these structures. Ex Vivo bone culture experiments quantify trabecular bone adaptation in response to stimuli, for example mechanical or biochemical. These experiments measure: metabolic biomarkers, bulk bone core stiffness, static and dynamic histological measures, and morphology quantified with micro computed tomography (μ CT). The objective of this study is to present a methodology to conduct μ FEA of bone cores from an *ex vivo* bone culture experiment.

Methods

Forty-Eight bone cores (10 mm diameter x 5 mm length) were extracted from residual tissue donated by total hip replacement recipients for an *ex vivo* bone culture experiment. The 22 full-factorial experimental design measured the response of 2 stimuli, load and endothelin, on trabecular bone adaptation. All bone cores were scanned (Siemens MicroCAT II 34 μ m, 80 kVp, 50 μ A) and segmented (Mimics v18, Materialise). Twenty-two STL models from the center of the tested cores (8 mm diameter x 4 mm length, 201³ total volume) were modelled, meshed (n=12 controls, and n=10 endothelin as stimulus) and analysed (ANSYS v18.1, Ansys) to calculate linear tissue stress-strain fields. The trabecular tissue (37.2-159 mm³ bone volume) of each bone core was meshed with 200-627K linear tetrahedral (SOLID72) elements with assumed mechanical properties (E=350 MPa,

$\nu = 0.3$). Boundary conditions were defined to model unconfined compression with 0.01 mm axial displacement ($-2500 \mu\epsilon$). Nodes on the base of the core were constrained against vertical displacements. Mesh sensitivity analysis found less than 10% change in bulk stiffness. Apparent elastic modulus (E_{app}) was calculated by normalising bulk stiffness (K) to core dimensions, area $A=50.2 \text{ mm}^2$ and length $L=4 \text{ mm}$ ($E_{app} = KL/A$). Porosity was calculated as (total volume – bone volume)/(total volume). Results were evaluated against compression testing of bone cores and 3D printed PLA (E=1248 MPa) models (Mbot grid II).

Results

As in other foam structures, a negative power law related apparent elastic modulus (12-239 MPa control; 14-252 MPa) to porosity (21-72% control; 22-75% treatment) for both groups ($R^2 = 0.94$ control; 0.96, treatment). With this numerical approach tissue level strains in bone cores can be calculated to feed algorithms to predict trabecular response to mechanical and biochemical stimuli.

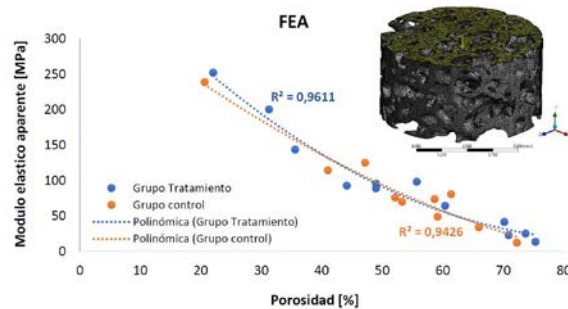


Figure 1. Apparent Elastic Modulus versus Porosity, and Finite Element Mesh

Xray Dosimetry for in vivo MicroCT Scans: MOSFET Personal Skin Detectors Compared with Modeled Output from Tungsten Anode Sources.

Phil Salmon*¹

¹ Bruker MicroCT

Introduction

In vivo MicroCT scanners provides rapid low dose whole body imaging for quantification of rodent body tissue composition (bone mineral density and content, adipose and lean tissue mass and lung volume). As with all in vivo microCT imaging it is important to know the absorbed xray ionizing dose from scans.

Method

Here, xray doses are quantified for whole body mouse imaging with the SkyScan 1278, an in vivo scanner using a flat panel camera for fast acquisition of a whole mouse in a single scan. MOSFET (Metal Oxide Semiconductor Field Effect Transistor) detectors allow dose measurements in real time by a simple digital readout, thus giving dose data much more quickly and straightforwardly than with ionization chambers whose raw output requires several processing steps. Dose measurements by a MOSFET detector are compared with the doses calculated by modeling the xray output from tungsten-

anode sources with known power, filter and distance parameters. These calculations are based on published modeled doses and are performed by an xray dose calculator “CT-ion”.

Results

Doses measured by the MOSFET detector and those calculated by CT-ion from source emission data were in general agreement. However at lower xray photon energies, obtained with lower filter and voltage settings, the MOSFET detector underestimated doses due to the fall-off of sensitivity to xrays at photon energies below 30 keV. This fall-off is modest and should be straightforward to correct in practice.

Conclusion

MOSFET semiconductor skin detectors are simple to use and give real time digital dose data, and their output is in agreement with dose calculated from source emission data, albeit with a small correction required at low xray photon energies.

Prevalence of Osteoporotic Vertebral Fractures in the UK Biobank Study - A Preliminary Analysis

Paul A. Bromiley^{*1}, Eleni P. Kariki², Timothy F. Cootes¹

¹ Division of Informatics, Imaging and Data Sciences, University of Manchester

²Radiology & Manchester Academic Health Science Centre, Manchester University Hospitals NHS Foundation Trust

Introduction

Osteoporosis is a common skeletal disorder associated with considerable increases in morbidity and mortality. Vertebral fragility fractures (VFFs) are an early manifestation and indicate significantly increased risk of future fractures. However, VFF prevalence is poorly established since they are underdiagnosed in clinical practice [1] and previous cohort studies have produced varying estimates [2]. The UK Biobank, a nationwide prospective cohort study [3], has collected health, genetic and other data from 500,000 participants aged between 40-69 years in 2006-2010, and primary care data will continue to be collected until at least 2022. A subset of 100,000 participants were selected for multimodal imaging including lateral spinal dual X-ray absorptiometry (DXA); acquisition is ongoing. The UK Biobank therefore represents an unparalleled resource to establish VFF prevalence in the UK. We present a preliminary analysis based on a sub-set of the first UK Biobank imaging release.

Method

Lateral DXA images of the spine in 2,384 subjects were collected from the first UK Biobank imaging release and analysed by four expert radiographers using the AVERT(tm) software package (Optasia Medical, Cheadle, UK) [4]. All visualised vertebrae between T4 and L4 inclusive were classified using the Genant et al. SQ method [5]. The software supported this through semi-automatic segmentation of vertebral bodies [6], providing accurate height measurements.

Results

The study cohort was 48.5% male with a mean age of 62.2(\pm 8.7) years. Ethnic diversity was representative of the UK population; 85.7% \pm 3.7% (95% CI) Caucasian compared

to 87.1% \pm 0.023% (95% CI) in the 2011 national census [7]. VFFs (Genant et al. grade 1 to 3) were found in 256 of 1156 male participants (22.1% \pm 2.7%, 95% CI) and 221 of 1228 female participants (18.0% \pm 2.5%, 95% CI).

Conclusions

Analysis of the UK Biobank participants has suggested a "healthy volunteer" selection bias [8], but VFF prevalence in this study was not significantly different to the range reported in previous cohort studies [2]. Notably, whilst men are known to be under-represented in fracture liaison services [9], prevalence in men was found to be higher than in women. We conclude that the full UK Biobank imaging dataset, when available, will provide a valuable resource with which to estimate VFF prevalence, and investigate associated risk factors, in the UK population.

References

- [1] Am J Med 2016, 129(2):221.e1-221.e10.
- [2] Osteoporos Int 2017, 28:1531-42.
- [3] www.ukbiobank.ac.uk
- [4] www.optasiamedical.com
- [5] J Bone Min Res 1993, 8(9):1137-48.
- [6] Lecture Notes in Computational Vision and Biomechanics 2015, 20:159-172.
- [7] www.nomisweb.co.uk/census/2011
- [8] Am J Epidemiol 2017, 186(9):1026-1034
- [8] BMC Musculoskelet Disord 2012, 13:3.
- [9] Osteoporos Int 2013, 24(2):393-406

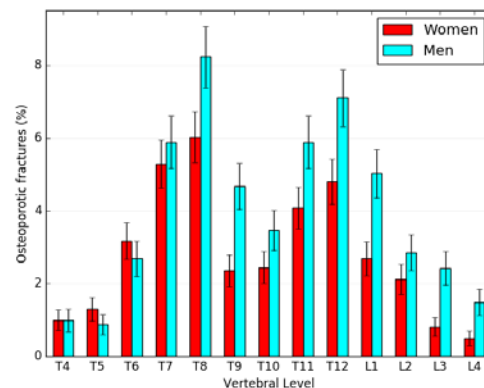


Figure 1. Percentage distribution of vertebral fractures by level. Total annotated vertebrae were: T4=2214, T5=2366, T6-L3=2384, L4=2368.

Alterations in Bone Density Due to Fracture Healing at the Distal Radius is Correlated with Age

Phillip J.C. Spanswick*¹, Danielle E. Whittier¹, Cory Kwong², Robert Korley^{1,2}, Steven K. Boyd¹, Prism S. Schneider^{1,2}

¹ McCaig Institute for Bone and Joint Health, University of Calgary

²Department of Surgery, Division of Orthopaedic Trauma, Cumming School of Medicine, University of Calgary

Introduction

Distal radius fractures (DRF) are most commonly treated non-operatively with cast immobilization. Currently there is insufficient evidence to guide the duration of cast immobilization. High-resolution peripheral computed tomography (HR-pQCT) offers an approach to non-invasively quantify fracture healing. The goal of this study is to quantify the healing process and aid clinicians in determining the appropriate duration of immobilization. Total volumetric bone mineral density (BMD) and trabecular bone volume fraction (BV/TV) have shown potential to be used as metrics for the study of fracture healing and preliminary results have shown correlation with age. However, the patient and fracture variables that may influence this relationship remain unknown. Potential factors include the severity or type of fracture, the duration of immobilization, and biological factors. In this study we aim to: (1) validate the correlation between age and change in BMD, and (2) investigate the relationships between fracture classification, initial BMD, and the duration of immobilization with fracture healing.

Methods

Twenty-two participants (19 Female, 3 Male) with a stable DRF have been recruited for the study. Participants are having scans using HR-pQCT (XtremeCT II, Scanco Medical) of their fractured distal radius at approximately

2, 4, 6, 8, 12, and 27 weeks post-fracture. A scan of the contralateral wrist was also completed to represent baseline conditions. Each scan consists of a 20.4 mm long section beginning at the distal radius endplate with a 61 μm nominal isotropic resolution. Total BMD and BV/TV were measured from each scan. Fractures were classified by a senior orthopedic resident. Linear regression models were used to generate the coefficient of determination and the probability value.

Results

Changes in BMD stabilized by 6 months post-fracture, suggesting fractures were healed and remodeling has plateaued. To date, 10 female and 1 male participant have completed these scans, with a mean age of 48.2 ± 13.1 years. Linear regression between BMD at 6 months and age showed a moderate correlation and strong significance was present ($R^2 = 0.42$, $P\text{-value} = 0.03$). There was no significant correlation found between BMD at 6 months and type of fracture, duration of immobilization, or baseline BMD.

Conclusions

The results suggest that while the correlation between the change in BMD and age is significant, the underlying factors causing this correlation remains unknown. Further research into biological factors and patient comorbidities that may affect callus formation and the fracture healing process may provide more insight into this relationship.

Influence of the Analysis Software to Calculate Direct Bone Structural Parameters

Karen Mys^{*1,2}, Peter Varga², Filip Stockmans³, Boyko Gueorguiev², Caroline E. Wyers^{4,5},
Joop P.W. van den Bergh^{4,5,6}, G. Harry van Lenthe¹

¹ KU Leuven, Biomechanics Section, Belgium

²AO Research Institute Davos, Biomedical Development, Switzerland

³KU Leuven (Kortrijk), Development and Regeneration, Belgium

⁴Department of Internal Medicine, VieCuri Medical Center, the Netherlands

⁵NUTRIM School for Nutrition and Translational Research in Metabolism, Maastricht University, the Netherlands

⁶Department of Internal Medicine, Subdivision of Rheumatology, Maastricht University Medical Centre, the Netherlands

Introduction

The last decades, the use of high-resolution imaging systems to assess trabecular and cortical bone morphological parameters in animal and human specimens has grown immensely. Several commercial scanners with corresponding software packages are on the market. Yet, no standard exists on the calibration of the morphological analysis software; hence, different packages may have different implementations leading to differences in reported bone morphological parameters. Therefore, the aim of this paper was to compare the bone structural parameters obtained with two widely used commercial software packages, namely IPL (Scanco, Switzerland) and CTan (Bruker, Belgium).

Materials & methods

Nineteen trapezia and nineteen radii were scanned at two resolutions (1) microCT-Scanner (SkyScan1172, Bruker, Belgium, @19.84 μm for the trapezia; and VivaCT40, Scanco, Switzerland, @19 μm for the radii) and (2) high-resolution peripheral computed tomography (XTremeCT-II, Scanco, Switzerland @60.7 μm). The scans were reconstructed and segmented following the manufacturer guidelines and a direct analyses method was used in both IPL and CTan to calculate the bone structural parameters:

bone volume fraction (BV/TV), trabecular thickness (Tb.Th), trabecular separation (Tb.Sp) and trabecular number (Tb.N).

Results

Only small differences were found between the BV/TV results of both software packages. For Tb.Th and Tb.Sp, the results of CTan and IPL were highly correlated. However, there was a relative offset, which was different for the different scanners and anatomic location (ranging from +11% to +31% for Tb.Th and from -6% to +6% for Tb.Sp). For Tb.N, the results obtained with CTan and IPL showed poor correlation for all tested cases.

Conclusion

We conclude that morphometric parameters obtained with CTan and IPL cannot be compared directly with the exception of BV/TV. For Tb.Th and Tb.Sp, correction factors could be determined, but these depend on the resolution of the scanner, the segmentation method and on the specific anatomic location. The results of the bone structural parameter Tb.N did not correlate well for our tested cases. The development of a universal standard with or without general open source software accessible to all research groups is desirable.

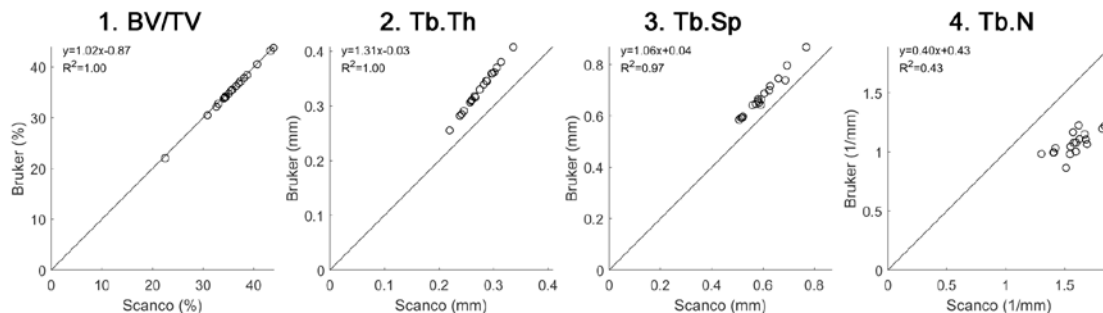


Figure 1. Scatter plots between IPL (Scanco) and CTan (Bruker) for the trapezii scanned with XTremeCT-II

Contrast-Enhanced X-ray Microscopy of Articular Cartilage for Quantitative Analysis

Ying Zhu^{*1,2}, Dragana Ponjevic^{1,3}, John R. Matyas^{1,3}, Steven K. Boyd^{1,2}

¹ McCaig Institute for Bone and Joint Health, University of Calgary, Calgary, Canada

²Department of Radiology, University of Calgary, Calgary, Canada

³Department of Comparative Biology & Experimental Medicine, University of Calgary

Osteoarthritis (OA) is a common chronic disease of joints typically characterized by degenerative changes of articular cartilage, which is comprised of chondrocytes embedded in a composite of water-imbibing proteoglycans restrained by a fibrillar collagen network. Early diagnosis of OA requires sensitive imaging, ideally at the histological i.e., cellular-molecular, level. Whereas cartilage histopathology is destructive, time-consuming and limited to 2D views, contrast-enhanced x-ray microscopy (XRM) provides images of articular cartilage and subchondral bone in 3D at high resolution. This study establishes a correlation between contrast-enhanced XRM and the gold-standard histology for the evaluation of the articular cartilage.

Osteochondral plugs were excised in 3 x 3 mm² cross-sectional area from healthy bovine knees and stained in phosphotungstic acid (PTA) for 0, 4, 8, 12, 16, 20, 24, 28 and

32 hours. XRM imaging was performed after each staining time and repeated imaging for 4, 12, 20 and 28 hours. An optimal staining time of 16 hrs and a saturated staining time of 24 hrs were determined for this sample. Polarized light microscopy (PLM) and second-harmonic-generation dual-photon microscopy (SHG-DP) of a histology section from the same sample were analyzed and compared with the matching XRM slice, in terms of tidemark, averaged image pixel intensity along the cartilage depth, and the chondrocytes and nuclei position and counts. The cartilage collagen network and chondrocytes from the PTA-enhanced XRM were well correlated with the histology. This technique has two distinct advantages over routine histopathology of articular cartilage: (1) the avoidance of demineralization, and hence enables imaging of the intact subchondral bone plate, and (2) the ability to image the entire osteochondral sample in 3D.

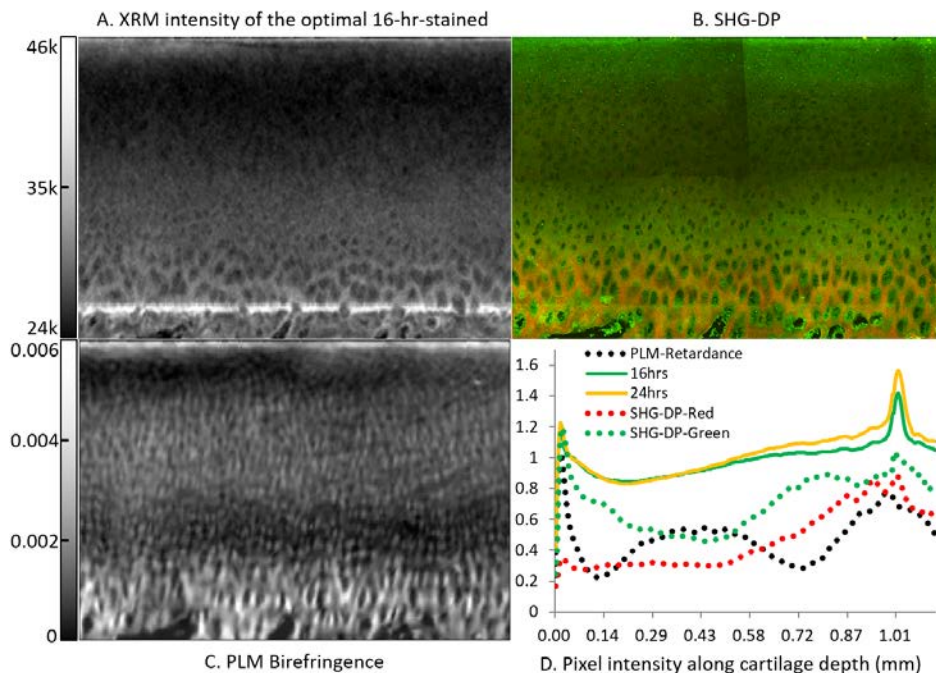


Figure 1. Resized ROIs in the optimal PTA-stained (16 hrs) XRM (A) vs. SHG-DP histology (B) and PLM histology (C) with their pixel intensity plots (D).

Development of a Subchondral Knee Bone-Muscle Imaging Protocol on pQCT

Rachel Whyte^{*1,2}, Jonathan D. Adachi³, Andy Kin On Wong^{2,4}

¹ Rehabilitation Sciences Institute, University of Toronto

²Centre of Excellence in Skeletal Health Assessment, Joint Department of Medical Imaging, University Health Network

³Division of Epidemiology, Dalla Lana School of Public Health, University of Toronto

⁴Division of Rheumatology, Department of Medicine, McMaster University

Introduction

We recently showed among knee osteoarthritis patients who concurrently have osteoporosis, pain was better related to subchondral bone (MRI) than to cartilage. This study motivated exam of subchondral bone using CT. Peripheral quantitative CT (pQCT) has been used to image up to the 66% tibia. However, it has the potential to image the knee, especially in thinner individuals.

Objective

Develop a pQCT knee imaging protocol to quantify subchondral bone and peri-articular muscle.

Acquisition

Using XCT2000 (pQCT, Stratec Medizin-technik), knee imaging was optimized based on a distal tibia 4% protocol (CT speed:20 mm/s, 38 kVp, 0.3 mA, in-plane pixel size: 200 μ m, 2.3 \pm 0.5mm thickness). The right knee of a single healthy male with no OA (age: 33, BMI: 23.3 kg/m²) was used.

Positioning

The leg was positioned parallel to the cart at minimum height, and knee inserted into the scanner with 10 cm clearance between the gantry and the start position. The laser was positioned just distal to the patella and a 45-line scout was obtained at 90 degrees, 50 mm/s speed to display the knee joint in sagittal view.

Scan prescription

The reference line was centred within the joint space defined by fringes of the tibiofemoral cortices. 3 slices were prescribed beginning +15 mm (distal) to the reference line, each separated by 2.5 mm to measure the subchondral tibia. Similarly, 3 slices were prescribed beginning -10mm (proximal) to the reference line to measure the subchondral femur.

Safety

Effective dose was 2.66 μ Sv/slice.

Analysis

Due to thicker skin around this region, the usual muscle segmentation protocol failed to peel away subcutaneous fat. Instead, the ROI was drawn within the subcutaneous fat region. Contour mode 3, peel mode 2, filter: F03F05F05 yielded the muscle segmentation. Within the same ROI, bone was segmented using contour mode 31 for thin cortices, peel mode 2, inner and outer thresholds of 280 and 400 mg/cm³, respectively.

Results

Muscle density ranged 66.16-74.44mg/cm³ from the most proximal femoral slice to the most distal tibial slice. Trabecular density was higher near the joint line and at the distal femur (201.65 mg/cm³) than the proximal tibia (168.68 mg/cm³). Regions of higher density were notable in the anterior femoral condyles and medial tibial plateau.

Conclusions

Optimizing knee angle to prevent oblique transaxial slices was a challenge due to limited-length scout views. However, this protocol was otherwise feasible, can be analyzed with existent manufacturer software, and yields both bone and muscle information.

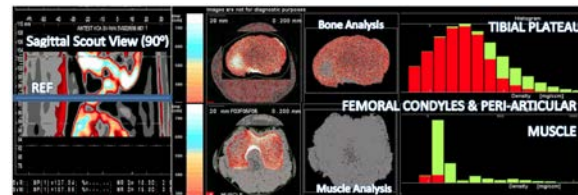


Figure 1. Subchondral bone & peri-articular muscle measurement on pQCT. Left) sagittal scout with reference line placement, Right) Bone and muscle analysis.

Relationship Between Osteocyte Lacunar Morphology and the Fatigue Life of Human Cortical Bone

Lindsay L. Loundagin^{1,2}, David M. L. Cooper³, W. Brent Edwards^{*1,2}

¹ Human Performance Laboratory, Faculty of Kinesiology, University of Calgary

² McCaig Institute for Bone and Joint Health, Cumming School of Medicine, University of Calgary

³ Department of Anatomy, Physiology & Pharmacology, College of Medicine, University of Saskatchewan

Introduction

Local strain concentrations up to 4 times the applied nominal strain have been directly measured around osteocyte lacunae within the cortical bone matrix (1), the magnitude of which is influenced by both lacunar size and orientation (2). The functional relevance of these strain concentrations remains unknown, so the purpose of this study was to quantify the effect of lacunar volume and orientation on the fatigue life of human cortical bone in both tension and compression.

Methods

Cortical bone samples were prepared from cadaveric femoral and tibial shafts obtained from two females (71 and 99 years old) and one male (77 years old). Cylindrical cores were extracted and machined into a waisted geometry with a central diameter of 2.5 mm. A region 2.8 x 2.25 mm was imaged using synchrotron x-ray microCT (BMIT, Canadian Light Source) with a resolution of 1.8 μm . Fiji software was used to quantify the osteocyte lacunar volume (Lc.V) and orientation (Lc. ϕ) within a 2.5 mm³ volume of interest. Lc. ϕ was calculated as the absolute angle (0 to 90°) between the longest lacunar axis relative to the loading axis. Samples were cyclically loaded following imaging in either zero-compression (n=11) or zero-tension (n=8) at a frequency of 4.35 Hz. Loading magnitude was held constant at 45% of the estimated ultimate strength, corresponding to 88 MPa in compression and 51 MPa in tension. Fatigue life was quantified as the number of loading cycles until complete fracture.

Results

Lc.V was not correlated with fatigue life in either mode of loading ($p \geq 0.71$). Lc. ϕ illus-

trated a strong correlation with fatigue life in tension ($R^2=0.66$, $p=0.01$), with lower angles demonstrating longer fatigue lives (Figure 1); no relationship between Lc. ϕ and fatigue life was observed in compression ($p > 0.68$).

Conclusions

The findings from this study suggest that lacunar orientation, but not volume, may have an important influence on the fatigue life of cortical bone. The strain concentration of an elliptical shaped lacuna will, in theory, increase as the angle between the major elliptical axis and loading axis is increased, independent of the axial-mode of loading. The fact that lacunar orientation was only related to fatigue life measurements in tension, suggests an important interaction between microarchitecture and loading mode on the fatigue behavior of human cortical bone.

References

- [1.] Nicolella, DP, et al. (2006). J Biomech. 39(9): p1735-17432. Hemmatian, H., et al. (2018). 8th World Congr. Biomech. P4355. <https://tinyurl.com/ycv71dof>

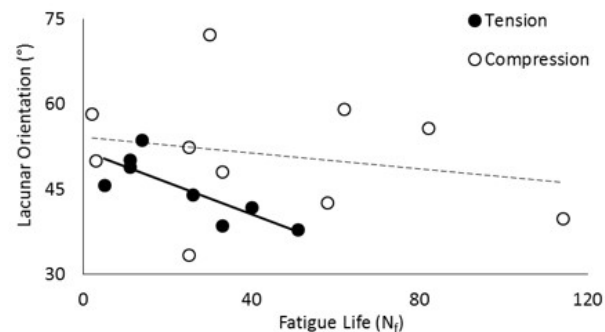


Figure 1. Lacunar orientation explained 66% of the variance in fatigue life in tension; no relationship was observed in compression.

A Rat Model of Implant Fixation with Dynamic Histomorphometry of the Peri-implant Space after Contamination with Low Virulence Micro-organisms

Vincent A Stadelmann^{*1,2}, Keith Thompson¹, Ursula Eberli¹, Fintan Moriarty¹

¹ AO Research Institute

²Schulthess Klinik

Introduction

The kinetics of bone changes adjacent to a bacteria-colonized implant are not fully characterized but are fundamental for understanding the progression of implant-related infection, and potentially for diagnostics and prevention. Here we present a rat model with standardized outcomes to study the temporal patterns of bone changes resulting from infections with various bacterial strains.

Methods

Fifty-one skeletally mature female Wistar rats received a contrast-enhanced PEEK miniscrew, sterile or pre-incubated with bacteria in the medial tibia (Fig. 1a). Bone changes were monitored by *in vivo* microCT (25 μm) at 0, 3, 6, 9, 14, 20, 28 days post-operatively. Scan series were registered then two ROIs were generated 75 and 700 μm from the implant (1b&1c). Bone-implant contact (BIC) was computed in ROI1, bone fraction (BV/TV) in ROI2. Quiescent, resorbed, and newly formed bone were computed from differences between subsequent scans in ROI2. Image processing was developed with EasyIPL, a high-level library of macros using IPL. After euthanasia, the screws and bones were collected for bacteriology or histology. Data tidying and processing with R.

Results

At euthanasia, all control animals were found culture negative, S.Epi and S.Aureus inoculated rats positive, and P.Acnes largely negative, suggesting an immune reaction. Less than 4% of the scans were excluded due to motion artefacts. In healthy animals, BIC and BV/TV increase rapidly until plateau within 14 days. Screws incubated with S.Aureus showed rapid bone loss and disconnection from bone within 14

days. With S.Epidermidis, bone loss was observed until day 9 followed by recovery, and P.Acnes did not show significant effect. Interestingly, each bacterial strain displayed a unique signature in the timeline of bone formation/resorption ratio (1e).

Discussion

The model presented here requires a relatively simple and robust surgical procedure. Image processing has a high CPU cost but is fully automated and user independent, making data comparable between studies or laboratories. The model is sensitive enough to decipher between bacterial strains, suggesting potential applications for diagnostics. Currently, the time course of bone changes under antibiotics treatment is under investigation.

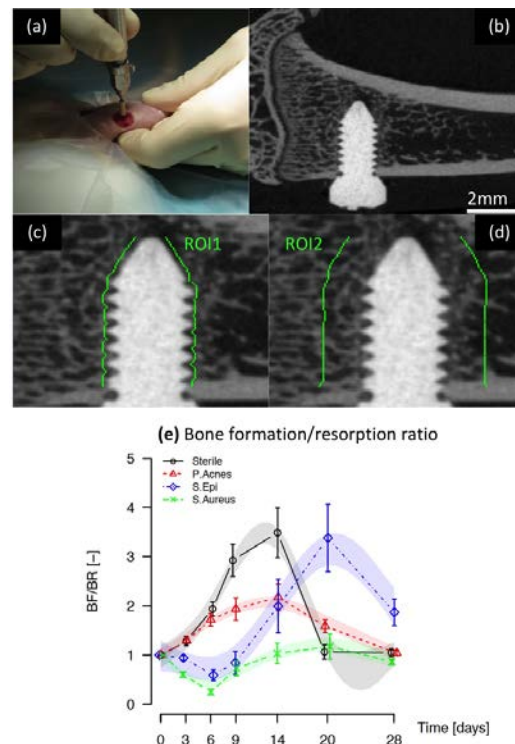


Figure 1. (a) surgical photo (b) post-op microCT (c) ROI1 (d) ROI2 (e) bone formation/resorption ratios

In-Vivo Monitoring of Degradable Processes of Bioresorbable Implants in Bone

Timo Damm^{*1}, Olga Will¹, Jana Humbert¹, Claus-C. Glüer¹

¹ Section Biomedical Imaging, Molecular Imaging North Competence Center (MOIN CC), Department of Radiology and Neuroradiology, University Medical Center Schleswig-Holstein (UKSH), Kiel University

Introduction

There is currently a lot of interest in the evaluation of degradable implants and their impacts on bone. We have developed methods for accurate 3D investigation of in-vivo μ CT data. After implantation, bone healing and its underlying biochemical machinery is influencing (and at the same time influenced by) implant alloy composition. The BMBF “MgBone” project aims to investigate these complex mutual dependencies in a multimodal setup.

Methods

The Bone-Implant Contact (BIC) region is difficult to assess using μ CT. Consequently, quantitative assessment of standard μ CT-derived material- and bone-characterizing parameters is achieved using an evaluation procedure in equidistant shells from the implant surface incorporating principal component analysis (PCA) to position the geometrically defined VOIs. Moreover, we compute the intra-individual changes to take full advantage of the longitudinal in-vivo follow-up scan procedure, which results in a more precise characterizing of both the degradation process as well as the bone healing adjacent to the implant. Evaluation of in-vivo μ CT data of 16 Sprague Dawley rats is presented. Each animal received one of two different magnesium-gadolinium (MgGd) alloy implant screws into one tibia and either a titanium (Ti) or a polyether-ether-ketone

(PEEK) plastic screw of equal dimension as control implant into the other. Scans have been acquired directly post-OP and at week 1, 4 and 8, 12 and 16 with a voxel size of 26 μ m.

Results

Contradicting the normal expectations according to results from material science, MgGd-alloy degradation in living tissue leads to increasing segmentation volumes of the implants using threshold-based methods. Relative segmentation volume increases of $(+2.9 \pm 0.3)\%$ for Mg10Gd and $(+7.9 \pm 1.2)\%$ for Mg5Gd per week have been calculated. Decreasing mean densities do not fully compensate. Mass collected in geometrically defined cylinder shells, which have been positioned by PCA onto the implants show degradation rates in the core implant significantly lower than in-vitro results. In outer shells, mass increases more rapidly than in the Ti control group.

Conclusions

The preliminary evaluation shows differences in degradation rates between the MgGd alloys. They are in-vivo substantially lower than in-vitro estimates. The local situation in bone with less diffusion matters and the implant neighborhood appears to be characterized by Mg-alloy degradation and simultaneous density increase.

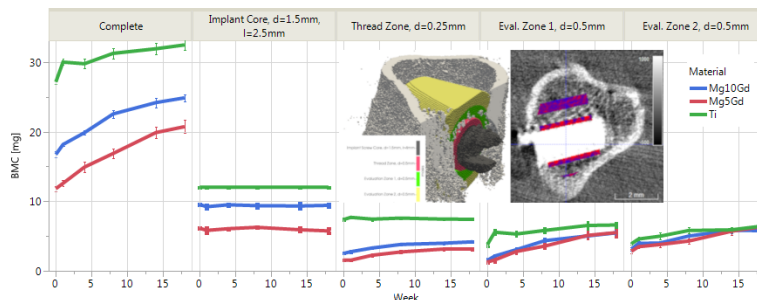


Figure 1. The diagram shows mass content changes in five different compartments over time. Inset shows segmented compartments in 3D and 2D.

Regional Discrepancies in Proximal Femur and Femoral Shaft Strain Following Two Years of Simulated Zoledronic Acid Treatment

Ifaz T. Haider^{*1,2}, Paul Kostenuik^{3,4}, W. Brent Edwards^{1,2}

¹ McCaig Institute for Bone and Joint Health, University of Calgary

² Human Performance Laboratory, University of Calgary

³ School of Dentistry, University of Michigan

⁴ Phylon Pharma Services

Introduction

Prolonged use of antiresorptive drugs has been associated with rare but serious atypical femur fractures (AFF), characterized as low-energy, fatigue-like fractures of the lateral femoral shaft or subtrochanteric region. The pathophysiology of AFF is poorly understood, but regional discrepancies in changes to density and geometry resulting from antiresorptive drugs may help explain their occurrence. In this study, we simulated regional changes to the femur after two years of antiresorptive treatment or placebo and examined the impact of these changes on strains at the proximal femur and femoral shaft.

Methods

A subject-specific finite element (FE) model was generated with material properties and geometry based on femoral CT scans from a 72-year-old female cadaver. From this base model, we generated FE models representing the femur of an average patient before and after two years of treatment with zoledronic acid (ZOL) or placebo [1] using density scaling and parametric morphing. We matched the periosteal diameter of the femoral neck as well as volumetric bone mineral density and cortical thickness of the neck, intertrochanteric, and shaft regions. Loading was simulated using physiological boundary conditions representing a sideways fall onto the greater trochanter or the stance phase of gait. Peak maximum (tensile) principal strains at the proximal femur and femoral shaft were compared between treatments.

Results

Simulated treatment with ZOL was associated with lower femoral strains compared with placebo. Differences were greatest at the proximal femur, where strains were 10.8% and 10.1% lower with ZOL under fall and walking conditions, respectively. Simulated

treatment with ZOL was less effective at the femoral shaft, where strains were only 5.8% lower than placebo (Figure 1).

Discussion

Two-years simulated ZOL illustrated a preferential reduction of strain at the proximal femur over the femoral shaft, suggesting greater reductions to hip fracture risk than shaft fracture risk. We speculate these differences may become larger with prolonged therapy, and that this phenomenon may contribute to AFF pathophysiology. Specifically, the avoidance of fall- or fatigue-related hip fracture via ZOL-related reductions in proximal femur strains may allow some individuals to continue ambulating and accumulating mechanically-induced damage at the less-fortified femoral shaft; some percentage of those individuals may then develop fatigue-related AFF. Given the extremely low absolute incidence of AFF, this phenomenon may explain some of the increased relative risk observed in antiresorptive drug patients. However, further investigation is required to confirm this hypothesis.

References

Ito et al. (2018). JBMR, 30: 2127-2132.

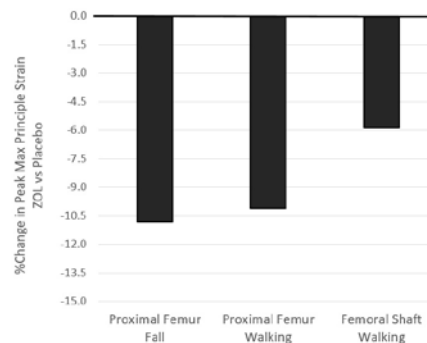


Figure 1. %Change in peak maximum principle strain after two-year treatment with ZOL relative to placebo

Differences in Hip Geometry Between Female Subjects with and without Acute Hip Fracture

Ling Wang^{*1}, Yongbin Su¹, Yandong Liu¹, Ruopei Yang¹, Zhe Guo¹, Minghui Yang², Xinbao Wu², Manyi Wang², Xiaoguang Cheng¹, Klaus Engelke³

¹ Department of Radiology, Beijing Jishuitan Hospital, Peking University

²Department of Orthopaedic Trauma, Beijing Jishuitan Hospital, Peking University

³Institute of Medical Physics, FAU Erlangen-Nürnberg

Introduction

While it is well known that hip BMD is reduced in patients with hip fracture, differences in geometrical parameters such as cortical volume and thickness between subjects with and without hip fracture are well less known.

Methods

CT scans from 421 independently community-dwelling elderly women, enrolled in the China Action on Spine and Hip Status (CASH) study (NTC 01758770) between March 2016 and May 2017, were included in the study. 230 of the women had acute hip fractures. CT scans were taken within 48 hours after fracture to minimize changes in vBMD and body composition. 191 age matched women served as controls. CT scans were analyzed with MIAF – Femur. For the purpose of this analysis integral and cortical volumes of total hip, head, neck, trochanter and intertrochanter were analyzed. In the head and neck the volumes were further subdivided into superior anterior (SA) and posterior (SP) as well as inferior anterior (IA) and posterior (IP) quadrants. In addition cortical thickness was determined for all sub VOIs listed above. Differences between fractured and unfractured females were compared by Ancova, using age, height and weight, CT pixel size and slice thickness as covariates.

Results

Results of the univariable analysis are shown in the table for those variables that remained significant after adjustments. Integral volume of the total femur, neck and intertrochanter did not significantly differ between groups. Cortical volume and thick-

ness were significantly lower in the fractured subjects with exception of the trochanter where cortical thickness was slightly higher in the fractured subjects and cortical volume did not change. In unfractured subjects, the ratio of cortical to total volume was significantly greater for total femur, neck, trochanter and intertrochanter but differences in the trochanter were small. A closer inspection of the quadrants (details omitted) showed that at the neck, in the fractured subjects, cortical thickness was significantly lower in all quadrants whereas cortical volume was significantly higher (n.s. in quadrant SA). Femoral head volume of all quadrants was higher ($p < 0.05$ for quadrants SP and SA) higher in fracture subjects. Total neck volume of IP and IA quadrants was numerically higher and of SP and SA quadrants numerically lower than in fractured patients ($p < 0.05$ for SA).

Conclusion

Differences in total and cortical volume as well as cortical thickness between fractured and unfractured females vary substantially across the proximal femur.

Variable/VOI	SubVOI	Mean \pm SD unfractured	Mean \pm SD fractured	p
Age		70.8 \pm 6.8	71.3 \pm 7.8	n.s.
Height		157.9 \pm 5.7	159.0 \pm 5.7	n.s.
Weight		62.7 \pm 9.8	60.1 \pm 9.9	0.008
Total Femur	cort vol	15.8 \pm 3.7	15.1 \pm 2.9	<0.001
	cort thick	1.84 \pm 0.25	1.76 \pm 0.23	<0.001
Head	int vol	35.5 \pm 5.3	38.0 \pm 5.9	<0.001
	cort vol	4.15 \pm 1.0	4.07 \pm 1.3	0.001
Neck	cort thick	1.74 \pm 0.25	1.63 \pm 0.35	<0.001
	int vol	24.7 \pm 4.3	26.5 \pm 5.2	<0.01
Trochanter	cort thick	1.71 \pm 0.21	1.73 \pm 0.24	<0.001
	cort vol	5.9 \pm 2.9	4.9 \pm 1.4	<0.001
Intertroch.	cort vol	5.9 \pm 2.9	4.9 \pm 1.4	<0.001
	cort thick	2.07 \pm 0.37	1.90 \pm 0.24	<0.001

Table 1.

Comparison of Finite-Element-Derived Strength, Cortical and Trabecular Bone Micro-Architecture in Postmenopausal Women With and Without Recent Distal Radius Fracture

Chantal E Kawalilak¹, Saija A Kontulainen², Morteza A Amini¹, Josje AG van Rens³, Cathy M Arnold⁴, James D Johnston^{*1}

¹ Department of Mechanical Engineering, College of Engineering, University of Saskatchewan

² College of Kinesiology, University of Saskatchewan

³ Department of Biomedical Engineering, Eindhoven University of Technology

⁴ School of Physical Therapy, College of Medicine, University of Saskatchewan

Introduction

We characterized differences in finite element derived strength estimates, bone area, density, and micro-architecture between postmenopausal women who sustained a recent (<2 years) distal radius fracture (DRF) compared to their non-fracture counterparts.

Methods

Using high-resolution peripheral quantitative computed tomography (HR-pQCT), we scanned the non-dominant or non-fractured distal radius of 75 postmenopausal women (mean age, SD: 64, 9 years). Finite element derived strength estimates included: compressive failure load, torsional failure moment as well as anteroposterior (AP) and mediolateral (ML) bending failure moments. Bone measures included: total, cortical, and trabecular area and density. Cortical microarchitectural outcomes included: BV/TV, porosity, pore volume, pore diameter and thickness. Trabecular micro-architectural outcomes included: BV/TV, trabecular num-

ber, thickness, separation, and heterogeneity. Multivariate ANOVAs were used to compare means of all outcomes for the radius between fracture and non-fracture groups.

Results

Women with a recent DRF (when compared to the non-fracture group), had lower strength in compression (-9.4%), torsion (-10.5%), as well as in AP and ML bending (AP=-12.5%; ML=-11.8%). Regarding bone micro-architecture, women with a DRF had lower trabecular density (-17.8%), trabecular bone volume fraction (-17.7%), trabecular number (-20.4%), trabecular thickness (-2.9%) and trabecular separation (-20.1%) at the distal radius compared to their non-fracture counterparts.

Conclusion

Results indicate that postmenopausal women with recent (<2 years) DRF had noticeable lower bone strength estimates and trabecular deterioration and at the distal radius.

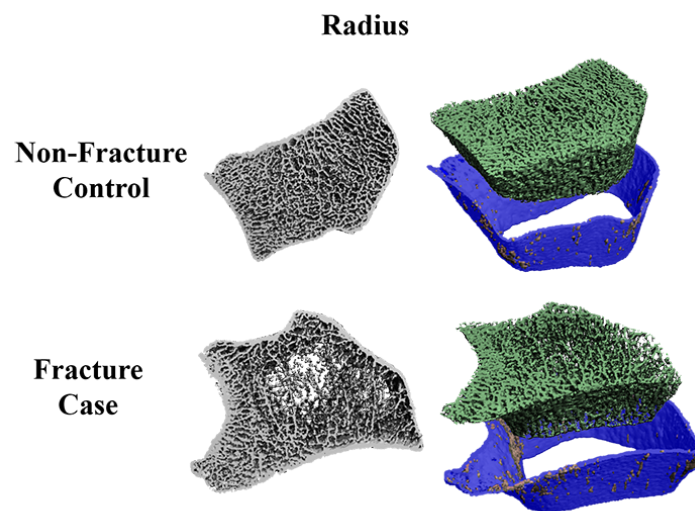


Figure 1. HR-pQCT images of distal radius from postmenopausal women with recent distal radius fracture (bottom) and age-matched fracture-free counterpart (top)

Workshop Hands-on transparent QMSKI: Open-access data, reproducible workflows, and interactive publications

Serena Bonaretti¹

¹ Stanford University

Course description

Open science and reproducible research have progressively gained attention in the scientific community as the main tools to practice transparent and rigorous research. Openness and reproducibility are fundamental to assess the value of scientific claims, build on previous work with reliability and efficiency, and strengthen collaborations to improve and expand robust scientific workflows, which will become fundamental for the whole scientific community [1]. In this new context, papers, intended as the tool we use to communicate our findings to our peers, are evolving to become more interactive, by including links to data and code repositories for reproducibility [2].

In this workshop, we will collectively define the terminology relative to transparent research and we will critically discuss how the principles of open-source and reproducible research can be successfully used for transparent QMSKI. In addition, we will share concrete solutions to practice transparent QMSKI. Specifically, we will focus on that segment of the research workflow that includes acquisition of new data, development of methods to analyze the data, and publication of findings. Topics will include:

- Open data: Available data repositories (e.g. Zenodo, Figshare), importance of metafiles to describe data, and importance of documentation to describe code (e.g. websites)
- Reproducible research: Use of open-source programming languages (e.g. Python), creation of workflows with computational notebooks that integrate narrative text, algorithm execution, and visualization of results (e.g. Jupyter Notebook), and version

control tools (e.g. Github)

- Paper of the future: Preprint on archives (e.g. bioRxiv), open source journals, interactive publications, and reproducible figures. The discussion will be supported by a practical demonstration. We will segment and analyze femoral knee cartilage using pyKNEEr, a modular software written in python with Jupyter Notebooks as interface.

In addition, we will discuss an example of paper of the future, with links to repositories. All materials will be on the workshop's webpage on Github¹.

Target audience

Anybody interested in open science, reproducible research, and interactive publications to support transparent QMSKI.

Objectives

- To define and discuss open science, reproducible research, and interactive publications
- To get familiar with practical tools for open-source and reproducible research
- To promote the use of open-source and reproducible research tools at a community level

References

- [1] Donoho D. et al. Reproducible Research in Computational Harmonic Analysis. *Comput. Sci. Eng.* 11,1,8-18. 2009
- [2] Claerbout JF et al. Electronic documents give reproducible research a new meaning. *SEG Technical Program Expanded Abstracts.* 11,1,601-604, 1992

¹https://github.com/sbonaretti/2019_QMSKI_Transparent_Research_WS/

Workshop High Resolution Image Processing – From Acquisition to Outputs

Bert van Rietbergen

¹ Eindhoven University of Technology

Course description

High-resolution imaging of bone typically is used to measure bone density and microstructural parameters. As the full 3D bone microstructure is available, however, it is possible as well to perform more advanced analyses. This workshop will focus on micro-Finite Element (FE) analysis and 3D rigid image registration of baseline and follow-up images. With micro-FE analysis, it becomes possible to translate (changes in) the microstructure directly to mechanical properties without involving any statistical model and to calculate local (tissue level) loading conditions as sensed by the cells. With 3D rigid registration it is possible to identify exactly the sites where bone is gained or lost. Performing such analyses, however, typically involves many processing steps, such as image-processing steps (e.g. image filtering, thresholding, removal of unconnected parts) and steps to perform the actual analyses (e.g. solving the FE problem, post-processing the FE-results, performing 3D registration, image transformation). In particular when performing large number of analyses, these steps need to be automated to get consistent results. The aim of this workshop is to demonstrate how such fully automated and complex micro-FE and 3D registration tasks can be created and processed using the Scanco IPL software, thus to stimulate ideas for your own novel analyses.

Program of activities

The workshop will first explain the basics of the scripting and IPL language. Following, a simple script is generated that can read a micro-CT scan, pre-process it and perform a

micro-FE analysis. In a second example a simple script for 3D rigid image registration of a BL and FU scan is generated that can also be used to visualize the results. This script then will be modified to a more sophisticated version of this script that can also account for mineralization thresholds set to the bone gain/loss. Finally it will be demonstrated how such scripts can be combined to, for example, generate a script that can evaluate the local tissue stresses in the regions where bone is gained or lost.

Target Audience

Anybody with an interest in sophisticated 3D high-resolution image processing. As the software is already available to users of the Scanco system this workshop is of particular interest for those users.

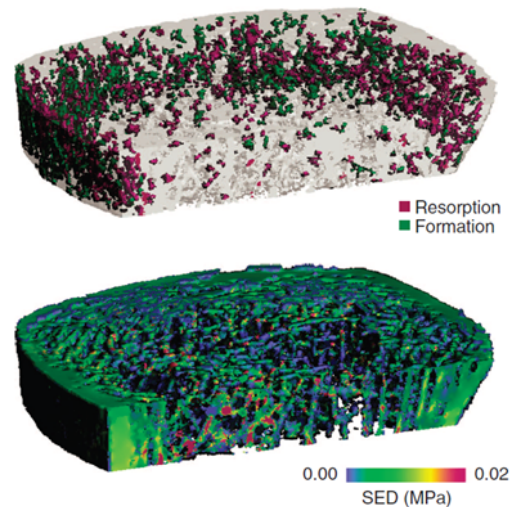


Figure 1. 3D image registration (top) and micro-FE results of longitudinal HR-pQCT images

Topological Properties of Trabecular Bone and Their Biomechanical Significance

Natalie Reznikov^{*1}, Ammar Alshegri², Mathieu Gendron³, Nicolas Piché³, Iskandar Tamimi⁴, Jun Song², Faleh Tamimi¹

¹ Faculty of Dentistry, McGill University

² Faculty of Engineering, McGill University

³ Objects Research Systems Inc.

⁴ Hospital Regional Universitario de Malaga

Introduction

Trabecular bone is sometimes described as a porous solid, which implies certain randomness. However, it undergoes continuous structural optimization that is not random. During fetal development, redundant trabecular elements are pruned (topological optimization). Remaining trabeculae continue life-long morphological optimization which involves thickening and alignment of some elements, resulting in a net increase of tissue anisotropy. While the morphological characteristics of trabecular bone are mutable and responsive to loading conditions, its topological blueprint is conserved. Of note, topology is decoupled from bone volume fraction, and from size and shape of the structural elements.

Methods

To analyze trabecular bone topology, each trabecula can be “skeletonized” to a centroid (edge). These edges connect at nodes and form a skeleton/graph (in topological space). In a typical graph of trabecular bone, the abundances of nodes having 3, 4, 5 and more connections decay exponentially. The edges connected at nodes approximate symmetrical configurations such that the maximal volume is spanned with the given number of connected elements (approaching 120° for triple nodes, 109.5° for quadruple nodes, and so). Here, we tested *in silico* the singular significance of topological blueprint for the mechanical behavior of normal and pathologic trabecular bone. Normal, osteoarthritic and osteoporotic human proximal femur sam-

ples were scanned using μ CT at 30-50 microns per pixel. The images were segmented, cropped to 1 cm³ cubic shape, analyzed morphometrically, and then reduced to 3D graphs (DragonflyTM). Using finite element analysis (Abacus) each edge of a graph was substituted by a Timoshenko beam; the bottom 20% of the nodes were constrained in the direction of compressive loading, and compression to 0.7% strain was applied. Stiffness (modulus) and von Mises stress were monitored.

Results

The osteoporotic fragility fracture samples demonstrated lower apparent moduli and higher von Mises stress in comparison to the normal samples. Surprisingly, the 3D graph models of the osteoarthritic bone samples had the same simulated mechanical behavior as the osteoporotic fracture samples, although their morphological characteristics (e.g., bone volume fraction, trabecular thickness) were comparable to those of the normal samples. While both groups of pathologic samples were topologically inferior in comparison to normal samples, the suboptimal topology may (as in osteoarthritis) or may not (as in osteoporosis) be partly compensated by trabecular morphology.

Conclusion

We conclude that trabecular bone is not a porous solid, but rather is a self-architected structure. Trabecular bone topology, rather than morphology, might be the core determinant for optimized biomechanical behavior.

Individual Trabecula Segmentation (ITS) Based Analysis of XCTII Compared to Gold-Standard μ CT Scans of the Human Distal Radius and Tibia

A. Teodora Dinescu^{*1}, Yizhong Hu¹, Sanchita Agarwal², Elizabeth Shane², X. Edward Guo¹

¹ Department of Biomedical Engineering, Columbia University in the City of New York

² Division of Endocrinology, Columbia University Medical Center

Introduction

High-resolution peripheral quantitative computed tomography (HR-pQCT) has been used for in vivo 3D visualization of trabecular microstructure with low radiation. Second-generation HR-pQCT (XCTII) has been shown to have good agreement with first generation HR-pQCT (XCTI) and has an enhanced resolution from 82 μ m to 61 μ m. Individual Trabecula Segmentation (ITS) is a technique used to decompose the trabecula network into individual plates and rods. ITS based on XCTI showed strong correlation to ITS based on gold-standard micro computed tomography (μ CT) and identified important trabecular microstructural changes in various diseases. ITS based on XCTII has new potentials in musculoskeletal studies but has yet to be validated. The objective of this study was to assess the agreement between ITS based on XCTII and ITS based on μ CT to assess the capability of ITS on XCTII as a clinical tool.

Methods

Twenty-seven sets of fresh-frozen tibia and radius bones obtained from the Life Legacy Foundation (Tucson, AZ) were scanned in the distal region using XCTII at 61 μ m and μ CT at 25 μ m. The μ CT image of each sample was registered to the corresponding XCTII image to ensure analysis of corresponding regions. A Gaussian filter was applied to the μ CT images for noise reduction and a global thresh-

old of 20% of the maximum voxel value was used to binarize the images. Standard patient evaluation was used to segment the XCTII images. ITS analysis was performed on the trabecular region of the registered images. Bone volume fraction (pBV/TV, rBV/TV), number density (pTb.N, rTb.N), thickness (pTb.Th, rTb.Th) and plate-to-rod (PR) ratio (pBV/rBV) of trabecular plates and rods were obtained. Difference between these measurements in XCTII and μ CT was calculated. Paired student's t-tests were used to examine the difference between XCTII and μ CT measurements. Linear regression was used to determine the correlation coefficient of these parameters.

Results and Discussion

Mean and standard deviation of ITS based microstructural measurements are shown in Table 1. All of the XCTII parameters were statistically different from the μ CT measurements except BV/TV and rTb.N in the distal tibia. There was a high correlation between BV/TV of XCTII and μ CT images in both the radius and tibia ($r=0.95$ and $r=0.94$ respectively). Other parameters ranged from fair to strong correlation ($r=0.24$ to $r=0.92$). The strong correlation of BV/TV, pBV/TV, and rBV/TV between XCTII and μ CT microstructural analysis suggests that XCTII can be used to clinically assess changes in plate and rod microstructure.

	Distal radius				Distal tibia			
	XCTII	μ CT	Difference	r	XCTII	μ CT	Difference	r
BV/TV	0.172 \pm 0.043	0.182 \pm 0.023	-0.010*	0.95	0.195 \pm 0.039	0.185 \pm 0.026	0.011	0.94
pBV/TV	0.108 \pm 0.037	0.156 \pm 0.024	-0.048*	0.92	0.139 \pm 0.034	0.165 \pm 0.024	-0.026*	0.91
rBV/TV	0.065 \pm 0.014	0.027 \pm 0.008	0.038*	0.84	0.057 \pm 0.012	0.020 \pm 0.004	0.037*	0.85
pTb.N	1.480 \pm 0.133	2.167 \pm 0.074	-0.686*	0.24	1.503 \pm 0.102	1.982 \pm 0.109	-0.479*	0.54
rTb.N	1.523 \pm 0.081	1.573 \pm 0.133	-0.050*	0.66	1.412 \pm 0.093	1.370 \pm 0.104	0.043	0.56
pTb.Th	0.191 \pm 0.009	0.136 \pm 0.009	0.055*	0.71	0.208 \pm 0.012	0.156 \pm 0.013	0.052*	0.80
rTb.Th	0.175 \pm 0.008	0.126 \pm 0.009	0.050*	0.72	0.184 \pm 0.011	0.133 \pm 0.011	0.051*	0.79
PR Ratio	1.703 \pm 0.613	6.425 \pm 2.243	-4.722*	0.84	2.494 \pm 0.637	8.457 \pm 1.724	-5.963*	0.79

Table 1. Microstructural measurements and correlations by XCTII and μ CT

An Automatic MicroCT Workflow for Relating Subchondral Bone Morphology to the Overlying Cartilage Damage in Osteoarthritic Human Knees

Vincent A Stadelmann^{*1}, Birgitta Gatenholm^{2,3}, Carl Anders Lindahl³, Mats Brittberg^{2,4}

¹ SCANCO Medical AG

²Department of Orthopaedics, University of Gothenburg

³Sahlgrenska University Hospital

⁴Department of Orthopaedics, Hallands Sjukhus

Introduction

Osteoarthritis (OA) causes morbidity and disability in patients worldwide. OA is now considered a whole joint disease where subchondral bone plays an important role in pain and disease development. We combined standard and contrast-enhanced microCT for simultaneous mapping of cartilage and subchondral bone morphology. In “traditional” microCT image processing, regions of interest (ROIs) are defined (semi-)manually. For articular OA this approach is tedious and imprecise because of low contrast and complex spatial geometry of cartilage. Therefore we developed an automatic workflow generating ROIs of cartilage, bone and defects, and validated it in OA specimens.

Methods

Specimens Twelve fresh tibia plateaus from patients with advanced OA after total knee replacement were photographed and split into medial and lateral condyles, then scanned at 36 μm resolution, stained with Hexabrix and re-scanned. Three specimens were also processed histologically (Saffranin-O).

Image processing Bone and cartilage were segmented from the baseline scans. The articular surface was contoured manually. Multiple ROIs were then automatically generated (Figure 1): the articular surface contour was projected onto the bone surface. Cartilage defects were identified. The articular surface and defect ROI were projected axially and intersected with trabecular and cortical bone to define the sub-ROIs. Total articular surface (AS.S), defect surface (D.S) and cartilage surface (C.S) were computed by triangulation of the respective ROIs. Cortical and trabecular bone morphometry as well as cartilage volume and thickness were com-

puted. Finally, stained scans were registered to baseline scans to compute sGAG distribution within the same ROI.

Validation Defect surface was validated against post-op photography. Cartilage thickness and sGAG distribution were validated against histology.

Results

23 condyles were analyzed; 13 had a cartilage defects, all medial. Defect surface correlated well with photographic examination ($R^2 = 0.83$, $p < 0.001$). Cartilage thickness and sGAG distribution correlated well with histology ($R^2 = 0.83$, $p < 0.011$). Cartilage was significantly thicker in intact condyles ($p = 0.02$) and bone morphometry and density correlated with overlying cartilage damage level ($p < 0.05$).

Discussion

The precision of the method was successfully validated against visual photography examination and histology. It enables high-throughput microCT analysis of OA simultaneously in cartilage and subchondral bone, for example as an additional patient evaluation tool for large outcome research cohorts.

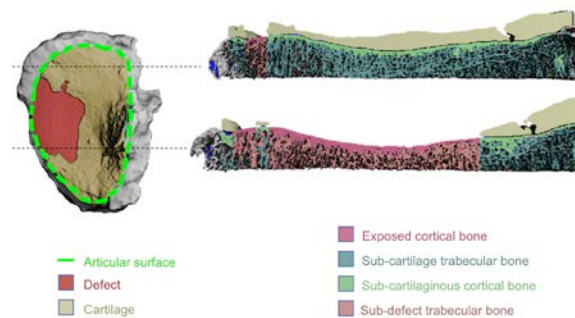


Figure 1. Automatically generated ROIs for cartilage and bone

High-Performance 3D Image Processing for Large-Scale Structure Analysis Workflows

Diego Rossinelli^{1,2}, Tor Hildebrand^{*1}

¹ Lucid Concepts AG

²University of Zurich

Introduction

Recent advancements in imaging technology enable the capturing of structures at unprecedented resolution, opening up for opportunities to extract novel insight in the fields of biology and medicine. These images, however, may have a footprint up to multiple terabytes (TB), which in turn poses major challenges to imaging applications:

- TB images do not fit into single-node HPC workstations. Even if TB RAM machines are available at exorbitant prices, the necessary compute power to process the images would still be insufficient.
- Supercomputers are readily available both within premises and the public clouds, and offer the potential for analyzing TB images in short time. However, most commercial imaging software is not supercomputing-ready.
- Offloading the calculations to supercomputers is not obvious to the user, as it requires a stateful and asynchronous interaction with the job scheduler.
- Contemporary 3D rendering software seems incapable to visualize TB images at scale.

Solution

Supercomputing-ready processing modules for advanced image analysis have been developed including segmentation, histomorphometry, visualization and CFD analysis with state-of-the-art accuracy and performance. This enables not only the processing of very large images, but also the evaluation of large sequences of images (high throughput analysis), and the tuning of image processing algorithms by efficient exploration of the parameter space using e.g. Monte Carlo methods.

Using a recently developed workflow system (XamFlow) the modules can be combined in processing graphs for solving arbitrarily complex evaluations, in a user-friendly and intuitive way. The computational workloads are orchestrated by an elaborate job scheduling system. Developed supercomputing modules for large-scale image processing include:

- 3D image compression with state-of-the-art compression rates, with an unparalleled throughput of 2-8 GB/s per node. Furthermore, the resulting compressed images are both resolution and quality scalable, enabling fast progressive viewing for interactive exploration of huge images.
- Image processing tools like denoising and enhancement via local 3D curvelets transform, global wavelet transform on the interval, statistical models, morphological operators, component labeling.
- Morphometric analysis using large-scale thickness calculation with sub-voxel accuracy.
- HQ large volume rendering and accurate mesh-based segment visualization with poster-size images and 4K/8K video output.
- State-of-the-art CFD solver outperforming commercial solvers both in terms of accuracy and performance

In case of images larger than the aggregate available RAM, these modules can operate out-of-core, making them feasible not only for supercomputers but also for on-premises workstations.

Results

The processing modules have been successfully tested for processing TB sized mouse kidney images from a synchrotron CT (The Interface Group, University Zürich), as depicted in Figure 1.

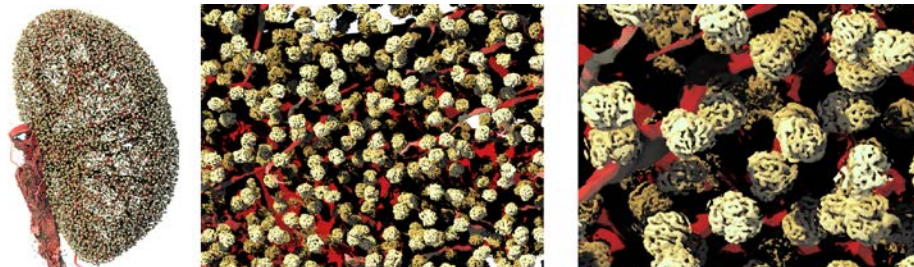


Figure 1. Glomeruli segmentation, classification and visualization, full image and zoomed in crops.

Level Set Motion as a Framework for Computational Modeling of Bone Adaptation

Bryce A. Besler^{*1,2}, Leigh Gabel^{1,2}, Lauren A. Burt^{1,2}, Nils D. Forkert^{1,3}, Steven K. Boyd^{1,2}

¹ Department of Radiology, University of Calgary, Calgary, Canada

² McCaig Institute for Bone and Joint Health, University of Calgary, Calgary, Canada

³ Hotchkiss Brain Institute University of Calgary, Calgary, Canada

Introduction

Bone is constantly remodeling to balance dietary, hormonal, and mechanical factors. The basic multicellular unit coordinates cytokines and biochemical signals to orchestrate removal of old bone and replacement of new bone. These signals add coherently and are measured as a surface remodeling rate. Incorporating the surface remodeling rate into computational models can enable prediction of changes in bone microarchitecture.

In this study, a mathematical framework is formulated for long- and short-term prediction of adaptation of bone microarchitecture. A simplified model of aging, equivalent to simulated bone atrophy (SIBA; Müller 2005), is presented as a proof-of-principle for the general approach.

Methods

A level set method was established as the foundation to simulate age-related changes in bone microarchitecture given a known surface remodeling rate. The model includes a natural definition of homeostasis, the ability to adopt around foreign objects (e.g. surgical screw), and a natural interpretation in Hamiltonian mechanics.

After developing the theory, a two-parameter model of aging was proposed. The model conceptualizes the bone surface as a wave front, shrinking with age. The surface remodeling rate is a summation of terms of advection (forward movement) and diffusion (increased loss in thin structures), mathematically motivated by the SIBA algorithm.

To demonstrate equivalence, the distal tibia of ten participants (5 women, 5 men) were im-

aged using high-resolution peripheral quantitative computed tomography (XtremeCT II; SCANCO Medical, Switzerland). Participants ranged in age from 56 to 67 years. 30 years of loss was simulated. Bone volume fraction (BV/TV) and bone surface to volume ratio (BS/BV) were quantified with simulated age.

Results

Percent loss of BV/TV as a function of baseline BS/BV is shown in Figure 1 (right). Baseline BS/BV predicts percent loss of BV/TV over 30 years ($R^2 = 99\%$), a key finding in the original SIBA algorithm. In Figure 1 (left), a cross section of the microarchitecture from (a) in vivo data at baseline and simulated bone loss at (b) 10 years and (c) 30 years is shown. Accelerated loss is observed in the middle of the cancellous region.

Conclusions

A unified framework for prediction of bone microarchitecture is presented. SIBA is implemented in the framework as a proof-of-principle of the generality. Future work aims to validate the method against in vivo data.

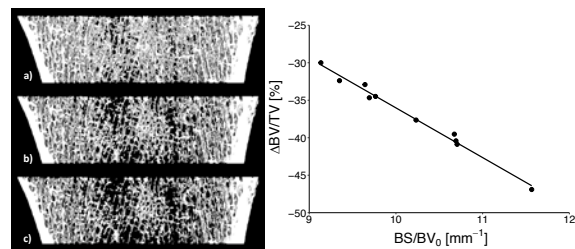


Figure 1. Simulated bone loss with age (left) and percent change in BV/TV as predicted by BS/BV at baseline (right).

Super-Resolution Images Reduce Voxel Size Effects of a Load-Adaptive Bone Remodelling Algorithm

Nicholas Ohs^{*1}, Duncan Betts¹, Stephanie Sebastian¹, Bert van Rietbergen², Ralph Müller¹, Patrik Christen^{1,3}

¹ Institute for Biomechanics, ETH Zurich

² Orthopaedic Biomechanics, Department of Biomedical Engineering, Eindhoven University of Technology

³ Institute for Information Systems, FHNW

Introduction

Bone microstructure can be resolved with clinical high-resolution peripheral quantitative CT (HR-pQCT). A validated *in silico* model of bone remodelling has the potential to extrapolate bone morphology changes and identify patients at risk of osteoporosis. However, current simulation models were developed using high resolution images unavailable in the clinics. Therefore, in this study we test the following hypotheses: Firstly, bone remodelling simulations on images with HR-pQCT resolution yield comparable bone microstructures to simulations run at high resolutions. Secondly, up-scaling those images to super-resolution prior to running the simulation will improve those results.

Methods

Five cadaveric distal radii were scanned using micro-CT with a voxel size of 25 μm . The original images were Gauss-filtered and segmented with a threshold of 450 mg HA/cm³. The Gauss-filtered greyscale images were then down-scaled to voxel sizes of 40, 61, and 82 μm , where 61 and 82 μm are the voxel sizes of current clinical HR-pQCT systems. The down-scaled images were then also up-scaled to a super-resolution of 25 μm . Finally, thresholds were applied such that the mean strain energy density (SED) for each low resolution and each super-resolution image matched with that of the corresponding high-resolution image. Using an in-house

advection-based bone remodelling algorithm, a 5-year period was simulated for the high, low, and super-resolution images and bone morphometric parameters were determined for each time step.

Results, Discussion and Conclusion

Figure 1 shows the results of simulating images of 25 μm , 61 μm up-scaled to 25 μm , and 61 μm voxel resolution for one representative radius. Visually, the simulation of the super-resolution image matches well the simulation of the original high-resolution image, whereas the simulation of the down-scaled 61 μm image is visually very different, illustrating massive resorption of the trabecular structure, especially in areas close to cortical bone. These visual findings were also supported by quantitative morphometry computed for all five radii. On average, BV/TV deviated less than 0.5, 2, and 5%, respectively, for the super-resolution 40, 61, and 82 μm images when compared to the original high resolution images, where Tb.N, Tb.Sp, and Tb.Th differed by less than 1, 7, and 15%, respectively. For the down-scaled low resolution images, morphometric parameters deviated by more than 50% on average.

Our findings show that voxel sizes available in clinical HR-pQCT systems seem to yield acceptable results for bone remodelling simulations, when using super-resolution images at 25 μm voxel size.

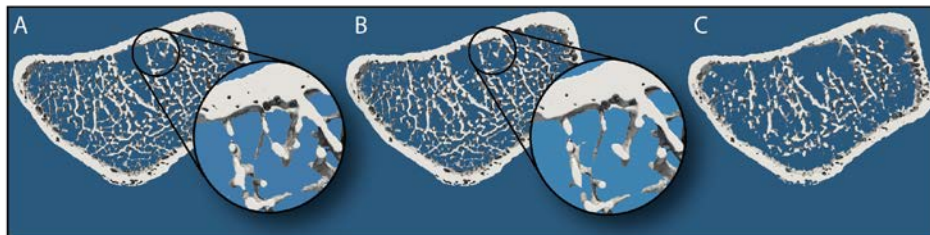


Figure 1. A 10% bone slab from the middle of the same radius after simulation. Image resolution: A) 25 μm , B) 61 μm up-scaled to 25 μm , C) 61 μm

Low Sound Wave Propagation in Cortical Bone as a Novel, Non-Invasive Imaging Biomarker in Children and Adolescents with Hypophosphatemic Rickets

Adalbert Raimann¹, Johannes Schneider², Andrea Boni-Mikats³, Radka Tuskova⁴, Patricia Feil⁵, Sarah Mehany³, Peter Pietschmann⁶, Martin Krssak⁷, Gabriele Haeusler¹, Janina Patsch¹, Kay Raum^{*2}

¹ Department of Pediatrics and Adolescent Medicine, Medical University of Vienna

²Berlin-Brandenburg Center for Regenerative Therapies, Charité – Universitätsmedizin Berlin

³Department of Biomedical Imaging and Imaged Guided Therapy, Division of General Radiology and Pediatric Radiology, Medical University of Vienna

⁴Department of Biomedical Imaging and Imaged-Guided Therapy, High Field MR Centre, Medical University of Vienna

⁵Department of Pediatric Surgery, Medical University of Vienna

⁶Department of Pathophysiology and Allergy Research, Center of Pathophysiology, Infectiology, and Immunology, Medical University of Vienna

⁷Department of Internal Medicine III, Division of Endocrinology and Metabolism, Medical University of Vienna

Background

The assessment of ultrasound wave propagation in cortical bone is a novel, noninvasive quantitative imaging tool in bone research. The purpose of this study was to determine wave propagation properties in the distal extremities in pediatric patients with X-linked hypophosphatemic rickets (XLH) and healthy controls.

Methods and Materials

Following study approval by institutional review and written informed consent, we performed quantitative bone ultrasound in children, adolescents and young adults with XLH (n=8) and healthy controls (n=30). The majority of patients and controls also underwent high-resolution peripheral quantitative computed tomography (HR-pQCT) of the radius and tibia as a standard of reference. Bone ultrasound was performed at the distal radius and the distal tibia according to a structured examination protocol, using a dedicated linear 1MHz transducer with one receiver array and two transmitter arrays. Based on bidirectional axial transmission and propagation of ultrasound waves, the first arriving signal velocity' (vFAS) was measured and post-processed. HR-pQCT images were reviewed by a board-certified radiologist, data were evaluated by the manufacturer's quantification software.

Results

Quantitative bone ultrasound of wave propagation was feasible in all study participants. At the distal radius, we found vFAS to be significantly lower in XLH patients than in healthy controls (-8.3%; p<0.001). A similar reduction of vFAS was observed in the distal tibia (-6.0%; p = 0.019). HR-pQCT scans revealed heterogenous microstructural deficits in both, cortical and trabecular bone.

Conclusion

Quantitative bone ultrasound of wave propagation is a promising imaging biomarker in children and adolescents with hypophosphatemic rickets

PATIENTS	XLH	Controls
n	8	30
Age at US (m)	155 ± 70.0	168 ± 46.3
Sex (m:f)	1:3	1:4

RESULTS	XLH	Controls
tibia vFAS	3531 ± 156	3757 ± 119
	-6.0%, p=0.019	
radius vFAS	3553 ± 196	3873 ± 143
	-8.3%, p<0.001	

Figure 1. Study population and main results.

Comparison of *in vivo* Cortical Parameters Obtained at the Radius by HR-pQCT and Bi-Directional Axial Transmission.

Donatien Ramiandrisoa¹, Sylvie Fernandez², Christine Chappard^{*3}, Martine Cohen-Solal², Jean-Gabriel Minonzio^{4,5}

¹ Bleu Solid

²Department of rheumatology, Hôpital Lariboisière, Inserm U1132, USPC Paris-Diderot

³B2OA, UMR CNRS7052, University Denis Diderot, PRES Sorbonne Paris Cité

⁴CNRS, INSERM, Laboratoire d'Imagerie Biomédicale (LIB), Sorbonne Université, Paris, France

⁵Escuela de Ingeniería Civil en Informática, Universidad de Valparaíso, Valparaíso, Chile

Introduction

Osteoporosis is a skeletal disease leading to bone fragility and increasing the risk of fractures. Current clinical gold standard, Dual-energy X-ray Absorptiometry (DXA), is limited by its projection technique and poor spatial resolution. High Resolution-peripheral Quantitative Computed Tomography (HR-pQCT) is able to provide estimates of cortical thickness (Ct.Th) and volumetric bone mineral density (Ct.vBMD) highly correlated to cortical porosity (Ct.Po). Ultrasound technologies have the advantages of portability, low cost, absence of radiation. Recent studies showed that measurement ultrasonic guided waves associated with an appropriate waveguide model can provide estimates of Ct.Th and Ct.Po using bidirectional axial transmission (BDAT). The aim of this study is to compare BDAT parameters, (Ct.Th, Ct.Po) with HR-pQCT measurements (Ct.Th, Ct.vBMD) performed at the site-matched (one-third distal) and conventional (distal) radius locations.

Material and Methods

Measurements were performed in a small population but largely representative of age and sex distribution. Forty four subjects (27 females, 17 males, 19-87 years, Body Mass Index 18-30 kg.m⁻²) were recruited from the rheumatology department in Lariboisière hospital, Paris, France. BDAT measurements were performed using a 1-MHz prototype (Azalée, Paris, France). Singular value decomposition-based approach, combined with a 2D transverse isotropic free plate waveguide model, was used to estimate Ct.Th and Ct.Po, assuming a constant bone matrix. Subjects were scanned with HR-pQCT (XtremeCT, Scanco Medical, Brüttisellen,

Switzerland). In the distal case, Ct.Th and Ct.vBMD (Dcomp) were provided by the device software. For the one-third distal position, Ct.Th and Ct.vBMD were obtained by averaging the values obtained for each slice of the 3D site-matched volume.

Results

BDAT measurement failed for two subjects. Highly significant ($p < 10^{-5}$) Pearson correlations were found between Ct.Th estimates obtained by the two methods at the one-third ($R^2=0.86$) and distal location ($R^2=0.59$). A weak correlation between Ct.Po and vBMD was observed at the one-third distal radius ($R^2=0.11$, RMSE=2.8%, $p < 0.03$), while no correlation existed with the distal Ct.vBMD. Note that the site matched correlation between Ct.Po and vBMD increased ($R^2=0.58$, RMSE=1.7%), while keeping the 29 patients associated with the highest quality factor of the BDAT measurements.

Conclusion

This study shows the potential of BDAT measurements to provide *in vivo* cortical thickness and porosity estimates. These parameters may improve the identification of patients at high risk of fracture.

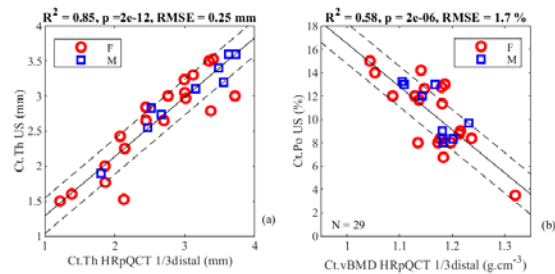


Figure 1. correlations between BDAT and HR-pQCT parameters: Ct.Th (a), Ct.Po vs Ct.vBMD (b)

Quantitative Ultrasound Assessment of Cortical Bone: Is Ultrasonic Velocity a Surrogate Of Porosity?

Quentin Grimal^{*1}, Pascal Laugier¹

¹ Sorbonne Université, CNRS, INSERM, Laboratoire d'Imagerie Biomédicale

Innovative QUS approaches have emerged to assess bone beyond BMD, e.g., providing intrinsic bone properties such as cortical bone thickness and material properties. Such developments rely on a fine knowledge of the ultrasonic properties of cortical bone. We present a review of the current knowledge on the ultrasonic properties of cortical bone that could be considered as biomarkers of bone health. The review is complemented by an analysis of data collected in our laboratory. Specifically we analyze the dependence of radial and axial ultrasound velocities on porosity. The work sheds light on the inter-individual range of variation of velocities and their relationship with porosity. We discuss the practical consequences of these variations for the design of bone QUS methods. Currently, some QUS methods targeting cortical bone assume that ultrasonic velocities do not vary across individuals, while others try to measure individual-specific velocities.

Our data consisted of elasticity measurements (stiffness tensor measured with resonant ultrasound spectroscopy) from 29 elderly human donors (mean age 77.8 (11.4)) prepared from the mid-diaphysis of the femur. Ultrasonic velocities in radial (V1) and axial (V3) directions were calculated from stiffness and apparent mass density. Vascu-

lar porosity ϕ was obtained from SR-micro computed tomography.

The anisotropy of cortical bone (due to the preferential alignment of vascular pores and mineralized collagen fibers) was reflected in the difference between V1 (typically 3200 m/s) and V3 (typically 3900 m/s). Three published studies consistently pointed at a decrease of V1 and/or V3 with increasing porosity, porosity explaining 30 to 50% of velocity variations. None of the published studies have concurrently investigated variations of V1 and V3. In our dataset, mean porosity was 0.074 (minimum 0.02, maximum 0.21); mean [range of variation] of V1 and V3 were (unit m/s) 3190 [2130-3460], and 3870 [2580-4050]. Regression equations were $V1 = 3402 - 2364 \phi$ and $V3 = 4040 - 1837 \phi$.

A 1% porosity increment induced a decrease of 0.74% and 0.47% of V1 and V3 respectively, to be compared to the precision of QUS measurements which is typically a few percents. Interestingly, the radial velocity is more sensitive to porosity variations. This is of practical importance as radial velocity is involved in pulse-echo measurements. Innovative bone imaging methods involve both radial and axial velocities.

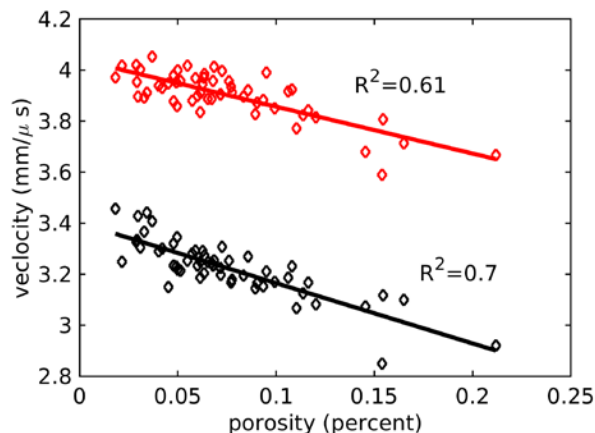


Figure 1. Ultrasonic velocity in axial (red) and radial (black) directions of bone diaphysis, as a function of vascular porosity

Automated 3D Ultrasound for Quantitative Assessment of Mechanical Properties of Skeletal Muscle

Leon de Jong^{*1}, Anton Nikolaev¹, Anna Greco², Jurgen J. Fütterer¹, Chris L. de Korte¹

¹ Department of radiology and nuclear medicine, Radboud University Medical Center

² Department of neurology, Radboud University Medical Center

Introduction

This study focuses on providing quantitative parameters within the diagnostic workup for patients having (suspicion of) neuromuscular disease. Although many of these patients show muscle weakness, the underlying mechanism of the disorder varies heavily. Over 600 different types of disorders are known in literature, indicating the need for adequate diagnostics. Myopathies form a group of neuromuscular disorders that results in mechanical changes in skeletal muscle tissue. In this study, we assess automated 3D ultrasound data to quantify parameters related to these mechanical properties in a healthy population. These parameters will form a control dataset for future patient studies. The study was performed on site at NEMO science museum Amsterdam to gain a large and balanced dataset.

Study population

124 healthy volunteers with 11 different nationalities participated after signing informed consent; 65 males and 59 females, age 38 ± 16 , BMI 21.4 ± 4.3 . Volunteers declared to have no prior medical conditions relevant to this measurement. This study was approved by the local ethical board.

Methods

The overall parameters measured prior to the ultrasound examination are; weight, bone mass and water fraction. Segmental parameters (arms/legs/core) are; fat fraction and muscle mass. Medical Research Council (MRC)-scores were acquired by physical ex-

amination by a physician and maximum hand grip strength was measured for both hands. Automated 3D ultrasound scans of the tibialis anterior muscle were performed whilst maintaining isometric contractions at 0, 20% and 40% of maximum voluntary contraction (MVC) force. Acquisition planes were in transversal as well as sagittal direction, the scanned volume covered the full width and 15 cm of the length of the tibialis anterior. The volume was centered at the nominal width of the muscle.

Results

Initial analysis of 10 subjects show an increasing pennation angle with respect to the initial angle from 1.1° (0-20% MVC) via 1.8° (20-40% MVC) to 3.0° (0-40% MVC), where positive values represent increasing angles. Initial analysis of corrected echogenicity values throughout the tibialis anterior result in subject specific curves between echo intensity and transversal slice location (proximal to distal). Considering the subject's demographics, a trend is expected between subject categories.

Conclusion and future implications

This study provides a non-invasive method to assess quantitative parameters of interest for neuromuscular disorder diagnostics, especially myopathies. We suggest that the parameters (echogenicity, muscle volume and architecture, fascicle length and pennation angles) of this dataset can be used to investigate disease gradation, progression and treatment effect.

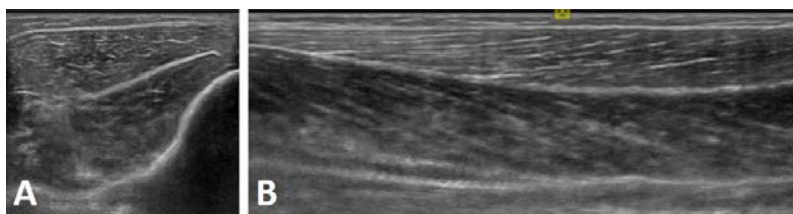


Figure 1. Resulting images of 3D dataset in plane of acquisition (A) and reconstructed sagittal plane (B).

Correlation between the Gold-Standard DXA with Axial-Transmission Ultrasonic Velocity and Attenuation for Osteoporosis Diagnosis: A Pilot Study

Lawrence H. Le^{*1,2,3}, Tho N.H.T. Tran¹, Mauricio D. Sacchi², Dean Ta³, Jacob L. Jaremko¹

¹ Department of Radiology and Diagnostic Imaging, University of Alberta

² Department of Physics, University of Alberta

³ State Key Laboratory of ASIC and System, Fudan University

Introduction

Osteoporosis is a skeletal disease characterized by low bone mass, deterioration of bone tissue, and cortical thinning, leading to high risk of fracture. Currently, dual energy X-ray absorptiometry (DXA), which relies on ionizing radiation to measure bone mineral density (BMD), is the gold standard for osteoporosis assessment. However, bone strength is not determined by bone mass only but also mechanical properties. This leads to studies for alternative osteoporosis diagnostic modalities, which can provide better quantitative assessment of bone quality. Ultrasound has several advantages mainly due to its lack of ionizing radiation and its sensitivity to the mechanical elasticity of bone tissues.

Axial transmission ultrasonography (ATU) has shown great potential to be a non-invasive diagnostic tool to characterize cortical bone at multiple peripheral skeletal sites, e.g. radius and tibia. Recent preliminary studies using ATU technique, which uses a set of transducers positioned linearly along the bone axis, have shown that quantitative ultrasound is a valid modality for cortical bone quality assessment. The objectives of this work are to extract the ultrasonic velocity and attenuation information from the human tibia datasets and to correlate the ultrasonic indicators with DXA-BMD.

Methods

The ultrasonic data were collected at a Medical Imaging Consultant (MIC) clinic in Edmonton with Ethics approval from the University of Alberta. A TomoScan Focus LTTM phased array ultrasound system (Olympus NDT Inc., Canada) was used for the data acquisition. The left mid tibia was chosen as the measured site for this clinical study. 100 consented subjects, who had bone densitometry examinations, were recruited. Each subject was scanned 3 times using dif-

ferent beam-steering configurations at a fixed transmitter-receiver distance.

Results

Data from 20 subjects aged 50 to 80 years were used for this pilot study. For each dataset, the transit times and amplitudes of the first detectable signals at the receiving probes were measured. The mid-tibial ultrasound velocity and attenuation coefficient could then be estimated by linear regression. The average speed and attenuation were estimated from the 3 ultrasound records for each subject. The cortical speed of sound was found to increase ($R^2 = 0.337$) while cortical attenuation decreases ($R^2 = 0.247$) with BMD, i.e. they are sensitive to osteoporosis-related changes in bone. This may be due to the trabecularization of cortical bones, leading to cortical thinning and increasing intracortical porosity. The preliminary result will be used as a basis for the analysis of the remaining subjects' data and to further examine the relationship between ultrasonic parameters and skeletal health status.

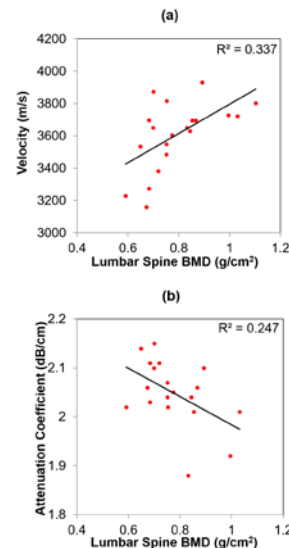


Figure 1. Correlation of (a) ultrasonic velocity and (b) attenuation coefficient with the subjects' BMD.

Estimation of Cortical Micromorphology from High-Frequency Ultrasound Backscatter

Juan Du¹, Huong Nguyen Minh¹, Gianluca Iori¹, Kay Raum^{*1}

¹ Berlin-Brandenburg School for Regenerative Therapies, Charité - Universitätsmedizin Berlin

Introduction

Cortical bone microarchitecture, i.e., porosity (Ct.Po), pore diameter (Ct.Po.Dm) and pore density (Ct.Po.Dn) are important factors in determining bone toughness and strength. Ultrasound backscattered from cortical bone carries information about the morphology of unresolved structures, but multiple scattering, mode conversions, and attenuation caused by absorption and scattering may influence the backscatter spectrum. We have conducted a parametric sound propagation simulation study to establish the associations between pore morphology and backscatter properties and to develop a theoretical cortical bone backscatter model.

Methods

A 2D parametric Finite-Difference Time-Domain (FDTD) study was performed using a 4-mm thick plate with randomly distributed spherical pores yielding Ct.Po (4–18%), Ct.Po.Dm (40–120 μm) and Ct.Po.Dn ($< 100 \text{ mm}^{-2}$). Isotropic material properties were used for bone ($c_{11}=c_{22}= 23.7 \text{ GPa}$, $c_{12}=9.5 \text{ GPa}$, $c_{66}=6.6 \text{ GPa}$, $r=1.93 \text{ g/cm}^3$, $a=2.1 \text{ dB/mm}$) matrix and pores ($c_{11}=c_{22}= c_{12}=2.25 \text{ GPa}$, $c_{66}=0 \text{ GPa}$, $r=1.00 \text{ g/cm}^3$, $a=0.002 \text{ dB/mm}$).

The plate was placed 4 mm below the surface of an unfocused linear array (single element size: 0.3 mm, Ntransmit = 16, Nreceive = 32). A broadband (BW = 57 %) 6-MHz pulse was used for excitation. All simulations were performed using Simsonic (<http://www.simsonic.fr/>).

A sliding-window spectral analysis was performed for each receive channel Spectra originating from the plate surface were averaged to serve as a reference spectrum. The apparent integrated backscatter amplitude

(AIB) was derived and a plane was fitted to $Y_{\text{norm}}(f, z)$ in frequency and depth ranges of $3.5 \leq f \leq 8.5 \text{ MHz}$ and $1 \leq z \leq 3 \text{ mm}$, respectively:

$$Y_{\text{norm}}(f, z) = a_0 + a_z z + a_f f \quad (1)$$

Each model was generated ten times and the derived coefficients were averaged.

Results

All pore properties were associated with at least one backscatter parameter ($0.59 \leq R^2 \leq 0.56$). Multivariate analysis revealed highly significant prediction models for all pore properties (Table I). A unique cortical bone backscatter coefficient (BSC) model was derived (Fig. 1).

	R^2	RMSE
<u>Ct.Po.Dm</u> = $f(\alpha_f)$	0.56	11.5 μm
<u>Ct.Po</u> = $f(\alpha_z, AIB)$	0.65	2.2 %
<u>Ct.Po.Dn</u> = $f(\alpha_f, AIB)$	0.50	11.4 mm^{-2}

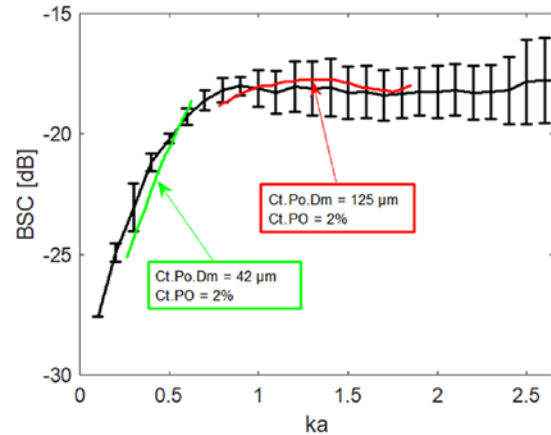


Figure 1. Multivariate prediction models. Cortical bone backscatter coefficient model that describes $BSC(ka) = f(\text{Ct.Po.Dm}, \text{Ct.Po}, \text{Ct.Po.Dm})$.

Ascites Distorts Trabecular Bone Score and Hip/Spine Bone Mineral Density

Madeline Dwyer^{*1}, Scott Fung^{2,3}, David Wong^{4,5,6}, Jordan Feld^{2,5}, Florence Wong^{2,5}, Queenie Wong⁵, Diana Yau⁵, Anita Colquhoun⁷, Angela M. Cheung³

¹ Institute of Medical Science, University of Toronto

²University of Toronto

³Toronto General Hospital Research Institute, University Health Network

⁴Krembil Research Institute

⁵University Health Network

⁶St Michael's Hospital

⁷Women's College Hospital

⁸Divisions of General Internal Medicine and Endocrinology, Department of Medicine, University Health Network, University of Toronto

Introduction

Osteoporosis is a skeletal disorder characterized by the degradation of bone resulting in increased fracture risk. Bone mineral density (BMD) and trabecular bone score (TBS) derived from dual-energy X-ray absorptiometry (DXA) scans are used to diagnose osteoporosis through measurement of bone quantity and quality, respectively. Osteoporosis is prevalent in 12-55% of patients with chronic liver disease. Cirrhosis is a late complication of chronic liver disease. Ascites, an accumulation of transudative fluid in the peritoneal cavity, can complicate cirrhosis. Therapeutic paracentesis is a procedure where a large volume of ascites is drained over a few hours. Therefore, DXA scans should be completed in order to monitor bone health in this high risk population however, their accuracy has been questioned due to the possibility of abdominal fluid distorting DXA images. This study aims to evaluate the effect of ascites on TBS and hip/spine BMD measurements.

Methods

This prospective study aims to recruit 60 patients to undergo large volume (> 4L) paracentesis at Toronto General Hospital, Toronto, Canada. Participants received a hip/spine DXA scan by ISCD-certified technologists before and after paracentesis. In

addition, participants' body measurements (height, weight, waist circumference, hip circumference, and sagittal abdominal diameter) and a medical history questionnaire were obtained. BMD and TBS scores were derived from DXA scans and percent changes from pre- to post- paracentesis values were calculated. Differences were statistically assessed using paired t-tests.

Results

Thirteen participants have completed the study (mean age= 67, SD= 9.38), with the average volume of fluid drained being 5.66 L (SD=1.39). Mean TBS and BMD at the lumbar spine, total hip and femoral neck were significantly higher after paracentesis, with the greatest change after fluid removal being in TBS values, which showed an average increase of 23.4% pre- to post-paracentesis. Results are shown in the table below.

Conclusion

Following paracentesis, patients had greater BMD and TBS values. Large volume ascites causes falsely low hip/spine BMD and TBS. BMD and TBS measurements should ideally be done immediately post-paracentesis in this population.

Measure	Pre-Paracentesis	Post-Paracentesis	Mean % Change	p
Lumbar Spine BMD (g/cm ²), mean±SD	0.962 ± 0.143	0.987 ± 0.143	2.7	<0.05
Total Hip BMD (g/cm ²), mean±SD	0.917 ± 0.105	0.932 ± 0.102	1.7	<0.05
Femoral Neck BMD (g/cm ²), mean±SD	0.690 ± 0.085	0.707 ± 0.074	2.6	<0.05
TBS, mean±SD	0.994 ± 0.152	1.215 ± 0.118	23.4	<0.05

Figure 1. Mean Percent Changes for BMD and TBS

Automated Detection of Vertebral Fractures on Dual Xray Absorptiometry Vertebral Fracture Assessment Images Using Supervised Machine Learning via a Trained Convolutional Neural Network

Sheldon Derkatch¹, Steven Reda¹, Davis McClarty¹, Mark Bryanton^{*1}, Mike Davidson¹, Bill Leslie¹

¹ St Boniface Hospital, University of Manitoba

Introduction

Significant advances have been made in the power of deep learning via neural networks to perform a variety of tasks in the past decade. Specifically, the application of convolutional neural networks (CNN) for computer vision has dramatically increased image recognitions tasks to human-like performance. Supervised machine learning is a subset of artificial intelligence research, where an artificial intelligence algorithm is trained on a dataset to attempt to learn the relevant features to predict a desired category or outcome. This category is known and has often been assigned previously by a human. In Manitoba, we have been performing vertebral fracture assessment since 2010, and have a database of over 10,000 labelled VFA images. Using the image data from these scans, we trained a convolutional neural network to predict vertebral fractures on lateral spinal vertebral fracture assessment images (VFA).

Methods

The CNN was coded in Python using the Keras graphical processing unit accelerated framework. The VFA dataset was split into a training dataset, a validation dataset, and a testing dataset. The neural network was

trained off of the training dataset and optimized on the validation dataset. Final predictions were made on the testing dataset. The Nuclear Medicine Physician interpreted the VFA images clinically and captured the interpretation in the Manitoba Bone Density Database. The physician's' interpretations were used as the training label that the neural network was optimized to predict. Generally, the Nuclear Medicine Physicians were using the Algorithm Based Qualitative method or the modified Algorithm Based Qualitative method during their assessment. However, some physician gestalt was also undoubtedly applied. Once the CNN was trained and it's fracture predictions were made, heatmaps were generated to indicate the location on the VFA image that the convolutional neural network deemed to be the most relevant location demonstrating the fracture.

Results

The convolutional neural network was able to learn the underlying pattern associated with vertebral fractures on VFA images, and successfully predicted fracture presence with 95% overall accuracy on the independent testing dataset.

Standardization of a Knee DXA Protocol - Is it time?

Lindsie A. Blencowe*^{1,2}, Nahid Raja², Lora M. Giangregorio³, Angela M. Cheung^{4,5}, B. Catharine Craven^{2,5}

¹ Institute of Medical Science, University of Toronto

²Toronto Rehabilitation Institute- University Health Network

³Dept. of Kinesiology, University of Waterloo

⁴Dept. of Medicine and Joint Department of Medical Imaging, University Health Network

⁵Dept. of Medicine, University of Toronto

Introduction

Dual energy x-ray absorptiometry (DXA) at the knee has become a frequently used research and clinical outcome measure. Unfortunately, there are currently no consensus derived standard methods for acquisition and analysis of distal femur or proximal tibia bone mineral density. Patients with neuromuscular impairment typically fracture at peripheral sites such as the knee and are less likely to experience fractures at more centrally located sites like the hip and spine – making knee region DXA a more clinically relevant site for fracture risk prediction. A review of knee region DXA methodologies currently used for research in patients with neuromuscular impairment is presented.

Methods

A review of knee region DXA measurement techniques used in patients with neuromuscular impairment.

Results

Our review has revealed that DXA of the distal femur and proximal tibia are commonly used as a research tool in Spinal Cord Injury (SCI) and Duchenne Muscular Dystrophy (DMD). Eleven distinct knee region DXA methodologies were identified internationally. The protocols used vary in choice of scanner, anatomic site, region(s) of interest (ROI) assessed, analysis software and reported least significant change (LSC). Typically, scanning protocols and software designed to assess the spine or forearm are used to scan the knee, with variability in knee positioning.

No authors reported on the availability of normative data, except for our group. At Toronto Rehab Lyndhurst Centre, University Health Network (TRI-LC-UHN), our knee region DXA protocol is used for both research and clinical assessment. Currently, 600 patients have knee region BMD assessment at

our centre annually and include patients with SCI, Spina Bifida, DMD, Multiple Sclerosis, and stroke. The normative knee region DXA dataset constructed at our centre is the only dataset to our knowledge and is comprised of 200 patients.

Conclusions

The number of research groups who currently use knee DXA highlights the need for a standardized knee DXA protocol. A standard protocol will enable clinicians to better compare BMD outcomes between research sites and facilitate large, multi-centre studies. While knee region DXA is primarily used in SCI, it has potential utility as a research and clinical tool in those with other musculoskeletal conditions that preclude accurate assessment of lumbar spine and hip region BMD. Given that knee region DXA is a clinically relevant scanning site for many patient populations, a standard protocol with available normative data and established LSC will enhance fracture risk prediction and improve patient care.

Author, Year	Population	Scanner Brand	Scanning Site	Analysis Protocol	Least Significant Change Reported
Kiralfi, et al. 2000	Spinal Cord Injury	Hologic QDR 1000/W	Midshaft and Distal Femur	Lumbar spine Software, Hologic, Inc.	No
Moreno, et al. 2001	Spinal Cord Injury	Hologic Discovery QDR 4500	Distal Femur and Proximal Tibia	Lumbar Spine Software, Hologic, Inc.	Yes
Garland, et al. 2001	Spinal Cord Injury	Hologic QDR 2000	Combined, distal femur and proximal tibia	Forearm software, Hologic, Inc.	No
Warden et al. 2002	Spinal Cord Injury	Hologic QDR 1000/W	Proximal Tibia	Lumbar spine Software, Hologic, Inc.	No
Medlesky, et al. 2004	Spinal Cord Injury	Hologic Delphi A	Proximal Tibia	Forearm software, Hologic, Inc.	No
Shields, et al. 2005	Spinal Cord Injury	Hologic QDR 2000	Distal Femur	Lumbar Spine Software, Hologic, Inc.	No
Morse, et al. 2009	Spinal Cord Injury	4 th Generation GE Lunar Prodigy Advance	Distal Femur and Proximal Tibia	Customised GE research software, enCORE v10.2.105	Yes
McPherson, et al. 2014	Spinal Cord Injury	Hologic QDR 47400A	Distal Femur and Proximal Tibia	Forearm software, Hologic, Inc.	Yes
Cowley, et al. 2017	Spinal Cord Injury	Hologic QDR 4500A Pediatric Scanner	Distal Femur and Proximal Tibia	Forearm software, Hologic, Inc.	Yes
Edwards, et al. 2018	Spinal Cord Injury	GE Lunar iDXA Scanner	Distal Femur and Proximal Tibia	Lumbar spine, GE enCORE v14/16	Yes
Zemel, et al. 2009	Duchenne Muscular Dystrophy	Hologic Discovery/Delphi	Lateral Distal Femur	Not reported	No

GE – General Electric; Shading indicates the protocol used at TRI-LC-UHN

Figure 1. Current Knee Region DXA Measurement Techniques

Approaches to Analyzing DXA Data Using Convolution Neural Networks

John A. Shepherd^{*1}, Bennett K. Ng¹, Benjamin J. Hinton², Thomas K. Wolfgruber¹

¹ University of Hawaii Cancer Center, University of Hawaii

²Department of Bioengineering and Therapeutic Sciences, University of California - San Francisco

Dual-energy X-ray Absorptiometry (DXA) has long been used as a proprietary technology with the only data representations being provided by the system's manufacturer in the form of a summary report. These reports provide average or sum mass values for predetermined regions of interests (ROIs). This approach is equivalent to stating the hypothesis that these predefined regions are the most relevant DXA measures to osteoporosis, obesity, fitness and other musculoskeletal conditions. We have long explored ways to interrogate DXA images without constraint to the predefined ROIs. Here we discuss different approaches to represent DXA scans in more ad-

vanced modeling and statistical methods. We will show examples of unsupervised learning approaches including active shape modeling, pixel-based morphometry, and deep learning. We will show how these methods can be used for deriving new hypotheses for specific disease outcomes as well as to apply automated delineations to DXA data. Lastly, we will show how DXA images can be derived from other imaging methods using hallucinatory algorithms. We conclude our investigations that DXA scans have much more to offer than the predefined summary statistics currently in clinical practice.

Impact of Thickness-Based Correction for Soft Tissue Effects on TBS

Franck Michelet^{*1}, François De Guio¹, Christophe Lelong¹, Didier Hans^{1,2}

¹ Medimaps

² Center of Bone diseases, Bone and Joint Department

Purpose

TBS is a textural parameter for DXA spine scans that provides an indirect estimation of trabecular microarchitecture status. To account for soft tissue variability between individuals, current TBS iNsight (v3.0 and older) integrates a correction based on BMI. We aimed at improving this correction by using the tissue thickness measured by the DXA device, which is a better estimate of patient morphology at the spine than BMI. We evaluated the impact of this new correction in terms of in-vivo reproducibility, correlations with BMI and diagnostic value for GE-Lunar (GE) and Hologic (HLX) DXA manufacturers.

Methods

We acquired scans of dried ex-vivo human vertebrae with several thicknesses of tissue-equivalent material and estimated the relationship between TBS and soft tissue thickness. This correction model was applied retrospectively on several datasets: 2 reproducibility studies with individuals having two scans with repositioning (Cohort A, GE, N=37; Cohort B, HLX, N=27), 3 population-based cohorts (Cohort C, HLX, N=6742 women, age=61±9; Cohort D, GE, N=6361 women, age=63±9, Cohort E, HLX, N=1343 men, age=56±11) and 2 case-control studies (Cohort F, GE, N=191 women, Fx=83, age=63±10; Cohort G, HLX, N=189 women, Fx=44, age=64±9).

For both current and new TBS, we computed

root mean square standard deviation (rms-SD) as an estimate of the reproducibility for Cohorts A-B. We computed correlation coefficients of TBS with BMI for Cohorts C-D-E. We computed odds ratio per TBS SD decrease in the logistic regression models (adjusted for age, BMD and BMI) for Cohorts F-G.

Results

(see Table 1) TBS in vivo reproducibility was improved by the new correction based on tissue thickness. While the current TBS was negatively correlated with BMI, the new TBS is positively correlated with BMI, which is consistent with expectations. Positive significant correlations between BMD and BMI were also reported (Cohort C: 0.23, Cohort D: 0.19, Cohort E: 0.26). Diagnostic value is either maintained or improved for the new TBS when compared to the current TBS.

Conclusions

With the new corrective model based on soft tissue thickness, we obtained an improved TBS in-vivo reproducibility, a correlation with BMI of the same sign as the one observed for BMD, and a maintained or improved diagnostic performance. This method also no longer depends on manual inputs (weight, height), and it is a promising approach for longitudinal studies and for assessing inter-individual variability hardly captured by BMI. Clinical performance for fracture prediction for this new TBS will be evaluated in further studies.

Outcome	Cohort	Device	Sample size	Current TBS based on BMI	New TBS based on tissue thickness
rms-SD	A	GE	37	0.030	0.018
	B	HLX	27	0.025	0.023
TBS – BMI correlation coefficient	C	HLX	6742	-0.24	0.08
	D	GE	6361	-0.17	0.07
	E	HLX	1343	-0.27	0.08
OR per SD	F	GE	191	1.77 95% CI = 1.14 – 2.85	1.78 95% CI = 1.13 – 2.87
	G	HLX	189	2.41 95% CI = 1.66 - 5.93	3.06 95% CI = 1.66 - 5.93

Table 1. Impact of the new correction on TBS in-vivo reproducibility, correlation with BMI and diagnostic value.

Direct Hip Fracture Risk Assessment Using a Deep Learning Approach

Thomas K. Wolfgruber^{*1}, Bennett K. Ng¹, Benjamin J. Hinton², John A. Shepherd¹

¹ University of Hawaii Cancer Center

²Department of Bioengineering and Therapeutic Sciences, University of California - San Francisco

Dual-energy X-ray Absorptiometry (DXA) derived bone density metrics are the gold standard for diagnosis of osteoporosis and can be used in the prediction of bone fracture risk. Our hypothesis was that an understanding of the fat and lean mass contained in a Hologic DXA femur scan would provide enhanced sensitivity and specificity to DXA-derived hip fracture risk. We previously explored unsupervised principal component analysis to examine the association of fat, lean, and bone mass variance and fracture risk using deconvolved images of fat, lean and bone masses. In this work, we ask if deep learning models could further improve fracture risk assessment using similar training data. Models were built using ResNet50 architecture running on a NVIDIA DGX-1. Saliency mapping was used to visualize what of the fat, lean, and bone images and influenced the fracture risk prediction for each participant. We conclude that deep learning is a promising new approach to the analysis of DXA images.

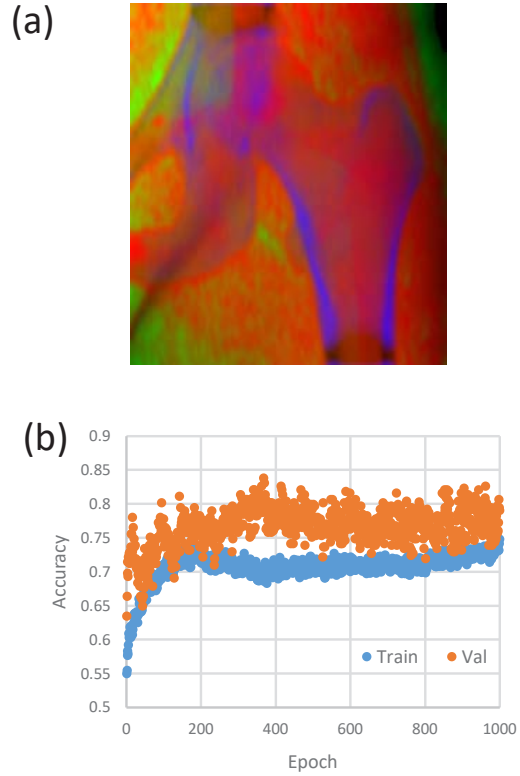


Figure 1. (a) input, (b) training results.

A Feasibility Study using the Texture Research Investigational Platform (TRIP) to Assess Bone Texture on VFA Lateral Spine Images to Discriminate Vertebral Fracture - Application of a Modified TBS Algorithm

Ryleigh White¹, Diane Krueger¹, Francois De Guio², Franck Michelet^{*2}, Didier Hans³, Neil Binkley¹

¹ University of Wisconsin Osteoporosis Clinical Research Program

²Research and Development Department, Medimaps

³Center of Bone diseases, Bone and Joint Department, Lausanne University Hospital

Trabecular Bone Score (TBS) is derived from software utilizing PA lumbar spine DXA images to generate grey-level texture scores as a surrogate for trabecular microarchitecture. This technology has enhanced DXA by improving fracture discrimination and risk assessment independent of bone mineral density (BMD). Recently, TBS use has been extended to a low-dose radiographic imaging system (EOS[®]) where a proof-of-concept study found lower TBS in patients with prior fragility fracture than BMD matched non-fractured controls. However, TBS has not been evaluated on DXA based VFA images which are more widely available and in which the posterior elements can be excluded from the region of analysis. A new tool, Texture Research Investigational Platform (TRIP) can provide bone texture scores (BTS) based on a derived approach of the TBS algorithm and can be used on any skeletal site imaged by various modalities. We hypothesized that BTS analysis can be performed on lumbar spine lateral VFA images and could potentially differentiate fractured from non-fractured patients.

To explore the feasibility of this approach, we evaluated 15 subjects (12F/3M) greater than 70 years old, mean age 78.2 years, BMI 26 kg/m² who had PA lumbar spine and lateral VFA scans. Five subjects were in each of three vertebral fracture categories; none, one or two respectively. All scans were acquired on a Lunar iDXA densitometer in standard clinical manner (GE Healthcare, WI, USA). TBS and BMD were measured at the L1-4 spine in all subjects using v3.0.3 and enCORE v17.10.077 respectively. BTS was

measured by TRIP v1.0 (Medimaps, France) employing manual 8-point morphometry on DICOM lumbar spine VFA images (Figure 1). Fracture group differences in PA L1-4 BMD, TBS and lateral BTS on VFA were assessed by ANOVA.

BTS values differed based on fracture number ($p < 0.01$). L1-L4 mean BTS for those with 0 fractures, 1 fracture, and 2 fractures were 1.358, 1.216, and 1.028 respectively. Mean PA spine BMD and TBS values for the 3 fracture groups did not differ, 1.114 g/cm², 1.148 g/cm², 1.211 g/cm², and 1.357, 1.333, and 1.346 respectively.

In conclusion, despite the small sample size, this feasibility study demonstrates the possibility of obtaining BTS values at the lateral lumbar spine using VFA images. Lower BTS values were observed in subjects with more prevalent vertebral fractures. Further work with a larger sample size is indicated to assess the clinical relevance of these results.



Figure 1. Example of TRIP analysis on lateral VFA

An Exploratory Study of the Texture Research Investigational Platform (TRIP) to Evaluate Bone Texture Score of Distal Femur DXA Scans - A TBS-Based Approach

Ryleigh White¹, Diane Krueger¹, Francois De Guio², Franck Michelet^{*2}, Didier Hans³, Paul Anderson⁴, Neil Binkley¹

¹ University of Wisconsin Osteoporosis Clinical Research Program

² Research and Development Department, Medimaps

³ Center of Bone diseases, Bone and Joint Department, Lausanne University Hospital

⁴ University of Wisconsin Department of Orthopedics and Rehabilitation

Periprosthetic fractures can be catastrophic events with morbidity and mortality comparable to osteoporosis-related hip fracture. Moreover, poor bone status is associated with increased complication risk following orthopedic surgery. Therefore, assessing site-specific skeletal status prior to and/or after orthopedic surgery to optimize outcomes and reduce subsequent fracture risk is appealing. Trabecular Bone Score (TBS) is derived from software utilizing lumbar spine DXA images to generate grey-level texture scores, a surrogate for trabecular microarchitecture. This technology has enhanced DXA by improving fracture discrimination and risk assessment independent of bone mineral density (BMD). This methodology has been adapted to Texture Research Investigational Platform (TRIP), new software that allows assessment of other skeletal sites imaged by various modalities, e.g., x-ray, DXA, or CT. TRIP generates a bone texture score (BTS) which could offer insight into periprosthetic fracture risk and guide surgical decision-making. Thus, as distal femur bone loss occurs following total knee arthroplasty (TKA), we hypothesized that BTS values in those with unilateral TKA would identify poorer texture on the operated femur compared to the contralateral limb.

We evaluated 30 subjects (15M/15F) with unilateral TKA 2-5 years previously, mean age was 67.9 years and BMI 30 kg/m². Using Lunar iDXA (GE Healthcare, WI USA), lumbar spine and entire femur scans were obtained, the latter using atypical femur fracture feature of enCORE v17.10.077 software. BMD and BTS measurements were obtained at the distal femur by placing manual regions

of interest (ROI) of 2 cm in height at 15% and 25% of leg length from the intercondylar notch. TBS v3.0.3 measured L1-4 vertebrae in all subjects and BTS was determined using DICOM images of the distal femur with TRIP v1.0 (Medimaps, France). Differences in operated versus non-operated distal femur were evaluated by paired t-test.

As previously reported, operated leg BMD was 9% lower at 15% and 25% ROIs. Similarly, BTS values in the operated leg were 5% lower at these same ROIs (Fig. 1). Distal femur BTS and BMD were unrelated at the 15% and 25% ROIs (data not shown). Additionally, distal femur BTS was unrelated to L1-4 TBS.

In conclusion, this pilot study documents the feasibility of obtaining BTS values at the distal femur. Lower BTS values were observed in the surgical leg, which is consistent with the bone loss known to occur following TKA. Further work is indicated to refine TRIP use and evaluate whether such data improves prediction of periprosthetic fracture.

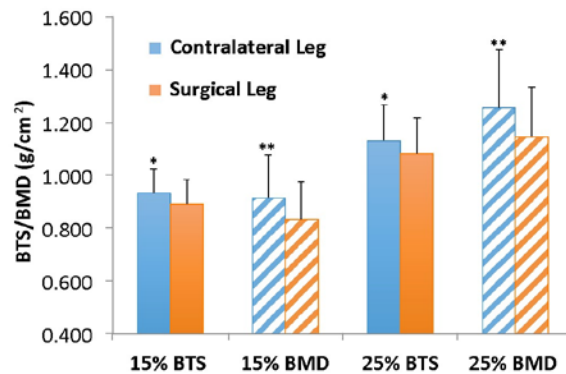


Figure 1. Distal femur Bone Texture Score (BTS) and BMD. Data as mean (SD)

Automatic Quantification of Intermuscular Fat in Standard Mouse Proximal Tibia MicroCT Scan.

Vincent A Stadelmann^{*1,2}, Lucie Bourgoin³, Nicolas Bonnet³

¹ SCANCO Medical AG

² Schulthess Klinik

³ Services of Bone disease, University Geneva Hospital

Introduction

Intermuscular fat (IMAT) is a fatty infiltration in muscle. This includes adipocytes located between the muscle fibers (also termed intramuscular fat) and also between muscle groups (literally intermuscular). IMAT is associated with increased risk of sarcopenia and mobility loss in elderlies.

The skeletal and the muscular systems are tightly associated: the mechanical forces applied by muscles highly influence bone structure; and decrease in muscle strength leads to lower bone strength.

This association is the center of strong interest in the research community. Here we present a simple add-on algorithm to estimate IMAT and muscle volume from standard bone microarchitecture microCT scan of mouse proximal tibia.

Methods

Mouse tibia scans were acquired in-vivo with a VivaCT40 following standard bone microstructure protocol: scan was ϕ 21 mm x 2.2 mm in length, 1 mm off the growth plate. Tube operated at 55 kV, 145 μ A, 200ms IT and 1000 proj./180°, resulting in 210 slices of 2048 x 2048 voxels of 10.5 μ m.

Characterization of bone is not described here; it is well established. For soft tissues, limb and bone were contoured using the dual-threshold approach. Bone was masked off the image using the bone contour, skin was

masked off using 0.15mm peeling (average skin thickness from 10 scans) of the limb contour, and the remaining grayscale data was scaled down by a factor 2 and smoothed out with a median filter (kernel=3).

Muscle and fat were roughly segmented from the median image ($\mu=0.52\text{cm}^{-1}$ for muscle and 0.01cm^{-1} for fat) then smoothed with an open/close sequence (3 voxels) to generate the muscle and fat masks. The fat mask was intersected with muscle mask to compartment fat into subcutaneous (SCF) and IMAT. Finally, Muscle, IMAT and SCF volumes were computed from their respective masks.

The algorithm was developed with EasyIPL, a high-level library of macros using the scanner software IPL. The method was compared to manual contouring from microCT and to histology.

Results

The method was tested on scans from control and obese db/db mice (a leptin receptor mutation) (Fig1). Fat volume correlated to manual analysis with $R^2=0.88$ and $p<0.001$. Comparison to histology is on going.

Discussion

The algorithm presented here can be used as an add-on to standard bone microstructure scans without requiring additional animal scanning.

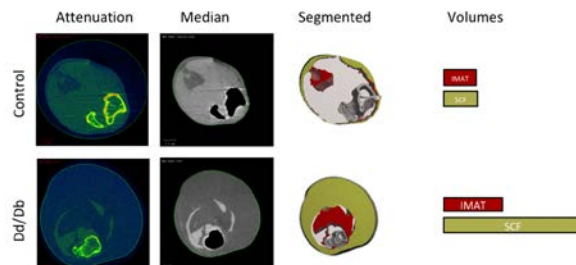


Figure 1. A control and an obese mouse tibia scan analyzed with the IMAT algorithm.

Side-To-Side Differences in Bone Density and Strength at the Distal Tibia in Canadian Figure Skaters

Lauren A Burt^{*1}, Erik M Groves², Kelly Quipp², Steven K Boyd¹

¹ McCaig Institute for Bone and Joint Health, Cumming School of Medicine, University of Calgary

²Canadian Sport Institute Calgary

Introduction

Mechanical loading increases bone mineral density (BMD) using high-resolution peripheral quantitative computed tomography (HR-pQCT) among many athletic populations. While moderate loading is required to maintain or increase BMD, loading can cause deleterious effects such as stress fractures when the balance between training intensities/volumes and nutrition are not aligned.

Figure skating is an aesthetic based sport associated with high training demands, negative energy balance and stress fractures. Figure skating can be broken down into four categories: single skating for men and women, pairs and ice dancing. Both single and pairs skaters participate in frequent jumps (high mechanical loading) whereas ice dancing has a ballroom dancing influence and, as a result applies lower mechanical loads to the bones (low mechanical loading). The current study explores the bone health of Canadian figure skaters. Specifically, we aimed to determine if there is a difference in BMD and bone strength between 1) figure skaters and normative data, 2) jumpers and dancers, and 3) the landing and non-landing leg.

Methods

National and junior development skaters had their non-dominant distal radius and both tibia scanned using second-generation HR-pQCT (XtremeCT II, SCANCO Medical).

BMD was determined at the total (TtBMD), cortical (CtBMD) and trabecular (TbBMD) compartments, and finite element analysis estimated bone strength. *Normative.ca* compared the BMD of skaters to normative data. Independent T-tests compared differences between skating discipline. Paired T-tests compared BMD and bone strength for the landing and non-landing leg. Statistical analyses were performed in Stata and significance was set at $p < 0.05$.

Results

Twenty skaters (mean age 22 ± 6.2 , range 14-33 years; women: 11, men: 9) completed HR-pQCT scans. Due to previous surgery one skater was unable to have both tibia scanned. Compared to the general population, the mean percentile rank for skaters' TtBMD at the tibia and radius were 53rd and 33rd, respectively. Bone density and strength were not different between jumpers and dancers. The landing leg had higher TtBMD (2.3%), TbBMD (5.5%), and bone strength (6.6%) than the non-landing leg ($p < 0.05$).

Conclusion

Figure skaters have average tibia bone density compared with the general population. The landing leg is denser and stronger than the non-landing leg. However, there are no density or strength differences between jumping and dancing figure skaters.

The Correction of Quantitative Computed Tomography Measurements of Vertebral Bone Mineral Density for Marrow Fat using Magnetic Resonance Imaging

Ling Wang^{*1}, Xiaoguang Cheng¹, J. Keenan Brown², Li Xu¹, Zhe Guo¹, Glen M. Blake³

¹ Department of Radiology, Beijing Jishuitan Hospital

²Mindways Software Inc.

³Biomedical Engineering Department, King's College London

Introduction

Single-energy quantitative computed tomography (SEQCT) measurements of volumetric bone mineral density (vBMD) are subject to errors due to variations in bone marrow composition. We describe a method of using chemical shift-encoded magnetic resonance imaging (CSE-MRI) measurements of marrow fat to correct these errors, together with a validation study in which CSE-MRI corrections to SEQCT vBMD measurements of L1 trabecular bone were compared with the same corrections derived from dual-energy QCT (DEQCT) scans.

Methods

We describe a method based on the H₂O and K₂HPO₄ equivalent densities of bone, red and yellow bone marrow to correct SEQCT vBMD measurements for marrow fat using

CSE-MRI measurements of proton density fat fraction (PDFF). Using data from earlier studies, we show that PDFF measurements provide a reliable estimate of the yellow marrow content of bone marrow. The resulting corrections to spine SEQCT vBMD measurements were compared with similar corrections obtained by performing DEQCT scans in 18 subjects enrolled as healthy controls in the China Action on Spine and Hip Status study.

Results

Plots of the MRI vBMD corrections against the DEQCT corrections showed statistically significant correlations for 80 kVp ($R^2 = 0.541$; $P < 0.001$) and 120 kVp vBMD data ($R^2 = 0.620$; $P < 0.001$). Bland-Altman plots showed a bias of 1.1 (95% LOA: -7.7 to 10.0) mg/cm³ at 80 kVp and 1.5 (95% LOA: -10.3 to 13.3) mg/cm³ at 120 kVp.

The Calgary Vitamin D Study - Bone Density, Strength and Microarchitecture Differences Associated with Lower Limb Arterial Calcification: Baseline Comparisons of a Randomized Controlled Trial

Ryan M. Plett^{*1}, Lauren A. Burt¹, Emma O. Billington¹, David A. Hanley¹, Steven K. Boyd¹

¹ McCaig Institute for Bone and Joint Health, University of Calgary

Introduction

Vitamin D deficiency is associated with bone loss and cardiovascular disease. Vitamin D supplementation is known to promote vascular and bone health and is considered part of preventative or mitigative strategies against bone loss and possibly vascular calcification. High resolution peripheral quantitative computed tomography (HR-pQCT) is an advanced imaging modality that can assess bone quality and detect lower limb arterial calcifications (LLAC) at the distal tibia. The purpose of this study was to investigate the differences between bone quality in individuals with and without LLAC. We also assessed the relationship between LLAC and bone quality.

Methods

This study was a University of Calgary randomized, double-blinded clinical trial (n=311). Participants were healthy men and women 55-70 years, each given one of three daily doses (400, 4000, 10000 IU) of vitamin D for the duration of the trial. Second-generation HR-pQCT scans (Scanco Medical, Switzerland) at the distal radius and tibia were acquired from each participant at baseline. Total bone mineral density (TtBMD), cortical BMD (CtBMD), trabecular BMD (TbBMD), trabecular number (TbN), cortical porosity (CtPo), and failure load (FL) were measured using standard image processing methods. LLAC mass (mgHA) was quantified using a semi-automated computer algorithm developed for HR-pQCT. Independent t-tests were performed on baseline parameters between individuals with and without LLAC. Pearson correlations were performed in LLAC positive individuals to test the relationship between LLAC and bone quality.

Results

LLAC were identified in 85 participants (28%) with a mean baseline mass of 2.8 mgHA. T-tests revealed no significant differences between bone parameters in LLAC positive and negative individuals ($p>0.05$). Although confounding factors such as BMI and sex were not controlled for in this analysis, weak correlations were found between LLAC and FL ($r=0.25, p=0.021$), CtBMD ($r=0.28, p=0.011$), and CtPo ($r=-0.26, p=0.018$) at the tibia. At the radius, a weak positive correlation was also found between LLAC and FL ($r=0.28, p=0.0098$).

Conclusions

Measures of bone density, and most measures of strength and microarchitecture appear to be unrelated to the presence of small LLAC in the distal tibia. Weak correlations were found between LLAC and some strength and microarchitectural parameters, providing some evidence of a relationship. Our future work will control for confounding factors and compare three year changes in LLAC and bone quality.

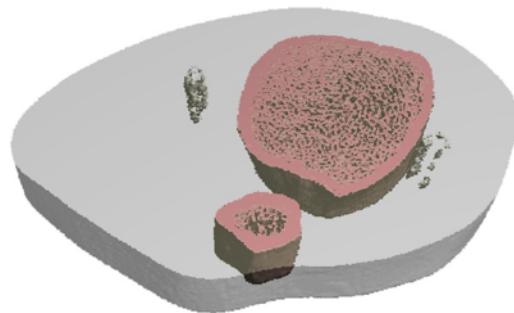


Figure 1. Cross-sectional HR-pQCT image at the distal tibia, with segmented calcifications located in the anterior and posterior tibial arteries.

Fully Automated Segmentation of Wrist Bones in Early Rheumatoid Arthritis

Lun M. Wong^{*1}, Lin Shi¹, Fan Xiao¹, James F. Griffith¹

¹ Department of Imaging and Interventional Radiology, The Chinese University of Hong Kong

Introduction

Detection of rheumatoid arthritis (RA) at an early stage is key to reducing long term damage. Accurate assessment of RA regarding the level of inflammation present is possible by magnetic resonance imaging (MRI) of the wrist as this is one of the earliest affected joints. The current method to measure inflammation on MRI in RA patients is the semi-quantitative RA-MRI scoring system (RAMRIS). To realize fully quantitative RA scoring systems for clinical practice, automatic segmentation of wrist bones is required. Most previous work outlining the wrist bone segmentation extracted these bones from T1-weighted (T1W) images, on which bone oedema/inflammation is not obvious, and then obtain segmentation on T2W through registration techniques for bone marrow edema evaluation. This method introduces spatial misalignment and uncertainty. Relatively less work has been undertaken to directly segment the wrist bones on T2W fat-suppressed images. No previous studies utilized convolution neural network (CNN) to segment the wrist bones. Preliminary tests suggested that the performance of out-of-the-box segmentation CNN U-NET is hindered by the close apposition of tendons and elongated bony regions. With respect to this, we separated these specific features prior to segmentation to achieve a better result in this study.

Method

We adopted a novel strategy of coupling a classification network and U-NET to separate images with conflicted features for wrist bone segmentation in RA patients. We systematically define three classes of slices: Type A) superficial slices, Type B) slices that contains tendons and Type C) otherwise. A classification network is trained and applied for pre-segmentation classification. By definition, Type A slices have no region of interest, Types B and C are then fed into two individually trained U-Net for carpal segmentation. To minimize the impact caused by misclassification of Types B and C into Type A, slices classified as Type A but surrounded by Types B and C are forcefully converted to Type B before proceeding.

Experiment and Results

Using the proposed strategy, the networks were trained over 40 cases until convergence ensured and then tested on 11 cases. These cases were obtained from 51 individuals with varying degrees of RA. The automatic segmentation achieved an average DICE score of 0.859 when compared against the manually drawn labels. The mean DICE score obtained by U-Net trained under same conditions but without pre-segment classification is 0.813. Details are tabulated in Table 1.

Tested group	N	Similarity		Distance	
		DICE	JAC	VD	GCE
No Classification	188	0.813±0.145	0.704±0.168	0.079±0.124	0.056±0.030
Type B	109	0.829±0.096	0.718±0.124	0.070±0.078	0.039±0.029*
Type C	73	0.903±0.037*	0.825±0.060*	0.023±0.025*	0.070±0.023*
Type B + Type C	182	0.859±0.086*	0.761±0.115*	0.051±0.067*	0.052±0.031

* Significant mean difference ($p < 0.05$) between tested group and "No Classification" group.

Table 1. Quantitative Analysis of Segmentation Performance by Slices

Large-scale Knee Osteoarthritis Prediction from Spherical Coordinate Encoding of Bone Shape with Deep Learning Classifier

Alejandro Morales Martinez^{*1}, Io Flament¹, Felix Liu¹, Jinhee Lee¹, Peng Cao¹, Sharmila Majumdar¹, Valentina Pedoia¹

¹ University of California San Francisco

Introduction

Osteoarthritis (OA) is a degenerative joint disease which affects 27 million U.S. adults. The onset of OA is related to several factors such as cartilage loss, changes in the meniscus and in the subchondral bone. While previous studies showed associations between bone shape and OA, inferential statistics does not guarantee actual prediction abilities. This study explores the ability of deep learning convolutional neural networks (CNN) to use knee bone shape features in diagnosing and predicting future onset of radiographic OA based on Kellgren-Lawrence (KL) grade.

Methods

The Osteoarthritis Initiative data set used for this study contains 3D double-echo steady-state (3D-DESS, 3T Siemens; image resolution in mm, [0.346 0.346 0.7]) MRI knee scans from a total of 4,796 unique patients for 10 different time points for both knees. Overall processing pipeline is shown in Figure 1. The femur, tibia and patella were segmented using a CNN. The bones were then turned into a RGB image that was used as an input for two binary classifiers. The first one aimed to

diagnose OA (KL=0-1 vs KL=2-3) and the second one aimed to predict future onset of radiographic OA (KL=2-3) within two years of the last healthy time point. The segmentation CNN was trained with 40 manually segmented bone masks split into 25/5/10 sets for the training, validation and holdout sets respectively. OA diagnosis dataset included was split into 14,776/4,935/4,208 sets. The training data for the OA progression model was split into 590/139/182 sets. Both models were then connected to a gradient boosting shallow classifier to incorporate demographics data for each patient such as gender, age, and body mass index.

Results

The holdout mean DICE coefficients for the femur, tibia and patella segmentation range from 88.9-95.2%, 87.0-95.8% and 85.1-92.2% respectively. The holdout sensitivity/specificity for the OA classifier was 79.0/77.1% and for the OA two-year progression classifier was 76.8/57.5%. For the shallow classifiers with demographics, the result for the OA diagnosis was 81.03/79.01% and the OA progression was 76.77/62.50%.

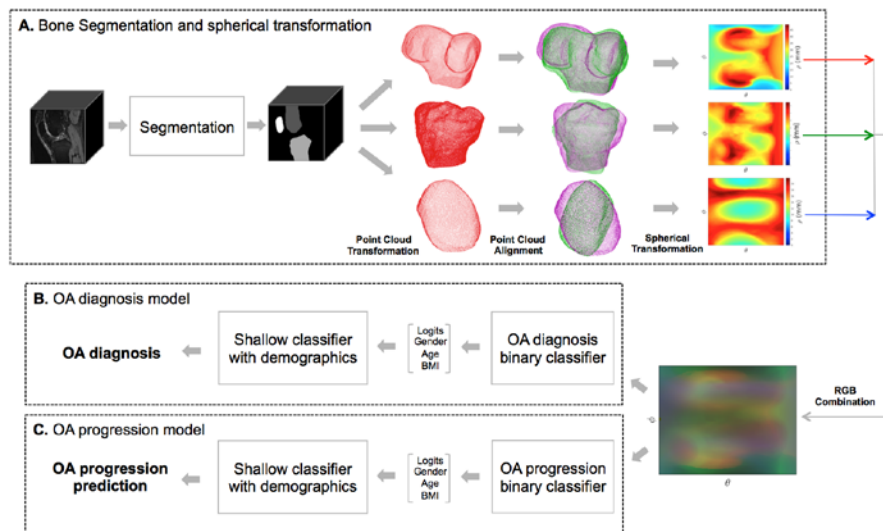


Figure 1. Overview of the processing pipeline. A. Segmentation. B-C. Diagnosis.

Discrimination of Hip Fracture Type for Men with Spatial Differences in the Distribution of Bone

Ling Wang^{*1}, Rui Zhang², Xin Gao², Xiaoguang Cheng¹

¹ Department of Radiology, Beijing Jishuitan Hospital

²Suzhou Institute of Biomedical Engineering and Technology, Chinese Academy of Sciences

Introduction

Little is known about the spatial distribution differences in volumetric bone mineral density and cortical bone structure at the proximal femur between femoral neck fractures and trochanteric fractures. Fracture types play a distinct role in predictors, but few studies have subdivided fracture into types. Further, dual-energy X-ray (DXA)-based methods or quantitative computed tomography (QCT) measures or combined assessments have shown limited ability in discrimination of hip fracture types.

Methods

In this case-control study, a total of 67 men with fragility hip fractures, 33 with femoral neck (FN) fractures (mean \pm SD age: 77.4 ± 9.5 years) and 34 with trochanteric (TR) fractures (76.9 ± 9.5 years), and 115 control subjects (71.0 ± 6.3 years) were included for the comparisons. By using cortical bone mapping (CBM) based on QCT data, we accurately assess the spatial distribution of cortical and trabecular bone related to hip fracture type. Differences in the spatial distributions of cortical bone mineral density (CBMD), cortical bone thickness (CTh), cortical mass surface density (CM), and endocortical trabecular bone mineral density (ECTD) were investigated using surface-based statistical parametric mapping (SPM). We compared these spatial distributions between controls and both types of fracture, and between the two types of fracture.

Results

Using SPM, we showed that all spatial assessments were significantly different in fracture cases versus cohort in some specific re-

gions, although CBMD, CTh and CM were not different in regions appropriate to fracture type. We also found spatially heterogeneous endocortical trabecular bone mineral density differences between control subjects and subjects with hip fracture that varied by fracture type. However, SPM results of direct comparisons of two fracture types indicated no spatial differences between FN and TR cases.

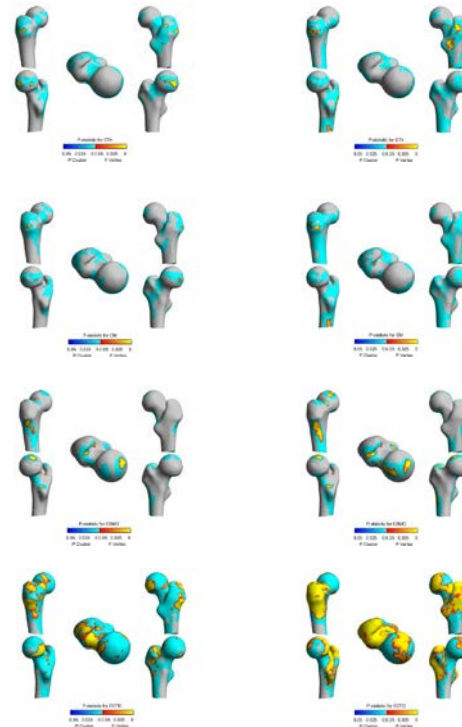


Figure 1. Results for femoral neck fracture (left) and trochanteric fracture (right). (fracture type versus control)

Assessing the Muscle-Bone Interaction in Pediatric Studies using HR-pQCT

Leigh Gabel*¹, Heather M. Macdonald², Heather A. McKay³

¹ McCaig Institute for Bone and Joint Health, Department of Radiology, University of Calgary

² Centre for Hip Health and Mobility, Department of Family Practice, University of British Columbia

³ Centre for Hip Health and Mobility, Departments of Family Practice and Orthopaedics, University of British Columbia

Introduction

Growing bones face their greatest mechanical challenge from increases in bone length and muscle forces. Muscle force is estimated using various imaging and biomechanical assessments; however, it is unclear which tool best describes the muscle-bone interaction in children and youth. Thus, we aimed to determine the relationship between changes in direct and surrogate measures of muscle force and bone strength during adolescence.

Methods

We assessed 385 children, adolescents and young adults (204 girls, 181 boys; 9 to 20 years at baseline) annually over a maximum of 4 years (1197 observations). We scanned the 8% site of the non-dominant tibia using high-resolution peripheral quantitative computed tomography (HR-pQCT, XtremeCTI, Scanco Medical) and applied finite element analysis to estimate bone strength (failure load, N). We measured muscle cross-sectional area (MCSA, mm²) at the 50% site of the tibia using pQCT (XCT 3000, Stratec) and leg lean body mass (LBM, kg) using DXA (Hologic QDR 4500W). We assessed maximal muscle power (Pmax, kW) and force (kN) using a counter-movement jump performed on a force plate (Leonardo, Novotec Medical) and estimated muscle power using vertical jump height (VJH, m) and the Gomez muscle power prediction equation ($P_{\text{max, predicted}} = 54.2 * \text{VJH} + 34.4 * \text{bodymass} - 1520.4$). We fit a base model using a mixed effects model

that included maturity offset (years from age at peak height velocity) as a random effect and sex, ethnicity and height as fixed effects. We added individual muscle variables (baseline and change values) as fixed effects to the base model and assessed change in pseudo-R² and effect size.

Results

Baseline and change values of all muscle measures were significantly correlated with one another (range: 0.46 to 0.94; $p < 0.001$). Baseline and change values of all muscle measures were positively associated with failure load across adolescence ($p < 0.001$), indicating that greater baseline muscle values were associated with greater failure load at all time-points and greater annual change in muscle values was associated with greater change in failure load. The base model (maturity, sex, ethnicity and height) predicted 62.3% of the total variance in failure load. Leg LBM demonstrated the strongest association with failure load (11.9% additional explained variance), followed by Pmax (7.2%), Pmax-predicted (6.6%), MCSA (5.7%) and muscle force (3.6%).

Conclusion

Future studies evaluating tibial bone strength using HR-pQCT should use leg LBM by DXA to characterize the muscle-bone unit. If DXA is unavailable, muscle power by mechanography or pediatric prediction equation is most appropriate.

Comparing Predicted Failure Regions of Femurs with Dynamic Hip Screws with Varying Tip Apex Distances using CT-Based Finite Element Analysis

Nicholas J. Yee^{*1}, Andrew S. Michalski², Ryan M. Plett², Steven K. Boyd²

¹ Faculty of Medicine & Dentistry, University of Alberta

² McCaig Institute for Bone and Joint Health, Cumming School of Medicine, University of Calgary

Introduction

Femoral neck fractures are common and present a high one-year mortality rate in older adults. Many adults over 50 years old are at a high risk for hip fractures, even without an osteoporosis diagnosis. Current fracture reduction surgical practices are based on evidence to implant dynamic hip screws (DHS) to treat nondisplaced subcapital femoral neck fractures. There are few computational studies in the literature examining the differences in predicted failure regions of DHS with different tip apex distances (TAD). This project compares the predicted fracture regions of DHS with a TAD of 10 mm (DHS10) and a TAD of 25 mm (DHS25) to determine an optimal DHS placement.

Methods

Seven cadaveric left femurs were scanned using clinical computed tomography (CT; Revolution CT, GE Healthcare, Chicago, USA) and resampled into 1 mm voxels. Simulated DHS with two-hole side-plates (DePuy Synthes, Raynham, USA) were manually aligned to each femur. The TAD was measured by the center of the lag screw's tip to the apex of the femoral head. A single limb stance finite element compression was performed to predict fracture regions using Mohr-Coulomb failure criterion. Garden fracture classification, where type 1 is a partial fracture and type 2 is a complete fracture, were qualitatively identified by visual inspection. Statis-

tical analysis used a paired t-test (alpha criterion = 0.05).

Results

Under the simulated compression, both DHS redistribute the load from the femoral neck to the head and diaphysis. Compared to the femurs without a DHS, the average predicted fracture size decreased with the DHS10 ($p < 0.01$) but not with the DHS25. An increased estimated failure load could be tolerated in both the DHS10 and DHS25 ($p < 0.01$ and $p < 0.05$, respectively). A Garden type 1 fracture was resolved by DHS10 while the DHS25 introduced an additional type 1 fracture. For Garden type 1 fractures, DHS10 decreased total predicted fracture size ($p < 0.05$), while DHS25 increased predicted fracture size ($p < 0.05$). However, DHS10 showed no significant increases in resistance to loads for the Garden type 1 fractures, but DHS25 did ($p < 0.05$).

Discussions and Conclusions

DHS10 appears to provide clinically-relevant bone stability by decreasing average fracture size. However, patient-specific bone properties may indicate a reduction with DHS25 over DHS10 for its mechanical benefits in improving load bearing capacity. Further exploration in computationally assessing internal fixation strategies is ongoing and tailored to improving precision-based surgical decision-making.

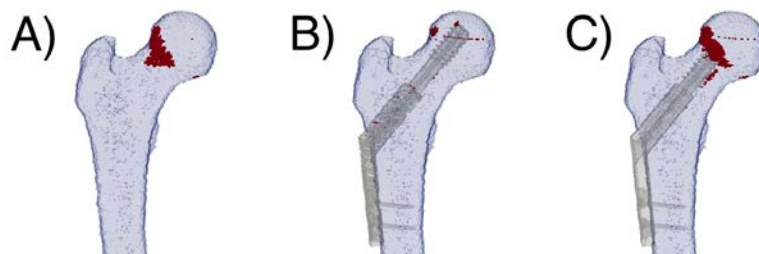


Figure 1. Predicted fracture zones of A) a femur without a DHS; B) a 10 mm TAD DHS-implanted femur; and C) a 25 mm TAD DHS-implanted femur

The Impact of the New Trabecular Bone Score Algorithm Using a Different Correction Model Based on Soft Tissue Thickness on the Prediction of Incident Atraumatic Fracture Risk in Elderly Women: The OsteoLaus Study

Enisa Shevroja^{*1}, Olivier Lamy¹, Berengere Aubry-Rozier¹, Gabriel Hans¹, Elena Gonzalez Rodriguez¹, Delphine Stoll¹, Didier Hans¹

¹ Center of Bone Diseases, RHU-DAL, Lausanne University Hospital

Introduction

Trabecular bones score (TBS) is a texture measurement computed from lumbar spine (LS) DXA scans that predicts osteoporotic fractures independently of BMD. The amount of soft tissue in the abdomen impacts the signal to noise ratio and eventually affects the TBS measurement. Thus, the current software (TBS iNsite[®]) integrates a correction for body mass index (BMI) in the TBS algorithm (TBSBMI). A residual negative correlation has been reported between TBSBMI and BMI. To address this issue, a new correction of the TBS algorithm, based on the regional soft tissue thickness (TTH) as estimated by the DXA machine, (TBSTH), has been developed. We aimed to compare the validity of TBSTH and TBSBMI in major osteoporotic fractures (MOF) prediction.

Methods

This study was embedded in the OsteoLaus Study, a prospective population-based cohort of 1,500 women living in Lausanne, Switzerland. All women had data on spine and hip BMD, TBS, incident MOF and FRAX. The correlations between BMI and TBSBMI or TBSTH were studied using Pearson's coefficient. Binary logistic regression models were performed to obtain the risk estimates for MOF per standard deviation (SD) decrease in TBSBMI or TBSTH in two different models: M1: adjusted for age+osteoporotic treatment+femoral neck BMD+weight+TTH; M2: adjusted for TTH+FRAXFN-BMD-MOF. To evaluate the prediction models and the perfor-

mance of both TBSBMI and TBSTH, the area under the receiver-operating-characteristic curve (AUC) was calculated for M, M+TBSBMI, and M+TBSTH.

Results

This analysis included 1,234 women (mean age=67.9±7.4 y; mean BMI=26.5±4.2 kg/m²). During the mean follow-up period of 5 years, 120 women sustained a MOF. BMI correlated negatively with the standard TBSBMI (r= -0.20) and positively with TBSTH (r=+0.25). Women who fractured were older, heavier, had thicker soft tissue and lower BMD. In overall, lower TBS values were significantly associated with an increased risk for MOF, but TBSTH was shown to be a better predictor of fracture risk than TBSBMI (Table). The AUC (95% CI) for M1 was 0.70 (0.65-0.75), M1+TBSBMI 0.71 (0.66;0.76), and M1+TBSTH 0.72 (0.67;0.77); M2 was 0.68 (0.63;0.73), M2+TBSBMI 0.70 (0.64;0.75), and M2+TBSTH 0.71 (0.66;0.76).

Conclusion

As hypothesized, the residual negative correlation between BMI and TBSBMI disappeared with TBSTH. Furthermore, the superiority of TBSTH versus TBSBMI in MOF risk prediction was demonstrated. This study contributes to the validation of the newly tested TBS algorithm in osteoporotic fractures prediction. The use of this improved TBS algorithm will further aid in the improvement of osteoporosis management.

	Model 1		Model 2	
	TBS _{BMI}	TBS _{TTH}	TBS _{BMI}	TBS _{TTH}
OR / SD (95% CI)	1.47 (1.14-1.90)	1.55 (1.20-2.00)	1.47 (1.17-1.86)	1.60 (1.27-2.01)
Model 1: age+OP treatment+femoral neck BMD+weight+tissue thickness; Model 2: tissue thickness+FRAX adjusted for femoral neck BMD; OR / SD odds ratio per standard deviation decrease; CI confidence interval; TBS _{BMI} trabecular bone score corrected for body mass index; TBS _{TTH} TBS corrected for the soft tissue thickness.				

Table 1. The results of the logistic regression analysis

Relationship of Fracture Risk to HR-pQCT Measures of Bone Microarchitecture: A Systematic Review and Meta-Analysis

Nicholas Mikolajewicz^{*1}, Kim Wager², Michael Molloy-Bland², Nick Bishop³, Andrew J Burghardt⁴, Lars Folkestad⁵, Anthony Hall⁶, Ken Kozloff⁷, Damien Lacroix³, Pauline Lukey⁸, Amaka C Offiah³, Jay Shapiro⁹, Bert van Rietbergen¹⁰, Suzanne Morin¹¹, Bettina M Willie¹, Svetlana V Komarova¹, Francis H Glorieux¹

¹ Shriners Hospital for Children-Canada
² Oxford PharmaGenesis
³ University of Sheffield
⁴ Department of Radiology, UCSF School of Medicine
⁵ Department of Endocrinology, Hospital of Southwest Denmark
⁶ Mereo BioPharma Group
⁷ University of Michigan
⁸ Target to Treatment Consulting Ltd
⁹ Kennedy Krieger Institute
¹⁰ Eindhoven University of Technology
¹¹ McGill University

Introduction

High-resolution peripheral quantitative computed tomography (HR-pQCT) is a non-invasive imaging modality for assessing volumetric bone mineral density (vBMD), and characterizing microarchitecture of cancellous and cortical bone, thus potentially providing information about bone quantity, quality and strength. The objective of this study was to determine if HR-pQCT-derived measures are associated with fracture.

Methods

We systematically identified 52 studies that used HR-pQCT bone imaging in 3941 individuals with and 10996 without incident or prevalent fractures, ranging in age from 10.9 to 84.7 years. Twelve HR-pQCT parameters describing bone density, microarchitecture and strength in radius and tibia were extracted and percent differences between populations with and without a fracture history were estimated using a random effects meta-analysis model.

Results

All HR-pQCT parameters, both in radius and tibia were significantly altered in individuals with fracture history. However, extent of differences in bone parameters ranged from 3% (95% confidence interval (CI): 2 to 4) for cortical vBMD to 14% (95% CI: 12 to 16) in trabecular vBMD. Importantly, fracture-related differences in HR-pQCT measures reported by prospective studies were consistent with those from retrospective studies, indicating that HR-pQCT parameters are pre-

dictive of fracture incidence. We found that fracture-related changes in HR-pQCT parameters were consistently larger in radius compared to tibia. After examining the effect of publication bias and heterogeneity, as well as accounting for reported short-term reproducibility, our study suggests that radial total and trabecular vBMD, cortical thickness and trabecular spacing were the most robust predictors of fracture at the patient level.

Conclusions

Taken together, our study demonstrates that HR-pQCT-derived parameters are strongly associated with clinically-relevant fractures. Work supported by Mereo BioPharma Group.

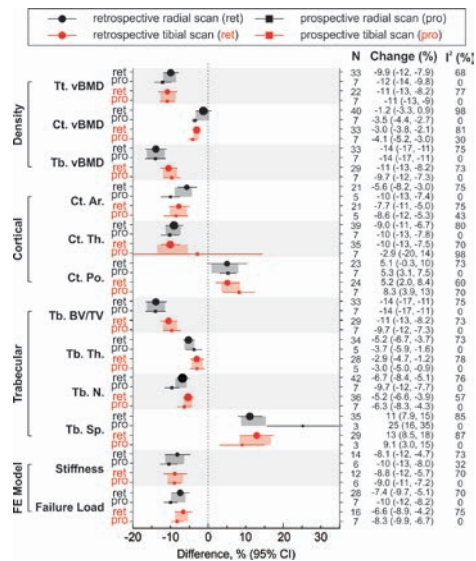


Figure 1. Fracture-related differences in radial and tibial HR-pQCT parameters acquired from prospective and retrospective studies.

Effects of Supplementation with Vitamin D3 400, 4000 or 10000 IU Daily for Three Years on Lower Limb Arterial Calcification: Secondary Analysis of a Randomized Controlled Trial

Emma O. Billington^{*1}, Lauren A. Burt¹, Ryan M. Plett¹, Marianne S. Rose², Steven K. Boyd¹, David A. Hanley¹

¹ McCaig Institute for Bone & Joint Health, Cumming School of Medicine, University of Calgary

²Research Facilitation, Alberta Health Services

Introduction

Arterial calcification has been associated with states of both vitamin D deficiency and excess in preclinical and epidemiologic studies. However, it is not known whether vitamin D supplementation has a dose-dependent effect on the development and progression of arterial calcification in healthy adults.

Methods

This was a three-year, double-blind, randomized controlled trial. Healthy adults (n=311) aged 55 to 70 with baseline serum 25-hydroxyvitamin D 30 to 125 nmol/L were randomized to take vitamin D3 400, 4000 or 10,000 IU/day for three years. Calcium supplementation was initiated if dietary calcium intake was <1200mg/day. Tibial artery calcification was identified and quantified (in milligrams of hydroxyapatite, mgHA) using high resolution peripheral quantitative computed tomography (HR-pQCT) at baseline and at 6, 12, 24, and 36 months. Between-group changes in the proportion of participants with arterial calcification were assessed. Among participants with evidence of arterial calcification at one or more time points, a constrained linear mixed effects model was used to evaluate changes in calcification over time and interaction with treatment group.

Results

311 participants were randomized; 302 (400: 105, 4000: 96, 10000: 101) were included in intent-to-treat analyses (54% male, mean [SD] age 62 [4] years, mean [SD] 25-hydroxyvitamin D 78.9 [19.9] nmol/L). Tibial artery calcification was identified in 85 (28%) at baseline, with mean (95% CI) calcification of 2.8 mgHA (95% CI: 1.7 to 3.9) among this subgroup. Compared to par-

ticipants without arterial calcification, individuals with calcification were more likely to be male (64% vs 50%, p=0.041), had lower systolic (126 mmHg vs 129 mmHg, p=0.0042) and diastolic (79 mmHg vs 82 mmHg, p=0.014) blood pressure and lower 24-hour urine calcium excretion (4.0 mmol/d vs 4.6 mmol/d, p=0.015). No participants developed new arterial calcifications during the study. One participant (400 IU group) with a small amount of calcification (0.67 mgHA) at baseline demonstrated complete resolution at month 36. Arterial calcification quantity increased linearly throughout the study (Figure), at a rate of 0.020 mgHA (95% CI: 0.012 to 0.029) per month of observation. There was no evidence of a treatment group effect (p=0.645 for interaction).

Conclusions

Tibial artery calcification was identified in over a quarter of this cohort of healthy adults, and the amount of calcification increased over three years of follow-up. Supplementation with vitamin D 400, 4000 or 10,000 IU/day did not have differential effects on the development or progression of arterial calcification.

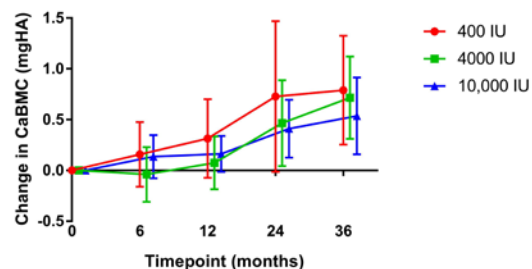


Figure 1. Changes from baseline in quantity of tibial artery calcification in healthy adults taking vitamin D3 for three years.

Study on Normative Data of vBMD and Bone Microstructure Measured by Second-Generation HR-pQCT in Japan: Comparison between the Fixed and Relative Offset Methods

Ko Chiba^{*1}, Narihiro Okazaki¹, Masako Ito², Makoto Osaki¹

¹ Department of Orthopedic Surgery, Nagasaki University Graduate School of Biomedical Sciences

² Center for Diversity and Inclusion, Nagasaki University

Purpose

HR-pQCT (High Resolution peripheral Quantitative CT) enabled us to perform in vivo analysis of patients' bone microstructure. Second-generation HR-pQCT was developed in 2014 with a higher spacial resolution and a faster scan time, and was installed at Nagasaki University, Japan in 2015.

Since then, we have worked on collecting normative data on the Japanese population (N=500) (J-CaraT study: Japanese study of bone miCrostructure and minerAl density in a noRmAtive cohorT measured by HR-pQCT). The data includes HR-pQCT (distal radius, distal tibia / standard fixed offset, relative offset), DXA (L1-4, hip total, neck), and bone markers (TRACP5b, P1NP, 25OH vitamin D, pentosidine).

In this presentation, we'll show the data on HR-pQCT in different scan protocols (standard fixed offset, relative offset).

Methods

A total of 116 healthy Japanese volunteers (46.6 years, 21-87 years, 75 females, 41 males) were analyzed. The distal radius and tibia were scanned using HR-pQCT (XtremeCT II; Scanco Medical, Switzerland) with a voxel size of 61µm by the standard fixed offset method (radius: 9 mm, tibia: 22 mm) and the relative offset method (radius: 4%, tibia:

7.3%).

Volumetric bone mineral density (vBMD) and microstructural parameters were measured, and the difference between the two methods were compared. In addition, the correlation between the difference and the limb lengths were analyzed.

Results

Mean body height was 162.1 cm (141-185 cm), the forearm length was 248.7 mm (214-291 mm), and the lower leg length was 342.2 mm (281-405 mm). Compared to the relative offset method, Ct.vBMD, Ct.Th, Tb.Th, and Tb.Sp by the fixed offset method were significantly higher, and Tb.vBMD, BV/TV, and Tb.N were significantly lower. The forearm length had a negative correlation with Ct.vBMD ($r=-0.59$) and Ct.Th ($r=-0.60$) at the distal radius ($p<0.001$). The lower leg length correlated with Ct.vBMD ($r=-0.85$), Ct.Th ($r=-0.92$), Tb.vBMD ($r=0.83$), BV/TV ($r=0.81$), Tb.N ($r=0.72$), and Tb.Sp ($r=-0.56$) at the distal tibia ($p<0.001$).

Conclusion

vBMD and bone microstructure were different between the fixed and relative offset methods. The differences were correlated with the limb length. Our data indicates that the scan region shifts at the anatomically more proximal sites when patients with short limb length are scanned.

HR-pQCT Measures of Bone Microarchitecture for Fracture Risk Assessment: Patient Covariate Meta-Analysis

Svetlana V Komarova*¹, Nicholas Mikolajewicz¹, Kim Wager², Michael Molloy-Bland², Anthony Hall³, Bettina M Willie¹, Suzanne Morin⁴, Francis H Glorieux¹

¹ Shriners Hospital for Children-Canada

² Oxford PharmaGenesis

³ Mereo BioPharma Group

⁴ McGill University

Introduction

High-resolution peripheral quantitative computed tomography (HR-pQCT) is a non-invasive imaging modality for assessing volumetric bone mineral density (vBMD), and characterizing microarchitecture of cancellous and cortical bone.

Methods

We have systematically identified 52 studies that used HR-pQCT bone imaging in 3941 individuals with and 10996 without incident or prevalent fractures. The objective of this study was to analyze the effect of patient covariates, including age, sex, trauma degree, fracture site, and clinical diagnosis on the performance of HR-pQCT-derived measures for fracture prediction. For 12 HR-pQCT parameters describing population level measures of bone density, microarchitecture and strength in radius and tibia, percent differences between individuals with and without a fracture history were estimated using a random effects model, and subgroup analysis and meta-regression were performed for patient covariates.

Results

When data was stratified by age, fracture-related changes in HR-pQCT parameters were more pronounced in older adults (over

50 years old), compared to pediatric (under 18) and young adult (18-50) groups. Fracture-related changes were higher in females compared to males. Nevertheless, in older males, and young males who experienced low trauma fracture, HR-pQCT measures were significantly different from individuals without fracture. For older adults, we assessed if the site of the fracture (peripheral, vertebral or hip) was associated with specific changes in HR-pQCT parameters and found higher cortical porosity in patients with hip fracture, as well as lower stiffness and failure load in patients with vertebral fractures compared to other fracture types. Published studies contained sufficient number of datasets to perform subgroup analysis of patients with osteoporosis and chronic kidney disease. Compared to individuals with osteoporosis, fracture-related differences in HR-pQCT measures of chronic kidney disease patients were significantly larger in cortical parameters.

Conclusion

Taken together, our study demonstrates that HR-pQCT-derived parameters can robustly predict clinically-relevant fracture in patients of different age, sex and underlying disease. Work supported by Mereo BioPharma Group.

Assessment of Muscle Quantity and Quality in Premenopausal, Postmenopausal and Women with Recurrent Falls

Marta C Erlandson^{*1}, Lora Giangregorio², Andy KO Wong^{3,4}, Eva Szabo⁵, Hunxian Hu⁵, Angela M Cheung^{3,6}

¹ College of Kinesiology, University of Saskatchewan

² Department of Kinesiology, University of Waterloo

³ Toronto General Research Institute, University Health Network, Centre of Excellence in Skeletal Health Assessment/ Joint Department of Medical Imaging, University Health Network

⁴ Department of Medicine, McMaster University

⁵ Osteoporosis Program, Centre of Excellence in Skeletal Health Assessment/ Joint Department of Medical Imaging, University Health Network

⁶ Divisions of General Internal Medicine and Endocrinology, Department of Medicine, University Health Network, University of Toronto

Introduction

Muscle size and neuromuscular function decrease with age, resulting in a loss of muscle strength and physical functioning. Women experience an additional decline in muscular strength around the time of menopause that accounts for a 10-15% loss above that associated with aging alone (Sirola et al., 2005). Muscular strength has been found to correlate with poor balance and increased falls; therefore, this drastic decline around menopause in muscle strength may put women at an increased risk of falls (Sirola et al., 2005; Tinetti et al., 1988). However, to date, the majority of the literature investigating the associations between declining muscle mass, aging, and function have primarily focused on men. Therefore, the purpose of this study was to assess muscle quantity and quality at the lower leg in premenopausal women (PRE), healthy postmenopausal women (POST) and postmenopausal women with recurrent falls (FALLS) (defined as 2 or more self-reported falls in the last 12 months).

Methods

30 PRE (age 38.0±14.8), 30 POST (age 69.4±12.3), and 26 FALLS (age 70.9±12.5) were recruited. Muscle cross-sectional area (MCSA) and density were assessed using peripheral quantitative computed tomography (pQCT) (XCT-2000L; Stratec Medizintechnik GmbH, Pforzheim, Germany). The lower leg was scanned at 66% of limb length according to manufacturer's recommendation

and muscle parameters were assessed using Stratec and BonAlyse software (BoneAlyse Oy, Jyväskylä, Finland). A threshold of 280 mg/cm³ was used to separate bone from soft tissue and 30 mg/cm³ was used to separate muscle from fat tissue. Anthropometric variables were assessed as well as physical activity (International Physical Activity Questionnaire) and function (Short Performance Physical Battery). MCSA and density were compared between groups using PROC GLM while adjusting for age, height, weight and physical activity.

Results

There was a trend for lower muscle density going from PRE to POST to FALLS group, but it was not statistically significant between groups (PRE=72.7±2.4mg/cm³, POST=71.6±2.2mg/cm³, FALLS=70.4±2.2mg/cm³, p>0.05). There was also a trend for lower MCSA going from PRE to POST to FALLS group, but only the FALLS group had significantly lower MCSA compared to the PRE group (PRE=6355.2±1027.3mm², POST=6080.4±820.1mm², FALLS=5510.7±703.4mm², p<0.05).

Conclusion

Women who experienced recurrent falls tend to have lower muscle density and smaller MCSA compared to healthy premenopausal women. Our study may be limited by our small sample size. pQCT may be a useful tool for the assessment of muscle quantity and quality.

Workshop Working Group on Standardization of Quantitative Metrics for 3D Imaging

Andrew J. Burghardt^{*1}, Philipp Schneider², Steven K. Boyd^{3,4}

¹ Department of Radiology & Biomedical Imaging, University of California, San Francisco

² Faculty of Engineering and the Environment, University of Southampton

³ McCaig Institute for Bone and Joint Health, University of Calgary

⁴ Department of Radiology, University of Calgary

Description

Quantitative musculoskeletal imaging research operates across multiple image formation modalities, scales, and processing pipelines. Recognizing the significant degree of variability in the implementation, availability, and application of methods to quantify bone from digital imagery, an ad hoc group convened at the 2017 IBDW to initiate a discussion on the need for greater standardization efforts in the field. For the 2019 QMSKI Workshop we propose to reconvene this group in a structured discussion with the goal to define concrete steps to operationalize a standardization framework for quantitative metrics of bone structure.

Program Activities

With the goal to This working group will be a structured discussion addressing the following topics:

1. The creation of an open reference data repository that would provide a platform for specific standardization development and evaluation
 - (a) in silico standards
 - (b) idealized phantoms
 - (c) biological phantoms
2. The creation of a certification framework for metric implementations that aids scientific communication and incentivizes developers to attain standards recognition.

- (a) Definition of reproducible, standardized, documented criteria
 - (b) Grading and or certification scheme to evaluate an implementations performance against said criteria
 - (c) Demonstrate proof of concept in an open platform
 - (d) Reporting on other available open and proprietary implementations
3. The creation of consensus-building body to direct key efforts
 - (a) Definition and organization of reference standards and repository
 - (b) Development and implementation of a certification scheme
 - (c) Development and dissemination of standardization guidelines to the community
 - (d) Coordination of a funding strategy to support these efforts

Target Audience

Quantitative imaging scientists at all career stages and industry partners with an interest in image analysis, algorithms, reproducibility, standardization, and open source software are encouraged to participate.

Objectives

Establish a plan to operationalize tools to evaluate and certify quantitative metrics for musculoskeletal imaging. Develop the organizational structure for a consensus-building body to direct the standardization project.

Quantifying (Re)modeling Over 5 Weeks of Mechanical Loading Using Time-Lapse In Vivo Micro-Computed Tomography

Samuel T. Robinson^{*1}, Yizhong Hu¹, X. Edward Guo¹

¹ Bone Bioengineering Lab, Columbia University

Introduction

Osteoporosis is a prevalent disease with dire consequences resulting from falls or even non-traumatic compression fractures. There are different treatment methods with varying efficacies and side effects and within those a range of delivery regimens. Two therapeutic means to maximize bone mass include anabolic therapies (e.g. PTH injections), and anti-catabolic therapies (e.g. anti-resorptive bisphosphonates). Mechanical loading is a known stimulus for enhancing bone mass, and the proteins involved in mechano-adaptation may provide avenues for enhancement of current treatments or new approaches. Maximizing bone mass without sacrificing healthy bone turnover is an optimal solution, and maintaining these dynamics over an extended period is critical. Thus, the effects of loading and therapeutics on remodeling (coupled formation/resorption) and modeling (uncoupled formation/resorption) independently is of critical interest.

Methods

16-week-old C57Bl/6 mice had one tibia loaded 5x/week for 5 weeks. μ CT scans were performed once per week for both limbs (loaded and contralateral nonloaded). Scanning was initiated two weeks prior to loading treatment such that immediate responses to loading could be classified as coupled or uncoupled to preceding baseline formation/resorption. Weekly grayscale images were registered to a common coordinate system wherein the formation/resorption history

of each voxel was tracked and quantified as modeling or remodeling using Matlab.

Results

In trabecular bone, there was significantly more bone formed on loaded bones through both the modeling and remodeling regimes and tended to diminish over time. The response was most significant in plate-like trabeculae regardless of orientation and interestingly just in transverse rod-like trabeculae. Catabolic modeling was largely similar between loaded/nonloaded limbs. In cortical bone, there was a similar trend of anabolic modeling and remodeling initially that came to be dominated by modeling and diminished after two weeks. Anatomically, the effects were more pronounced on the periosteum. On the endosteum there was an initial suppression of catabolic modeling, but over time, a surprising induction of catabolic modeling with loading (widening of the marrow cavity).

Conclusions

We have shown that mechanical loading is capable of stimulating bone formation through both the modeling and remodeling regimes, but has more pronounced effects through modeling and in areas that are mechanically beneficial, as trabecular plates have been shown to correlate well with whole bone stiffness, and an expansion of the periosteal surface is the most efficient way to increase polar moment of inertia (resistance to bending).

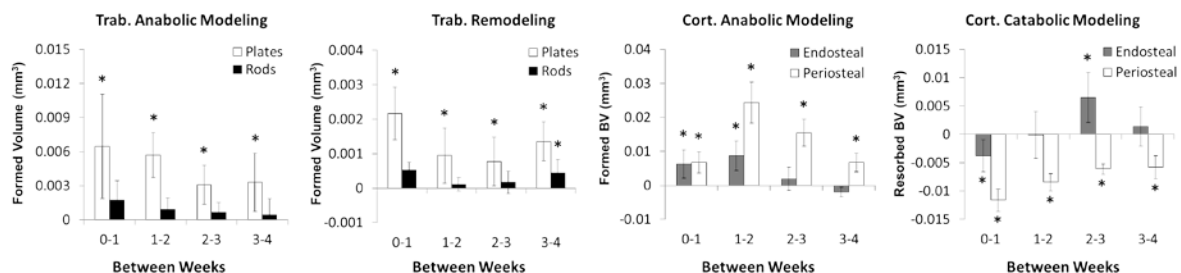


Figure 1. Differences between loaded and nonloaded contralateral controls, *p < .05 (loading)

Coupling Longitudinal Micro-CT Imaging and Frailty Assessments: Advancing Applications in Aging Mouse Studies

Ariane C Scheuren^{*1}, Gisela A Kuhn¹, Ralph Müller¹

¹ Institute for Biomechanics, ETH Zurich

Introduction

In-vivo micro-CT has already been used to monitor microstructural changes of bone in mice of different ages and in models of age-related diseases such as osteoporosis. However, as aging is accompanied by frailty and subsequent increased sensitivity to external stimuli (e.g., handling, anaesthesia), the extent to which longitudinal imaging can be applied in aging studies remains unclear. Consequently, the potential of monitoring individual mice during the entire aging process – from healthy to frail status – has not yet been exploited. Therefore, the aim of this study was to track individual mice for the development of osteoporosis and frailty in a model of accelerated aging (PolgA).

Methods

The caudal vertebrae of homozygous (PolgA) and wildtype-littermate (WTL) controls were monitored by in-vivo micro-CT (vivaCT40, Scanco Medical) every 2 weeks. To investigate a potential effect of increased imaging and handling, the mice were divided into 4 groups (with n=12 PolgA and n=10 WTL/group). The first group was scanned over 20 weeks (11 scans, age 20-40 weeks), whereas the other groups were scanned over 8 weeks (5 scans, weeks 26-34, 32-40 and 40-46, respectively). 3D static and dynamic bone morphometric parameters were assessed. Frailty was quantified longitudinally using the clinical mouse-frailty-index (FI).

Results

In agreement with previous results obtained by end-point X-ray densitometry, PolgA and WTL had similar bone morphometric parameters at 20 weeks of age, which then diverged over time such that PolgA had significantly lower bone mass at 40 weeks. However, longitudinal micro-CT revealed that this difference was not due to a loss in bone mass in the PolgA mice, but rather to the continuous increase in bone mass in the WTL (Fig-

ure 1). Monitoring over 20 weeks revealed an increase in heterogeneity within PolgA and WTL populations with age (Figure 1, B). Compared to WTL, FI scores of PolgA increased over time making these mice more frail.

Conclusion

Using a model of accelerated aging, the application of longitudinal micro-CT was expanded to monitor individual mice while transitioning from healthy to frail status thereby allowing to comprehensively characterize the bone phenotype in this model. Increased monitoring over 20 weeks did not negatively affect the mice. Considering the larger heterogeneity with age, longitudinal designs including baseline measurements at a young age are more powerful at detecting age-related phenotypic changes than those including multiple groups with fewer imaging sessions. Coupled with longitudinal frailty assessments, the data obtained from individual mice can be maximized even more.

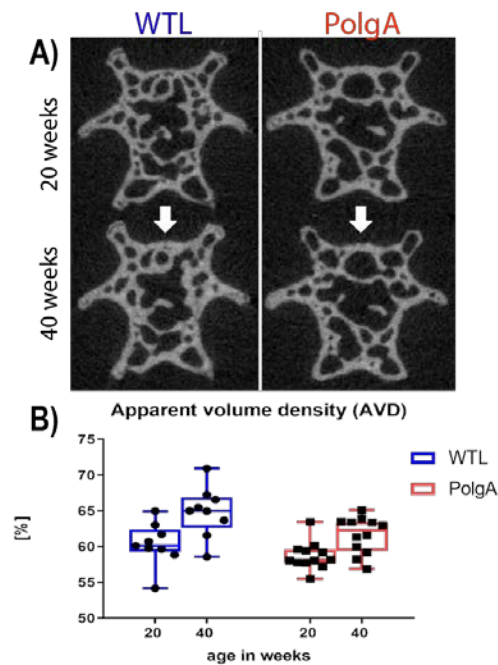


Figure 1. Bone morphometry in WTL and PolgA mice at age 20 and 40 weeks, respectively.

Time-Lapse MicroCT-Based *in vivo* Imaging Reveals Load-Induced Targeted (Re)Modeling at the Periosteal Surface in Mice With Multiple Myeloma Bone Disease

Maximilian Rummler^{*1}, Fani Ziouti², Maureen E. Lynch³, Franziska Jundt², Bettina M. Willie¹

¹ Shriners Hospital for Children - Canada, McGill University

²University Hospital of Würzburg

³University of Colorado

Introduction

Multiple myeloma (MM) is an incurable plasma cell derived neoplasia. Patients develop devastating osteolytic lesions that lead to non-healing fractures and pain. We aimed to assess the adaptive cortical bone (re)modeling response to mechanical loading in a mouse model of MM. We hypothesized *in vivo* tibial loading would have an anabolic and anti-catabolic effect in tumor-injected tibiae, rescuing bone loss.

Methods

Ten-week-old female Balb/c mice underwent *in vivo* strain-matched dynamic compressive loading of the left tibia (5d/wk for 20 days, M-F). The mice were injected 14 days prior to loading with either MOPC315.BM cells or PBS (left limb injected) or were not injected (left limb noninjected) (Fig. 1A). Tumor- and PBS-injected mice were randomized into loaded (left limb loaded) or nonloaded (left limb nonloaded) groups (n=6-9/group). *In vivo* microCT was performed at day 13, 18, 23, 28 and 33 post injection. MicroCT images from day 13 and 33 were geometrically registered to monitor bone formation and resorption at the endosteal and periosteal tibial cortical metaphyseal surface: normalized newly mineralized and eroded bone volume (MV/BV_{day0-20}, EV/BV_{day0-20}), bone surface areas (MS/BS_{day0-20}, ES/BS_{day0-20}), and mineralized thickness and eroded depth (MTh_{day0-20}, ED_{day0-20}). An ANOVA assessed effects of treatment (tumor injected/PBS injected/noninjected) and loading (loaded/nonloaded) ($p \leq 0.05$). Fluorochrome-based histomorphometry was also performed. Tumor progression was monitored using bioluminescence imaging and enzyme-linked immunosorbent assay to detect MOPC315. BM specific immunoglobulin

A (IgA) levels.

Results

Loading increased periosteal MV/BV and MS/BS and decreased periosteal EV/BV and ES/BS compared to nonloaded limbs in all groups (Fig. 1BC). Loading-induced increases in endosteal MV/BV was only observed in the tumor group. Endosteal MS/BS was diminished, while ES/BS was increased in tumor injected mice compared to PBS injected and noninjected groups. Loading-induced effects on the eroded surface and volume suggests fewer resorption sites at the periosteal surface. Injection, either tumor or PBS, altered periosteal and endosteal bone formation and resorption, suggesting a regional acceleratory phenomenon. Load induced increases in cortical bone mass were accompanied by decreased tumor burden as evidenced by MOPC315. BM specific IgA levels (Fig. 1D). Our data in young mice with MMBD indicate that mechanical loading not only rescues osteolytic bone loss but also has anti-myeloma effects. These data suggesting a combination of load-bearing exercise with bone resorption inhibitors in future clinical therapeutic strategies.

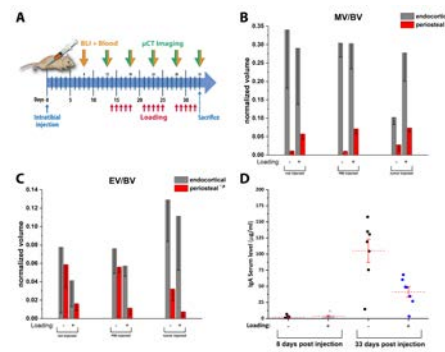


Figure 1. A) Timeline. B) Newly mineralized bone volume (MV/BV) and C) eroded volume (EV/BV) (ANOVA:(#) loading, (*) treatment/injection, $p < 0.05$) D) IgA-level.

Reproducible Positioning of the Mouse Knee for Longitudinal MicroCT Studies

Zihui Li¹, Ren Yan N. Kour¹, Kathryn S. Stok^{*1}

¹ Department of Biomedical Engineering, The University of Melbourne

Introduction

Longitudinal live imaging in animal studies allows monitoring of biomechanics, disease, and facilitates development of therapies. In order to accurately compare and quantify changes between non-rigid structures (i.e. joints) in longitudinal images, it is important to control the position from scan to scan. The aim of this study was to develop a mouse positioning system to ensure reproducible outcomes from longitudinal microCT imaging of mouse knee joints, and to assess its reproducibility for relevant outcome measures.

Methods

A custom mouse holder compatible with the in vivo microCT animal bed was designed in-house. Seven healthy excess male mouse carcasses, 10 – 20 weeks of age, were injected intraarticularly with CA4+, a contrast-agent specific for cartilage [1]; while a further seven did not receive injection. Mice were positioned in the holder, placed onto the animal bed, and the right knee was scanned with microCT (vivaCT80, Scanco Medical, Switzerland). Scans were performed with 10 μm nominal voxel size; 70 kVp; 57 μA ; 500 projections; and 350 ms integration time. Each mouse was scanned 5 times, including repositioning between scans. Reproducibility was assessed for joint angle (JA), joint space

width (JS.W) and joint space volume (JS.V) [2], as precision error (PESD and PE%CV), as well as intraclass correlation coefficient (ICC).

Results and Discussion

Figure 1 shows five measurements of the same knee joint, with repositioning, and including colour-mapped medial joint space width. The mean values of JA, JS.W and JS.V were 104°, 0.229 mm and 0.243 mm³ for the group with CA4+ contrast agent injection, and 105°, 0.232 mm and 0.248 mm³ for the group without injection. ICC of group with and without CA4+ injection respectively were 0.919 and 0.964 for JA, 0.639 and 0.810 for JS.W, and 0.625 and 0.768 for JS.V.

Conclusions

The highly reproducible JA in both groups with and without CA4+ injection, indicated by the high ICC confirmed that the positioning system is able to provide reproducible data of joints scanned longitudinally. This device will facilitate time-lapse comparison of microCT images. Further investigation on contrast agent diffusion-in kinetics in quantitative metrics will be conducted.

References

1. Joshi, et al. *J Am Chem Soc.* 2009, 131:13234-35.2. Stok, K.S. et al. *J. Rheum.* 2017, 44:1911-15.

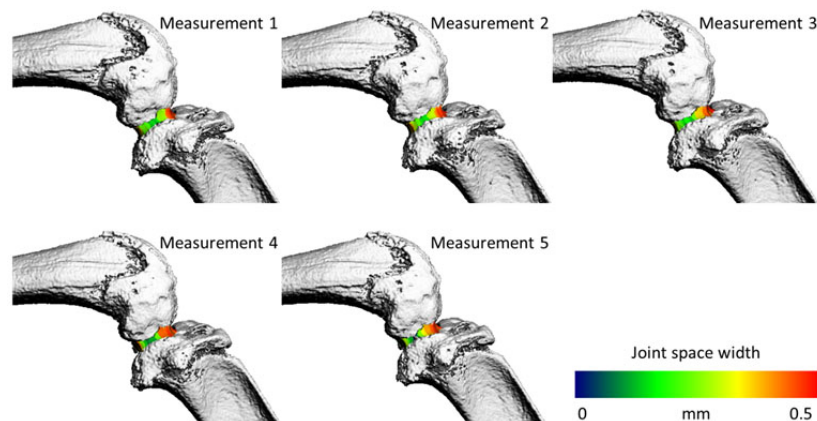


Figure 1. Five measurements of the mouse knee joint, including colour-mapped medial joint space width, using the novel holder.

Profile of Trabecular Architecture Downstream of the Mouse Tibial Growth Plate and where to Position the Volume-of-Interest for Trabecular Morphometry; Hint - Don't Scale with Bone Length

Phil Salmon^{*1}, Behzad Javaheri², Andy Pitsillides²

¹ Bruker microCT

²Royal Veterinary College

The mouse knee (proximal tibia, distal femur) is the most used site for trabecular bone morphometry by microCT. The widely accepted method for selecting a standard volume-of-interest (VOI) for trabecular bone, inherited from 2D histomorphometry, is to (a) identify the level of the growth plate; (b) move an “offset” distance from (a) to exclude primary spongiosal remnants; (c) choose an axial length (“height”) of the VOI sufficient to include most metaphyseal trabecular bone by volume. Within a study involving mice of the same strain, age and gender cohort, offset and height are kept equal, for equivalence of trabecular morphometry. However sometimes comparison is needed between mice of different ages, genders or transgenic strains, where the bone length and overall architecture are significantly different, and where the same values of offset and height cannot be used. Here the question arises – on what basis to adjust offset and height for anatomical equivalence in the size and position of the VOI. In some previous studies offset and height have been simply scaled to bone length. Here we investigate whether such scaling is appropriate. C57BL/6 mouse tibias from animals aged 2-20 months were imaged by microCT in the proximal metaphysis, and the cross-sectional profile of trabecular per-

cent bone area and other parameters was assessed starting from the growth plate and extending downstream of the growth plate until trabecular bone almost disappeared. Analysis of this “metaphyseal profile” showed that anatomically appropriate values of both offset and height decrease with age. While tibial length did not change much after 2 months, the axial extent of the growth plate diminished rapidly with age as one would expect with declining growth rate. Thus the optimal offset value decreased from about 0.5 mm at 2 months to around 0.3 mm by 5.5 months with little change thereafter due to an invariant calcified primary spongiosal architecture. However the height of metaphysis containing significant trabecular bone declined with age until the amount of metaphyseal trabecular bone at 16 months or more became extremely small. In conclusion, simple scaling with bone length is a wrong way to adjust trabecular VOI position; instead the adjustment needs to be based on the growth status of the mice. This can be assessed objectively by analysis of the metaphyseal profile of trabecular parameters with distance downstream of the growth plate, to allow equivalent morphometric comparison between mice of different age, experimental treatment or transgenic strain.

Printed Lacuno-Canalicular Network (pLCN): An Engineered 3D Environment for Multi-Modality Imaging of Osteocyte Networks

Felicitas R. Flohr^{*1}, Nina Derron¹, Jens Moeller², Ralph Müller¹

¹ Institute for Biomechanics, ETH Zurich

² Laboratory of Applied Mechanobiology, Department of Health Sciences and Technology, ETH Zurich

Introduction

Osteocytes, the mechanosensory cells of bone, are buried deep inside the calcified bone matrix within lacunae and are connected by dendritic cell processes passing through sub-micron canalicular channels. This three-dimensional environment is thought to regulate osteocyte mechanosensing but also severely limits their accessibility for functional investigations.

We have developed a novel in vitro osteocyte model using a micro-3D printed lacuno-canalicular network (pLCN) to mimic the osteocyte extracellular environment. Uniquely, it allows to independently manipulate osteocyte morphological parameters such as shape and number of dendrites through design changes in the pLCN. Here, we demonstrate the capabilities of this model for multi-modality imaging using live-cell fluorescence microscopy as well as high-resolution imaging by FIB-SEM and confocal microscopy.

Methods

pLCNs were fabricated by two-photon-polymerization micro-3D printing (Nanoscribe Photonic Professional GT) using the inorganic-organic hybrid polymer OrmoComp[®] and coating with collagen-I. Osteocytic IDG-SW3 cells were seeded on the structures after 35 days of osteogenic differentiation. For cell morphology analysis, cells were fixed with paraformaldehyde, stained with Phalloidin-TRITC, and mounted with Fluoroshield[™] containing DAPI. For live-cell imaging and fluorescence recovery after photobleaching (FRAP), cells were stained using Calcein-AM

and Hoechst. Photobleaching and image acquisition were performed on a confocal laser scanning microscope (Zeiss LSM880). For high magnification imaging of osteocytes and pLCN, cells were fixed with glutaraldehyde, followed by osmium tetroxide postfixation, ethanol gradient dehydration and critical point drying. After sputter coating with Pt-Pd, focused ion beam milling and scanning electron microscopy (FIB-SEM) were performed on a Zeiss NVision40.

Results & Discussion

Osteocytes were found to grow into pLCN and form actin-rich dendritic processes within 24 hours after seeding (Figure 1A). Using cytoplasmic Calcein staining, we were able to follow dendrogenesis in live osteocytes in pLCNs over several hours (1B). Dye transfer between osteocytes indicated the presence of intercellular connections and the formation of a functional osteocyte network (1C). High magnification images using FIB-SEM revealed details of osteocyte morphology, internal structure and their interface with pLCNs (1D).

We believe that pLCNs are a valuable platform to study osteocyte networks in a biomimetic 3D environment with a variety of complementary imaging methods. In the future, calcium and nitric oxide indicators will be used to follow osteocyte mechanosensation and signal propagation in live osteocyte networks.

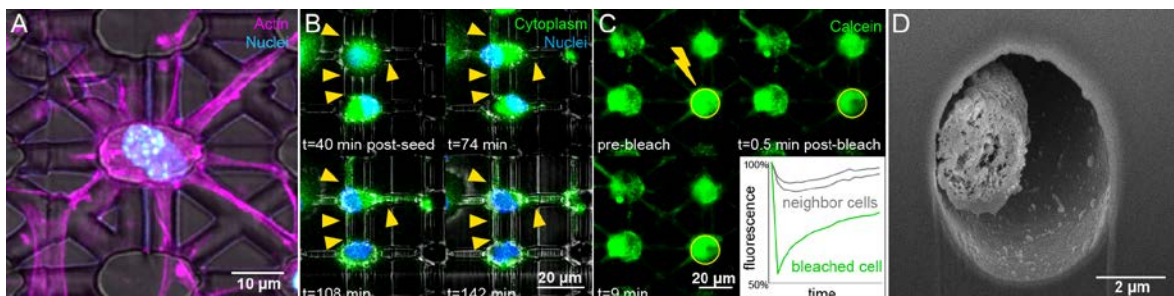


Figure 1. Fluorescence (A-C) and electron (D) microscopy of live (B,C) and fixed (A,D) osteocytes in pLCNs

Can Texture Analysis on MR Images Identify Intervertebral Disc Phenotypes Related To Back Pain?

Vahid Abdollah*¹, Eric C Parent¹, Michele C Battie²

¹ Department of Physical Therapy, Faculty of Rehabilitation Medicine, University of Alberta

² School of Physical Therapy, Faculty of Health Sciences, University of Western Ontario

Introduction

The lumbar intervertebral disc is the focus of much clinical imaging and research, as low back pain has often been attributed to disc degeneration and pathology. Although conventional MRI is a sensitive modality for depicting structural abnormalities of the discs, findings are often clinically inconclusive as both symptomatic and asymptomatic individuals often demonstrate the same degenerative features. Texture analysis, which computes the pattern of signal intensity variations within a region of interest, may be useful for stratifying degeneration phenotypes. This study aimed to determine if texture features extracted from T₂ maps differ in lumbar discs of participants with and without low back pain.

Methods

Fifteen volunteers with chronic back pain (6 males and 9 females) were matched for age, weight, and gender with 15 healthy volunteers. Mid-sagittal T₂ multi-echo images were acquired using a 3T whole-body Philips Intera MRI. Acquisition parameters were: repetition time: 2500 ms; echo time (five echoes): 16.9, 44, 71, 98 and 125 ms; field of view: 500x500 mm; matrix size: 1024x1024 pixel; and slice thickness: 5 mm. Image processing was carried out offline using Matlab[®] software developed in-house. T₂-maps were constructed using the Nelder-Mead Simplex method. The software deploys a texture-based algorithm to semi-automatically segment discs and nucleus from adjacent tissue between L1 and L5. A grey-level co-occurrence matrix with one-pixel offset was constructed to extract second order texture features: contrast, correlation, energy, and homogeneity. Mean, coefficient of variation and signal intensity range were also extracted for each region of interest. A repeated measures analysis of variance and Sidak post-hoc comparisons were employed to compare dif-

ferent measures between groups with or without pain at each level. The effect size of differences between groups in texture features and other disc measurements was estimated using Cohen's d.

Results

A significant difference was observed between controls and low back pain participants in disc contrast (Effect size: 0.39; P-value=0.04, Figure 1). No statistically significant difference between groups was observed for the energy, correlation, and homogeneity for both disc and nucleus between two groups. The mean T₂ of the pain group for both the disc and nucleus was lower than the controls, but the difference did not reach significance (Effect size: 0.18). Although the coefficient of variation and the range were higher in the pain group for disc and lower for the nucleus than the in the controls, no statistically significant difference was observed between groups.

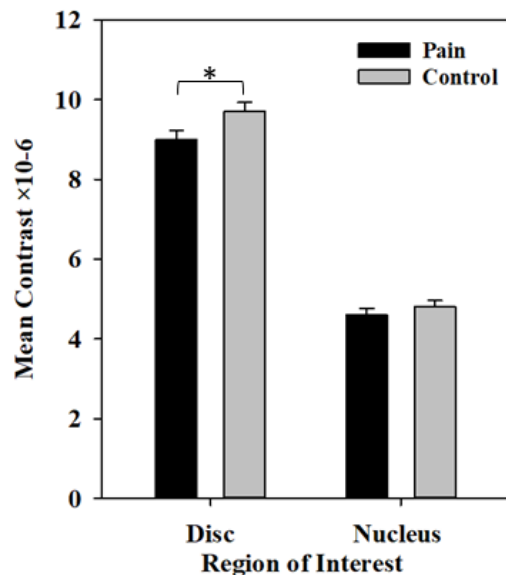


Figure 1. Mean contrast for the disc and nucleus of participants with and without pain (mean \pm SE)

Establishing an Imaging Protocol for Bone Marrow Lesions and Cysts in the Dunkin-Hartley Guinea Pig Knee using Magnetic Resonance Imaging and Micro-Computed Tomography

Destiny Francis^{*1,2,3,4}, Alicia Gabilondo^{1,2,3}, Jeffrey F. Dunn^{1,2,3}, John R. Matyas^{1,5}, Sarah L. Manske^{1,2,3,4}

¹ McCaig Institute for Bone and Joint Health, University of Calgary

² Department of Radiology, University of Calgary

³ Cumming School of Medicine, University of Calgary

⁴ Biomedical Engineering Graduate Program, University of Calgary

⁵ Faculty of Veterinary Medicine, University of Calgary

Introduction

Bone marrow lesions (BMLs) are associated with pain in late-stage knee osteoarthritis (OA). The Dunkin-Hartley (DH) guinea pig develops spontaneous OA as early as three months of age, allowing us to study the pathogenesis of OA in a trauma-free model. Our goal is to establish imaging techniques to investigate the occurrence of subchondral BMLs and cysts in DH guinea pigs to better understand how they contribute to OA progression.

Methods

The left hind limbs of 16 guinea pigs ranging from 2-26 months of age were dissected *ex vivo*. FLASH scans were obtained using a 9.4T MRI with a CryoProbe to produce a T2-weighted image with and without fat suppression (Bruker, TE = 6.5 ms, TR = 1500 ms, 0.0375 mm x 0.0375 mm x 0.5 mm). On a 1.0T MRI, STIR images were obtained on a retired breeder (Bruker, TE = 10.07 ms, TR = 600 ms, TI = 280.7 ms, 0.156 mm x 0.156 mm x 1.000 mm). The MRI scans were accompanied by μ CT scans using the vivaCT40 (Scanco Medical, 55 kVp, 72 mA, Integration time = 250 ms, 15 μ m isotropic), and a histological analysis. The MR and μ CT images were registered to overlay bone and lesioned tissue.

Results

The μ CT scans showed a bone cavity in the central femoral epiphysis in all retired breeders. While some absence of trabecular bone was observed in 2-month old animals, it was more apparent in 4-month old animals. A hyperintense region was observed in the central femoral epiphysis on most MR sequences in the retired breeders. Brighter regions were observed in 4-month but not 2-month old animals. The relationship between this region and the bone cavity observed in the μ CT images can be seen in Figure 1 (A: 2-months, B: 4-Months, C: Retired breeder). The 1.0 T images produced contrast suggestive of a cyst in hematopoietic marrow. Histological analysis confirmed the presence of a cyst.

Conclusions

Increased MR signal in regions of the 4-month old and retired breeder hindlimbs with an absence of femoral trabecular bone is an encouraging step towards identifying bone marrow cysts. We will image DH guinea pigs at a wider range of ages to assess whether BMLs precede the development of cysts, which is hypothesized to occur during the pathogenesis of human OA. Understanding the pathogenesis of BMLs and cysts will improve our understanding of the development of a structural feature strongly associated with symptomatic knee OA.

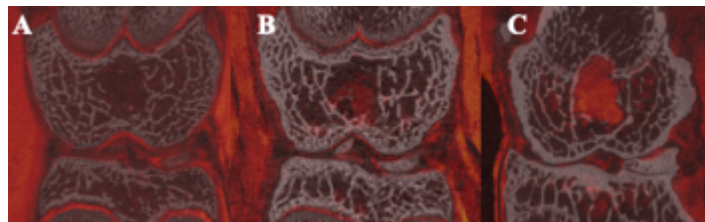


Figure 1. Registration of MR (colour) and μ CT (white) images. A) 2 months, B) 4 months, and C) retired breeder

MRI Hip Joint Effusion Measurement by Two Different Techniques: Single Measurement vs. Volumetric Quantitative Measurement.

Vanessa Quinn-Laurin^{*1}, Adrian Schankath¹, Laurence Stillwater¹, Ramin Mandegaran¹, Robert G.W. Lambert¹, Jacob L. Jaremko¹

¹ Department of Radiology & Diagnostic Imaging, University of Alberta Hospital

Introduction

Being one of the largest weight-bearing joints of the body, the hip is prone to osteoarthritis (OA), especially in an ageing and increasingly overweight population. Joint effusion is a feature of OA well seen on magnetic resonance imaging (MRI). We sought to determine to what extent volumetric quantitative measurement (VQM) of every pixel of joint fluid was reliable and how well a single measure of anterior effusion thickness at the apex of the femoral head (AETH) correlated with more laborious VQM, which we considered to be an imaging gold standard.

Methods

Fifty-seven hips in 45 consenting patients with highly symptomatic hip OA were recruited immediately prior to a fluoroscopically-guided hip corticosteroid injection. A full MRI protocol including a variety of sagittal and coronal sequences was performed in these patients. AETH was measured on sagittal proton-density fat saturated sequences (PD FS) at the most superficial portion of the femoral head (apex). VQM was performed using a custom MATLAB segmentation software on coronal STIR sequences. Interobserver reliability (ICC) with two readers was calculated for each method (n=50 for AETH and n=20 for VQM). Correlation between AETH and VQM was assessed using a Pearson correlation coefficient (r).

Results

The VQM method was more reliable than the AETH method (ICC=0.96 vs 0.75). The correlation between MRI joint effusion measurements by AETH versus VQM was moderate (r=0.75, p<0.0001). For an experienced user, the mean time to obtain a VQM for one hip is 3 min 53 s (range 2 min 12 s – 6 min 22 s).

Conclusions

Volumetric quantitative measurement of a hip joint effusion, although somewhat time-consuming, is highly reliable and likely represents a gold standard for measuring accurately the total amount of hip joint fluid. However, a single measurement of the anterior hip effusion thickness at the femoral head apex is also reliable and is much faster than performing VQM. Moreover, AETH has been demonstrated to correlate to WOMAC pain, stiffness, and function scores, functional tests and physical tests in a previous study. Further studies are required to assess correlation of VQM to other methods of measuring hip effusion such as by ultrasound, and to clinical parameters.

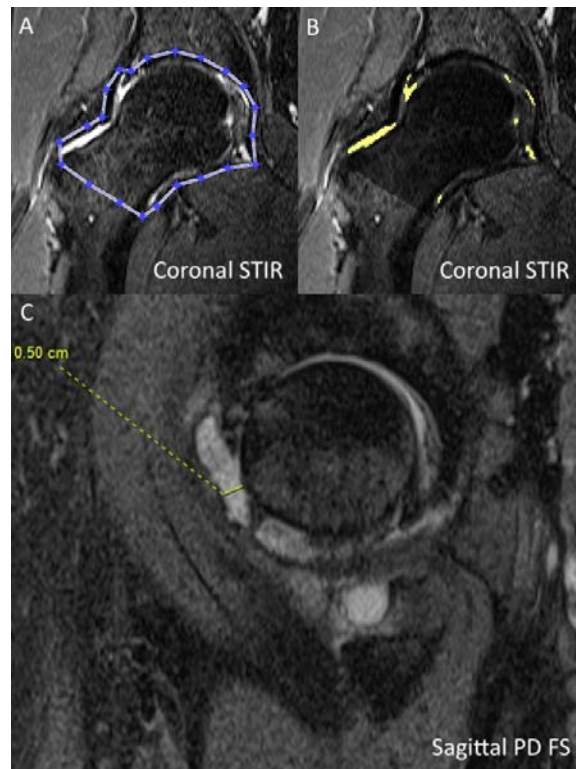


Figure 1. (A-B) Segmentation for VQM of hip joint effusion. (C) Single measurement of anterior hip effusion thickness at apex (AETH).

Upright MRI for Investigating Lumbar Muscle Morphometry, Posture, and Lordosis

Noor Shaikh^{*1,2,3}, Honglin Zhang⁴, John Street⁵, David Wilson^{2,4}, Thomas Oxland^{2,6}

¹ Biomedical Engineering, University of British Columbia

²ICORD, University of British Columbia

³Department of Mechanical Engineering, University of British Columbia

⁴Centre for Hip Health and Mobility, University of British Columbia

⁵Vancouver Spine Surgery Institute, Department of Orthopaedics, University of British Columbia

⁶Departments of Orthopaedics & Mechanical Engineering, University of British Columbia

Introduction

Lumbar spinal musculature aids in spine equilibrium, stability and control. Previously, most magnetic resonance imaging (MRI) of the spinal musculature was supine, however recent upright work has presented some varying results from supine. Postural alignment consideration is needed to determine whether these differences are due to changes in muscle cross-sectional area (CSA) or from changing spinal curvature resulting in muscle elongation. This study's objective was to assess the effect of posture and lordosis on lumbar muscle morphometry.

Methods

Six healthy volunteers were imaged in a 0.5 T upright MRI (MROpen, Paramed) using a T1-weighted Spin Echo sequence (TR/TE=300/20 ms, FOV 20 cm, scan matrix 224x160, slice thickness 7 mm with 0.7 mm gap, NEX=1, 111 s imaging time). Each volunteer was scanned in 7 postures: standing, standing holding 8kg, standing 45° flexion, seated 45° flexion, seated 90°, seated 45° extension, and supine. Three slices were prescribed (parallel to disc) at L3/L4, L4/L5 and L5/S1. Muscle CSA, radius, and angle were taken for the multifidus/erector spinae (MF/ES) combined and the psoas major (PS) muscles (Figure 1). The effect of posture was evaluated by ANOVA ($P < 0.05$) and correlation between CSA and posture lordosis was analyzed using Pearson's correlation coefficient. Repeatability was evaluated using intraclass correlation coefficient ((ICC) (3,1)).

Results

Posture affected the MF/ES CSA (both sides, all levels). Generally, there was decreasing CSA with seated postures and increased flexion (up to 35%) (Figure 2). For the PS, posture affected CSA for both sides at L3/L4

and for the right at L5/S1. Interestingly with seated postures and increased flexion there was increasing CSA at L3/L4 and decreasing CSA at L5/S1 (up to 40%). The PS CSA had little change at L4/L5 (average 5%). Radius and angle had smaller changes with some significant effects. With increasing flexion there was increasing angle and decreasing radius (up to 10%). CSA in different postures and lumbar lordosis had a significant Pearson's correlation coefficient ($P < 0.05$) for 5 of 6 MF/ES ($r = 0.33-0.49$). There was no significant correlation between the PS CSA and lumbar lordosis. Posture repeatability in 4 rescanned volunteers ICC(3,1) was 0.59-0.92 (MF/ES) and 0.77-0.93 (PS). Intra-rater repeatability (4 raters) was 0.73-0.99 (MF/ES) and 0.61-0.97 (PS). Inter-rater repeatability was 0.79-0.95 (MF/ES) and 0.67-0.87 (PS).

Discussion/ Conclusion

The changes in CSA are likely detecting passive muscle stretching between seated, upright and flexion postures. With generally good/excellent repeatability despite the MRI's lower resolution, the correlation between MF/ES CSA and lumbar lordosis starts to highlight the importance of postural alignment on muscle morphometry.

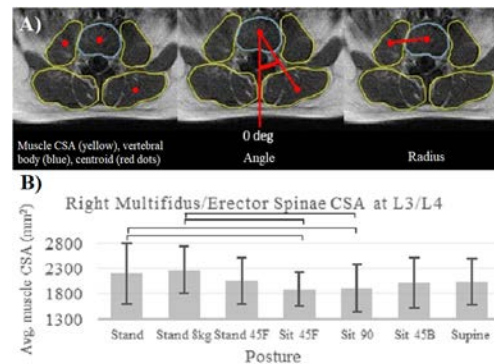


Figure 1. A) Measurements of muscle CSA, angle, radius; B) Example results, right MF/ES CSA at L3/L4

Segmentation of Single Muscles of the Thigh in T1 Weighted MRI Images by Clustering Region Sizes

Oliver Chaudry^{*1}, Frederike Sannmann¹, Wolfgang Kemmler¹, Klaus Engelke¹

¹ Institute of Medical Physics, University Erlangen-Nuremberg

Introduction

Sarcopenia is evident as a progressive loss of skeletal muscle mass, substituted by adipose tissue. Dual energy x-ray absorptiometry can only differentiate overall lean and fat mass. However, not every muscle is affected the same. Therefore, a local muscle analysis requires 3D imaging, like magnetic resonance imaging (MRI) and additional segmentation methods for the fascia and muscles. The aim was to develop a method to segment the different thigh muscles in T1 weighted turbo spin echo (T1wTSE) images and measure the fat content in corresponding 6pt Dixon images. Usually due to insufficient distinction between individual muscles, this requires an atlas which maps the separate muscle regions. Often such an atlas is not available or does not fit the patient group properly. We present a semi automatic method for segmenting muscles, which can also help building or expanding an atlas.

Methods

MRI acquisition was performed using a 3T scanner (MAGNETOM Skyrafit Siemens; 18-channel body surface coil). T1wTSE sequences were measured at the mid-thigh (length 10 cm, voxel size $0.5 \times 0.5 \times 3.0 \text{ mm}^3$, 34 slices). In the T1wTSE images, the fascia was already segmented. For identifying individual muscles, a coarse grid of seed points was applied to the intrafascial region, slice by slice. Each seed point started a region growing. Non-muscle seeds were omitted. Each point of the grid is associated with a certain region size. Under the assumption that regions obtained from seed points located in a given muscle will have rather similar sizes, individual muscles can be separated by region

size and seed positions. This is evident in a region size image obtained from the grid. Each voxel value corresponds to the muscle size. Consequently, this image is used to differentiate muscles by size and spatial distribution. We used the HDBSCAN clustering algorithm, which identifies different muscles as separate clusters. Finally volume growing and morphological operations were used to obtain the muscle segmentation.

Results

Fig. B shows a T1wTSE image with successfully segmented vastus medialis muscle, Fig. A shows the corresponding region size image. So far 10 datasets were segmented. Fully automatic computation detected flexor and extensor muscles in 68 % and most of the smaller muscles in 34 % of the slices.

Conclusion

The method developed to separate individual muscles worked well in the thigh. Compared to a purely manually approach, it will significantly accelerate the creation of a gold standard required to build larger atlases or training sets. Manual corrections will still be necessary.

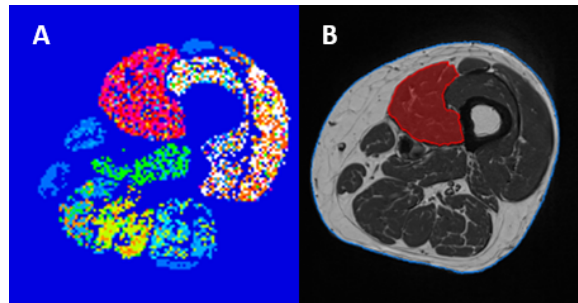


Figure 1. (A) Region size image, (B) T1wTSE image with segmentation

Multi-modality in vivo Detection of Cortical Bone Vasculature: Comparison of Diabetes Patients to Healthy Controls

Po-hung Wu¹, Matthew Gibbons¹, Sarah Foreman¹, Julio Carballido-Gamio², Roland Krug¹, Jing Liu¹, Thomas Link¹, Galatea Kazakia^{*1}

¹ Department of Radiology and Biomedical Imaging, UCSF
²University of Colorado, Denver

Individuals with type II diabetes (T2D) exhibit 40-70% higher risk of fragility fractures than non-diabetics. This increased fracture risk occurs despite normal or elevated aBMD. Increased cortical bone porosity appears to be associated with fracture prevalence in T2D. Despite the biomechanical importance of cortical bone porosity, the biological drivers of cortical porosity are unknown.

The content of cortical pore space can indicate pore expansion mechanisms; both primary components of pore space, vessels and adipocytes, have been implicated in pore expansion. The purpose of our study was to develop a novel multimodal dynamic contrast-enhanced MRI (DCE-MRI) and high resolution peripheral QCT (HR-pQCT) analysis pipeline to detect vessel-filled cortical bone pores and to differentiate them from fat-filled pores.

Distal tibiae of 9 T2D patients and 6 controls were imaged using HR-pQCT to visualize bone morphology, and 3D DCE-MRI to visualize vessels. HR-pQCT scans were acquired at a nominal resolution of 82 μm isotropic (XtremeCT Scanco Medical). 3D DCE-MRI series were acquired using Spoiled Gradient Recalled (SPGR) pulse sequences on a 3T scanner (MR750, GE Healthcare). The spatial resolution of each MRI slice was 230 μm x 230 μm , slice thickness 500 μm . Contrast agent (Gadavist, Bayer HealthCare) was injected at 0.1 mL/kg and 2 mL/sec. Total scan time was 9 min. Data were reconstructed to

30s temporal resolution.

To identify vessel-filled pores, each DCE-MRI volume was first registered to the HR-pQCT cortical mask. A Frangi vessel enhancement filter was applied to the MR data. Enhancement curves features (1st PCA component projection, area under curve, temporal standard deviation, and sum of absolute temporal intensity difference) were extracted for all voxels inside the cortical mask. These features were used to classify pores as vessel-filled or not vessel-filled by k-means clustering. Vessel-filled pore density, total pore density, and vessel pore percentage (number vessel-filled pores/number all pores) were calculated. Perfusion metrics were calculated for detected pore vessels: max intensity (MI), enhancement slope, area under the curve (AUC), and transition time (TT). Two-sample t-tests were performed to compare T2D and control groups.

Comparison of pore metrics found a significantly lower proportion of vessel-filled pores in T2D compared to controls (Fig.1). Perfusion metrics were significantly different with higher MI, slope, and AUC in T2D compared to controls ($p < 0.05$). These results indicate that fewer vessels – with elevated perfusion profiles – infiltrate T2D bone, and suggest that microvascular disease may be implicated in the skeletal complications of T2D.

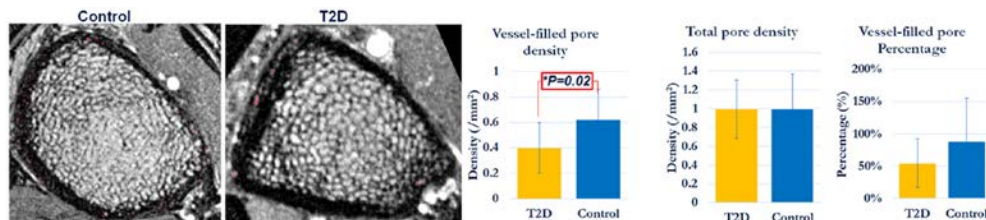


Figure 1. LEFT: Representative control and T2D MRI with detected vessel-filled pores in red. RIGHT: Comparison of pore metrics.

Modeling Bone Architecture and Fracture Risk In Hypophosphatasia by Image-Based Finite Element Analysis

Karamjot Sidhu*^{1,2}, Steven Boyd^{1,3}, Aneal Khan⁴

¹ McCaig Institute for Bone and Joint Health, University of Calgary

²Medical Genetics, Alberta Children's Hospital

³Department of Radiology, Cumming School of Medicine, University of Calgary

⁴Medical Genetics and Paediatrics, Cumming School of Medicine, University of Calgary

Introduction

Hypophosphatasia (HPP) is a rare in-born error of metabolism characterized by low serum tissue non-specific alkaline phosphatase (TNSALP; OMIM 171760). Low levels of this enzyme results in the accumulation of its natural substrate, inorganic phosphate, a potent inhibitor of mineralization. Hypomineralization of the skeleton can lead to debilitating complications, including osteopenia which can increase the risk of fractures. Monitoring bone mineral density (BMD) changes with dual energy x-ray absorptiometry (DXA) is not a measure that has been shown to correlate with fracture risk in this group of patients. We investigated the use of high-resolution peripheral computed tomography (HR-pQCT) and finite element (FE) analysis to evaluate bone architecture and model fracture risk. In a cross-sectional study we examined HR-pQCT data and performed FE analysis in HPP patients.

Methods

We analyzed data from 7 patients recruited from the Metabolic Clinic at Alberta Children's Hospital with a diagnosis of HPP. Patients ranged from 8 to 69 years of age. Both the distal radius and distal tibia were scanned using HR-pQCT (Scanco Medical, Switzerland). Measurements included BMD (HA/mg³), cortical and trabecular BMD (HA/mg³), cortical thickness (mm), and trabecular number. FE analysis was done on both the tibia and radius scan data using a finite element solver (FAIM, Numerics88 Solutions Ltd., Calgary, Canada). Bone stiffness, ultimate stress and failure load were determined. All results were compared to established reference data (<https://normative.ca>). Clinical history included fracture history, treatment interventions and other rele-

vant clinical data.

Results

Four out of 7 of the study participants have been scanned, with FE analysis in its early stages. Figure 1 shows the range of percentile rank on bone densitometry for the HPP patients that have been scanned. Overall, HPP patients scored below average on most measured outcomes, with cortical thickness most negatively affected in all patients. Trabecular was more preserved in comparison to cortical bone, specifically trabecular number, relative to our normative cohort. In conclusion, HPP is a rare metabolic disease where mineralization is impaired and HPP patients from our study had bone densitometry and architecture values far below the 50th percentile in comparison to the healthy population.

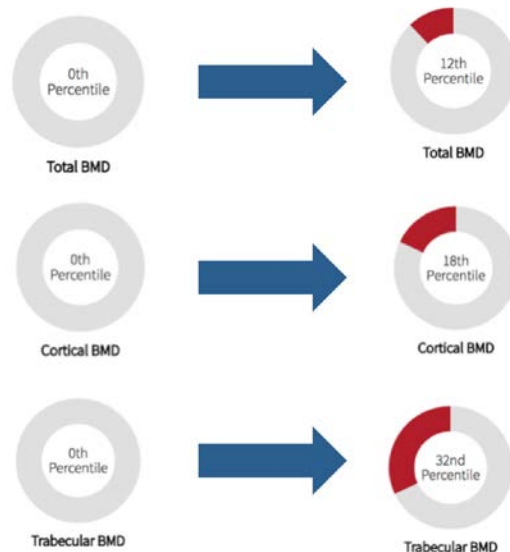


Figure 1. Range of bone densitometry measurements of HPP patients. Percentile calculation was sex- and age-specific.

Large Pores within the Cortical Bone of the Tibia Reflect Stiffness and Strength of the Proximal Femur

Gianluca Iori^{*1}, Johannes Schneider¹, Andreas Reisinger^{2,3}, Frans Heyer^{4,5}, Laura Peralta⁶, Caroline Wyers^{4,5}, Melanie Gräsel⁷, Reinhard Barkmann⁷, Claus-C. Glüer⁷, J.P. van den Bergh^{4,5}, Dieter Pahr^{2,3}, Kay Raum¹

¹ Berlin-Brandenburg Center for Regenerative Therapies, Charité - Universitätsmedizin Berlin

²Institute for Lightweight Design and Structural Biomechanics, TU Wien

³Division Biomechanics, Karl Landsteiner University of Health Sciences

⁴Department of Internal Medicine, NUTRIM School of Nutrition and Translational Research in Metabolism, Maastricht University Medical Center

⁵Department of Internal Medicine, VieCuri Medical Center

⁶Sorbonne Universités, UPMC University Paris 06, INSERM UMR-S 1146, CNRS UMR 7371, Laboratoire d'Imagerie Biomédicale

⁷Sektion Biomedizinische Bildgebung, Klinik für Radiologie und Neuroradiologie, Universitätsklinikum Schleswig-Holstein, Campus Kiel, Christian-Albrechts-Universität

Introduction

To date, a large number of women at risk of fragility fracture is not diagnosed with osteoporosis (OP). Hip fracture is the most severe osteoporotic fracture, for patients and, due to costs, for society. Recent studies on cortical bone remodeling have linked the age induced uncoupling between bone resorption and formation with a progressive enlargement and coalescence of the pores. The cortical bone of the tibia has attracted the interest of researchers since structural modifications that are measurable in patients were associated with fragility fractures. We characterized *ex vivo* the microstructure of cortical bone from the tibia of 20 human donors as well as the mechanical competence of the proximal femur from the same leg. Our aim was to identify architectural features in cortical bone reflecting an impairment of the femoral mechanical properties.

Methods

Cadaver legs (age: 69-94 years) were obtained in accordance with the German law. Proximal femur samples were scanned with Dual X-ray Absorptiometry (DXA) and High-Resolution peripheral Quantitative Computed Tomography (HR-pQCT). Finite element (FE) models were generated from HR-pQCT images and provided measures of the quasi-static femoral stiffness and strength. Femoral failure was simulated in standing conditions as well as during a fall to the side. The microstructure and density of tibial cortical bone were characterized with scanning acoustic microscopy (SAM) and microCT. Associations between the mechanical compe-

tence of the proximal femur and tibial cortical bone properties were investigated using uni- and multivariate linear regressions.

Results

The thickness of tibial cortical bone (Ct.Th) showed the strongest associations with the stiffness and strength of the proximal femur, followed by hip aBMD from DXA. Associations between tibial cortical porosity (Ct.Po) and the mechanics of the proximal femur were not significant. However, when only large (diameter > 100 μm) cortical pores were considered, their contribution to the total sample porosity (relCt.Po_{100 μm}) was associated with femoral stiffness and strength. Multivariate regressions suggested that relCt.Po_{100 μm} could help explain up to an additional 17% of the femoral stiffness and strength when added to aBMD.

Conclusions

Our data demonstrate that the thickness and prevalence of large pores within tibial cortical bone are relevant indicators of the stiffness and strength of the proximal femur.

(n=19)	STANDING		FALL	
	stiffness	strength	stiffness	strength
microCT				
Ct.Th [mm]	0.50	0.64*	0.63*	0.69*
vBMD _{DCort} [mgHA/cm ³]	0.69*	0.65*	ns	ns
SAM				
Ct.Th [mm]	0.67*	0.80**	0.75**	0.78**
Po.D [1/mm ²]	ns	ns	ns	ns
Po.D _{100μm} [1/mm ²]	-0.55	-0.58*	ns	ns
Po.Dm [mm]	ns	ns	ns	ns
SD(Po.Dm) [mm]	-0.56	-0.59*	ns	ns
Ct.Po [%]	ns	ns	ns	ns
relCt.Po _{100μm} [%]	-0.62*	-0.65*	-0.49	-0.51
DXA				
aBMD _{tot} [mgHA/cm ²]	0.54	0.69*	0.70**	0.74**
aBMD _{DCort} [mgHA/cm ²]	0.62*	0.74**	0.66*	0.78**

Pearson's coefficients are reported only for p-values < 0.05.

* p < 0.01; ** p < 0.001.

Table 1. Correlation of tibial structure and density with HR-pQCT based FE measurements of the proximal femur mechanical competence.

Fast and Accurate Estimation of Colles' Fracture Load Based on Homogenized Finite Element Analysis of Double HR-pQCT Sections

Denis E. Schenk^{*1}, Philippe K. Zysset¹

¹ Institute for Surgical Technology and Biomechanics, University of Bern

Introduction

Availability of high-resolution peripheral quantitative CT (HR-pQCT) scanners allows a detailed representation of trabecular bone structure at peripheral sites and its differentiation from the cortical phase. Homogenized finite element models (hFE) based on multiple section HR-pQCT reconstructions offer a fast bone strength prediction *in vivo*. We propose an accurate pre-processing pipeline including a new method for two phase material mapping in mixed elements and a fast fabric computation. Additionally, we developed a fast pipeline trimmed on minimizing prediction time.

Material and Methods

The accurate model is based on HR (61 μm) reconstructions and distinguishes cortical and trabecular bone phases with distinct material properties based on BMD distribution and bone orientation (fabric). Fabric tensors were evaluated using a fast implementation of the MSL method and homogenized by an image convolution filter. In contrast to similar models, material properties of mixed phase elements were assigned based on a new superposition method, respecting both material phases. In contrast, the fast model is based on LR (82 μm) reconstructions and a single isotropic bone phase. Estimated stiffness and ultimate load were compared to an existing experimental dataset [1] using linear

regression analysis.

Results

The non-linear hFE models achieved a coefficient of determination $R^2 = 0.877$ and $R^2 = 0.906$ for fast and accurate prediction of stiffness and $R^2 = 0.971$ and $R^2 = 0.973$ for estimation of bone strength respectively. There was no significant ($p > 0.001$) for bone strength.

Discussion and Perspectives

Both models showed high potential in the estimation of experimental fracture load. Evaluation time including scanning, reconstruction, image processing and hFE analysis still remains a challenge for clinical application, although image processing time for fast hFE was reduced to roughly one minute for double section measurements. To quantify reproducibility, we are now evaluating the distinct influence of machine and calibration errors using a human radius phantom. A currently ongoing clinical study (NODARATIS) aims at assessing clinical reproducibility of the procedures and defining a reference database for hFE-based bone strength of the young healthy Swiss population.

[1] Hosseini et al., Fast estimation of Colles' fracture load of the distal section of the radius by homogenized finite element analysis based on HR-pQCT, Bone 2017

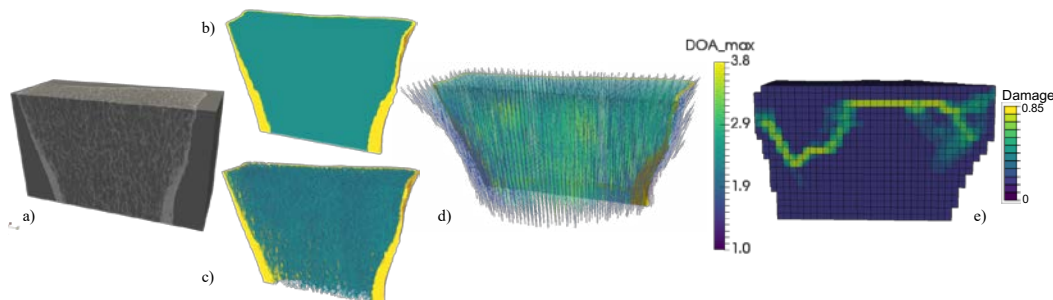


Figure 1. (a) HR-pQCT BMD reconstruction, (b) two phase masking, (c) segmentation, (d) fast MSL fabric degree of anisotropy, (e) hFE model - element damage

The Effects of Boundary Conditions and Microarchitecture on the Accuracy of QCT-based Finite Element Model

Yuanqiao Wu¹, Elise Morgan^{*1}

¹ Orthopaedic and Developmental Biomechanics Laboratory, Mechanical Engineering, Boston University

Introduction

Vertebral Fractures are the most common types of osteoporotic fracture. Finite Element (FE) models built from quantitative computed tomography (QCT) scans are increasingly used for non-invasive estimates of vertebral strength. However, the accuracy of these QCT-based FE models has not been fully established. Two key assumptions that are typically made in generating QCT-based FE models are that the net force borne by the vertebra is distributed uniformly over the vertebral endplate and that the local material properties of the trabecular bone and cortical-like shell can be estimated from local values of bone mineral density (BMD). These assumptions may not be appropriate for elderly vertebra, given the age-related changes in the mechanical behavior of the intervertebral disc and in the trabecular microarchitecture. The goal of this work was to use a novel method of quantitative failure visualization to assess the impact of these assumptions on the accuracy of QCT-based FE models of the vertebra. The failure visualization method uses time-lapse μ CT scans obtained during compression testing of the vertebra and a computer vision technique, digital volume correlation (DVC), to quantify the deformations that occur throughout the vertebral body under compression.

Method

27 L1 vertebrae with adjacent IVDs were obtained from fresh-frozen human spines (age: 80.5 ± 10.4 years; 14 males, 13 female).

Following QCT imaging ($0.31 \times 0.31 \times 0.625$ mm/voxel), the lumbar segments were loaded in axial compression, past yield point, and a μ CT scan ($37 \mu\text{m}/\text{voxel}$) was performed before every compression step. After coarsening to $1.24 \times 1.24 \times 1.25$ mm, the QCT voxels were converted into hexahedral finite elements. Elements were assigned material properties based on local BMD (QCT) or local values of volume fraction and fabric (μ CT). Boundary conditions were either uniform displacements across the endplates (“uniform”) or the displacements measured from DVC (“experimentally matched”).

Results

The assumption of uniform loading of the endplate diminished the accuracy of the FE predictions (14.55% vs. 76.81% error), whereas the choice of material properties had no effect (25.93% vs. 26.13% error; Figure 1). These results suggest that even for a relatively simply loading mode, the vertebral endplates are not loaded uniformly by the adjacent discs. Methods of obtaining more realistic endplate loading are likely to have profound effects on the accuracy of QCT-based vertebral FE models.

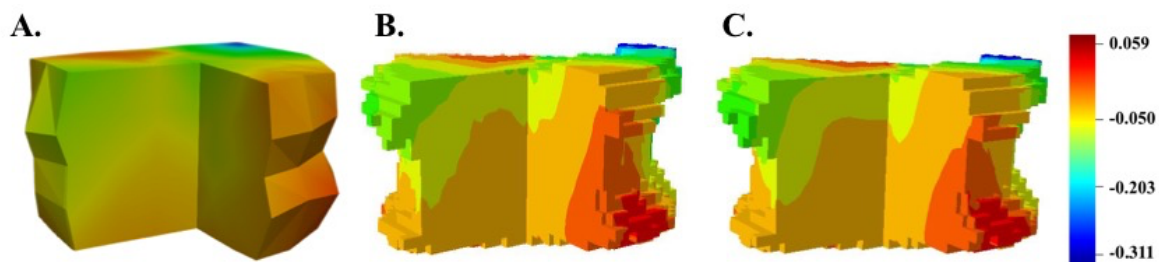


Figure 1. Axial Displacements for a representative specimen predicted from DVC (A); BMD-based (B); Fabric-based (C).

The Relevance of Bone Shape in Colles' Fracture using HR-pQCT

Julio Carballido-Gamio^{*1}, Sundeep Khosla², Andrew J. Burghardt³

¹ Department of Radiology, University of Colorado Denver, Anschutz Medical Campus

²Division of Endocrinology, Diabetes, Metabolism and Nutrition, Department of Internal Medicine, College of Medicine, Mayo Clinic

³Department of Radiology and Biomedical Imaging, University of California, San Francisco

Introduction

Since the introduction of HR-pQCT to the bone research field, a number of measures for bone density, geometry, architecture and biomechanics have been investigated for numerous clinical conditions. However, although femoral shape assessed by DXA and QCT has shown to improve hip fracture prediction, HR-pQCT has not been used to evaluate the relevance of bone shape to clinical outcomes. Here, we assess the discriminatory capabilities of the shape of the distal radius in an existing case-control study of recent Colles' fractures using HR-pQCT.(Melton-OsteoporosisInt-2010)

Methods

Bone shape was evaluated from HR-pQCT images of the unaffected radius in postmenopausal women with a recent Colles' fracture, and from the non-dominant radius of age-matched controls. Common anatomical landmarks were automatically identified on the periosteal surface of each scan to align all surfaces (anisotropic scaling) and generate a statistical shape model (SSM). Shape scores for the modes capturing 90% of the variance in the SSM were used with machine learning logistic lasso to simultaneously perform feature selection and fracture discrimination. The classification model was evaluated in terms of 1) its fracture discrimination capabilities independent of T-scores, and 2) its ability to improve fracture discrimination when added to a model based on T-scores. T-scores were defined as the minimum T-score from the total femur, femoral neck (FN) and lumbar spine. Assessments were done with areas under the receiver operating characteristic curve (AUCs), differences of AUCs (DeLong's method), and the integrated discrimination improvement (IDI) index. The impact of age, height and weight on these models was also evaluated. Validation of the full discrimination pipeline, including the

SSM, was performed with stratified 10-fold cross-validation. Discrimination was evaluated between controls (n=98) and fracture cases (n=84), and between non-osteoporotic controls (n=91) and non-osteoporotic fracture cases (n=67).

Results

Table 1 summarizes the results of this study showing that shape significantly improved the fracture discrimination of T-score models with both AUCs (trend in one non-osteoporotic model) and IDIs.

Conclusions

Melton et al. investigated the discriminatory capabilities for several HR-pQCT measures using multivariable models, demonstrating that FN-aBMD plus the structure model index yielded the highest AUC (0.71), although it was not significantly different from that of the FN-aBMD model (0.66). Here, we have shown that incorporating HR-pQCT-derived shape features to aBMD models significantly improved fracture discrimination ($0.724 < \text{AUCs} < 0.757$), demonstrating that bone shape might play a relevant role in the pathogenesis of forearm fractures, warranting its assessment in HR-pQCT studies of the distal radius.

Initial Features in the Model	AUC [95% CI]	AUC Difference [95% CI] (P Value)	IDI Index (P Value)
Controls (n=98) vs. Fracture Cases (n=84)			
T-scores	0.685 <i>[0.607, 0.763]</i>		
Shape scores	0.679 <i>[0.600, 0.757]</i>	-0.006 [-0.117, 0.106] (NS)	-0.051 (NS)
Shape scores + T-scores	0.746 <i>[0.673, 0.818]</i>	0.061 [0.022, 0.100] (<0.01)	0.045 (<0.001)
Non-osteoporotic Controls (n=91) vs. Non-osteoporotic Fracture Cases (n=67)			
T-scores	0.723 <i>[0.648, 0.798]</i>		
Shape scores + T-scores	0.638 <i>[0.557, 0.719]</i>	-0.085 [-0.188, 0.018] (NS)	-0.107 (<0.001)
Shape scores + T-scores + Age + Height + Weight	0.757 <i>[0.686, 0.828]</i>	0.034 [0.005, 0.064] (<0.05)	0.041 (<0.001)
Non-osteoporotic Controls (n=91) vs. Non-osteoporotic Fracture Cases (n=67)			
T-scores	0.673 <i>[0.587, 0.759]</i>		
Shape scores	0.639 <i>[0.551, 0.728]</i>	-0.034 [-0.161, 0.094] (NS)	-0.057 (NS)
Shape scores + T-scores	0.724 <i>[0.642, 0.806]</i>	0.051 [0.005, 0.097] (<0.05)	0.042 (<0.01)
T-scores + Age + Height + Weight	0.721 <i>[0.628, 0.794]</i>		
Shape scores + T-scores + Age + Height + Weight	0.622 <i>[0.533, 0.712]</i>	-0.089 [-0.204, 0.026] (NS)	-0.102 (<0.01)
Shape scores + T-scores + Age + Height + Weight	0.748 <i>[0.668, 0.827]</i>	0.036 [-0.001, 0.074] (0.056)	0.039 (<0.01)

NS=Non-significant. *Italic* fonts represent reference models. *11 initial shape scores at each 8-fold; with modes 1, 3 and 5 (Figure 1; among others) being consistently selected by lasso. T-scores, age, height and weight were forced to be part of the lasso models. Age, height and weight were not significantly different between groups.

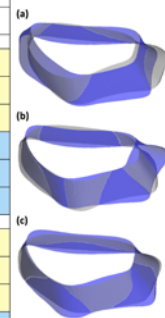


Figure 1. Mean shapes±3 standard deviations for the (a) 1st, (b) 3rd and (c) 5th principal modes, showing patterns of shape variation between controls and cases.

Figure 1.

Effect of Peak Stress and Stressed Volume on the Fatigue Life of Bovine Cortical Bone

Lindsay L. Loundagin^{*1,2}, W. Brent Edwards^{1,2}

¹ Human Performance Laboratory, Faculty of Kinesiology, University of Calgary

²McCaig Institute for Bone and Joint Health, Cumming School of Medicine, University of Calgary

Introduction

Fatigue fractures occur in both clinical (e.g., atypical femoral fracture) and athletic (e.g., stress fracture) populations. The fatigue life of bone, or the number of cycles to failure, for a given stress range can vary orders of magnitude (1). Our recent work suggests that intracortical microarchitecture is heavily associated with this variance (2). Canal microarchitecture may determine both the magnitude and volume of stress concentration – known mechanical determinants of fatigue strength – and the purpose of this study was to quantify their potential relationship with fatigue life.

Methods

Cortical bone samples were prepared from skeletally mature bovine tibiae and femora ($n = 10$). Samples were machined into a standardized ‘dog-bone’ geometry with a gauge length of 7 mm and diameter of 5.25 mm. Samples were imaged using a Scanco microCT 100 (Scanco Medical AG, Switzerland) at 5 μm resolution and then cyclically loaded in zero-compression at a stress range of 95MPa and frequency of 4.35Hz. Fatigue life was defined as the number of cycles until complete fracture. MicroCT images were coarsened to a 10 μm resolution and a central 2.5 mm region was converted to finite element (FE) models with linear hexahedral elements. Elements were assigned linear-elastic material properties with a modulus of 18GPa and Poisson’s ratio of 0.3. Models were loaded using boundary conditions consistent with experimentation and solved using FAIM (v8.0, Numerics88 Solutions Ltd, Canada). Peak stress was quantified as the 95th percentile von Mises stress measured from FE analysis. Stressed volume was quantified as the volume of elements experiencing a von Mises stress greater than yield. The rela-

tionship between logarithmic fatigue life and FE predicted peak stress and stressed volume were examined using Pearson correlation coefficients.

Results

Despite being loaded to the same apparent stress, fatigue life measurements ranged almost two orders of magnitude. Peak stress explained 62% of the variance in fatigue life ($r = 0.79$, $p = 0.007$), while stressed volume explained nearly 75% ($r = 0.87$, $p = 0.001$; Figure 1).

Conclusions

The findings from this study suggest that the fatigue life of cortical bone is not solely determined by the magnitude of the stress concentration associated with canal microarchitecture, but the size of the stress concentration may also play an important role. Microdamage within larger stress concentrations may grow and reach a critical size more rapidly, thereby decreasing fatigue life.

References

1. Taylor et al. (1999). *J Biomech.* 32(11):1199-12032. Loundagin et al. (2018). 8th World Congr. Biomech. O1178. <https://tinyurl.com/ybsdxxsbx>

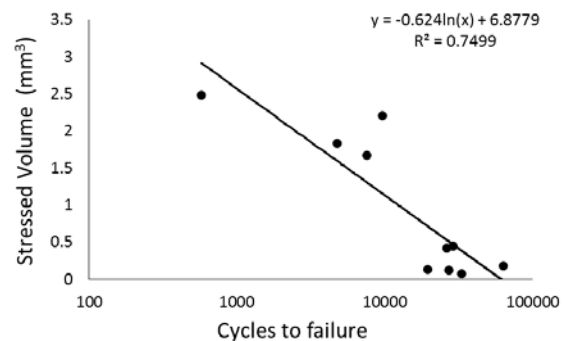


Figure 1. Relationship between stressed volume and number of cycles to failure (log scale).

A Phantom-less Calibration Technique for use in Femur Strength Prediction

Carla Winsor¹, Leticia Campello^{2,3}, Muhammed Qasim^{2,3}, Ju Zhang⁴, Xinshan Li^{2,3}, Corinne Henak¹, Perry Pickhardt⁵, Heidi-Lynn Ploeg*¹, Marco Viceconti^{6,7}

¹ Mechanical Engineering, University of Wisconsin

² Mechanical Engineering, University of Sheffield

³ INSIGNEO Institute for in silico medicine, University of Sheffield

⁴ Auckland Bioengineering Institute, University of Auckland

⁵ Radiology, University of Wisconsin

⁶ Department of Industrial Engineering, Alma Mater Studiorum, University of Bologna

⁷ Medical Technology Lab, IRCCS Rizzoli Orthopedic Institute, Bologna

Introduction

Quantitative computed tomography (CT) based patient-specific finite element models (FEM) have been proposed for improved osteoporotic hip fracture risk assessment. CT scans are usually calibrated by scanning a calibration phantom containing materials of known densities. This enables the estimation of bone density from CT attenuation. However, it is not a universal clinical practice to scan patients with an in-line phantom and not always possible to calibrate the CT scan using off-line phantom. CT calibration using patient's own tissues as the reference materials have been proposed as an alternative. The aim of this study, therefore, is to investigate use in FEM.

Materials and Methods

This study was conducted on a subset of 11 patients (5 controls and 6 fractures) from a larger cohort [1]. Bilateral proximal femur scans were performed on GE LightSpeed: 16, Pro 16, Ultra or VCT (120 kV, variable I). Phantom-less calibration was conducted. Internal Hounsfield Units (HU) to assumed CT-density relationships were obtained through linear regression of average HU against reference densities for skeletal muscle (1050 mg/cc) and adipose tissue (950 mg/cc) [2].

Two FE models were generated for each patient: FE_{phantom} , using phantom calibration results [3], and $FE_{\text{phantom-less}}$, using phantom-less calibration. Femur strength (FS) under side-fall was estimated following a well-validated pipeline [4]. The difference in the estimated force at fracture (N) using two calibration techniques was analysed.

Results

The Bland-Altman plot showed a mean difference bias of 0.05%, equivalent to 0.09 mg/cc, between the two calibration techniques indicat-

ing that phantom-less calibration is an acceptable clinical substitute for phantom-based calibration. Mean absolute error was 8%. One outlier demonstrated a larger variation due to higher HU in the adipose tissue. Estimated FS differed by 7% on average between the two calibration techniques (Fig. 1).

Discussion and Conclusions

This study showed the promising nature of phantom-less CT calibration using internal tissues as the reference materials. The difference observed in the Bland-Altman plot was small enough to be clinically equivalent with phantom-based methods. The differences in the estimated femur strength between the two calibration methods were within appropriate limits. Additional patients will be processed to further confirm this methodology.

References

- [1] Lee SJ et al. Am J of Roent. 209:2, 395-402. (2017). [2] Hubbell JH et al. NIST [Online] Available: <http://www.nist.gov/pml/x-ray-mass-attenuation-coefficients>. [2018, 02 16]. [3] Brown K. personal communication. [4] Qasim M. et al. Osteoporos Int. 27: 2815 (2016).

Acknowledgements

The Whitaker Foundation provided financial support.

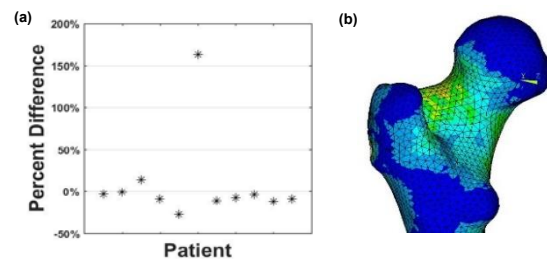


Figure 1. Left: Differences between $FS_{\text{phantom-less}}$ and FS_{phantom} . Right: representative FE model showing 1st principal strain (0-3000 microstrain).

QCT-Based Finite Element Estimation of Periprosthetic Fracture Sites

Johanna Baetz^{*1}, Finn Brose¹, Philipp Messer-Hannemann¹, Frank Lampe², Michael M Morlock¹, Graeme M Campbell¹

¹ Institute of Biomechanics, TUHH Hamburg University of Technology
²Department of Life Sciences, Hamburg University of Applied Sciences

Introduction

Periprosthetic fractures (PPF) are a major cause for revision (11.6%) in total hip arthroplasty (THA; 1). Uncemented prostheses are implanted in the bone with a press-fit fixation to improve implant longevity, but can cause fractures when exaggerated. In addition to bone quality, femoral shape is a predetermining and subject-specific factor for PPF risk (2). Insufficiently seated prostheses can lead to reduced primary stability and subsequent loosening (3).

The aim of this study was to estimate the subject-specific PPF location for different periprosthetic bone densities and femoral shapes using homogenized finite element (hFE) models to study possible causes of PPF and determine critical influencing factors.

Methods

THA with uncemented stems (Corail[®], Depuy Synthes, collarless) was performed on eight cadaveric femur pairs by an experienced surgeon. PPF were then introduced using a drop tower (Fig. 1a) that loaded the prostheses in the femoral axis with increasing drop heights until the fracture occurred. Quantitative computer tomography scans (QCT, isotropic voxel length: 0.5 mm) were performed initially, after broaching, implantation and fracture. Three femora of characteristic shapes (Dorr types A, B and C) were selected for the hFE models. QCT scans after broaching were converted in quadratic tetrahedral element meshes with bone mineral density-based stiffness (Avizo, Bone-

mat). Identical meshes were mapped on initial QCT scans to model periprosthetic stiffness of non-densified bone. Implants were inserted path-based to the final position determined from the QCT scans after implantation (Abaqus). This simulated the subject-specific press-fit. Computed stress maps were compared to fracture sites determined in the QCT scans after fracture.

Results

Computed sites of increased stresses match the fracture sites (Fig. 1b). Stresses are highest for the Dorr type C femur, which showed the highest fracture risk in the tests. Higher periprosthetic bone stiffness tended to increase resulting maximal stresses.

Discussion

The model was shown to be suitable for the prediction of later fracture sites by simulating the press-fit at the implanted position before fracture occurred. Periprosthetic bone densification might increase PPF risk. In further studies, the models will be used to compare subject-specific press-fit to a line-to-line implantation simulation. In the next step micromotion caused by joint forces will be analysed to compare primary stability of implanted collared and collarless prostheses for different femoral shapes and periprosthetic bone densities. The study has been financially supported by DePuy Synthes.

[1] EPRD 2017 [2] Bonnin et al. 2015, BJJ 97B [3] Abdul-Kadir et al. 2008, J Biomech 41

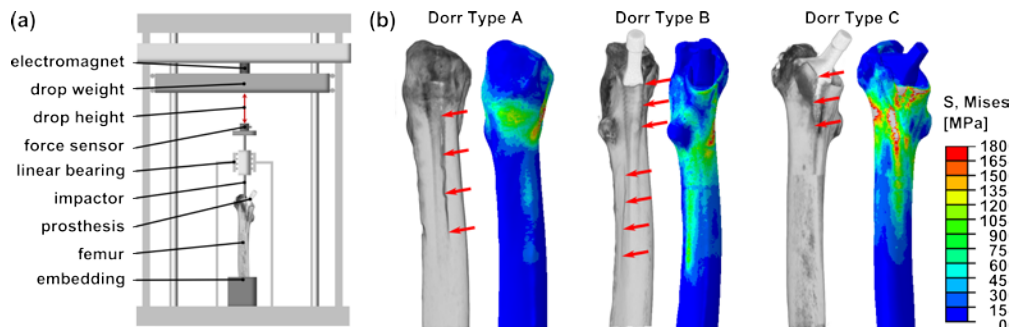


Figure 1. (a) Drop tower setup (b) QCT scans of fractured femora with corresponding simulated stress maps for Dorr types A, B and C.

Internal BMD Calibration does not Correct for Table Height Dependent X-Ray Field Inhomogeneity Effects

Eva Hufnagel¹, Peter Dankerl², Klaus Engelke^{*1}

¹ University of Erlangen, Inst of Med Physics

²Dept of Radiology, University Hospital, University of Erlangen

Introduction

Opportunistic screening is a promising approach to use existing CT scans from clinical routine to determine BMD for an assessment of osteoporosis. Clinical CT scans do not contain a calibration phantom (simultaneous calibration, SC), which is used to convert the measured CT to BMD values. One alternative is internal calibration (IC). Recent studies indicated a high correlation between IC and SC.

Methods

68 CT spine scans obtained for QCT trials of osteoporosis including a Mindways phantom (Siemens Sensation 64, GE BrightSpeed S, TOSHIBA Aquilion) and 53 CT scans from clinical routine that for the purpose of this study included a Siemens Osteo phantom (Siemens Definition AS and AS+) were used. Slope and intercept were obtained by linear regressions using known SC slope and intercept as dependent and HU values of VOIs positioned in the aorta and air as independent parameters. Second, the SC of one arbitrarily selected scan was used for all other scans of the same scanner. Third, the effect of table height on SC and IC was compared in the scans from clinical routine. SC was carried out with and without a table height specific field inhomogeneity correction (THC). Table height varied up to 10 cm from 'standard' values recommended for QCT.

Results

Scans from clinical trials: 1. The table shows that several linear regressions to determine IC slope and intercept were not significant. Nevertheless, % BMD difference between SC and IC assuming CT values of 50, 100 and 200 HU were small (Δ BMD SC-IC). 2. However, differences were similar when using the SC of one scan for calibration of all other scans (Δ BMD SC-SC). 3. Scans from clinical routine: SC differences in BMD between THC and non THC increased with differences in table height. Average BMD differences for the two scanners were 5.4% and 11.3%, respectively. Internal calibration resulted in BMD differences of 3.3% and 8.4% relative to SC with THC, i.e. IC did not compensate for table height related field inhomogeneity differences as expected.

Conclusion

IC worked well in scans obtained from highly standardized acquisition and reconstruction protocols. The three scanners included in the investigation were stable over time, a single calibration from one patient applied to all other patients gave the same result. Thus the validity of IC cannot be proven in such data. IC using air and aorta did not compensate for field inhomogeneities, which would require a table height specific IC.

scanner	slope		intercept		Δ BMD SC-IC [%]			Δ BMD SC-SC [%]		
	R ²	p	R ²	p	50 HU	100 HU	200 HU	50HU	100HU	200HU
Siemens Sensation 64	0.039	0.215	0.155	0.033*	1.77	1.01	0.71	1.07	0.62	0.41
GE BrightSpeed S	0.414	0.009**	-0.026	0.471	2.20	1.11	0.64	0.89	0.65	0.55
Tochiba Aquilion	0.533	0.001**	0.197	0.068	0.99	0.55	0.42	0.51	0.41	0.46

Table 1.

Standardization of Bone Mineral Density and Microstructure for Spinal High Resolution Quantitative Computed Tomography in a Multicenter Setting

Jaime A. Peña^{*1}, Timo Damm¹, Stefan Reinhold², Reinhard Barkmann¹, Claus-C. Glüer¹

¹ Biomedical Imaging Section, University Clinic Schleswig-Holstein, Kiel.

²Multimedia Information Processing Group. Computer Science Institute. University of Kiel.

Introduction

During clinical trials in osteoporosis different CT-scanners are often used. High Resolution Quantitative Computed Tomography (HR-QCT) allows trabecular separation (Tb.Sp) assessments in vertebral spongiosa to measure bone microstructure. However, it is not clear whether data from different CT-scanners can be pooled to achieve standardization for Tb.Sp. Here, we have examined the usage of a set of embedded human vertebrae for cross-calibration of densitometric and microstructural HR-QCT based measurements.

Materials & Methods

Six human vertebral bodies were defatted, embedded in epoxy-resin and scanned inside an abdomen phantom in 12 centers with CT-scanners from different vendors (typical settings range: 110-120kVp; 345-355mAs; voxel-size: 0.156-0.188 mm and 0.25-0.3 mm in-plane and in the z-axis, respectively). CT-images were density calibrated by means of a calibration phantom (QRM, Germany). “Pacman” volumes of interest in the spongiosa were drawn and co-registered from a reference center (RefCenter) to all other centers (StructuralInsight, in-house software). For Tb.Sp, two methods for image-binarization were employed. Tb.Sp^{FT}: Fixed threshold setting ($t = 300 \text{ mg/cm}^3$). Tb.Sp^{AT}: Adapted threshold with fixed bone volume fraction (BV/TV) for each scanner to yield

an average BV/TV of 0.21 across all six vertebrae, as obtained previously on an XtremeCT device (Scanco Medical, Switzerland). Pearson R correlation coefficients for each center’s data compared to RefCenter were calculated and Bland-Altman (Mean and linear Fit) analyses were performed to estimate residual errors.

Results

Median (min, max) BMD values of the RefCenter were 174.4 (140.3, 210.5) mg/cm^3 . For Tb.Sp^{FT} and Tb.Sp^{AT} these values were 1.055 (0.916, 1.369) mm and 1.33 (1.1, 1.88) mm, respectively. Strong correlations for BMD (Median $R=0.996$) and Tb.Sp (Median $R=0.973$ and $R=0.969$, for Tb.Sp^{FT} and Tb.Sp^{AT}, respectively) were observed. Table 1 shows the results of the Bland-Altman analysis for BMD and Tb.Sp.

Conclusions

With Tb.Sp^{AT} the residual error of Tb.Sp across all centers could be drastically reduced. The mean Offset was reduced by 49.7%; the RMSE[SD] and RMSE[linear Fit] were reduced by 73.5% and 56.8% (down to 180 μm), respectively. These data document the feasibility of HR-QCT based standardization of Tb.Sp in a multicenter setting. For in vivo scenarios additional errors need to be considered to test whether spinal Tb.Sp provides insight beyond BMD in assessing treatment effects.

	BMD [mg/cm^3]	Tb.Sp ^{FT} [mm]	Tb.Sp ^{AT} [mm]
Offset ⁽¹⁾	-5.24 (-21.96, 6.24)	0.994 (0.067, 3.739)	0.50 (0.08, 0.93)
RMSE [SD] ⁽²⁾	3.51	1.66	0.44
RMSE [linear fit] ⁽²⁾	3.31	0.42	0.18
R ² [linear fit] ⁽¹⁾	0.21 (0.01, 0.44)	0.884 (0.001, 0.969)	0.79 (0.018, 0.91)
N [linear fit] ⁽³⁾	0	8	6

⁽¹⁾Median (min, max). ⁽²⁾RMSE average of all centers. ⁽³⁾Number of centers with significant slope ($p<0.05$).

Table 1. Bland-Altman analysis of BMD and Tb.Sp across different scanner types compared to a reference center (RefCenter).

Establishing a Population-Based Cohort from Opportunistic CT Assessment from Large Clinical Databases

Andrew S Michalski^{1,2,3}, Bryce A Besler^{1,2,3}, Steven K Boyd^{1,2}

¹ Department of Radiology, Cumming School of Medicine, University of Calgary

²McCaig Institute for Bone and Joint Health, University of Calgary

³Biomedical Engineering Graduate Program, University of Calgary

Introduction

Computed tomography (CT) has the potential to opportunistically assess hip skeletal health by secondary analysis of bone mineral density (BMD) and finite element (FE) predicted bone strength. Abdominal/pelvic CT images are ideal candidates for retrospective opportunistic screening for osteoporosis (Figure). However, there is little evidence supporting the use of these clinical scans for hip health assessment, and there is a need to establish image selection parameters to produce reproducible results. We are replicating the clinical imaging protocol in a research setting to assess density calibration techniques for quantitative skeletal health assessment and using these data, establish an acceptance criterion to accurately determine FE estimated hip strength. These findings will serve as a basis to establish a large population-based cohort from existing clinical databases.

Methods

Ten participants were imaged using a clinical abdominal/pelvis protocol on a research dedicated clinical CT scanner (Revolution CT, GE Healthcare, Waukesha, WI). Density calibration was performed using both an in-scan density calibration phantom and an internal density calibration technique. Skeletal health assessment included integral BMD and FE estimated hip strength from a sideways fall loading configuration. Additionally, ten full-body cadavers were imaged using CT and phantom-based density calibration to generate proximal femur FE models. FE models were cropped at 5 mm intervals over a 60 mm region, centered about the distal end of the lesser trochanter. Failure load was measured for each cropped FE model. Relative differences were calculated from the model at length = 0 mm. Least significant change in force (36N, LSC) determined from unpublished data defined an acceptance criterion.

Results

From the abdominal/pelvic CT scans, internal density calibration underestimated phantom-based calibration for both BMD (mean bias = 15 mg/cc, 5.2%) and FE estimated hip strength (mean bias = 106 N, 8.1%). Cropped finite element models at length = -20 mm had a mean difference of 23.8N (4.7%) from the reference length = 0 mm. Models with cropped lengths -20 mm to +30 mm consistently were less than the LSC, suggesting a range of acceptable images for clinical interpretation of estimated hip strength.

Conclusions

These data provide bounds on the use of CT opportunistic assessment of hip skeletal health. Based on our acceptance criterion, large numbers (approximately 80%) of clinically acquired abdominal/pelvic CT scans are suitable for retrospective assessment. This provides an opportunity to establish a normative database, and to identify individuals for subsequent osteoporosis examination to prevent low trauma osteoporotic fracture.



Figure 1. Reference volume rendering from an abdominal/pelvic CT imaging protocol used to establish a population-based cohort.

X-Ray Scattering is Limited in Cone-Beam Computed Tomography of Extremities

Karen Mys^{*1,2}, Guozhi Zhang³, Filip Stockmans⁴, Caroline E. Wyers^{5,6}, Joop P.W. van den Bergh^{5,6,7}, G. Harry van Lenthe¹

¹ KU Leuven, Biomechanics Section, Belgium

²AO Research Institute Davos, Biomedical Development, Switzerland

³Department of Radiology, University Hospitals Leuven, Belgium

⁴KU Leuven (Kortrijk), Development and Regeneration, Belgium

⁵Department of Internal Medicine, VieCuri Medical Center, the Netherlands

⁶NUTRIM School for Nutrition and Translational Research in Metabolism, Maastricht University, the Netherlands

⁷Department of Internal Medicine, Subdivision of Rheumatology, Maastricht University Medical Centre, the Netherlands

Introduction

Cone-beam computed tomography (CBCT) seems an attractive imaging tool to visualize and quantify the bone microstructural parameters and to use for micro finite element simulations. In a previous study [1], we have shown that enhanced CBCT-images can be used to quantify bone microstructural parameters adequately. Yet, CBCT is considered to induce artefacts that reduce image contrast and hamper quantitative structural analyses. Scattering within the projection image is often seen as the main challenge of CBCT-imaging. Another important artefact is beam hardening. Therefore, the aim of this study was to quantify the amount of scattering as well as the amount of beam hardening for CBCT imaging of extremities.

Materials & methods

One trapezium bone was scanned with a microCT-scanner (Bruker, Belgium) and one entire wrist with high-resolution peripheral quantitative computed tomography (XTremeCT-II, Scanco, Switzerland). The scattering as well as the beam hardening was calculated on those scans. Scattering was quantified with the MonteCarlo software EGSnrc and the beam hardening with in-house developed C++ software. Quantification of those artefacts was performed by observing the change in gray value through the bone. To quantify size effects, the trapezium bone was magnified with a factor ranging from 1 to 5.

Results

For the wrist, the simulated beam hardening was around 35% and the maximum scattering simulated in the projection data is around 6%. Beam hardening on a single trapezium

was 40%, and increased to 50% when the bone was magnified five times. The scattered signal was significantly lower and contributed to around 14% of the gray value of the 3D image for a bone magnified five times (Fig. 1). Scattering increased exponentially with the size of the bone, whereas beam hardening stayed rather constant.

Conclusion

When scanning extremities, the scattering is limited, and it is more important to correct the beam hardening adequately instead of the scattering.

References

[1] Mys et al, Bone 114: 206-2014, 2018

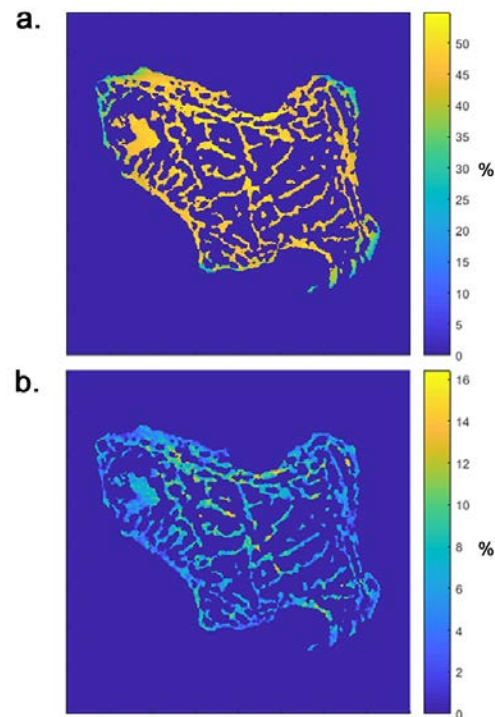


Figure 1. (a) beam hardening, (b) scattering on a trapezium bone scaled with a factor 5

Workshop Quantitative Imaging in Inflammatory Arthritis

Stephanie Finzel¹, Klaus Engelke², Kathryn S Stok³, Andrew J Burghardt⁴, Sarah L Manske⁵

¹ Department of Rheumatology and Clinical Immunology, Medical Center University of Freiburg, Faculty of Medicine, University of Freiburg

²Institute of Medical Physics, University of Erlangen

³Department of Biomedical Engineering, University of Melbourne

⁴Musculoskeletal Quantitative Imaging Research Group, Department of Radiology & Biomedical Imaging, University of California

⁵Department of Radiology, McCaig Institute for Bone and Joint Health, Cumming School of Medicine, University of Calgary

Inflammatory arthritis are diseases characterized by inflammation of the joints and other tissues. Rheumatoid arthritis, the most common form of inflammatory arthritis, is a chronic autoimmune condition targeting the synovium of the small joints of the hands, wrists and feet. Imaging plays an important role in inflammatory arthritis assessment, including evaluating disease onset and progression, as well as treatment effectiveness. As inflammatory arthritis affects the bones as well as soft tissues of the joint, different imaging modalities can inform different aspects of the disease. The workshop will discuss imaging modalities relevant to assessing inflammatory arthritis as well as quantitative analyses and semi-quantitative scoring systems. While outcome measures based on conventional radiography, ultrasound and MRI have traditionally relied on semi-quantitative scoring systems, HR-pQCT utilizes quantitative outcomes calculated based on operator-dependent and independent algorithms. Dr. Stephanie Finzel will present recent work comparing bone erosion detection with ultrasound and high-resolution peripheral quantitative computed tomography (HR-pQCT).

Dr. Jacob Jaremko will present an overview of imaging in inflammatory arthritis with MRI. Dr. Kathryn Stok, on behalf of the Study group for xtrEme Computed Tomography in Rheumatoid Arthritis (SPECTRA) will present recent progress towards a harmonized algorithm for joint space width assessment using HR-pQCT. Finally, a group discussion will focus on developing strategies methods to validate and approve new algorithms for quantifying outcomes in inflammatory arthritis.

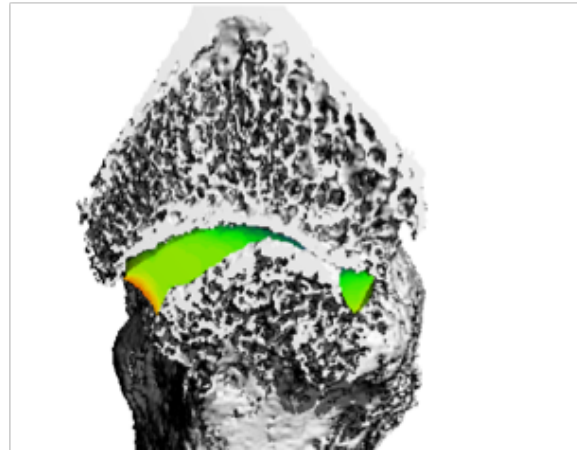


Figure 1. Distance transform of joint space width

Quantifying Femoral- and Tibial-Subchondral Bone and Microvessel Changes in Rats with Surgically-Induced Osteoarthritis using Dual-Energy Micro-Computed Tomography

Justin J. Tse^{*1,2}, Vasek Pitelka^{2,3}, Joy Dunmore-Buyze^{1,2}, Maria Drangova^{1,2,4}, David W. Holdsworth^{1,2,4,5}

¹ Robarts Research Institute

² University of Western Ontario

³ Department of Physiology and Pharmacology

⁴ Department of Medical Biophysics

⁵ Department of Surgery

Introduction

The degeneration of osteoarthritis(OA)-associated bone and cartilage, is hypothesized to result from changes in the joints' microvascular environment. The nutritional supply of cartilage, an avascular tissue, from the underlying subchondral bone microvessels is poorly understood. These microvessels has been difficult to study due to their small size (< 10 μm), lack of contrast against surrounding tissues, and proximity to dense bone. Combining an ex vivo Er-based vascular perfusion contrast agent and optimized dual-energy micro-CT (DECT)1 with a surgical hindlimb model of OA, we investigated the vascularized bony regions underlying the cartilage of the knee joint (i.e. distal femoral and proximal tibial epiphysis) during the initiation and progression of OA.

Methods

Sprague Dawley rats (N=54) were separated into sham and surgery-induced OA (i.e. anterior cruciate ligament transection (ACLX) and partial medial meniscectomy (PMM)) groups. Rats were further divided into 0, 1, 2, 4, and 8-weeks post-surgery time-points. At end-point, rats were perfused with an Er-based contrast agent, DECT-scanned, and decomposed into segmented and quantitative volumes of soft tissue, bone, and microvessels. Means values from the distal femoral and proximal tibial epiphysis from each hindlimb and each decomposed volume were recorded. Statistical analysis was performed, and significance achieved if $p < 0.05$.

Results

DECT decompositions of perfused rat hindlimbs (Fig. 1) revealed a significant increase ($p=0.0472$) in microvessel density 1-week post-operatively within the tibia of the operated ACLX +PMM hindlimb when

compared to the non-operated hindlimb. No significant microvessel differences were observed for the remaining time-points. No significant differences in soft tissue or bone, between the ipsilateral and contralateral hindlimb within either surgery group were observed at any time-point.

Discussion

The 1-week post-operative vascularity increase was due to an inflammatory response to the OA surgery; as 2-weeks post-operative results displayed baseline levels. The combination of an Er-based contrast agent, DECT, and ACLX+PMM model of OA, provided segmented and quantitative soft tissue, subchondral bone, and microvessel results within the distal femoral and proximal tibial epiphysis. The ability to automatically segment tissues could facilitate the study of other vascular-related disease (i.e. musculoskeletal, cardiac, neurological, and oncological).

1. J. J. Tse, J. Dunmore-Buyze, M. Drangova, D. W. Holdsworth, Dual-Energy Computed Tomography for a Gantry-Based Pre-Clinical Cone Beam Micro-CT Scanner. Journal of Medical Imaging, DOI: 10.1117/1.JMI.5.3.033503 (2018)

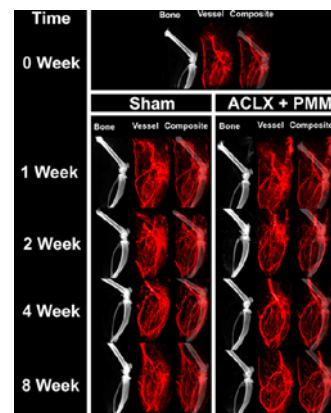


Figure 1. Representation of DECT decomposition results

Optiray350 and Iomeron350 as alternatives for contrast-enhanced micro-computed tomography of cartilage

Colet E.M. ter Voert¹, R.Y. Nigel Kour¹, Bente van Teeffelen¹, Kathryn S. Stok^{*1}

¹ Department of Biomedical Engineering, The University of Melbourne

Aim

Non-ionic, low-osmolar contrast mediums, such as Optiray350 and Iomeron350, are associated with reduced risks of adverse reactions and toxic effects in comparison to alternative contrast agents such as Hexabrix, which has been recently discontinued by the FDA. For Optiray and Iomeron, this study aims to provide an optimal methodology for the visualisation of articular cartilage in small animal joints through contrast-enhanced microCT, as well as assess detectability of glycosaminoglycan (GAG) content; thereby furthering insight into their preclinical properties in relation to contemporary alternatives.

Methods

Twenty-four mouse femurs were immersed in contrast agent-PBS solutions with agent concentrations ranging from 20% - 50% for cumulative periods of time starting at 5 minutes. Samples were scanned *ex vivo* using microCT. For each sample, regions of articular cartilage were manually contoured to calculate mean CECT attenuation at each time-point and concentration. Additionally, 5 mm plugs of bovine femoral cartilage were digested in Chondroitinase ABC to produce a measured spectrum of glycosaminoglycan content, immersed in contrast agent, and scanned using microCT. Correlations between mean CECT attenuation and GAG content was assessed.

Results

For both contrast agents, a 30% contrast agent concentration produced a mean CECT attenuation optimally distinct from both bone and background signal, whilst 5-minute and 10-minute immersion times were sufficient for equilibration of contrast agent absorption for Optiray and Iomeron, respectively. No significant correlation was found between CECT attenuation and GAG content for both contrast agents.

Conclusions

Optiray350 and Iomeron350 are capable of enabling high-resolution morphological assessment of articular cartilage in small animals using microCT under optimised conditions, whilst mitigating the health risks of ionic and high-osmolar contrast mediums. However, unlike Hexabrix, both Optiray and Iomeron are unable to detect loss of GAG content.

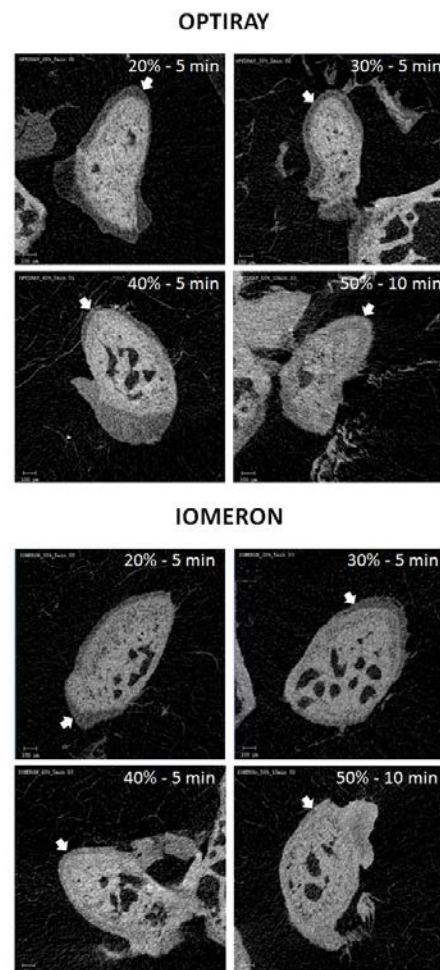


Figure 1. User definition of cartilage volumes for (a) 20%, 30%, 40% and 50% Optiray, and (b) 20%, 30%, 40% and 50% Iomeron.

Why Every Hospital Should Have a Micro-CT: 3D X-Ray Histology, Let'S Go Beyond Standard 2D Histology

Philipp Schneider^{*1}, Orestis Katsamenis², Gareth Thomas³, Anton Page⁴, Simon Cox⁵, Ian Sinclair⁶, Peter Lackie⁷

¹ Bioengineering Science Research Group, Faculty of Engineering and Physical Sciences, University of Southampton

² μ -VIS X-ray Imaging Centre, University of Southampton

³Cancer Sciences Unit, Faculty of Medicine, University of Southampton

⁴Biomedical Imaging Unit, University of Southampton

⁵Aeronautics, Astronautics and Computational Engineering, Faculty of Engineering and Physical Sciences, University of Southampton

⁶Engineering Materials, Faculty of Engineering and Physical Sciences, University of Southampton

⁷Clinical and Experimental Sciences, Faculty of Medicine, University of Southampton

Living structures are an intricate three-dimensional (3D) arrangement of cells and tissue matrix across many length scales. Contemporary capabilities to quantify tissue architecture, connectivity and cell relationships are however fundamentally constrained by a lack of 3D analytical platforms with appropriate resolution, penetration, structural differentiation, consistency, volumetric analysis capability and sample throughput. Structural analysis of tissues, whether for research or diagnostic purposes, remains overwhelmingly bounded and constrained by microscopic examination of relatively sparse 2D tissue sections, providing only a snapshot from which 3D spatial relationships can only be inferred. Therefore, whilst 3D medical imaging is commonplace, microscopic tissue structure analysis (i.e., histology) remains overwhelmingly wedded to 200-year-old practices of microscopic 2D examination of tissue sections.

We have demonstrated previously that X-ray imaging by micro-computed tomography (μ CT) allows non-invasive 3D imaging of the microstructure of standard tissue biopsies¹. This yields details comparable to two-dimensional (2D) optical microscope sections but for the whole tissue volume, which can for example overturn misconceptions of disease development based on 2D assessment. One exemplar is the pathogenesis of idiopathic pulmonary fibrosis², where 3D structural insight into co-localisation of tissue features and dysmorphia within substantive tissue volumes suggested previously unrecognised fibroblast foci plasticity.

Based on this encouraging μ CT results for soft tissues, in collaboration with an industrial partner, we developed a custom-design and soft-tissue optimised μ CT scanner (Wellcome Trust Pathfinder Award, 2016-17). Currently, we are establishing the foundations for routine 3D X-ray histology (Wellcome Trust Biomedical Resource and Technology Development, 2019-2022), including new X-ray equipment and standardised & automated workflows, where sample throughput will be increased and scan times reduced, providing the foundations for day-to-day 3D X-ray histology.

Applicable to vast existing sample archives and a wide range of soft tissue types including musculoskeletal tissues, the technology will open new research areas, such as large-scale 3D histological phenotyping (i.e., histomics). Furthermore, 3D X-ray histology can translate directly into next-generation clinical image-based diagnostics and patient stratification using artificial intelligence and deep learning, and time-critical intraoperative 3D examination of tissue biopsies will become a realistic future target in this research programme.

Here, we will present first results of our 3D X-ray histology approach and portray a vision, how high-throughput and non-destructive 3D histological assessment can offer new opportunities in basic biomedical and translational research, following our ambition to provide a day-to-day imaging tool that complements and augments standard 2D histology.

¹Scott et al. 2015, <http://dx.doi.org/10.1371/journal.pone.0126230>

²Jones et al. 2016, <http://dx.doi.org/10.1172/jci.insight.86375>

Evaluation of Bone Microstructural of Distal Radius and Distal Tibia on Human Objects using Phase-Contrast Synchrotron Radiation Computed Tomography

Ali Ghasem-Zadeh*¹, Rachel A Davey², Michele V Clarke², Cat Shore-Lorenti³, Simon S Murray⁴, Duncan Butler⁵, Chris Hall⁵, Peter Ebeling³, Jeffrey D Zajac², Ego Seeman¹

¹ Departments of Endocrinology and Medicine, Austin Health, University of Melbourne

²Department of Medicine, Austin Health, University of Melbourne

³Department of Medicine, School of Clinical Sciences at Monash Health, Monash University, Clayton

⁴Department of Anatomy and Neuroscience, University of Melbourne

⁵Australian Synchrotron Radiation, Clayton

Introduction

There are challenges in accurately determining cortical porosity using High Resolution peripheral Quantitative Computed Tomography (HR-pQCT) due to issues in image resolution, segmentation, beam hardening associated with poly-energetic photons and blurred interface edges produced by larger point spread function. These issues are critical because porosity reduces bending strength disproportionate to the bone loss producing it so that errors in quantification underestimate fracture risk and fail to identify persons at risk of fragility fracture (Zebaze et al 2010).

During radiation transmission of x-ray photons, regardless of the attenuation, photons undergo small phase shifts, which can be converted into changes in amplitude, and observed as in images with different contrast. Australian Synchrotron Radiation provides computed tomographic images, 9.6-micron voxel size, using monochromatic and parallel x-ray photons. We hypothesised that HR-pQCT images used to measure cortical porosity produced by Haversian canal cross-sections and small pores produced by osteocytic lacunae would be quantifiable despite the relatively lower resolution of the HR-

pQCT images. We compared the bone microstructural indices using Synchrotron Radiation photon attenuation and phase contrast-based computed tomography images versus images obtained using HR-pQCT.

Methods

Thirty-two post-mortem human radii and tibiae, fresh and dry specimens, were imaged at the Australian Synchrotron Radiation-Imaging and Medical Beamline (IMBL), using 60kV monochromatic x-ray based tomography. Silicon amorphous detectors with voxel sizes of 9.6 and 14.6 microns have been used to create x-ray photons attenuation and phase-contrast based tomographic images.

Results

Preliminary comparison of axial images has shown higher visibility for small pores and Haversian canals in the phase contrast-based images.

Conclusion

We infer that accuracy of distal radial and distal tibial cortical porosity using HR-pQCT can be validated using synchrotron imaging as a referent gold standard. Further analyses are ongoing.

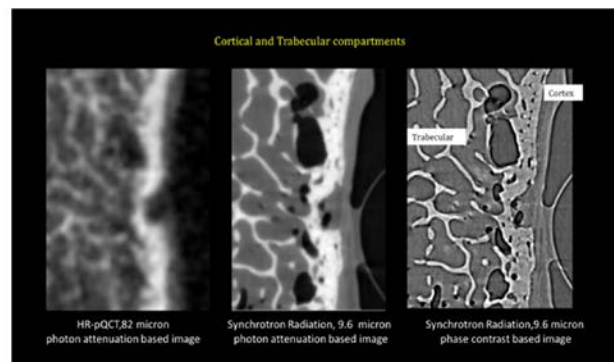


Figure 1. HR-pQCT vs SR and PR

Investigating Bone Microstructure using 3D Synchrotron Radiation Micro-Computed Tomography

Claire Acevedo*¹

¹ Fracture and Fatigue of Skeletal Tissues Lab, University of Utah

Introduction

The mechanical properties of bone tissues deteriorate with aging and bone fragility disease. Because bones have a hierarchical structure, with characteristic features from the nanometer to the micron level, it is necessary to analyze the contributions to bone quality and resistance to fracture at nearly each size-scale. Indeed, some of the most important fracture resistance qualities of bone occur at the micrometer length-scale. We investigate here how certain bone fragility diseases and treatment can increase the risk of bone fracture through their multiscale effects on bone quality.

Cortical bone's characteristic structure at the micron level consists of osteons and osteocyte cells embedded in the mineralized matrix. Using Synchrotron Radiation Micro-Tomography (SuRT), we can characterize these salient microstructural features and how they change with bone fragility.

Method

Synchrotron Radiation Micro-Tomography (SuRT) at the Advanced Light Sources (ALS at Lawrence Berkeley National Lab) was used to capture unparalleled 3D images of the bone microstructure. Human and murine cortical bones were examined for high-resolution imaging (1.3 μm voxel size) to identify microstructural changes associated with several bone fragility diseases such as osteonecrosis, osteogenesis imperfecta or glucocorticoid and bisphosphonate treatments. Samples were scanned in monochromatic mode at 20 keV at beamline 8.3.2 of the ALS to visualize and quantify 1) tissue mineral density, 2) microscale vascular porosity in the center of osteons, 3) osteocyte lacunar morphometry and 4) crack path. Data from scans will be reconstructed using commercial and custom software (Avizo, ImageJ).

Results

We found a significant increase in vascular porosity with age and osteogenesis imperfecta, but a reduction with bisphosphonate treatment. We also observed the osteons to play a prime role in fracture resistance during crack extension by twisting/deflecting the crack path along its anisotropic structure and by leaving uncracked regions in the crack wake (i.e., crack bridges) of healthy bones. In brittle bones, these mechanisms are challenged. In parallel, studies on Osteogenesis Imperfecta and Glucocorticoids have indicated a significant reduction in osteocyte lacunar size which in turn (Fig. 1), compromising bone mineralization and quality. Hallmark of hypermineralized regions has also shown to be a sign of brittle bones.

Therefore, SuRT allows us to understand how various biological factors change the bone's complex structure and thereby affect its resistance to fracture to induce bone fragility. These results also suggest that osteocytes play a central role in maintaining cortical bone matrix quality, organization and function.



Figure 1. Synchrotron X-ray micro-computed tomographic image of osteocyte network in trabecular bone.

Improving the study of bone diseases by correlative electron-, ion- and X-ray microscopy including their analytical techniques

Silke H Christiansen^{*1,2,3}, Lasse Kling^{1,3}, Leonid Mill^{3,5}, Anika Grüneboom⁵, George Sarau^{1,3}, Martin Herrmann⁴, Georg Schett⁴, Andreas Maier⁵

¹ Christiansen Research Group, Helmholtz Zentrum Berlin für Materialien und Energie

² Physics Department, Free University

³ Max Planck Institute for the Science of Light

⁴ Universitätsklinikum der Friedrich-Alexander-Universität Erlangen-Nürnberg, Med. 3

⁵ Friedrich-Alexander-Universität Erlangen-Nürnberg, Informatik 5

Introduction

In ageing societies all over the globe, the number of people suffering from bone disease, e.g. osteoporosis (OP) in the first place, has increased dramatically. OP considerably impairs patients' life quality, and results in high societal costs. However, current understanding of OP is still insufficient due to the lack of appropriate high resolution tools that permit a thorough analysis of scale bridging bone architectures from macro to nano with statistical significance to support the development of better treatments by drugs or surgical intervention. To revolutionize our knowledge of bone diseases based on an increase in understanding of the underlying bone anatomy, cutting-edge correlative high-resolution microscopy and spectroscopy together with advanced data analysis even including machine learning approaches permit reaching the next, so far unprecedented level of understanding.

Methods

Correlative workflows starting from X-ray microscopy (XRM) volume analysis, which is only since a few years possible outside of synchrotrons with voxel sizes of $< 1 \mu\text{m}$, over large scale scanning electron microscopy data acquisition, to dual beam microscope analysis (focused electron- and ion beams) permit the scale bridging investigation of bone architectures and thus merging the “big picture” and the underlying ultrastructure with statistical significance. In combination with additional analytical add-ons to these microscopes, physical properties such as optical, mechanical, compositional, structural etc. deliver a highly detailed correlative dataset of bone (cf. Figure 1. Right). The present paper demonstrates novel findings related to various partly age related bone diseases using advanced correlative data acquisition (cf. Figure 1, Right).

Results

Figure 1 (Left) shows the different bone fine structures, composed of trabecular-, vascular-, canalicular-networks as well as a three-dimensional arrangement of osteo-lacunae that host osteocytes, as obtained by volume analysis in a new generation of lab-based x-ray microscope (Zeiss XRM Versa 520). These fine structures can be assessed quantitatively with statistical significance and can be correlated with additional modalities as shown in Figure 2. Elucidating examples demonstrating the power of such an approach will be given^{1,2,3}. Figure 1 (Right) shows the correlative workflow from sample collection over sample preparation and the acquisition of various image modalities utilizing correlated data from electron-, ion-beam imaging and analytics, probes and focused laser light to study scale bridging bone architectures. We will demonstrate how these correlative workflows will permit to advance the current understanding of bone architectures and function substantially and will show some first systematic correlative microscopy and spectroscopy studies on mouse tibia and human bone^{1,2,3}.

Discussion

Based on our correlative analytics and the data availability, the advanced data interpretation using machine learning approaches will be discussed. Using this approach, all details of bone micro-/nano-architecture can be used to provide a novel clinical tool-set for future improved prediction of bone fractures e.g. hip fractures to occur in analyzed individuals. In addition, based on correlative bone architecture analysis, early detection of disease will be possible, much earlier than conventional bone mass assessing procedures do permit today.

¹ P. Milovanovic et al., Bone (2018). ² A. Grüneboom et al., Nature Metab. (2019). ³ P. Milovanovic et al., Small(2017).

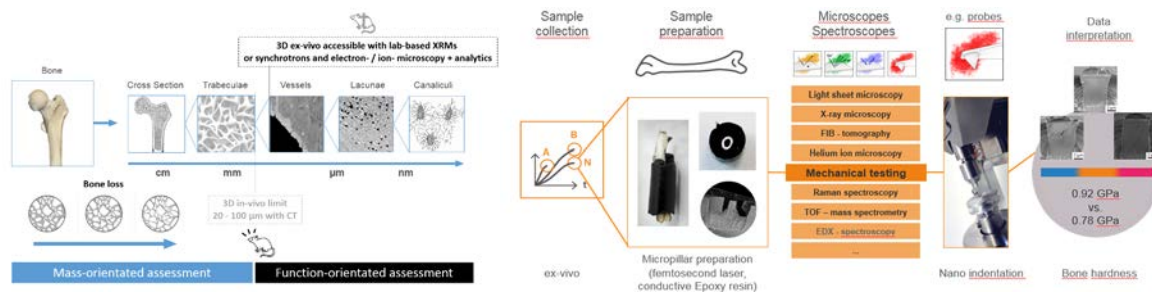


Figure 1. (Left) Bone anatomy with scale – bridging architecture. (Right) Correlative microscopy / spectroscopy workflow in bone research.

Comparison of In vivo Cortical Mikrostruktur and Porosity of Distal Tibia and Distal Radius HR-pQCT Measurements from Male and Females of all Ages by Osteoporosis, Rheumatoid Arthritis, Gonarthrosis, and Healthy as an Early Indicator of Bone Fracture Risk

Zully Ritter¹, Klaus Engelke*², Dieter Felsenberg³, Gabriele Armbrrecht¹

¹ Center for Muscle and Bone Research, Charité Universitätsmedizin Berlin

²Institute for Medical Physics, Friedrich Alexander University

³Center for Muscle and Bone Research, Universitätsmedizin Berlin

Introduction

Osteoporosis (O), Rheumatoid Arthritis (RA) and Gonarthrosis (GA) are the most frequent human bone diseases and responsible for bone fractures (O) as well as for immobility and pain (RA or GON). Their occurrence increases dramatically due to higher life expectancy and life-style changes and adiposity in young people. In vivo monitoring of bone microstructure and density using high-resolution peripheral computed tomography (HR-pQCT) is a reliable tool for evaluating bone quality. Detrimental changes at the cortical bone microstructure are an indubitable first indicator of fracture risk even before trabecular bone is damaged at least for the diseases compared in this study.

Methods

Microstructural bone parameters at the distal tibia and radius were quantified and compared after HR-pQCT measurements in 223 females and 263 males of different ages with aging osteoporosis, early osteoporosis, gonarthrosis and rheumatoid arthritis. Subsequently, 10 per group were matched by age (<60 YO mean 46YO; <60 mean 77 YO) and gender for each disease and their cortical thickness, porosity, density and pore diameter compared. The aim was to find out if there are specific differences for each diseases and if an age range exists in which the cortical microstructure starts to decline to judge group-specific fracture risk. Med-

ical drug treatments and training could be accordingly selected.

Results

As expected overall highest mean values of cortical porosity (CoPo) at the tibia (8%) compared with radius (3%) were found. It appears that until 50 YO the CoPo remains stable for both genders independent of location and bone disease. After that, CoPo increases about to 5% for tibia and 3% for radius. Highest CoPo values before 50 YO were caused due to early osteoporosis in the female group. Similar CoPo values were found for gonarthrose and aging osteoporosis. CoPo was below 2% for RA at the female radius in comparison with the other diseases but the pore diameter (PD) higher (18mm) as those measured for osteoporosis and gonarthrose. PD at the tibia was less than in radius (15 mm) but with higher variability. Cortical density is maintained with age in radius male and decreased in tibia for male and females after 50 YO.

Conclusion

Prevention for cortical bone deterioration should be initiated at age of 50 YO. Early osteoporosis triggers imply rapid increment of CoPo. It appears that for RA cortical trabecularization occurs in specific regions with locally higher pore diameters instead of uniformly distributed as for the other bone diseases.

The Association of Calcium Intake with Osteoporotic Vertebral Fractures and QCT Bone Mineral Density in a Large Chinese Cohort

Ling Wang^{*1}, Lu Yin², Xiaoguang Cheng¹, Kai Li¹, Wei Li², Wei Tian³

¹ Department of Radiology, Beijing Jishuitan Hospital

² Medical Research & Biometrics Center, National Center for Cardiovascular Disease

³ Department of Spine Surgery, Beijing Jishuitan Hospital

Introduction

Calcium is widely recognized as an effective intervention for the prevention of osteoporosis. However, some recent studies and meta-analyses indicate that calcium supplements may be ineffective to prevent fracture. The association of dietary calcium intake with vertebral fracture and spinal volumetric bone mineral density (vBMD) in low calcium intake population is unknown.

Methods

China Action on Spine and Hip Status (CASH) study is a multi-center, community-based cohort study of 3,457 participants from 12 centers across China from March 2013 and August 2017. We documented their baseline dietary calcium intake using validated food frequency questionnaires with a median of 10 years before the spine CT screening of CASH study. Vertebral fracture of CT images was defined as the primary outcome and the main measures included volumetric bone mineral density at participants' median of 10 years visit and dietary calcium intake at baseline. Odds ratio (OR) and 95% confidence interval (CI) were obtained for the associations of vertebral fracture with dietary calcium from logistic regression models. Because only 14.5% reached Chinese Dietary Reference Intakes (CDRI) calcium target of ≥ 800 mg/day, we selected 500, 600, 700, 800 mg/day of calcium

intake from food as cutpoints for modeling, respectively.

Results

Of the 3457 CASH participants, 3273 (94.7%) were used for analysis including 2052 women (mean [SD] age, 52.1 [9.0] years) and 1221 men (53.3 [9.1] years). Total vertebral fracture prevalence was 16.5% (n=551). The mean daily calcium intake from the FFQ was calculated as 517.0 ± 266.4 mg. 8% reduction of fracture risk was observed per 100 unit increase of calcium intake from food among females (OR, 0.92; 95% CI, 0.87-0.97), but results among males were not significant (OR, 0.98; 95% CI, 0.92-1.04). No interaction was detected between vBMD and calcium intake from food ($P > 0.05$). When high calcium intake groups had enough sample sizes (i.e. calcium ≥ 500 or ≥ 600 mg/day), negative associations of fracture risk with calcium intake were found among females (≥ 500 vs. < 500 mg/day: OR, 0.62; 95% CI, 0.47-0.80; ≥ 600 vs. < 600 mg/day: OR, 0.59; 95% CI, 0.44-0.79), but this trend as not shown when cutpoints of calcium intake were set as 700 or higher. The same regressions were performed for male participants, but no significance was found. A positive correlation of calcium intake and vBMD was observed for females ($P = 0.01$), but there was a non-significant negative trend for males ($P = 0.16$).

Computed Tomography - Based Texture Analysis Improves the Prediction of Incident Vertebral Fracture

Fjola Johannesdottir^{*1,2}, Brett Allaire¹, Dennis E. Anderson^{1,2}, Elizabeth J. Samelson^{2,3}, Douglas P. Kiel^{2,4,5}, Mary L. Bouxsein^{1,2}

¹ Center for Advanced Orthopaedic Studies, Beth Israel Deaconess Medical Center

²Harvard Medical School

³Institute for Aging Research, Hebrew Senior Life, Department of Medicine Beth Israel Deaconess Medical Center

⁴Institute for Aging Research, Hebrew Senior Life

⁵Department of Medicine Beth Israel Deaconess Medical Center

Introduction

Although vertebral fractures (VF) are common, the current clinical standard for VF fracture risk assessment, bone mineral density (BMD) by DXA, is inadequate. Less than half of adults who fracture have osteoporosis according to their BMD. The purpose of this study was to determine if co-occurrence textural features (Haralick 1973) from computed tomography (CT) images combined with BMD predict incident VF better than BMD alone.

Methods

We conducted a case-control study of 22 incident VF cases (11 men, 11 women) and 54 age and sex-matched controls aged 50 to 85 years, selected from the Framingham multi-detector computed tomography cohort. Textural analysis was performed on a volume of the L3 trabecular bone incorporating the middle 11.6 mm of vertebral body height. Gray level co-occurrence matrices were calculated (distance of 1 voxel in each neighboring direction) and the Haralick textural features were derived from the matrices to quantify textural patterns. We also measured L3 trabecular vBMD and DXA-equivalent aBMD from the CT scans. The prediction of incident VF was evaluated using conditional logistic regression analysis including age, height and weight as covariates. The model discriminative capability was assessed with the area under the

receiver operating characteristic (ROC) curve (AUC).

Results

We found that combining L3 DXA-equivalent and two textural features (sum average and difference variance) improved the fracture prediction over aBMD alone ($p=0.02$). ROC analysis showed that aBMD yielded AUC of 0.77, whereas a combination of aBMD and the two textural features yielded a significantly higher AUC of 0.87. AUC for trabecular vBMD alone was 0.74, and was significantly higher when textural features were added to trabecular vBMD (AUC = 0.86, $p=0.01$ vs trabecular vBMD AUC alone). These findings imply that VF is associated with decreased image brightness (sum average) and increased local heterogeneity (difference variance).

Conclusion

Although limited by a small number of individuals with VF, these results suggest that incorporation of textural features from clinical-CT may enhance VF prediction. Larger studies are needed to confirm these results.

This work was supported by a grant from the National Institutes of Health (R01 AR053986) and by the National Heart, Lung, and Blood Institute (NHLBI) Framingham Heart Study (NIH/NHLBI Contract N01-HC-25195).

Increased Cortical Porosity and Reduced Trabecular Density are Not Necessarily Synonymous With Bone Loss and Microstructural Deterioration

Ali Ghasem-Zadeh^{*1}, Roger Zebaze¹, Elizabeth J. Atkinson², Yu Peng³, Sundeep Khosla², Ego Seeman^{1,4}

¹ Departments of Medicine and Endocrinology, Austin Health, University of Melbourne

² Mayo Clinic, Rochester

³ Straxcorp Pty Ltd

⁴ Mary Mackillop Institute for Health Research, Australian Catholic University, Melbourne, Australia

Measurements of cortical porosity and trabecular density are used to estimate fracture risk. However, absolute values of these traits are the net result of their growth-related assembly and age-related deterioration. As bone loss affects both cortical and trabecular compartments, we hypothesized that the desirable characteristic of a surrogate of bone fragility is a measure of the age-related deterioration of both cortical and trabecular compartments, not just one compartment, and values free of any contribution of growth to peak microstructure. Accordingly, we developed a Structural Fragility Score (SFS), a single measurement which quantifies the bone loss dependent age-related increment in cortical porosity and decrement in trabecular density relative to their premenopausal mean values. We compared ultra-distal radial microstructure in 99 postmenopausal women with forearm fractures and 105 controls using high resolution peripheral computed tomography. Results are presented as Odds Ratio (95% confidence intervals CI). Cortical porosity was associated with fractures provided women with deteriorated trabecu-

lar density were included (2.30, 1.30 – 4.05, $p = 0.004$), but not if trabecular deterioration was absent (0.96, 0.50 – 1.86; $p = 0.91$). Likewise, trabecular density was associated with fractures provided women with high cortical porosity were included (3.35, 1.85 – 6.07, $p < 0.0001$), but not if women with high porosity were excluded (1.60, 0.78 – 3.28, $p = 0.20$). By contrast, the SFS, a measure capturing coexisting deterioration in cortical porosity and trabecular density, was associated with fractures (4.52, 2.17 – 9.45, $p < 0.0001$). BMD was associated with fracture before accounting for the contribution of the SFS (5.79, 1.24 – 27.1, $p = 0.026$), not after (4.38, 0.48 – 39.9, $p = 0.19$). The SFS was associated with fracture before (4.67, 2.21 – 9.88) and after (3.94, 1.80 – 8.6, both $p < 0.0001$) accounting for BMD. The disease of bone fragility is captured by cortical and trabecular deterioration and a measurement of coexisting cortical and trabecular deterioration is likely to identify women at risk for fracture more robustly than absolute values of cortical porosity, trabecular density, or BMD.

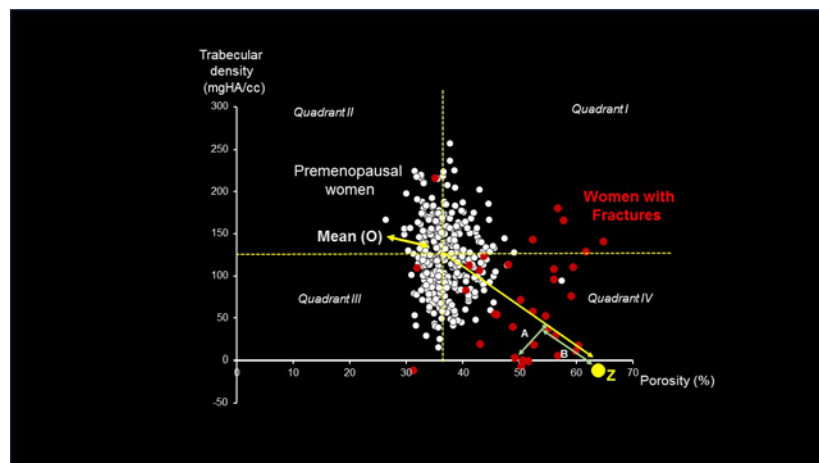


Figure 1. Structural Fragility Score

Cone-Beam Computed Tomography as a Fast Alternative for High-Resolution Peripheral Computed Tomography

Karen Mys^{*1,2}, Peter Varga², Filip Stockmans³, Boyko Gueorguiev², Caroline E. Wyers^{4,5},
Joop P.W. van den Bergh^{4,5,6}, G. Harry van Lenthe¹

¹ KU Leuven, Biomechanics Section, Belgium

²AO Research Institute Davos, Biomedical Development, Switzerland

³KU Leuven (Kortrijk), Development and Regeneration, Belgium

⁴Department of Internal Medicine, VieCuri Medical Center, the Netherlands

⁵NUTRIM School for Nutrition and Translational Research in Metabolism, Maastricht University, the Netherlands

⁶Department of Internal Medicine, Subdivision of Rheumatology, Maastricht University Medical Centre, the Netherlands

Introduction

High-resolution peripheral computed tomography (HR-pQCT) is considered as the best technique to measure human bone microarchitecture *in vivo*. However, a breakthrough for daily clinical applications is inhibited, due to the restricted field of view (FOV) and a relatively long acquisition time, which inhibit scanning of large FOV *in vivo*. High-resolution cone-beam computed tomography (CBCT) is a relatively new alternative in the orthopedic field. It is already used in daily clinical practice for dental application because of the large FOV (around 12x12x8 cm³), fast scanning time (around 18 – 31 s), high resolution (voxel size down to 75 μm) and low radiation dosage. The aim of this work is to evaluate the accuracy of a CBCT on human trapezia and radii relative to micro-computed tomography (microCT) as the gold standard and to compare it with the accuracy of HR-pQCT when quantifying trabecular bone microstructural parameters and bone mechanical parameters.

Materials & methods

Nineteen trapezium bones of arthritic patients (Fig. 1) and nineteen distal radii were scanned four times *ex vivo*; (1) microCT (SkyScan1172, Bruker, Belgium, @19.84 μm for the trapezia; and VivaCT40, Scanco, Switzerland, @19 μm for the radii), (2) HR-pQCT (XTremeCT-I, Scanco, Switzerland, @82 μm), (3) HR-pQCT (XTremeCT-II, Scanco, Switzerland, @60.7 μm) and (4) CBCT (NewTom 5G, Cefla, Italy, @75 μm). HR-pQCT and microCT were re-

constructed and segmented following the manufacturer guidelines. CBCT was reconstructed with in-house developed software and segmented using an adaptive technique. Bone morphometric parameters were calculated using the Scanco software including bone volume fraction (BV/TV), trabecular thickness (Tb.Th), trabecular separation (Tb.Sp) and trabecular number (Tb.N). Bone stiffness was calculated using micro-finite element analyses with loading of the joint proximally.

Results

Evaluated over all parameters measured from the trapezia, the coefficient of determination (R^2) were higher than 0.68, 0.72 and 0.67 for XtremeCT-I, XtremeCT-II and CBCT, respectively. HR-pQCT was better than CBCT in capturing very thin trabeculae located close to each other. Interesting for clinical application is that such samples with very thin trabeculae could be detected automatically on the CBCT-images. Preliminary results suggest similar results for the radii.

Conclusion

We conclude that our enhanced CBCT-images have a comparable accuracy as HR-pQCT to quantify bone structural and mechanical parameters. The broader range of application, larger field of view and shorter acquisition time make CBCT a valuable alternative for HR-pQCT where high resolution is desired in clinical practice.

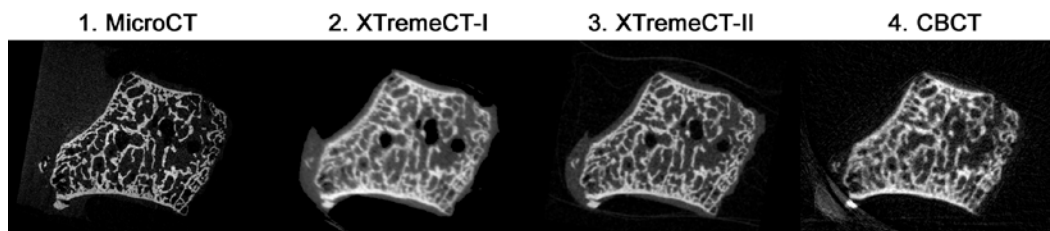


Figure 1. One representative reconstructed slice of a trapezium as obtained with microCT, XtremeCT-I, XtremeCT-II, and CBCT, respectively

Imaging of Muscle and Bone with pQCT and the Relationship to Muscle Function

Johannes Willnecker*¹

¹ Stratec Medizintechnik

The importance of the relationship of muscle and bone has long been recognized and several imaging methods of this relation have been established. Aside from hand grip measurements the direct measurement of muscle function and the comparison to imaging methods are not a standard tool so far.

X ray attenuation measurements by peripheral computed tomography allows the analysis of bone, muscle and fat cross sectional areas. Like bone density, also muscle density can be determined from pQCT scans. The small contrast between muscle and fat requires low-noise images or image filtration and absence of movement artefacts. In several studies the strong correlation between muscle and bone cross sectional has been shown. In addition, muscle density serves as an independent risk factor for falls, frailty and hospitalization. But muscle size measures do not account for changes in muscle composition and muscle function. The force or power output for a unit muscle mass or cross-sectional areas is different for different age groups. The high correlation between muscle and bone cross sectional areas seen in younger persons is weaker in an ageing population. But also force and power must be differentiated. While muscle force shows no or only moderate reductions with age in healthy subjects, muscle power is a far

better gauge to describe age-related loss of muscle function. Studies in master athletes have shown that even with high training efforts loss of muscle power can be slowed but not prevented. In measurements of jumping mechanography and pQCT in over 200 subjects (age 25-65y) significant correlations were observed between muscle cross sectional area and jumping force, muscle cross sectional area and bone mass and between muscle force and bone mass. Bone area and muscle force showed the highest correlations, even higher than between muscle force and muscle cross sectional area.

Measurements of muscle mass or muscle cross sectional area are an important tool for the analysis of the muscle-bone unit, but measurements of muscle force and power add substantial information to a better muscle-bone analysis and possibly for a differentiation between a true osteoporosis and a bone weakness caused by muscle weakness. The effects of motivation, diurnal effects and neuromuscular control need to be evaluated in further studies.

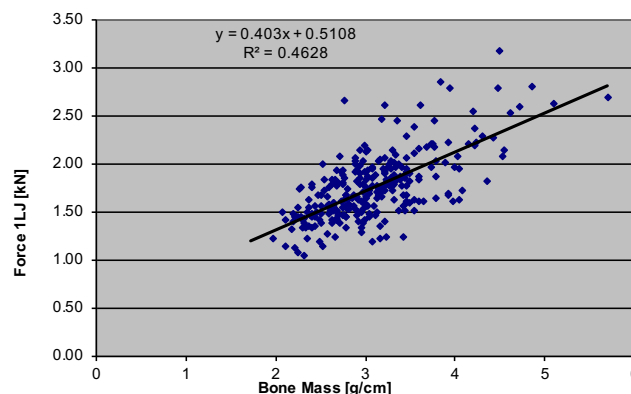


Figure 1. Correlation between muscle force and bone mass.

Automated Detection of Joint Ankylosis in Joint Space Width Assessments in Hands affected by Rheumatoid Arthritis using HR-pQCT

Michael T. Kuczynski^{*1,2}, Scott Burnet^{1,2}, Stephanie Finzel³, Kathryn S. Stok⁴, Steven K. Boyd¹, Cheryl Barnabe⁵, Sarah L. Manske¹

¹ Department of Radiology, McCaig Institute for Bone and Joint Health, Cumming School of Medicine, University of Calgary

² Biomedical Engineering Graduate Program, Department of Radiology, Cumming School of Medicine, University of Calgary

³ Department of Rheumatology and Clinical Immunology, Medical Center University of Freiburg, Faculty of Medicine, University of Freiburg

⁴ Department of Biomedical Engineering, The University of Melbourne

⁵ Department of Medicine, McCaig Institute for Bone and Joint Health, Cumming School of Medicine, University of Calgary

Introduction

One hallmark characteristic of Rheumatoid Arthritis (RA) is the emergence and progression of joint damage, including ankylosis (bone fusion). Ankylosis may be difficult to detect using conventional radiography (CR) due to thin bone fusion. High-resolution peripheral computed tomography (HR-pQCT) allows for 3D volumetric assessment of joint space width (JSW) in the metacarpophalangeal (MCP) joints with great accuracy and precision. Current JSW calculation uses an operator-independent algorithm developed with the consensus of the Study group for eXtreme Computed Tomography in Rheumatoid Arthritis (SPECTRA). This algorithm assesses the thickness of the joint space and will not detect ankylosis or bone-on-bone contact, since it does not count zero thickness joint space in its definition. We propose a method to automatically detect ankylosis using a connectivity filter to detect connections between bones in the joint and compare this with visual inspection of ankylosis.

Methods

Quantitative and volumetric measurements of the 2nd and 3rd MCP joints in 42 patients with rheumatoid arthritis at 3- and 12-month follow-ups were obtained using a second generation HR-pQCT scanner (XtremeCT II, Scanco Medical). The JSW was computed from HR-pQCT scans for joints of the patient's dominant hand using the standard automated algorithm using the Image Processing Language (IPL v5.42, Scanco Medical). An additional connectivity filter was applied to the segmented image to determine whether the metacarpal bone was connected to the phalanx. A rheumatologist manually identified the presence of ankylosis using 2D screen-

shots automatically output from the JSW algorithm. A contingency table was generated to compare the accuracy between the automated connectivity analysis and manually scored ankylosis.

Results

155 joints from 42 patients were analyzed. 7 joints were identified as ankylosed by the automated connectivity filter; 8 joints were identified as ankylosed by manual scoring. Comparing the two methods revealed a sensitivity = 0.99; specificity = 0.75; positive predictive value = 0.99; negative predictive value = 0.86; and accuracy of 0.9806 ($p < 0.05$).

Discussion

The proposed method for detecting ankylosis in MCP joints can be easily incorporated into existing JSW algorithm to adjust minimum JSW to be 0 when bones are connected. As manual scoring was performed using 2D images from HR-pQCT scans, performance of this algorithm needs to be confirmed against manually scoring of 3D images and conventional x-ray. Future work can address the ceiling effect of current x-ray scoring systems that does not allow assessment of progression after ankylosis.

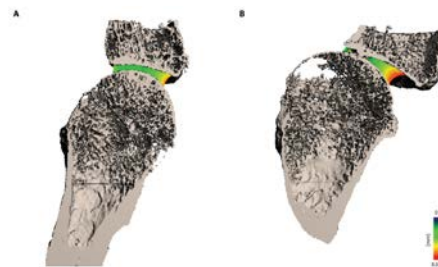


Figure 1. 3rd MCP joint for two different patients with (A) correct (JSW.min = 0.18 mm, no ankylosis) and (B) incorrect (JSW.min = 0.12 mm, ankylosis) JSW values

Estimated Bone Strength of the Metacarpal Phalangeal Head Using Finite Elements Analysis – A Pilot Study

Timo Meinderink^{*1}, Fabian Stemmler¹, David Simon¹, Georg Schett¹, Klaus Engelke¹, Steven K. Boyd^{2,3}, Arnd Kleyer¹, Anna-Maria Liphardt^{1,4}

¹ Friedrich-Alexander-Universität Erlangen-Nürnberg, Medizinische Klinik 3 - Rheumatology and Immunology, University Hospital Erlangen

²McCaig Institute for Bone and Joint Health, University of Calgary, Canada

³Department of Radiology, Cumming School of Medicine, University of Calgary, Canada

⁴German Sport University Cologne, Institute of Biomechanics and Orthopedics, Köln, Germany

Introduction

Rheumatoid arthritis greatly affects joint health, especially of the finger joints. Ultimately, degenerative processes can lead to joint deformation resulting in ulnar deviation. Bone strength of radius and tibia can be estimated using finite elements analysis (FEA) applied to images generated by high-resolution peripheral quantitative computed tomography (HR-pQCT). Currently, this method is not available for estimating bone strength of the metacarpal (MCP) heads. The aim of this study was to develop a FEA model for the MCP heads imaged with HR-pQCT with the long term goal to better understand the impact of changes in bone density and microarchitecture due to inflammatory degeneration on bone strength of the MCP head.

Methods

Segmented MCP heads of five humans HR-pQCT scans (motion grade ≤ 3) were divided into trabecular and cortical regions and modeled by FEA (Faim v8.0, Numerics88 Solutions Ltd., Canada). Failure load was based on 2% critical volume at 0.007 strain. To transfer the force of 100 N into the head, a polymethylmethacrylat (PMMA) cap was added at the distal end of the MCP head. The proximal end was fixed by constraining the movement of the voxels on the distal plane. Sensitivity of the model was tested

on a range of bone length (± 10 HR-pQCT slices on the proximal end) and PMMA cap thickness (4.46 mm, 4.96 mm and 5.46 mm).

Results

Bone dimensions ranged from 14 to 17 mm for transverse cross section and from 17 to 19 mm for proximal to distal length. Estimated Von Mises stress ranged between 2.1-3.1 MPa for trabecular and 2.2-3.4 MPa for cortical bone. Peak stress valued around 26-45 MPa for trabecular and 24-66 MPa for cortical bone. Bone stiffness ranged from 4.4-6.8 kN/mm and failure load from 540 N to 780 N. Displacement decreases in the proximal direction. Results of the sensitivity tests are summarized in Table 1.

Discussion

Applying FEA to metacarpal joint images allows estimation of intra-articular bone mechanics related to bone density and microarchitecture. High image and segmentation quality are necessary to avoid over or underestimation of bone strength. Future studies will validate cadaver material against mechanical testing and evaluate the impact of different orientation of the bone, bone size and loading conditions on estimated intra-articular bone strength to optimize monitoring of joint health in arthritic disease.

Parameter	[mm]	Δ stiffness [kN/mm]	Δ failure load [N]	Δ von Mises stress [MPa]	
				trabecular	cortical
Bone length	+0.82	-2.3 \pm 0.4 % *	0.8 \pm 0.2 % *	-0.3 \pm 0.4 %	-0.3 \pm 0.6 %
	-0.82	2.5 \pm 0.4 % *	-0.8 \pm 0.1 % *	0.3 \pm 0.4 %	0.2 \pm 0.7 %
PMMA cap	+0.5	11.0 \pm 3.0 % *	5.0 \pm 2.0 % *	-7.0 \pm 1.0 %	-2.0 \pm 0.0 %
	+1.0	20.0 \pm 5.0 % *	8.0 \pm 3.0 % *	-12.0 \pm 1.0 %	-3.0 \pm 1.0 %
	+1.5	28.0 \pm 7.0 % *	12.0 \pm 4.0 % *	-16.0 \pm 2.0 %	-4.0 \pm 1.0 %

Table 1. Sensitivity of bone strength at the MCP head to bone length and PMMA cap thickness. Asterisks indicate significance ($p < 0.05$).

Structural and Microstructural Intraarticular Bone Changes at the Metacarpal Heads in Patients with Psoriatic Arthritis Compared to Controls: A HR-pQCT Study

Dongze WU^{*1}, James F Griffith², Steven H.M. Lam¹, Priscilla Wong¹, Jiang Yue¹, Lin Shi³, Edmund K. Li¹, Isaac T. Cheng¹, Tena K. Li¹, Tracy Y. Zhu⁴, Vivian W. Hung⁴, Ling Qin⁴, Lai-Shan Tam¹

¹ Department of Medicine & Therapeutics, The Prince of Wales Hospital, The Chinese University of Hong Kong

²Department of Imaging and Interventional Radiology, The Prince of Wales Hospital, The Chinese University of Hong Kong

³Research Centre for Medical Image Computing, Department of Imaging and Interventional Radiology, The Prince of Wales Hospital, The Chinese University of Hong Kong

⁴Bone Quality and Health Centre of the Department of Orthopedics & Traumatology, The Prince of Wales Hospital, The Chinese University of Hong Kong

Introduction

Metacarpal head directly exposed to intra-articular inflammatory milieu, therefore may lead to abnormal bone remodeling (bone loss and new bone formation). The aims of this study are to investigate the structural (bone erosion and enthesiophyte) and microstructural bone changes in patients with PsA at the second and third metacarpal head (MCH2&3) compared with controls.

Methods

139 subjects (77 PsA, 62 control) underwent high-resolution peripheral quantitative computed tomography (HR-pQCT) scanning at the MCH 2 and 3 and distal radius. An integrative approach (Figure 1) was developed to calculate volume of bone erosion (A) and enthesiophyte (B) [crop of metacarpal bone (a,b); automated segmentation of periosteal surface (c,e); restoration of the missing cortical boundary based on anatomic curve (d,f); three-dimensional calculation of volume (g)] and volumetric bone mineral density (vBMD) and microstructure before and after exclusion of bone erosion (C) and enthesiophyte (D).

Results

15 patients with joint destruction were excluded from further analysis. 62 patients with PsA and controls were comparable in age, gender and body mass index (BMI). PsA patients not only had a significantly increased enthesiophytes number (2.4 ± 1.4 vs 1.3 ± 1.1 , $p < 0.001$) and total volume per person (8.75 ± 6.92 vs 4.36 ± 4.90 mm³, $p < 0.001$), but also erosion number (2.2 ± 1.3 vs 1.2 ± 1.0 , $p = 0.002$) and total erosion volume per person (5.59 ± 6.28 vs 3.17 ± 4.71 mm³, $p = 0.009$) compared with control. When more stringent criteria for erosions (diameter of cortical breaks of > 1.9 mm) were used, numerically greater number (total number 85 vs 50; mean number per patient:

1.39 ± 1.16 vs 1.05 ± 0.98 , $p = 0.110$) and significantly greater total volume of bone erosion (5.16 ± 6.01 vs 2.77 ± 4.49 , $p = 0.003$) in PsA compared with control was observed. Regarding microstructure, PsA patients had a significantly decreased total volumetric bone mineral density (vBMD), cortical vBMD and cortical thickness at the distal radius; while preferential bone loss at the trabecular compartment at the MCH was noticed compared to control.

Conclusions

Compared with controls, PsA patients without joint destruction have more prevalent enthesial driven new bone formation at metacarpal head and greater bone erosion and preferential trabecular bone loss. About 20% patients identified at least one joint destruction at MCH2&3.

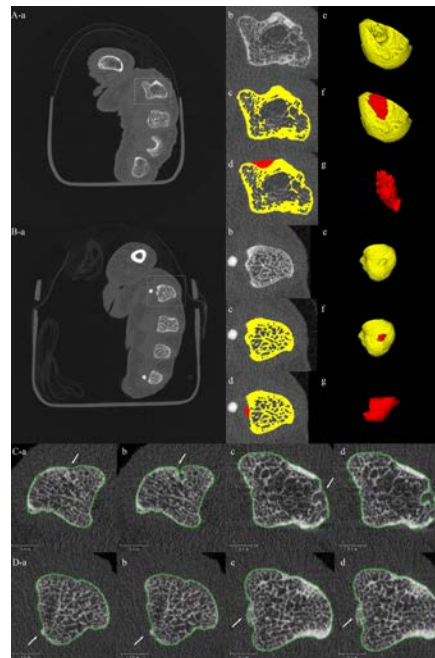


Figure 1. Image analysis on structural and microstructural bone changes

Carotid Atherosclerosis is Associated with Compromised Volumetric Bone Mineral Density and Microarchitecture in Patients with Inflammatory Arthritis

Cheng Tsz Ho^{*1}, Qin Ling¹, Tam Lai Shan¹

¹ The Chinese University of Hong Kong

Introduction

Inflammatory arthritis patients had increased risk of atherosclerosis and osteoporosis. The association between presence of carotid plaque and volumetric BMD (vBMD)/microarchitecture is yet to be explored.

Objective

The aim of this study was to explore the relationship between volumetric bone mineral density (vBMD)/microstructural features and presence of carotid plaque (CP) in patients with inflammatory arthritis.

Materials and Methods

175 inflammatory arthritis patients (81 [46%] PsA, 94 [54%] RA; 70 [40%] males; age: 53±12years) were recruited into an ongoing prospective study assessing the relationship between inflammation, osteoporosis and carotid atherosclerosis. Carotid plaque and intima-media thickness (IMT) were measured by carotid ultrasound. Areal BMD (aBMD) was measured by dual energy X-ray absorptiometry (DXA). Microarchitecture features and vBMD of distal radius were measured using high-resolution peripheral quantitative computed tomography (HR-pQCT).

Results

No patients had established cardiovascular disease (CVD). Data from 172 patients at

baseline were analyzed for this cross-sectional study. Patients were sub grouped according to the presence or absence of carotid plaque (CP+ group, n=68 [40%]) and CP- group, n=132 [60%]). CP+ group were older (59±10 vs 49 ±11, p<0.001), more likely to be male (54% vs 31%, p=0.002), had higher systolic blood pressure (130±19 vs 124±17 mmHg, p=0.034) and CVD risk (15.7±14.2 vs 7.9±8.6, p<0.001) according to the Framingham Risk Score (FRS) then the CP- group. aBMD, vBMD and microarchitecture were significantly compromised in the CP+ group. Distal radius aBMD, distal radius total vBMD, trabecular (Tb) vBMD, Tb thickness, cortical (Ct.) vBMD, Ct. thickness and bone volume fraction were 5% (p=0.004), 12% (p<0.001), 8% (p=0.007), 8% (p=0.004), 4% (p=0.007), 10% (p=0.001) and 8% (p=0.007) lower in the CP+ group. The differences remained significant after adjustment for gender, disease type and FRS (Table 1).

Conclusion

Inflammatory arthritis patients with carotid plaque had lower aBMD, vBMD and compromised bone microarchitecture in the distal radius even after adjustment for gender, disease type and FRS, suggesting that inflammation may be the common link for both conditions.

	Carotid plaque		p value	Adjusted p value*
	No (n=104)	Yes (n=68)		
Total radius				
aBMD, g/cm ²	.575 ± .087	.547 ± .091	0.095	0.004
Distal radius				
Total vBMD, mmHA/cm ³	353.8 ± 77.8	315.3 ± 69.7	0.001	<0.001
Trabecular BMD, mmHA/cm ³	141.5 ± 46.2	131.4 ± 38.8	0.138	0.007
Bone volume fraction	.118 ± .039	.110 ± .032	0.142	0.007
Trabecular thickness, mm	.077 ± .017	.071 ± .013	0.019	0.004
Cortical vBMD, mmHA/cm ³	902.6 ± 58.0	870.0 ± 63.5	0.001	0.007
Cortical Thickness, mm	.882 ± .177	.792 ± .211	0.009	0.001

* Adjusted for gender, disease type and Framingham Risk Score

Table 1. Distal radius vBMD/microarchitecture and presence of plaque

Joint Space Analysis of Metacarpal Joints Imaged via High-Resolution Peripheral Quantitative Computed Tomography (HR-pQCT) Shows Structural Differences Between Patients with Hemochromatosis Hand Arthropathy and Healthy Controls

Ursula Heilmeyer^{*1}, Andrew J. Burghardt¹, Puneet Kapoor¹, Vivek Swarnakar¹, Reinhard Voll², Stephanie Finzel²

¹ Department of Radiology and Biomedical Imaging, Musculoskeletal Quantitative Imaging Research Group, University of California San Francisco

²Department of Rheumatology and Clinical Immunology, University Medical Center Freiburg, Faculty of Medicine, University of Freiburg

Background

One of the earliest symptoms of hereditary hemochromatosis (HH) is joint pain due to excessive iron deposition in the joints. To date, the presence of HH arthropathy is still routinely determined using hand radiography, a 2D low-resolution technique limited in detecting early structural joint changes and limited in measuring subtle progression of joint damage. High-resolution peripheral quantitative computed tomography (HR-pQCT), instead, allows for in-vivo 3D characterization of human bone and joint microstructure at a spatial resolution of 130 μm . Due to its high sensitivity to detect and measure subtle short-term joint changes, HR-pQCT has been successfully employed on rheumatoid arthritic patients. However, HR-pQCT has not been utilized to characterize joint and bone structure seen in HH arthropathy.

Objectives

Here, we investigated a group of HH patients and compared to published values for healthy controls: 1) if the usage of HR-pQCT is feasible for HH arthropathy, and 2) what differences in joint microstructure may exist between metacarpophalangeal (MCP) joints of HH patients and healthy controls.

Methods

MCP joints 2, 3, and 4 of 24 HH patients were imaged on a HR-pQCT scanner (XtremeCT, Scanco Medical AG). Joint space (JS) morphology of each MCP was quantified from the HR-pQCT images semi-

automatically and joint-space volume (JSV), joint-space-width mean (JSW), JSW variance (JSW.SD), minimal and maximal JSW (JSW.MIN, JSW.MAX), and JSW asymmetry (JSW.AS) were calculated and compared to identical measures from a published study of healthy controls (Burghardt et al, Ann Biomed Eng 2013).

Results

Both groups were similar in age (54.7 vs. 50.1 years), BMI, and race. HH patients had been diagnosed with HH approximately 10 years ago and were treated with about 6 phlebotomies annually. Out of the 72 MCP HH joints available for analysis, 56 could be successfully segmented at the first attempt, 12 required additional manual segmentation to separate the individual bones. 3 joints were excluded due to motion artifacts, and 1 joint could not be segmented. Compared to healthy subjects, HH patients showed a lower JSW.MIN ($p < 0.01$ at MCP2 and 3) and a wider JSW.SD ($p < 0.045$ at MCP2, $p < 0.006$ at MCP3) across all MCP joints. JSW.AS was numerically larger in HH patients, with trending significance.

Conclusion

Our findings suggest that joint space characterization in MCPs via HR-pQCT in patients with hereditary hemochromatosis is feasible. Moreover, it can capture subtle structural differences compared to healthy controls. However, larger studies with matched controls are needed to validate our results.

The Relationship Between Subclinical Inflammation and Bone Damage in Patients with Rheumatoid Arthritis

Scott C Brunet^{*1,2}, Cheryl Barnabe^{1,3}, Glen Hazlewood^{1,3}, Peter Salat^{1,4}, Sarah L Manske^{1,4}

¹ McCaig Institute for Bone and Joint Health

² Biomedical Engineering Graduate Program, University of Calgary

³ Department of Medicine, University of Calgary.

⁴ Department of Radiology, University of Calgary.

Introduction

Inflammatory processes in rheumatoid arthritis (RA) lead to the damage of joints, which can lead to functional decline. High resolution peripheral quantitative computed tomography (HR-pQCT) allows 3-dimensional visualization of the bony microarchitecture allowing for improved erosion detection and bone microstructure measurements. Magnetic Resonance Imaging (MRI) gives excellent visualization of inflammation, including bone marrow edema (BME) and synovitis. Intervention with disease modifying agents reduces clinically detectable inflammation. However, many patients classified in remission due to the lack of clinically detectable inflammation have evidence of subclinical inflammation on MRI. This could result in continued erosive bone damage and functional declines. The purpose of this study was to determine whether BME on MRI could be co-localized with erosions on HR-pQCT and if these imaging findings had a relationship with disease activity and function.

Methods

10 participants with RA, in physician-classified remission, were recruited. Each participant received a contrast-enhanced MRI scan and a HR-pQCT scan of the dominant hand. Disease activity (DAS28) was determined by physician assessment and inflammatory biomarkers. A DAS28 less than 2.6 represents remission. Function was assessed by the Health Assessment Questionnaire (HAQ) and Disabilities of the Arm, Shoulder and Hand (DASH) questionnaire. A multimodal registration technique was developed to localize joint damage on HR-pQCT with synovitis and BME on MRI. Joint space was assessed using a volumetric approach derived from an international study group.

Results

All 10 participants had evidence of at least mild synovitis and/or BME on MRI. Six

participants had a DAS28 that met remission criteria. Five erosions from the 2nd or 3rd metacarpophalangeal joints seen on HR-pQCT were localized with BME seen on MRI (Figure 1). The mean HAQ and DASH scores at baseline were 0.86 (\pm 0.57) and 25.9 (\pm 16.3) respectively, representing moderate functional disability. There was a significant positive correlation ($r=0.610$, $p=0.016$) between minimum joint space width and DAS28.

Conclusions

This novel image registration technique for RA was able to localize areas of BME on MRI with joint damage on HR-pQCT, which could provide unique insights on the mechanisms of damage in RA that is not possible with either imaging approach alone. Erosions observed on HR-pQCT will be followed for 6 months to determine whether the presence of BME leads to increased erosion volume and functional declines. Demonstrating a relationship between joint structure and inflammation will provide important information on the progression of RA and further our knowledge of the current treatment targets.

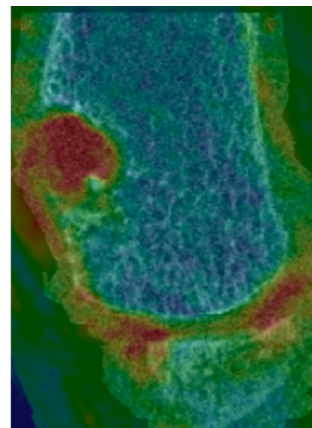


Figure 1. Example of registered and overlaid MRI and HR-pQCT images localizing inflammation and BME (red/orange) with erosive bone damage.

DIRECTORY OF AUTHORS

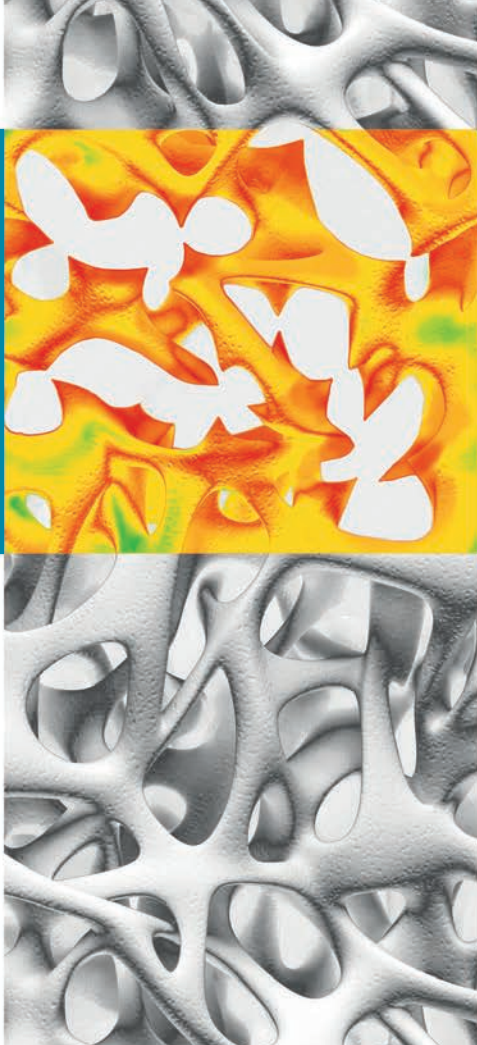
A. Teodora Dinescu	62	Berengere Aubry-Rozier	90
Abinaa Chandrakumar	27	Bert van Rietbergen	60, 66, 91
Adalbert Raimann	67	Bettina M Willie	91, 94, 99
Adrian Schankath	105	Bill Leslie	74
Alejandro Morales Martinez	86	Birgitta Gatenholm	63
Ali Ghasem-Zadeh	125, 131	Boyko Gueorguiev	50, 132
Alicia Gabilondo	104	Brett Allaire	40, 130
Amaka C Offiah	91	Bryce A Besler	65, 119
Ammar Alsheghri	61	Carl Anders Lindahl	63
Andrea Boni-Mikats	67	Carla Kinnunen	31
Andrea Garber	32	Carla Winsor	115
Andreas Maier	127	Caroline E. Wyers	50, 120, 132
Andreas Reisinger	110	Caroline Wyers	110
Andres Kroker	26, 43	Cat Shore-Lorenti	125
Andrew J Burghardt	91, 121	Cathy M Arnold	58
Andrew J. Burghardt	96, 113, 138	Chantal E Kawalilak	58
Andrew S Michalski	89, 119	Chantal MJ de Bakker	45
Andy KO Wong	95	Cheng Tsz Ho	137
Andy Kin On Wong	27, 52	Cheryl Barnabe	134, 139
Andy Pitsillides	101	Chris Hall	125
Aneal Khan	109	Chris L. de Korte	70
Angela M Cheung	73, 75, 95	Christine Chappard	30, 42, 68
Anika Grüneboom	127	Christophe Lelong	77
Anita Colquhoun	73	Claire Acevedo	126
Anja Niehoff	38	Claudia Iriondo	36
Anna Greco	70	Claus-C. Glüer	55, 110, 118
Anna-Maria Liphardt	38, 39, 135	Colet E.M. ter Voert	123
Annegret Mündermann	38	Corinne Henak	115
Anthony Hall	91, 94	Cory Kwong	49
Anton Nikolaev	70	Damien Lacroix	91
Anton Page	124	Daniel Chappell	33
Ariane C Scheuren	98	Danielle E Whittier	35
Arnd Kleyer	135	Danielle E. Whittier	49
B. Catharine Craven	75	David A Hanley	35, 45, 84, 92
Behzad Javaheri	101	David Lee	40
Benjamin J. Hinton	76, 78	David M. L. Cooper	53
Bennett K. Ng	76, 78	David Simon	135
Bennett Ng	32	David W. Holdsworth	122
Bente van Teeffelen	123		

David Wilson	106	Fjola Johannesdottir	130
David Wong	73	Florence Wong	73
Davis McClarty	74	Francis H Glorieux	91, 94
Dean Ta	71	Franck Michelet	77, 79, 80
Delphine Stoll	90	Francois De Guio	79, 80
Denis E. Schenk	111	Francoise Peyrin	30
Dennis Anderson	40	Frank Lampe	116
Dennis E. Anderson	130	Frank Zaucke	38
Destiny Francis	104	Frans Heyer	110
Diana Yau	73	Franziska Jundt	99
Diane Krueger	79, 80	François De Guio	77
Didier Cassereau	41	Frederike Sannmann	107
Didier Hans	77, 79, 80, 90	G. Harry van Lenthe	50, 120, 132
Diego Rossinelli	64	Gabriel Hans	90
Dieter Felsenberg	128	Gabriele Armbrecht	128
Dieter Pahr	110	Gabriele Haeusler	67
Donatien Ramiandrisoa	42, 68	Galateia Kazakia	108
Dongze WU	136	Gareth Thomas	124
Douglas P. Kiel	130	Garry Gold	29
Dragana Ponjevic	51	Gary Beaupre	29
Duncan Betts	66	Georg Schett	135
Duncan Butler	125	George Sarau	127
Edmund K. Li	136	Georg Schett	127
Ego Seeman	125, 131	Gert-Peter Bruegemann	38
Elena Gonzalez Rodriguez	90	Gianluca Iori	42, 72
Eleni P. Kariki	33, 48	Gianluca Lori	110
Elhadi Sariali	44	Gisela A Kuhn	98
Elise Morgan	112	Glen Hazlewood	139
Elizabeth J. Atkinson	131	Glen M. Blake	83
Elizabeth J. Samelson	130	Graeme M Campbell	116
Elizabeth Shane	62	Guillaume Renaud	41
Emily Russell	33	Guozhi Zhang	120
Emma O. Billington	35, 84, 92	Heather A. McKay	88
Enisa Shevroja	90	Heather M. Macdonald	88
Eric C Parent	103	Heidi-Lynn Ploeg	46, 115
Erik M Groves	82	Honglin Zhang	106
Eva Hufnagel	117	Hunxian Hu	95
Eva Szabo	95	Huong Nguyen Minh	72
Fabian Stemmler	135	Ian Pagano	32
Faleh Tamimi	61	Ian Sinclair	124
Fan Xiao	85	Ifaz T. Haider	56
Fani Ziouti	99	Io Flament	86
Felicitas R. Flohr	102	Isaac T. Cheng	136
Felix Eckstein	38	Iskandar Tamimi	61
Felix Liu	34, 86	J. Keenan Brown	83
Filip Stockmans	50, 120, 132	J.P. van den Bergh	110
Finn Brose	116	Jacob L. Jaremko	71, 105
Fintan Moriarty	54		

Jaime A. Peña	118	Kenneth Poole	33
James D Johnston	58	Kim Wager	91, 94
James F Griffith	136	Klaus Engelke	57, 107, 117, 121, 128, 135
James F. Griffith	85		
Jana Humbert	55	Ko Chiba	93
Janina Patsch	67	Lai-Shan Tam	136
Jay Shapiro	91	Lars Folkestad	91
Jean D. Sibonga	37, 39	Lasse Kling	127
Jean-Gabriel Minonzio	42, 68	Laura Peralta	110
Jeffrey D Zajac	125	Lauren A. Burt	45, 65, 82, 84, 92
Jeffrey F. Dunn	104	Laurence Stillwater	105
Jens Moeller	102	Lawrence H. Le	71
Jiang Yue	136	Leigh Gabel	39, 45, 65, 88
Jing Liu	108	Leon de Jong	70
Jinhee Lee	34, 86	Leonid Mill	127
Joachim Mester	38	Leticia Campello	115
Joes Staal	33	Li Xu	83
Johanna Baetz	116	Lin Shi	85, 136
Johannes Schneider	42, 67, 110	Lindsay L. Loundagin	53, 114
Johannes Willnecker	133	Lindsie A. Blencowe	75
John A. Shepherd	76, 78	Ling Qin	28, 136
John R. Matyas	51, 104	Ling Wang	57, 83, 87, 129
John Shepherd	32	Lora Giangregorio	95
John Street	106	Lora M. Giangregorio	75
Jonathan D. Adachi	52	Lu Yin	129
Joop P.W. van den Bergh	50, 120, 132	Lucie Bourgoin	81
Jordan Feld	73	Luis Carrenoco	46
Joseph Zmuda	27	Luis Perez Poro	46
Josje AG van Rens	58	Lun M. Wong	85
Joy Dunmore-Buyze	122	M. Kassim Javid	33
Ju Zhang	115	Madeline Dwyer	73
Juan Du	72	Makoto Osaki	93
Juan F. P. J. Abascal	30	Manyi Wang	57
Juan Francisco Vivanco	46	Marco Viceconti	115
Julio Carballido-Gamio	108, 113	Maria Drangova	122
Jun Song	61	Marianne S. Rose	92
Jurgen J. Fütterer	70	Mariya Shtil	43
Justin J. Tse	122	Mark Bryanton	74
Kai Li	129	Maroua Hammami	42
Karamjot Sidhu	109	Marta C Erlandson	95
Karen Mys	50, 120, 132	Martin Herrmann	127
Katelyn Burkhart	40	Martin Krssak	67
Kathryn S Stok	121	Martina Heer	39
Kathryn S. Stok	100, 123, 134	Martine Cohen-Solal	68
Kay Raum	42, 67, 72, 110	Mary L. Bouxsein	40, 130
Keith Thompson	54	Masako Ito	93
Kelly Quipp	82	Mathieu Gendron	61
Ken Kozloff	91		

Mats Brittberg	63	Peter Salat	26, 139
Matthew Gibbons	108	Peter Varga	50, 132
Maureen E. Lynch	99	Phil Salmon	47, 101
Mauricio D. Sacchi	71	Philipp Messer-Hannemann	116
Maximilian Rummler	99	Philipp Schneider	96, 124
Melanie Gräsel	42, 110	Philippe Douek	30
Michael M Morlock	116	Philippe K. Zysset	111
Michael Molloy-Bland	91, 94	Phillip J.C. Spanswick	49
Michael T. Kuczynski	134	Pieter Kruizinga	41
Michael Wong	32	Po-hung Wu	108
Michele C Battié	103	Priscilla Wong	136
Michele V Clarke	125	Prism S. Schneider	49
Mike Davidson	74	Prism Schneider	35
Minghui Yang	57	Puneet Kapoor	138
Morteza A Amini	58	Qianqian Pang	28
Muhammed Qasim	115	Qin Ling	137
Nahid Raja	75	Queenie Wong	73
Narihiro Okazaki	93	Quentin Grimal	42, 44, 69
Natalie Reznikov	61	R.Y. Nigel Kour	123
Neil Binkley	79, 80	Rachel A Davey	125
Nicholas J. Yee	89	Rachel D.A. Whyte	27
Nicholas Mikolajewicz	91, 94	Rachel Whyte	52
Nicholas Mohtadi	26, 43	Radhika Tibrewala	31
Nicholas Ohs	66	Radka Tuskova	67
Nick Bishop	91	Ralph Müller	66, 98, 102
Nicolas Bonnet	81	Ramin Mandegaran	105
Nicolas Piché	61	Raymond Hyatt	33
Nils D. Forkert	65	Reinhard Barkmann	42, 110, 118
Nina Derron	102	Reinhard Voll	138
Noor Shaikh	106	Ren Yan N. Kour	100
Olga Will	55	Richard E Walker	26, 35, 43
Oliver Chaudry	107	Richard Souza	31
Olivier Lamy	90	Rizwan Rajak	33
Orestis Katsamenis	124	Robert G.W. Lambert	105
Pascal Laugier	41, 42, 69	Robert Korley	49
Patricia Feil	67	Roger Zebaze	131
Patrik Christen	66	Roland Krug	108
Paul A. Bromiley	33, 48	Rui Zhang	87
Paul A. Hulme	39	Ruopei Yang	57
Paul Anderson	80	Ryan Cvejkus	27
Paul Kostenuik	56	Ryan M. Plett	84, 89, 92
Pauline Lukey	91	Ryleigh White	79, 80
Peng Cao	86	Saija A Kontulainen	58
Perry Pickhardt	115	Salim S. Si-Mohamed	30
Peter Dankerl	117	Samuel T. Robinson	97
Peter Ebeling	125	Sanchita Agarwal	62
Peter Lackie	124	Sarah Foreman	108
Peter Pietschmann	67		

Sarah L Manske	26, 35, 43, 104, 121, 134, 139	Vasek Pitelka	122
Sarah Mehany	67	Vincent A Stadelmann	54, 63, 81
Scott Burnet	134	Vivek Swarnakar	138
Scott C Brunet	139	Vivian W. Hung	136
Scott Fung	73	W. Brent Edwards	53, 56, 114
Scott M. Smith	39	Wei Li	129
Serena Bonaretti	29, 59	Wei Tian	129
Seungbum Koo	38	Weibo Xia	28
Sharmila Majumdar	31, 34, 36, 86	Wilhelm Bloch	38
Sheldon Derkatch	74	Wolfgang Kemmler	107
Silke Christiansen	127	X. Edward Guo	62, 97
Simon Cox	124	Xiaoguang Cheng	57, 83, 87, 129
Simon S Murray	125	Xin Gao	87
Stefan Reinhold	118	Xinbao Wu	57
Stephanie Finzel	121, 134, 138	Xinshan Li	115
Stephanie Sebastian	66	Yandong Liu	57
Steven Boyd	35, 109	Ying Zhu	51
Steven H.M. Lam	136	Yizhong Hu	62, 97
Steven Heymsfield	32	Yongbin Su	57
Steven K. Boyd	26, 39, 43, 45, 49, 51, 65, 82, 84, 89, 92, 96, 119, 134, 135	Yu Peng	131
Steven Reda	74	Yuanqiao Wu	112
Stéphanie Uk	30	Yuping Xu	28
Sundeep Khosla	113, 131	Zhe Guo	57, 83
Suzanne Bussod	30	Zihui Li	100
Suzanne Morin	91, 94	Zully Ritter	128
Svetlana V Komarova	91, 94		
Sylvie Fernandez	68		
Tam Lai Shan	137		
Tena K. Li	136		
Terence O'Neill	33		
Tho N.H.T. Tran	71		
Thomas K. Wolfgruber	76, 78		
Thomas Link	108		
Thomas Oxland	106		
Tijana Popovic	31		
Timo Damm	55, 118		
Timo Meinderink	135		
Timothy F. Cootes	33, 48		
Tony Keaveny	40		
Tor Hildebrand	64		
Tracy Y. Zhu	136		
Ursula Eberli	54		
Ursula Heilmeyer	138		
Vahid Abdollah	103		
Valentina Pedoia	31, 34, 36, 86		
Vanessa Quinn-Laurin	105		



TBS insight

bone structure matters

Identify

more patients at risk for fracture,

Finetune

therapy decision,

Improve

patient management.

www.medimapsgroup.com



LOW ALP

Are you looking for it?

Hypophosphatasia (HPP) is a life-threatening, progressive, inherited metabolic disorder caused by loss-of-function mutations in the ALPL gene, which leads to **low ALP activity**—the diagnostic hallmark of HPP.¹⁻³

COMMON HPP SYMPTOMS

- Fractures^{1,4}
 - Metatarsal
 - Non-healing
 - Pseudo
 - Atypical
- Osteomalacia¹
- Chondrocalcinosis¹
- Pseudogout¹
- Chronic pain⁴
 - Bone
 - Muscle
 - Joint
- Unusual Gait⁴
- Muscle weakness⁴
- Adult tooth loss¹

MAKE SURE TO INCLUDE HPP IN YOUR DIFFERENTIAL DIAGNOSIS

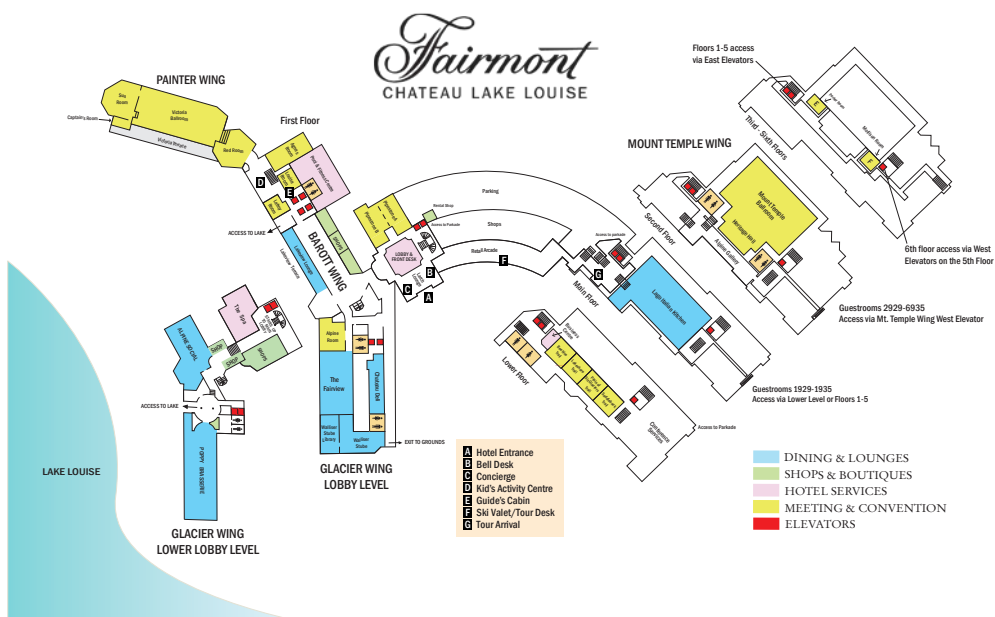
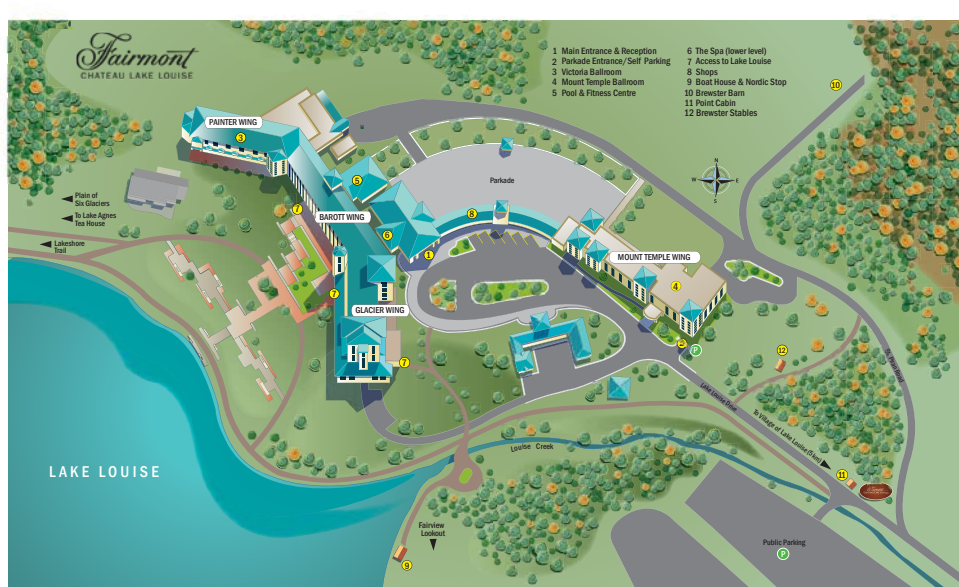
Alexion® is a registered trademark of Alexion Pharmaceuticals, Inc.
Copyright ©2019, Alexion Pharmaceuticals, Inc. All rights reserved. CA/UNB-H/19/0006

REFERENCES: 1. Rockman-Greenberg C. *Pediatr Endocrinol Rev.* 2013;10(suppl 2):380-388. 2. Mornet E, et al. Hypophosphatasia. In: Pagon R, Adam M, Ardinger H, eds. *GeneReviews*. Seattle: University of Washington, Seattle; 1993. 3. Whyte M. Physiological role of alkaline phosphatase explored in hypophosphatasia. *Ann N Y Acad Sci.* 2010;1192:190-200. 4. Kishnani, P et al. Biochemical and Physical Function Outcomes in Adolescents and Adults With Hypophosphatasia Treated With Asfotase Alfa for 5 Years. Results From a Phase 2 Study Poster presented at the 44th Annual European Calcified Tissue Society Congress (EOTS 2017), May 13-16, 2017, Salzburg, Austria

ALEXION

MAPS

All sessions of the workshop are held at the Chateau Lake Louise. The maps below provide an overview of the venue. Locations for each session or meal are listed in the program. Please note that the Victoria Ballroom is in the Painter Wing.



SCHEDULE

	Sunday Feb 24	Monday Feb 25	Tuesday Feb 26
07:00		Breakfast BR1	Breakfast
08:00			
09:00		Introductory Remarks RM1	Advanced Morphometrics
		Clinical Applications: Osteoarthritis SC1	
10:00		Coffee Break CB1	Coffee Break
11:00		Machine Learning & Artificial Intelligence SC2	Quantitative Ultrasound
12:00		Lunch LU1	Lunch
13:00			
14:00		Keynote: A. Feustel KN1	DXA 2.0
		Microgravity and the MSK System SC3	
15:00		Poster Session I + Coffee Break CB2 PS1	Poster Session II + Coffee Break
16:00		Fractures and Implants SC4	Clinical Applications: Osteoporosis I
17:00			
18:00		Dinner DI1	Dinner
19:00	Welcome Reception <i>Steven Boyd & Angela Cheung</i> RC1		
20:00		Workshops WS1 1. Hands-on transparent QMSKI 2. High resolution image processing	Workshops 1. Standardization of metrics for 3D imaging
21:00			
22:00			

Legend

Break/Meal

Keynote

Joint Session

Posters

Workshop

Wednesday Feb 27

Breakfast
BR3

Pre-Clinical In Vivo Imaging
SC9

Coffee Break
CB5

MRI Applications for MSK
SC10

Lunch
LU3

Networking Events
RC2

Thursday Feb 28

Breakfast
BR4

Finite Element Analysis & Bone Strength
SC11

Coffee Break
CB7

Clinical Computed Tomography
SC12

Lunch
LU4

Workshops
1. Quantitative Imaging in Inflammatory Arthritis
WS3

Coffee Break
CB8

Advanced X-Ray Imaging
SC13

Scientific Banquet
RC3

Friday Mar 01

Breakfast

Clinical Applications: Osteoporosis II

Coffee Break

Clinical Applications: Inflammatory Arthritis

Closing Remarks

qmski.org

info@qmski.org

+1 (403) 220-3664

PLEASE CONTACT US FOR MORE INFORMATION, AND WE WILL WORK WITH YOU
TO PREPARE A SUPPORT PACKAGE THAT FITS YOUR NEEDS